SAPIENZA
UNIVERSITÀ DI ROMA

Study on liquid metal magnetohydrodynamic flows and numerical application to a water-cooled blanket for fusion reactors

Facoltà di Ingegneria Civile e Industriale

Dottorato di Ricerca in Energia e Ambiente - Scuola di Dottorato in Scienze e Tecnologie per l'Innovazione Industriale – XXXI Ciclo

Candidate

Alessandro Tassone
ID number 1246505

Thesis Advisor

Prof. Gianfranco Caruso

January 2019

Thesis defended on 11th February 2019
in front of a Board of Examiners composed by:

Prof. Luciano Gramiccia (chairman)

Prof. Dario Ambrosini

Prof. Coriolano Salvini

Study on liquid metal magnetohydrodynamic flows and numerical application to a water-cooled blanket for fusion reactors

Ph.D. thesis. Sapienza – University of Rome

This thesis has been typeset by LaTeX and the Sapthesis class.

Version: 08th March 2019

Author's email: alessandro.tassone@uniroma1.it

To my little star
Σε αγαπώ

Abstract

One of the key components of a thermonuclear fusion reactor is the breeding blanket, which fulfills the essential functions of power extraction, tritium breeding, and shielding for radiation-sensitive components and personnel. Liquid metals, like the eutectic alloy lithium lead (PbLi), are considered attractive blanket working fluids due to their combination of excellent thermal properties, high boiling temperature, and tritium breeding capabilities. However, they are characterized also by less desirable features, one of which being the elevate electrical conductivity that results in the reactor intense magnetic field influencing the fluid motion in multiple and subtle ways. In such conditions, the liquid metal behavior can only by described by the governing equations of magnetohydrodynamics (MHD). The transition to the MHD regime is accompanied by several effects including, but not limited to, increased pressure losses due to resistive Lorentz forces, turbulence suppression, modified mass and heat transport mechanisms, etc. A complete understanding of these phenomena is of paramount importance to accurately assess the blanket performances and to realize a design able to fulfill the reactor requirements.

The Water Cooled Lithium Lead (WCLL) breeding blanket is one of the two concepts actually being studied for implementation in the DEMOnstration Fusion Power Plant (DEMO) reactor within the framework of the R&D activities coordinated by the EUROfusion consortium. This concept relies on the separate-cooled architecture, where the liquid metal is utilized exclusively as tritium breeder and neutron multiplier, whereas the role of coolant is fulfilled by pressurized water that, being a non-electrically conductive fluid, is not influenced by the MHD effects. Even if the liquid metal velocity can be minimized to a value determined only by the tritium management requirements, thus reducing the electromagnetic pressure losses compared with blanket where the liquid metal fulfills also the role of coolant, MHD phenomena are still going to drive the blanket design. Despite the importance of a full understanding of these aspects, in the past years only few research activities have been focused on the MHD phenomena occurring in WCLL concept and this was identified as a significant drawback for the blanket design hindering the achievement of a satisfying design maturity.

The research activity described in this PhD dissertation has the objective to characterize the basic MHD phenomena for the WCLL blanket with regard to pressure losses and heat transfer with the coolant. The dissertation is divided in two main parts. The first part, described in Part II, concerns a comparative analysis of several alternative configuration for the PbLi in-vessel flow path. The analysis is conducted to identify the solution with most potential for further optimization in the blanket development cycle. The main criteria adopted are MHD pressure losses minimization, flow path simplicity, ease of integration with the other reactor systems, and compliance with the remote maintenance requirements. Successively, in Part III, the effect of the magnetic field on the heat transfer is studied through numerical modeling of prototypical cases derived from the blanket configurations studied during the comparative analysis. The Computational Fluid Dynamics (CFD) code ANSYS CFX is used for this purpose and its thorough validation for several MHD benchmarks is a core part of the modeling section.

Four PbLi in-vessel flow path configurations (T01.A, T01.B, T02, and T03) are studied in the comparative analysis, investigating the effect of different preferential flow orientation, distribution and feeding scheme, cooling system layout, and structural elements arrangement on the MHD pressure losses. A detailed analysis of the PbLi path for each configuration is carried out, identifying possible critical elements and investigating alternative strategies to minimize the pressure drop for the liquid metal evolution. The study is divided according to the four main hydraulic regions of the flow path: feeding pipe, manifold, breeding zone, and draining pipe. Pressure drop correlations available in the literature are used for the estimate of both the two-dimensional and three-dimensional pressure drop term, whereas inertial and viscous effects are neglected. A detailed overview of the methodology adopted is available in Chapter 4.

In Chapter 5, the analysis results have highlighted how the bulk of the pressure drop is localized within the connection pipes with the PbLi ex-vessel loop, where the highest flow rate in the blanket is concentrated and velocity up to several cm/s is encountered. The routing scheme adopted for the feeding and draining pipe is found to significantly impact the pressure drop due to the different pipe size allowed by the remote maintenance constraints set upon the lower and upper vacuum vessel port. Although a routing through the former would be preferable due to the easier integration with the PbLi path in the blanket, the impossibility to accommodate a feeding pipe larger than 80 mm makes this approach unfeasible without recurring to electrically insulating flow channel insert (FCI) or coatings to minimize the pressure losses in the component. Moreover, the current PbLi ex-vessel loop design adopts a reference pressure of just 4.6 MPa, well below the maximum assumed value reached during the in-box LOCA transient (18 MPa). Since the wall thickness effect on the pressure losses is of paramount importance, the feasibility of feeding and draining pipes without electrical insulation for the WCLL is questionable and their layout is in need of urgent revision.

In Chapters 6 and 7, the flow in the manifold and the breeding zone is less important on the overall blanket pressure loss, but it is characterized by electromagnetic coupling and complex geometrical elements; phenomena that need to be thoroughly characterized to assess the flow distribution and avoid the formation of regions with stagnant fluid that can increase the tritium inventory above the safety limits in both the breeder and, through enhanced permeation, in the coolant. In particular, critical geometrical elements that have been identified for numerical modeling are orifices, contracting/expanding bends, and flow around obstacles. The relative slow velocity of the liquid metal in the breeding zone requires also to consider the influence of buoyancy effects on the fluid dynamics and heat transfer. Moreover, the prediction of the electromagnetic coupling effect on flow distribution is deemed to be another important aspect warranting in-depth numerical modeling.

Despite configuration T02 being the one with the lowest pressure losses, it is configuration T01.A that is found to be the one with the most potential for further optimization due to superior mechanical stability, flow path flexibility allowing alternative feeding scheme, and acceptable pressure losses in both the manifold and the breeding zone. The main uncertainties highlighted by the analysis, and that will require further study, are the complex flow distribution scheme, which relies on a complex system composed by three manifolds (one of which constituted by two

parallel arrays of channel arranged along the whole blanket spinal length), and the effect of the buoyancy forces on the breeding zone with regard to the flow around the cooling pipes and the heat transfer.

To study the influence of the magnetic field on the heat transfer, two numerical models have been created and investigated, representing the prototypical flow in the two best configurations emerged from the comparative study: T01.A and T02. The CFD code ANSYS CFX is used for this purpose. In Chapter 9, five benchmarks are carried out to validate the code performances for forced convection, natural convection (magneto-convection), and free surface flows. Theoretical solutions and experimental data are the means of comparison selected to evaluate the code capability.

For the forced convection flow, the laminar two-dimensional and three-dimensional MHD problems proposed by Smolentsev et al. [1] are carried out. For the former, the fully developed flow in a rectangular duct with insulating walls (Shercliff case) and with conducting Hartmann walls and insulating side walls (Hunt-II case) is simulated up to $Ha = 10^4$ with a 2% maximum error on the dimensionless flow rate. The flow in a circular pipe for a non-uniform applied magnetic field (fringing) is considered for the three-dimensional problem, being modeled over the experimental campaign described in [2, 3]. The code is found to have a reasonable agreement with the experimental data employed for the validation, with an error margin consistent with the results reported in the literature by other CFD codes. For the magneto-convection case, the fully developed flow in a differentially and internally heated rectangular duct are simulated and compared with the analytical solutions provided by Bühler [4], showing an excellent agreement. Finally, the thin-film flow in a rectangular chute with insulating walls is considered for the free surface benchmark. A good agreement is found with the analytical solution by Shishko [5], but the code is not able to simulate $Ha > 10^3$.

In Chapter 10, the forced convection around a single transverse pipe is studied in a configuration very similar to the one encountered in T01.A breeding zone. Both skewed magnetic field and duct walls of non-uniform thickness are preserved to model realistic electric boundary conditions. The case is analyzed in the parameter range $Re = 20 \div 80,\ Ha = 0 \div 100,\ \alpha = 0 \div 32°,$ and $c_o = 0 \div \infty$, where α is the magnetic field inclination on the obstacle axis and c_o is the obstacle wall conductance ratio. The heat transfer is found to increase with Ha due to the promotion of the flow rate in the sub-channel below the pipe, caused by leakage currents coming from the upper sub-channel through the duct electro-conductive wall. The flow pattern around the obstacle is dampened with increasing Ha and reverts to a creeping regime for $Ha \to \infty$. Pipe wall conductivity and magnetic field inclination are found to have negligible influence on both the heat transfer and three-dimensional obstacle pressure drop term, despite influencing significantly the problem flow pattern. The three-dimensional pressure drop term is estimated and found to be a weaker function of the magnetic field intensity compared with the two-dimensional pressure drop and its weight on the overall loss decreases with Ha. A correlation is proposed to estimate this quantity at higher Ha, derived from the numerical data gathered in this study and from basic physics considerations. Further studies considering mixed convection with non-uniform volumetric heating and a more complex geometry with multiple pipes are deemed necessary to completely characterize this case.

In Chapter 11, mixed convection flow in the upward direction in presence of transverse curved obstacles is investigated to gain some insights about the heat transfer for the elementary cell of configuration T02. The case is analyzed for a single cooling element of the FW channel (two nested double walled Eurofer U-pipes) in both hydrodynamic ($Ha = 0$) and MHD conditions ($Ha = 8.5 \cdot 10^3$). The non-uniform volumetric heating in the FW channel is accurately modeled with an exponentially decreasing function with average volumetric power density $Q = 7$ MW/m^3 corresponding to $Gr = 5.76 \cdot 10^{10}$, and the conservative boundary condition of perfectly conducting duct and pipe walls is assumed. The breeding zone cooling system is found to perform well in hydrodynamic conditions due to the flow being dominated by the buoyancy forces, which cause the onset of an intense turbulent regime. However, the transition to the MHD regime is accompanied by severely dampened velocity oscillations and heat transfer with the temperature in the cell exceeding 1000 K, which is not acceptable with the Eurofer temperature limit ($T_{\max} \leq 823$ K). To reduce the maximum PbLi temperature, a reduction in the vertical pitch separating two successive cooling elements (i.e. increasing their density) from 60 mm to 40 mm and moderate passive refrigeration from the first wall cooling system (100 kW/m^2) are adopted, bringing the maximum temperature in the cell at $T \approx 820$ K. Altering the pipe layout could conceivably result in enhanced performances, but it is unlikely to be feasible due to manufacturing issues in the fabrication of the curved Eurofer pipes. Overall, the proper refrigeration of the elementary cell seems to be quite challenging even considering less conservative boundary conditions for the solid surfaces. A possible strategy could involve a radical rearrangement of the breeding zone to allow the placement of pipes complying with the manufacturing requirements and more able to provide an effective cooling of the region close to the FW.

Sommario

Il breeding blanket è uno dei componenti chiave per il funzionamento di un reattore a fusione termonucleare, in quanto responsabile dell'estrazione della potenza termica generata dalle reazioni nucleari, della surgenerazione del trizio, e della schermatura per i componenti sensibili alle radiazioni e il personale. I metalli liquidi, come la lega eutettica di piombo e litio (PbLi), sono considerati come attraenti fluidi tecnici da impiegare in questo componente a causa della loro combinazione di eccellenti proprietà termiche, alta temperatura di ebollizione e capacità di generare trizio. Tuttavia, questi sono caratterizzati anche da caratteristiche meno desiderabili, una tra tante l'elevata conduttività elettrica che, interagendo con l'intenso campo magnetico del reattore, causa cambiamenti multiformi e significativi nel comportamento fluidodinamico. In tali condizioni, il moto del metallo liquido non può essere più descritto con le usuali equazioni della fluidodinamica, ma bisogna ricorrere alla teoria magnetoidrodinamica (MHD). La transizione al regime MHD è accompagnata da diversi effetti tra cui, a titolo esemplificativo, si possono ricordare maggiori perdite di carico dovute ad attrito elettromagnetico, soppressione della turbolenza, modifiche nelle caratterische di scambio termico e fenomeni di trasporto della massa, ecc. Una comprensione completa di questi fenomeni è di fondamentale importanza per valutare con precisione le prestazioni generali del componente e realizzare un progetto in grado di soddisfare i requisiti del reattore.

Uno dei due concept di breeding blanket attualmente studiati per l'implementazione nel reattore DEMO nell'ambito delle attività di ricerca e sviluppo coordinate dal consorzio EUROfusion è il Water Cooled Lithium Lead (WCLL). Questo blanket si basa sull'architettura a raffreddamento separato, dove il metallo liquido è utilizzato esclusivamente come breeder triziogeno e moltiplicatore di neutroni, mentre il refrigerante è acqua pressurizzata che, essendo un fluido non elettricamente conduttivo, non è influenzata dagli effetti MHD. In questo modello di blanket, la velocità del metallo liquido può essere minimizzata a un valore sufficiente a garantire l'estrazione del trizio ma, anche se le perdite di carico MHD sono ridotte rispetto a un blanket dove il fluido svolge anche la fuzione di refrigerante, i fenomeni MHD continuano a guidare il design globale. Nonostante l'importanza di una piena comprensione dei fenomeni MHD per progettare efficacemente una blanket a metallo liquido, negli anni passati non è stata condotta alcuna attività di ricerca dedicata sul WCLL e questa importante mancanza è stata identificata come pregiudizievole al raggiungimento di una soddisfacente maturità del progetto.

L'attività di ricerca descritta in questa tesi di dottorato ha come obiettivo la caratterizzazione dei principali fenomeni MHD nel WCLL blanket, in particolare riguardo alla stima della perdita di carico e dello scambio termico con il refrigerante. La tesi è divisa in due parti principali. La prima parte, discussa nella Parte II, copre l'analisi comparata di diverse configurazioni alternative per il percorso del PbLi all'interno del Vaacum Vessel (VV). L'obiettivo principale di questa analisi è l'identificazione della configurazione con il maggior potenziale, la quale verrà poi ulteriormente sviluppata nelle successive fasi del progetto del blanket. I criteri considerati sono stati l'entità della perdita di carico MHD, la semplicità del percorso idraulico, la facilità di integrazione con gli altri sistemi di DEMO e la capacità

di soddisfare i requisiti del Remote Maintenance. Nella seconda parte, descritta nella Parte III, l'effetto del campo magnetico sullo scambio termico è studiato con l'ausilio di codici numerici per alcuni casi prototipici sviluppati a partire da due delle configurazioni analizzate nella prima parte della tesi. Il codice di Fluidodinamica Computazione (CFD) ANSYS CFX è utilizzato per questo scopo e, all'interno della tesi, è sottoposto a un approfondito processo di validazione articolato in numerosi benchmark per i più comuni flussi MHD.

Quattro diverse configurazioni del WCLL (identificate dalle sigle T01.A, T01.B, T02 e T03) sono analizzate nel contesto dell'analisi comparata per evidenziare l'effetto sulla perdita di carico MHD di differenti direzioni preferenziali per il flusso, schemi di distribuzione e raccolta del metallo liquido, geometria del sistema di refrigerazione e disposizione degli elementi strutturali. Un'analisi dettagliata del percorso del PbLi è eseguita per evidenziare elementi geometrici critici e strategie alternative per la minimizzazione della perdita di carico. Lo studio è suddiviso secondo le principali regioni idrauliche identificate nel percorso del PbLi: il feeding pipe, il manifold, la breeding zone e il draining pipe. La stima della perdita di carico è effettuata attraverso correlazioni disponibili in letteratura per la valutazione dei termini bidimensionali e tridimensionali. L'effetto dell'attrito viscoso e delle forze inerziali è invece trascurato, seguendo la trattazione più comune per flussi MHD ad elevata intensità del campo magnetico. Una completa descrizione della metodologia adottata nello studio è presentata nel Capitolo 4.

Nel Capitolo 5, il feeding e il draining pipe sono il focus dell'analisi. I risultati dell'analisi hanno dimostrato come il massimo della perdita di carico sia localizzato nel feeding e draining pipe, ossia gli elementi di connessione tra il percorso del PbLi all'interno del VV e il loop principale dislocato al di fuori di questo, dove è concentrata tutta la portata in ingresso (o uscita) dal segmento di blanket e il metallo liquido raggiunge velocità di diversi cm/s. Lo schema di carico e scarico adottato dal blanket ha un effetto significativo sulla perdita di carico, giacché i vincoli imposti dal Remote Maintenance sulla dimensione del condotto sono più permissivi per la VV upper port rispetto alla lower port. Malgrado uno schema di carico attraverso quest'ultima sia preferibile per semplificare il percorso idraulico all'interno del blanket, la necessità di utilizzare un condotto con diametro massimo di 80 mm rende questo approccio impossibile da adottare a meno di revisioni consistenti nel progetto della lower port o tramite il disaccoppiamento elettrico del flusso di metallo liquido dal feedign pipe utilizzando appositi Flow Channel Inserts (FCIs). In aggiunta, l'attuale loop del PbLi adotta una pressione di progetto uguale a 4.6 MPa, insufficiente per sopportare il massimo valore (18 MPa) previsto per il transitorio accidentale dell'in-box LOCA, uno dei design basis accidents del blanket, e una revisione di questo parametro comporterebbe un sensibile incremento nello spessore della parete del condotto. Data la grande sensibilità della perdita di carico su questo parametro, l'utilizzo di feeding e draining pipe privi di un isolamento elettrico, come attualmente previsto nel WCLL, potrebbe non essere fattibile in condizioni più realistiche di quelle attualmente considerate nell'ambito del design del blanket.

Nel Capitolo **??**, il manifold e la breeding zone sono il focus dell'analisi. Il flusso nel manifold e nella breeding zone è meno importante in termini di perdita di carico, ma è in ogni caso caratterizzato da importanti fenomeni che impattano direttamente la distribuzione del metallo liquido e che devono essere investigati;

in particolare, l'accoppiamento elettromagnetico tra canali in contatto elettrico e la presenza di elementi geometrici complessi. Caratterizzare questi fenomeni è necessario per localizzare dove il fluido potrebbe accumularsi e stagnare: questo comporterebbe rilevanti problemi di sicurezza dovuti all'accumulo del trizio e alla sua permeazione nel refrigerante. Elementi geometrici che sono relativamente poco caratterizzati e che rivestono un ruolo fondamentale nel percorso idraulico del WCLL sono gli orifizi, curve con variazione di area di passaggio e flusso attorno ad ostacoli. Giacché il fluido si muove a basse velocità, l'influenza delle forze di galleggiamento sulla fluidodinamica e lo scambio termico vanno attentamente considerati.

Malgrado la configurazione con le minori perdite di carico sia la T02, la configurazione ad avere il miglior potenziale per il successivo sviluppo del blanket è la T01.A grazie alla sua maggiore stabilità meccanica, flessibilità nel variare il collegamento con il loop del PbLi e relativamente basse perdite di carico nel manifold e nella breeding zone. Tuttavia, alcune incertezze sono emerse nel corso dell'analisi, le quali meriteranno ulteriore studio nei prossimi anni: il complesso schema di distribuzione, che utilizza un complesso sistema composto di tre manifold (uno dei quali costituito da due insiemi di stretti canali rettangolari che corrono per tutta l'altezza del blanket), e l'effetto delle forze di galleggiamento sul flusso e lo scambio termico nella breeding zone, specialmente nel contesto del flusso intorno ai tubi di refrigerazione.

Per studiare l'effetto del campo magnetico sullo scambio termico, due modelli numerici sono stati creati per investigare il flusso in due configurazioni prototipiche rappresentative rispettivamente della breeding zone di T01.A e T02. Il codice CFD ANSYS CFX è stato utilizzato a questo scopo. Nel Capitolo 9, cinque benchmark sono impiegati per validare il codice per casi di magneto-idraulica (convezione forzata MHD), magneto-convezione (convezione naturale MHD) e flussi MHD a superficie libera. Soluzioni analitiche e dati sperimentali sono utilizzati per dimostrare la fisicità dei risultati ottenuti dal codice.

Due casi di magneto-idraulica sono utilizzati per validare il codice, un problema bidimensionale e uno tridimensionale, entrambi proposti da Smolentsev et al. [1]. Per il problema bidimensionale, il flusso completamente sviluppato in un canale rettangolare con pareti perfettamente isolate (flusso di Shercliff) e nello stesso canale con pareti di Hartmann perfettamente conduttive (flusso di Hunt-II) è simulato per un'intensità del campo magnetico fino a $Ha = 10^4$ con un errore massimo del 2% sulla portata adimensionale. Per il problema tridimensionale, il flusso in un condotto circolare sottoposto a un campo magnetico non uniforme è considerato, prendendo a modello l'esperimento descritto nelle Refs. [2,3]. Il codice riproduce con buona qualità i dati sperimentali, mostrando un margine d'errore consistente con quanto riportato in letteratura da altri codici simili. Due casi di magneto-convezione sono trattati per il flusso completamente sviluppato in un canale rettangolare verticale e infinitamente alto sottoposto a riscaldamento differenziale e interno. I risultati del codice sono confrontati con la soluzione analitica proposta da Bühler [4], dimostrando un'eccellente accuratezza. Come ultimo benchmark, un flusso completamente sviluppato a superficie libera per un condotto inclinato con substrato isolato è simulato fino ad $Ha = 10^3$ dimostrando una buona accuratezza con la soluzione analitica sviluppata da Shishko [5].

Nel Capitolo 10, il flusso in convezione forzata intorno a un cilindro transversale è studiato come rappresentativo della breeding zone della configurazione T01.A.

Realistiche condizioni al contorno elettromagnetiche, quali il campo magnetico inclinato e pareti del condotto con spessore non uniforme, sono impiegate per aumentare l'accuratezza del modello. Il caso è analizzato nello spazio dei parametri $Re = 20 \div 80,\ Ha = 0 \div 100,\ \alpha = 0 \div 32°,$ and $c_o = 0 \div \infty$, dove α è l'inclinazione del campo magnetico sull'asse dell'ostacolo e c_o è il rapporto di conducibilità caratteristico dell'ostacolo. Lo scambio termico aumenta con l'aumentare di Ha a causa della promozione del flusso nel sotto-canale inferiore, dove correnti indotte nel sotto-canale nella parte superiore dell'ostacolo penetrano e tendono a generare forze di Lorentz non resistive, con conseguente incremento localizzato della velocità media rispetto al caso puramente idrodinamico. Tuttavia, il regime di efflusso attorno all'ostacolo è gradualmente soppresso all'aumentare di Ha e assume le caratteristiche di un creeping flow per $Ha \to \infty$. La conducibilità dell'ostacolo e l'inclinazione del campo magnetico hanno un'influenza secondaria sullo scambio termico e la perdita di carico, malgrado alterino in maniera sensibile la fluidodinamica del problema. Il valore della perdita di carico tridimensionale è stimato e si osserva che la sua dipendenza da Ha sembra essere più debole rispetto alla componente bidimensionale, la quale tende a dominare la perdita di carico totale all'aumentare di Ha. Una correlazione per predire il valore della perdita di carico tridimensionale ad Ha più elevati di quelli considerati in questo studio è proposta a partire dai dati numerici raccolti. Un'estensione dell'analisi al flusso in convezione mista e per geometrie più complesse, per esempio cilindri multipli ravvicinati, è consigliabile per caratterizzare completamente questo problema.

Nel Capitolo 11, la convezione mista per un flusso ascendente in presenza di ostacoli curvi trasversali è analizzato nel contesto dello scambio termico tra il PbLi e il sistema di refrigerazione della breeding zone per la configurazione T02. L'analisi è focalizzata su un singolo elemento refrigerante (due tubi a U annidati) per il canale vicino alla FW, cioé la zona maggiormente sollecitata dal punto di vista termico, in condizioni puramente idrodinamiche ($Ha = 0$) e magnetoidrodinamiche ($Ha = 8.5 \cdot 10^3$). Il riscaldamento non-uniforme nel canale è modellato con una funzione esponenziale decrescente con valore medio $Q = 6.7$ MW/m^3, il quale corrisponde a $Gr = 5.76 \cdot 10^{10}$, e le superifici confinanti il metallo liquido sono ipotizzate avere conducibilità infinita. Il sistema di refrigerazione funziona in maniera accettabile in condizioni idrodinamiche grazie all'efficiente scambio termico promosso dal regime turbolento innescato dalle forze di galleggiamento. La transizione al regime MHD comporta la soppressione della turbolenza e il degrado dello scambio termico; la temperatura massima del PbLi nel canale supera i 1000 K, chiaramente incompatibile con i requisiti per il funzionamento dei materiali strutturali ($T_{\max} \leq 823$ K). Per ridurre la temperatura nel PbLi, il pitch verticale tra elementi di refrigerazione viene ridotto da 60 a 40 mm e un moderato flusso termico (100 kW/m^2) dovuto alla refrigerazione passiva della BZ da parte del sistema di raffreddamento della FW è introdotto, portando la temperatura massima nella cella a $T \approx 820$ K. Modifiche al layout dei tubi potrebbero portare a un ulteriore incremento nelle performance del sistema di refrigerazione. In ogni caso, garantire la refrigerazione del condotto sembra essere particolarmente complicato, anche considerando condizioni al contorno elettromagnetiche meno conservative di quelle ipotizzate in questo studio, a causa dei limiti imposti nella struttura degli elementi di rinforzo del blanket e dei tubi da parte delle tecniche di manufacturing.

Acknowledgments

It is normally suggested to keep the acknowledgments section brief and on point since it is not considered very professional to have a long (and personal) one in a scientific document. I must disagree on this topic since I could not considered this dissertation complete until I have thanked all the people that helped me in these three years.

My supervisor, Prof. Gianfranco Caruso, is the first one that I wish to thank. Prof. Caruso gave me the opportunity to work in this fascinating field. His constant advice, support and, above anything else, patience have been invaluable to me and he has always struggled to let me work in the best possible conditions. I hope that my work has matched his expectations. Special thanks are also due to Ing. Alessandro Del Nevo, who had first the merit to persuade Prof. Caruso to start this line of research and, afterwards, always had great interest in my work. I wish to thank my reviewers, Prof. Michele Ciofalo and Dr. Sergey Smolentsev, who took the time to examine this long dissertation. I can not say how much I appreciate their insights and, even if probably not enough to reward their efforts, they deserve a mention here.

I was very lucky to share these three years with a bunch of very fun and talented young scientists who I am proud to call my colleagues but, foremost, my friends. The first thought goes to Matteo Nobili, who I constantly pestered for two years before he got so annoyed that his only option was to find a job somewhere else to get rid of me. I can not tell you how much sad I was when you left and how much I miss your advice, so really thank you. Vincenzo who had and still has the honor to be my office "compagno di banco" is a not so distant second in my thoughts, and as well is the other Matteo, commonly known as "the Mamba", with both of whom I have shared so many moments in the last three years. Thank you guys. I take this time also to give a shout-out to Fabio, Paolo, Cristiano and, last but not least, Franco "the Chinese".

In the last year, I had the opportunity and pleasure to support four Master's students during the work for their thesis who, directly or indirectly, helped me to grow professionally and contributed to this dissertation: Letizia, Simone, Lorenzo, and Jasper. I wish to thank you for your confidence in me and I ask for your forgiveness for my shortcomings. You are all very talented and I am completely sure you will do great in the next part of your life.

My friends and family are the ones that probably deserve the most thanks, since they have done the most tricky task: loving and supporting such a difficult person as myself. They are too many to thank individually here, but I would like to acknowledge who has been, even if the farthest from me physically, the closest to my heart. Luca and Valentina, thank you. I hope it has been a fun ride.

Finally, thank you Vicky. You know why.

This work has been carried out within the framework of the EUROfusion Consortium and has received funding from the Euratom research and training programme 2014-2018 and 2019-2020 under grant agreement No 633053. The views and opinions expressed herein do not necessarily reflect those of the European Commission.

Contents

List of Figures

List of Tables

Acronyms and nomenclature

Acronyms and abbreviations

APG	Axial Pressure Gradient
BB	Breeding Blanket
BSP	Bottom Supporting Plate
BSS	Back Supporting Structure
BZ	Breeding Zone
BZO	Breeding Zone Orifice
CFD	Computational Fluid Dynamics
CM	Collection Manifold
CMHD	Computational Magnetohydrodynamics
CS	Central Solenoid
DCLL	Dual Coolant Lithium Lead
DEMO	DEMOnstration Fusion Power Plant
DM	Distribution Manifold
DMT	Distribution Manifold Tank
DP	Draining Pipe
D-T	Deuterium-tritium (fusion reaction)
DWT	Double Walled Tube
EOF	End-of-Flat-Top
EU	European Union
EUROfusion	European Consortium for the Development of Fusion Energy
FCI	Flow Channel Insert
FP	Feeding Pipe
FW	First Wall
HCLL	Helium-Cooled Lithium Lead
HCPB	Helium Cooled Pebble Bed
IB	Inboard blanket
ITER	International Thermonuclear Experimental Reactor
LM	Liquid Metal
LOCA	Loss of Coolant Accident
MHD	Magnetohydrodynamics
MMS	Multi Module System
OB	Outboard blanket
PbLi	Lithium lead eutectic alloy

PFC	Plasma-Facing Component
PFC	Poloidal Field Coil
PHTS	Primary Heat Transport System
PWR	Pressurized (light) water reactor
RAFM	Reduced activation ferritic martensitic (steel)
RL	Recovery Leg (spinal manifold)
RM	Remote Maintenance
SL	Supply Leg (spinal manifold)
SM	Spinal Manifold
SMS	Single Module System
SOF	Start-of-Flat-Top
SP	Stiffening Plate
SPO	Stiffening Plate Orifice
TBM	Test Blanket Module
TBR	Tritium Breeding Ratio
TFC	Toroidal Field Coil
TPD	Transverse Pressure Difference
V&V	Verification and Validation
VV	Vacuum Vessel
WCLL	Water-Cooled Lithium Lead

Nomenclature

Greek symbols

α	Magnetic inclination (on toroidal axis)
α_t	Thermal diffusivity
β	Thermal expansion coefficient
Γ	Mass flow rate
δ	Wall thickness
ζ	Local MHD resistance coefficient
θ	Angle
κ	Thermal conductivity
μ	Dynamic viscosity
ν	Kinematic viscosity
ρ	Density
σ	Electric conductivity
ϕ	Electric potential

Latin symbols

a	Half-width of rectangular duct parallel to magnetic field direction
b	Half-width of rectangular duct perpendicular to magnetic field direction
B	Magnetic field

d	Pipe diameter
g	Gravity acceleration
h	Duct height
J	Current density
L	Characteristic length
n	Normal direction
p	Pressure, poloidal coordinate
$q"$	Heat flux
Q	Volumetric power density
r	Pipe radius, radial (blanket) coordinate
R	Radial (tokamak) coordinate
S	Curvilinear length
t	time, toroidal coordinate
T	Temperature
u_0	Characteristic/average velocity
v	Velocity

Dimensionless groups

c	Wall conductance ratio
Gr	Grashof number
Ha	Hartmann number
Ly	Lykoudis number
N	Interaction parameter or Stuart number
Pe	Péclet number
Pr	Prandtl number
Ra	Rayleigh number
Re	Reynolds number
Ri	Richardson number
Rm	Magnetic Reynolds number

Part I

Introduction

Chapter 1

Research motivation and outline

1.1 Motivation and aim

One of the key components of a nuclear fusion reactor, arguably the most important, is the breeding blanket (BB). In a fusion power plant, the blanket must accomplish several functions that are critical for the reactor operation: extract the heat released from the nuclear reactions, generate the fuel necessary for the plant self-sufficiency, and provide radiation shielding to other reactor systems and personnel. The extreme and complex environment in which this component is envisioned to operate and the stringent requirements stemming from the necessity to achieve disparate, and sometimes conflicting, functional objectives combine to create a daunting engineering challenge that, however, must be overcome to move forward in the route to the development of fusion power.

Liquid metals (LM) are considered attractive blanket working fluids due to their combination of excellent thermal properties, high boiling temperature, and tritium breeding capabilities. However, in addition to these features, they pose significant engineering challenges as well due to the smaller operative experience accumulated in their handling (compared with more traditional fluids like water) and less desirable properties. Referring to the most prominent candidate fluid, which has been the lithium-lead eutectic alloy (PbLi) for at least 30 years, one must remember among its drawbacks the chemical reactivity with water and air, toxicity, and being violently corrosive. Moreover, liquid metals are electrically conductive and, in a magnetic confinement reactor like a tokamak, their motion is influenced by the plasma containment in complex and subtle ways. Therefore, it is evident that the proper engineering design of a LM breeding blanket is not a trivial task and calls for intense studies and research activities to accrue the required basic knowledge and know-how. In this context, the performing of high-quality experimental campaigns and the development of accurate predictive numerical tools play a key role.

Since 2014, the European R&D activities in the nuclear fusion field have been coordinate by the European Consortium for the Development of Fusion Energy (EUROfusion) to achieve the stated goal of an operative DEMOnstration Fusion Power Plant (DEMO) by 2050. In this framework, the development of two alternative blanket designs is being pursued in the DEMO pre-conceptual phase: the Helium Cooled Pebble Bed (HCPB), based on solid breeder technology, and the Water

Cooled Lithium Lead (WCLL), based on liquid breeder technology. The activities on this latter blanket concept are directly coordinated by the Italian national R&D agency ENEA through the Experimental Engineering Division (FSN-ING) of the Brasimone Research Center.

One of the open issues in the WCLL blanket development is to assess the influence of magneto-hydrodynamic (MHD) effects on the breeder fluid-dynamics and heat transfer mechanisms with the non-electrically conductive coolant. In particular, the presence of a voluminous breeding zone (BZ) cooling system composed by electro-conductive pipes is a distinguishing feature of the design and it is expected to significantly affect the breeder hydraulic path. Mixed convection phenomena, heat transfer suppression, and enhanced corrosion are other relevant side effects of the MHD flow regime that could significantly impact the blanket performances. Despite the importance of a full understanding of the MHD phenomena to effectively design a LM blanket, in the past years only few dedicated research activity were conducted on the WCLL concept and this lack was identified as preventing the achievement of a satisfying design maturity.

The research activity described in this PhD dissertation was started to address this issue and it is fruit of the cooperation between ENEA and one of its linked third parties, the DIAEE (Department of Astronautical, Electrical, and Energy Engineering) of Sapienza University of Rome. Due to the inherent complexity of the MHD phenomena and their significant impact on almost every aspect of the blanket design, the activity was focused on the study of two topics that were judged as the most relevant for the component development: electromagnetic pressure drop and MHD heat transfer regime. Despite being in a certain sense elementary, the influence of these effects on the component design can not be easily dismissed and, therefore, the scope of this activity was directed to investigate them and to lay the foundation for successive and more advanced research lines.

Numerical modeling employing Computational Magnetohydrodynamics (CMHD) codes was recognized from the beginning to be instrumental in achieving this goal. A relevant part of the research line was devoted to the verification and validation (V&V) of the electromagnetic module of the general-purpose CFD code ANSYS CFX and its subsequent use in the simulation of relevant MHD phenomena. Due to the limitation of direct numerical simulation tools in representing the MHD pressure drop at blanket-scale level, theoretically and numerically developed correlations were employed for its preliminary assessment on the global PbLi hydraulic path and the comparative analysis between proposed WCLL configurations.

1.2 Document outline

The present document is organized in four parts: introduction, blanket configuration comparative analysis, numerical modeling, and conclusions

In Part I, the framework and theoretical background necessary to introduce the research activity is laid out. The dissertation rationale is described in Chapter 1. An introduction to the technology of magnetic confinement fusion reactors is provided in Chapter 2 and an elementary description of the most prominent features of the WCLL blanket concept is given. In Chapter 3, the MHD transport equations for

an incompressible electrically conductive fluid are derived at first for the particular case of forced convection and isothermal fluid (magneto-hydraulics, Section 3.3), and are then extended to encompass the MHD-thermal coupling and the appearance of buoyancy forces that drive the fluid (magneto-convection, Section 3.4). The basic phenomena for both the magneto-hydraulic and magneto-convective regimes are then exposed with the aid of simple theoretical cases.

In Part II, four alternative blanket configurations are analyzed to assess the MHD pressure drop in the PbLi hydraulic path and to select the more favorable for further optimization. The methodology and boundary condition of the analysis are summarized in Chapter 4 and its results are reported in Chapters 5 to 7 for, respectively, the connection pipes with the ex-vessel PbLi loop, the manifolds, and the breeding zone. The comparative analysis conclusions are summarized in Chapter 8.

In Part III, some relevant WCLL phenomena are analyzed with the aid of a CMHD code. The tool selected for the numerical modeling is the general purpose CFD code ANSYS CFX. The validation of the code is performed through several benchmarks and it is covered in Chapter 9. Then, the code is applied to the investigation of the forced convection flow around a pipe of arbitrary conductivity for skewed magnetic field and inside a duct of non-uniform wall-thickness. The results of this activity are reported in Chapter 10. The mixed convection in a vertical rectangular duct with curved pipes is the subject of Chapter 11.

Finally, Part IV summarizes the main conclusions and recommends further activities to be conducted in the next years.

Chapter 2

Fusion reactor technology

2.1 Fusion energy

A nuclear fusion reaction is defined as the process through which two atomic nuclei overcome the mutual repulsive Coulombian force and form the nucleus of a heavier physical element plus other associated subatomic particles. In accordance with the mass-energy conservation principle, the reaction is accompanied by a net energy release (or absorption) equal to the difference between the total binding energy of the parent and child particles. The fusion of elements lighter than iron generally yields a net energy release, since these are characterized by the largest binding energy per nucleon, whereas the opposite is true for elements heavier than iron, which are more likely to release energy through natural radioactive decay or triggered fission reactions. Fusion energy is the most dense energy source known to mankind and it is the process that powers all main sequence stars, including the Sun, and, thus, is directly or indirectly the origin of all the accessible energy sources on Earth [6].

Since its discovery in the 30s of the past century, the quest to realize a device able to sustain controlled fusion reactions has been one of the main goals pursued by the worldwide scientific community. However, conversely to uncontrolled fusion, that has been employed with remarkable success since the 50s to power high-yield nuclear weapons, the realization of fusion reactions for civilian purposes has so far proven to be elusive and it has become in the popular view more an unattainable dream and the matter of bombastic headlines, rather than a tangible scientific goal [7].

A large-scale, sustainable and predictable low-carbon power source is needed now more than ever to match the increasing energy demand worldwide and to provide the stability to compensate the short-term and seasonal variations in the power

output foreseen for an energy mix heavily supplied by renewable sources such as wind and solar. Due to the struggle faced by nuclear fission in gaining large popular acceptability and the recognized necessity to phase-out heavy-carbon energy sources in order to address climate change, fusion energy is considered the ideal candidate to provide such baseload energy supply. However, to make a real contribution to the energy problem, fusion must demonstrate its feasibility and competitiveness in a reasonable time scale and attain the status of industrially exploitable power source in the course of the 22nd century [8].

To realize this goal, the 2018 EUROfusion Roadmap identifies three fundamental steps to be achieved [8]:

1. Demonstration of large scale fusion power (high power burning plasma)

2. Steady or quasi-steady supply of electricity to the grid employing a closed fuel cycle

3. Development of science, technology, and industry knowledge basis to allow large-scale commercial deployment

The demonstration of high power burning plasma is the main goal of the International Thermonuclear Experimental Reactor ITER, actually in construction in France, and scheduled to commence operation, after numerous delays, in 2025. It is still too much early to indicate a reasonable time frame for the accomplishment of the first step, but forecasts range between 2035 and 2040 [8].

Once large scale fusion power is demonstrated, the construction of a DEMOnstration Fusion Power Plant (DEMO) could begin in earnest in order to demonstrate the successive steps: the supply of electric power to the grid and the realization of a closed fuel cycle. In order to attain an operational DEMO around 20 years by the demonstration of plasma ignition in ITER, preliminary studies must be carried out to create a consistent conceptual design of the power plant and to allow the necessary degree of flexibility to eventually accommodate the outcomes of the experimental campaigns in ITER and the other satellites projects [8].

2.2 DEMO Reactor

The EU DEMO reactor relies on the thermonuclear method to produce thermal power via fusion reactions. The nuclear fuel is heated at extremely high temperature ($\approx$ 100 millions degrees) in order to maximize the reaction probability by relying on quantum tunneling to overcome the Coulombian repulsion. Due to the extreme temperature involved, the nuclear fuel is completely ionized and becomes a plasma that, as a result of the heating, tends to expand and dissipate its energy, thus terminating the fusion reactions [6].

The most convenient reaction for thermonuclear fusion is the one involving the two heavier hydrogen isotopes, deuterium (D) and tritium (T), that is described by the expression

$$\mathrm{D}_1^2 \ + \ \mathrm{T}_1^3 \ \rightarrow \ \mathrm{He}_2^4 \ (3.5 \text{ MeV}) \ + \ \mathrm{n}^0 \ (14.1 \text{ MeV}) \tag{2.1}$$

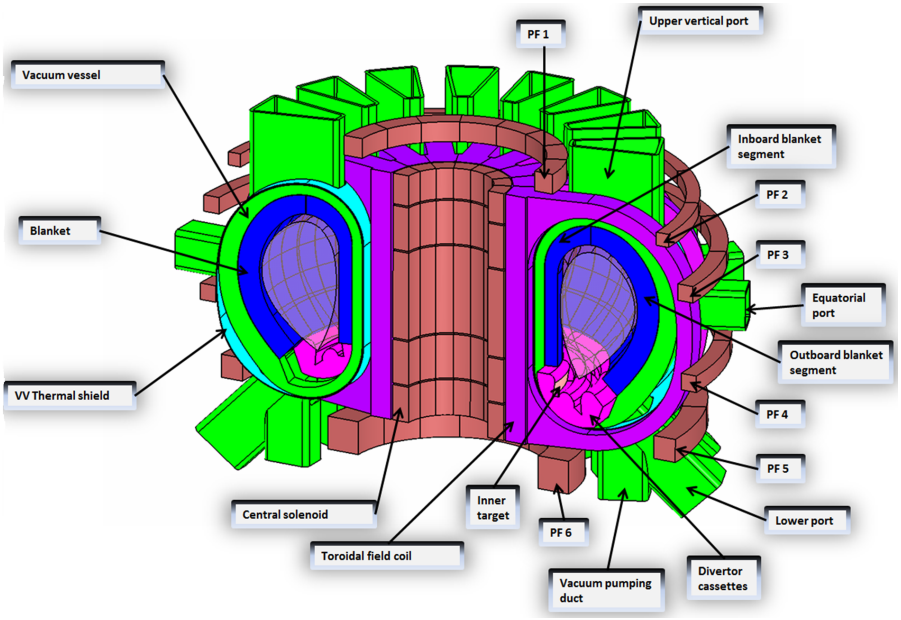

Figure 2.1. DEMO reactor general layout [9]

The D-T reaction is characterized by the highest reactivity at the lowest temperature of all the technical relevant fusion reactions [6]. The reaction products are an alpha particle that, being electrically charged, is relatively easy to keep in the plasma and whose energy can be usefully employed to maintain the desired temperature conditions, and a neutron. This latter particle is intensely energetic and it is very difficult to contain in the plasma, from which it escapes bombarding the reactor structural components and causes severe damage, heating and activation. These phenomena are deleterious with regard to the plant lifetime, but the fusion neutrons are also essentials for the reactor operation, since their energy can be easily extracted as thermal power by the reactor coolant and provide a mean to replenish the fuel supply via breeding.

To keep producing thermal power, a confinement scheme must be employed to contain the plasma in a stable state in such conditions that allow the continuous undergoing of nuclear reactions. As a secondary, but not trivial requirement, the confinement must provide thermal insulation and avoid the contact with the reactor structural materials and components. Several confinement methods are possible with the most mature and well understood being based on strong magnetic fields that trap the electrically charged plasma particles in orbit around the field lines. In the EUROfusion roadmap, two magnetic confinement devices are considered on the route to the DEMO reactor: the *tokamak* and the *stellarator*. The former is considered as the reference scheme and it constitutes the baseline for the DEMO design, whereas the latter is the main back-up that is considered the long-term alternative if the tokamak configuration will be eventually demonstrated to be unfeasible for implementation in a fusion power plant [8].

In Figure 2.1 the general layout of the integrated EU DEMO reactor is shown [9–11]. In a tokamak fusion reactor, the plasma is confined in a torus shape and the

reactor components are arranged around it. The main ones are [10]:

- **Vacuum Vessel (VV)**: encloses the plasma chamber, provides a high-vacuum environment which improves the plasma stability, and provides structural support for the in-vessel components (blanket, divertor, etc.).
- **Divertor**: is the particle and power exhaust system of the reactor and it is tasked with the removal of the spent helium ashes and other impurities from the plasma. As such, it is subjected to very intense heat loads. Water is the coolant of choice and tungsten is employed as plasma-facing armor. Ribbed copper tubes carry the coolant.
- **Magnet**: provides the magnetic field used for the plasma confinement and is composed by low-temperature superconducting Nb_3Sn coils refrigerated by liquid helium. It is composed by three different sub-systems: **toroidal field coils (TFC)**, **poloidal field coils (PFC)**, and **central solenoid(CS)**. The TFCs are wrapped around the plasma chamber and provide the principal magnetic field component, whose field lines are aligned with the torus axis. The PFCs are situated outside of the TFCs and are employed to improve the plasma stability by fine-tuning its shape. The CS is placed at the center of the torus and induces an intense current in the plasma which, in turn, creates a transient magnetic field that twists the main field lines and allows the stable plasma operation.
- **First wall/blanket**: is tasked with the extraction of the thermal power deposited by the fusion neutrons and plays a fundamental role in the reactor fuel cycle, since it is instrumental in achieving the plant tritium self-sufficiency. The first wall is a plasma-facing component that is integrated with the blanket and sustains a relative high thermal load.
- **Cryostat**: is situated outside of the vacuum vessel and the other in-vessel components. It provides the high-vacuum and ultra-cold environment necessary for the operation of the superconducting coils and the plasma chamber.

Other relevant auxiliary systems are the Tokamak External Heating, that employs injection of neutral particle beams and cyclotron heating to heat up the plasma to the target temperature required for the start of fusion reactions, and the Tritium Extraction System, that it is tasked for the removal of the tritium from the breeder and restore the reactor fuel supplies. Reduced activation ferritic martensitic (RAFM) steel Eurofer is employed as structural material for the in-vessel components, whereas AISI ITER-grade 316 stainless steel is adopted for the VV [10].

Due to the necessity to provide an intense internal current to guarantee the plasma stability and the inherent self inducting nature of the stabilizing magnetic field, fusion reactors based on the tokamak confinement scheme are pulsed machine, where a long burning phase, during which thermal power is generated, it is then followed by a shorter interval, called dwell, during which the central solenoid transformer is recharged in preparation for the next pulse. For EU DEMO, the pulse is assumed to last ≈ 2 hours, followed by a dwell ≈ 10 minutes long. Under these assumptions, the thermal fusion power is $\approx 2000\ \mathrm{MW_{th}}$ and the net electrical power is $\approx 500\ \mathrm{MW_e}$ [10].

The pulsed nature of tokamak devices poses another significant engineering challenge in the development of the balance of plant, since this regime of operation is quite undesirable for the turbo-machinery, and it is a favorable point for stellarator devices that are, in turn, inherently steady-state machines. To address this issue, several strategies have been proposed to mitigate the deleterious effect of plasma pulsing on the plant turbo-machinery and the electric grid as a whole. The current leading proposal relies on an intermediate heat transfer system that accumulates part of the energy released during the pulse in a tank filled with molten salt (Energy Storage System, ESS), that can then be used to continuously run the turbine during the dwell [11].

In order to successfully develop and deploy an operational DEMO reactor in the 2050s-2060s, eight key issues must be addressed [8]:

1. Demonstrate high power plasma operation regimes
2. Demonstrate efficient particle and power exhaust systems
3. Develop and extensively validate reduced activation and neutron tolerant materials
4. Demonstrate plant tritium self-sufficiency
5. Demonstrate fusion inherent safety features in a power plant environment
6. Develop an integrated DEMO design with high reliability and availability
7. Demonstrate that fusion power is a competitive and economical energy source
8. Bring the stellarator concept to maturity

Key issues no. 3-6 are the ones that directly impact the reactor component subject of this study, the breeding blanket. Due to the limited scope of this review, only key issue no. 4, tritium self-sufficiency, is outlined briefly in Section 2.3.

In the framework of the R&D activities coordinated by the EUROfusion consortium, two different breeding blanket configurations are investigated: the Helium Cooled Pebble Bed (HCPB), based on solid breeder technology, and the Water Cooled Lithium Lead (WCLL), based on liquid breeder technology [8]. More information about the EU DEMO R&D activities can be found in Ref. [10, 11].

2.3 Fuel cycle

The DT reaction has the most favorable characteristic of all the nuclear fuels considered to power a near-term fusion power plant, but it is plagued by the not easily solvable issue of fuel supply [6]. Deuterium is the second most abundant hydrogen isotope and it can be extracted from seawater: its available resources are, by all practical means, inexhaustible. Tritium is radioactive and it undergoes beta decay in helium-3 with a half-life $\lambda_{1/2} = 12.32 \pm 0.02$years following the process

$$T_1^3 \rightarrow He_2^3 + \beta^- + \bar{v}_e + 18.6\text{keV} \tag{2.2}$$

Due to its short half-life, tritium is exceedingly rare on Earth and it is mainly produced by the interaction of the atmosphere top strata with energetic cosmic rays and, therefore, no industrial exploitation of natural-occurring tritium sources is feasible.

Tritium is produced artificially in small quantities through the dismantling of retired thermonuclear warheads or as byproduct of the operation of CANDU fission reactors, where it is generated by neutronic irradiation of heavy water (D_2O). Although these artificial sources yield a tritium quantity useful to cater for the needs of small-scale experimental machines like the Joint European Torus (JET), they will not be able to fulfill the fuel requirements of an actual fusion power plant, even for a demonstrative one like DEMO. Moreover, tritium supply from external sources is influenced by a set of contingent externalities, such progressive retirement of CANDU reactors or demand from concurrent fusion programs, that makes it unreliable or, in the worst scenario, questionable [12].

Since the early stages of the DEMO development, it has been recognized that a closed, self-sufficient fuel cycle is an unavoidable necessity for the reactor operation. It is possible to exploit the fusion neutrons to generate tritium via capture reactions with lithium[1]:

$$n^0 \ + \ Li_3^6 \ \rightarrow \ He_2^4 \ + \ T_1^3 \ + \ 4.8 \text{ MeV} \tag{2.3}$$

$$n^0 \ + \ Li_3^7 \ \rightarrow \ He_2^4 \ + \ T_1^3 \ + \ n^0 \ - \ 2.5 \text{ MeV} \tag{2.4}$$

To maximize the tritium breeding, the lithium is placed in components that completely surround the vacuum chamber and compose the reactor breeding blanket. Due to the relative low neutronicity of the fusion reactions (≈ 1 reaction^{-1} compared with ≈ 2.5 reaction^{-1} for uranium-235 fission reactions), a neutron multiplier must be employed to supplement the reactor neutron economy. Beryllium and lead are the main candidates.

The realization of the closed fuel cycle is another engineering challenge of impressive difficulty that must be overcome to make fusion energy a viable prospect [8]. In particular, the tritium produced in-situ not only must be plentiful enough to ensure the reactor operation, but also it must generate a surplus thus that in a reasonable time (≤ 5 years) a stockpile can be created to start-up a new reactor, meanwhile keeping the tritium inventory low enough to comply with the safety regulations [13].

Defining the tritium breeding ratio (TBR) as the proportion between the tritium generated in the breeder and consumed in the reactor, the required TBR must be larger than unit to provide a margin to compensate for losses due to radioactive decay, accumulate start-up stockpile, and envision fuel reserves for continuous operation under unplanned shortages (i.e. failure of an extraction line). Determining the required TBR is quite difficult, since it is a complex function of many interrelated reactor variables, but is commonly assumed that to meet the tritium self-sufficiency goal it is mandatory a $\text{TBR}_r = 1.05 \div 1.15$, with the latter value being the maximal theoretical value in state-of-the-art blanket concepts [13].

[1] Ironically enough, these reactions were first discovered and employed to maximize the yield of thermonuclear warheads.

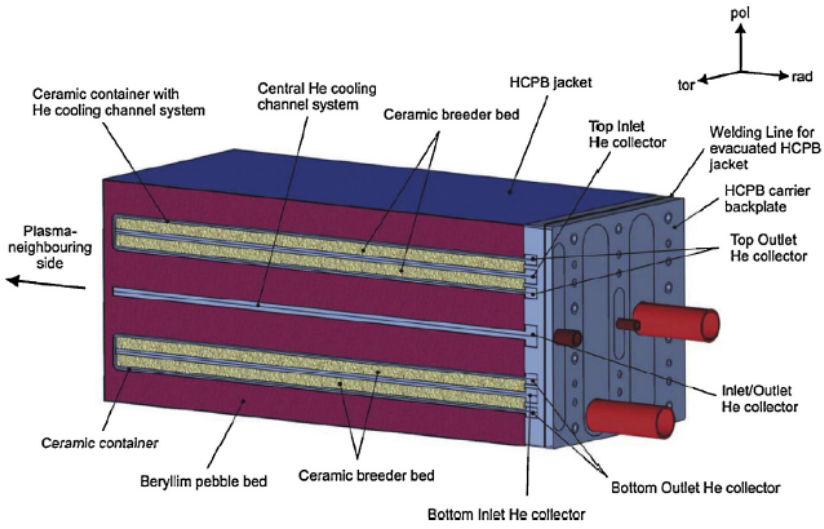

Figure 2.2. Helium Cooled ceramic Pebble Bed blanket, European Union [13]

2.4 Overview of breeding blanket concepts

The importance of tritium self-sufficiency and, in turn, of the breeding blanket can not be overstated, being one of the main technical challenges that still bar the road from the commercial exploitation of fusion power. In addition to the breeding requirements, the blanket fulfills the function of main radiation shielding and, thus, accumulates the bulk of the fusion energy transported by the neutrons, which is transformed into thermal energy through neutron-matter interactions. The thermal power responsible for the blanket heating is conveyed by the cooling system to the plant Primary Heat Transport System (PHTS), where it is then converted into electrical power. Several blanket concepts are and have been proposed in the past 40 years, but, in general, they can be classified according to the lithium physical state in *solid breeder* and *liquid breeder* technologies [13].

In a solid breeding blanket, lithium is contained in ceramic compounds either in the shape of small pebbles or blocks. The former is currently considered the superior concept and it is the base for the European HCPB blanket shown in Figure 2.2. Lithium orthosilicate (Li_4SiO_4) is the breeder chosen for the European HCPB with alternative concepts employing lithium metatitanate (Li_2TiO_3), orthosilicate-metatitanate mixture, and more advanced solutions being explored in other fusion programs [14].

The breeder is arranged in pebble beds that are placed alternatively with layers containing the neutron multiplier (usually beryllium) and cooling plates. A columnar layout is adopted where the pebble beds are placed perpendicular to the first wall [15]. Helium is the preferred coolant due to its chemical compatibility with lithium and the possibility to double as tritium purge gas, but alternative designs employing pressurized or even supercritical water have been proposed. The main drawbacks of this concept are related to the low blanket power density, the serious swelling of beryllium under neutron irradiation, and high coolant pressure drop [13].

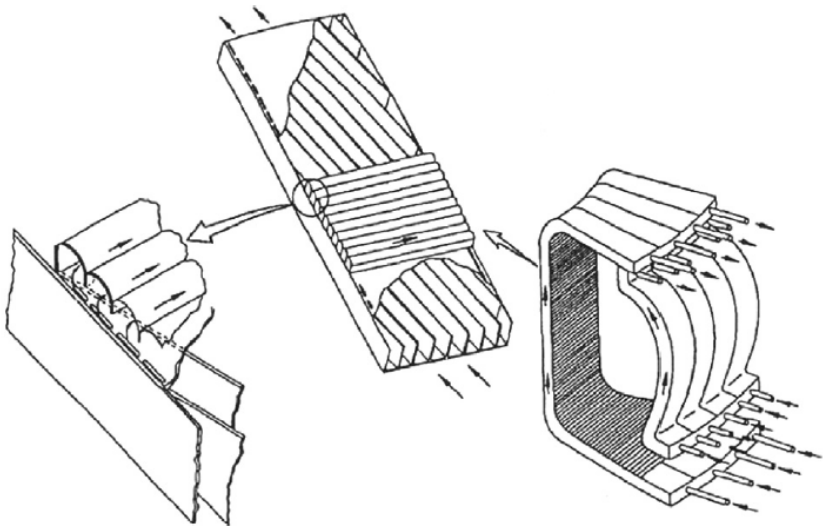

Figure 2.3. Self-cooled lithium/vanadium liquid metal blanket, US Blanket Comparison and Selection Study [13]

In a liquid breeding blanket, the breeder is pure lithium or the eutectic lithium-lead alloy. The latter is usually preferred due to lower reactivity with air, water and concrete, and direct integration with the neutron multiplier. Known drawbacks include high density, higher corrosion and more dangerous activation products. Compared with solid breeding blankets, LM designs can theoretically achieve higher power density and are less susceptible to radiation damage, but they face feasibility concerns due to MHD effects between the flowing conducting fluid and the magnetic field. Historically, this concern has driven the development of the liquid blankets concepts.

Self-cooled blankets were the first proposed concepts, where the liquid metal fulfills the function of both tritium breeder and coolant. An example of this concept is the Self-cooled lithium/vanadium, represented in Figure 2.3, studied during the 80s in the United States. Theoretically, this option is particularly attractive since it streamlines the blanket layout by removing the necessity for a separate coolant hydraulic circuit, but the high velocity required to effectively refrigerate the first wall caused unsustainable large pressure losses due to the MHD braking effect and resulted in intolerable pressure stresses on the structural materials. Insulating coating were initially proposed to solve this issue but were never successfully developed due to low cracking tolerance. Currently, R&D activities on these concepts have been abandoned worldwide.

The introduction of a non-electrically conductive coolant created the research line of separated-cooled blankets. In these concepts, the liquid metal fulfills only the breeder function and its velocity can be minimized with the inferior limit being determined by the requirements of the auxiliary tritium extraction and purification systems. Compared with the self-cooled concept, the importance of the MHD pressure drop is reduced, but magnetic field transients, mixed convection, flow distribution and instability, localized high velocities are some MHD effects that still drive the blanket design. Main drawbacks of these concepts are low exit temperature

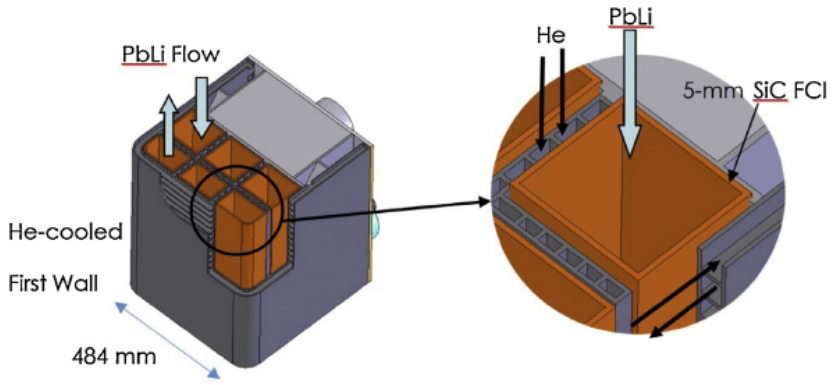

Figure 2.4. Dual-Coolant Lithium-Lead blanket, US [13]

for the coolant due to the operative limits of structural materials and high tritium permeation from the LM to the coolant. This last issue is particularly dangerous in regions where the breeder is stagnant or recirculates and the coolant is water. The main liquid breeder concept studied in the EUROfusion project is the Water-Cooled Lithium Lead (WCLL), which relies on the separated-cooled scheme and will be described in detail in Section 2.5.

Dual-coolant blankets have been proposed where the two ideas described previously are combined to provide a high-efficiency, high-temperature blanket. In such a concept, the surface heat flux at the first wall is removed by a non electrically conductive fluid, like helium, whereas the liquid metal is circulated at a velocity fast enough to effectively remove the volumetric power generation. To minimize the MHD pressure drop, flow channel inserts (FCI) are employed to electrically decouple the flowing fluid and the blanket walls. The leading concept for the FCI is a sandwich-like layout where a sheet of alumina is enclosed between thin steel liners. Qualification of alumina properties under irradiation is still undergoing. An example of such concept is the Dual-Coolant Lithium-Lead blanket, represented in Figure 2.4, currently studied in EU and US. Advanced concepts with PbLi temperature $\geq 550\,°C$ shows potential to achieve up to 45% thermal efficiency, but requires FCI able to provide thermal decoupling to preserve the structural materials properties.

Alternative concepts are also being explored with the most notable ones envisioning a combination of liquid and solid breeder, or employing molten salts containing lithium as working fluids. More recently, an hybrid design employing a solid ceramic breeder and molten Pb as neutron multiplier has been proposed [16]. However, these concepts are considerably less developed compared with the one discussed in this Section and, in some cases, are even more challenging by an engineering point of view [13].

2.5 The Water-Cooled Lithium Lead blanket concept

The Water-Cooled Lithium Lead (WCLL) breeding blanket is one of the two concepts studied in the framework of the R&D activities coordinated by the EUROfusion Consortium and the only one based on liquid breeder technologies. The WCLL was

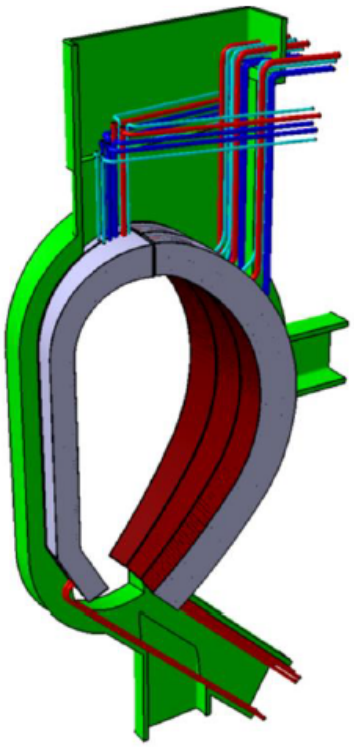

Figure 2.5. WCLL blanket layout and integration with DEMO systems. Green: Vacuum vessel, cyan and blue: breeding zone and first wall cooling system, red: PbLi (color online) [22]

selected in 2017, alongside the HCPB, from the original pool of four concepts[2] initially studied as the candidate for further optimization in the DEMO pre-Conceptual design phase. This choice was made to streamline the blanket R%D activities and to provide the possibility to test both high temperature (helium) and high pressure (water) coolant for solid and liquid breeder concepts during the Test Blanket Module (TBM) experimental campaign scheduled to be performed in ITER [10].

Since 2014, the development of the WCLL design has been carried over by ENEA and its linked Third parties continuing a research line first pioneered in the framework of the IN-TOR[3] and NET[4] studies [17] and further developed by several European research teams [18–20]. A complete review of the WCLL design evolution is outside of the scope of this dissertation, but can be found in Ref. [21].

In the most recent iteration, the WCLL design employs the RAFM steel Eurofer as structural material, tungsten for first wall armor, PbLi enriched at $90\%_w$ in lithium-6 as breeder and pressurized water as coolant. The general blanket layout is presented in Figure 2.5. It is divided into two main regions: the inboard, located

[2]The other two concepts are the Helium-Cooled Lithium Lead (HCLL) and Dual Coolant Lithium Lead (DCLL) that are still considered as advanced blanket designs for later implementation in DEMO

[3]INternational TOkamak Reactor: ITER forerunner, folded into it in 1987

[4]Next European Torus, anticipated successor of JET with DEMO-like objectives. Optimistically, it was scheduled to be completed by 2000

close to the central solenoid, and the outboard, found on the external side of the vacuum chamber. Following the Single Module System (SMS) approach, the inboard and outboard blanket are composed by a large continuous segment that is interrupted for the whole vertical extension of the component. This approach facilitates the PbLi drainage and helium bubbles removal from the segment compared with the Multi Module System (MMS) approach and, moreover, it provides superior thermo-mechanical performances during both normal operation and central major disruption events [22, 23]. Furthermore, the blanket is divided into 16 sectors, each one being composed by three outboard and two inboard segments. To date, only the design of the central outboard segment has been performed in detail and we will always refer to it in this Section.

The blanket can be divided into the following functional zones:

- **Structural components**: including first wall and back supporting structure (BSS)
- **Cooling system**: including the dedicated breeding zone and first wall systems
- **Breeding zone**: including the manifold and other PbLi in-vessel loop components

Various interfaces are present between these functional zones and the reactor systems. Blanket segments are anchored to the BSS that, in turn, is supported by the VV. Remote maintenance and system access to the in-vessel components is provided by three openings on the VV: the lower, upper and equatorial ports (see Figures 2.1 and 2.5). The water cooling system is connected to the Primary Heat Transfer System (PHTS) through pipes routed at the upper port, whereas the PbLi is conveyed to and from the breeding zone through pipes routed at the upper and lower port, linked to the ex-vessel PbLi loop.

2.5.1 Structural components

The structural components of the blanket are composed of RAFM steel Eurofer and can be divided into four broad categories: *first wall*, *stiffening plates*, *back plate*, and *back supporting structure*.

The first wall is a 25-mm thick plate that constitutes the boundary between the vacuum chamber and the blanket itself. A 2-mm thick liner made of tungsten covers the first wall and provides a high-temperature resistant shield (armor). In normal operation, the first wall must withstand a maximum heat load 0.5 MW/m^2, according to the design requirements. This component is refrigerated by a dedicated cooling system, presented in Section 2.5.2.

The blanket box is strengthened by a complex of internal structural elements that are collectively labeled *stiffening plates*. In Figure 2.6 their arrangement is represented: five vertical elements (poloidal-radial stiffening plate) that run for all the extension of the blanket segment connecting the top and bottom cap, and ≈ 120 horizontal elements (toroidal-radial stiffening plate) that are anchored to the first wall and the back plate. These latter elements bound the PbLi elementary cells and dampen the differential thermal expansion between the "hot" first wall and the "cold" back plate. In addition, thin baffle plates, that do not serve any mechanical

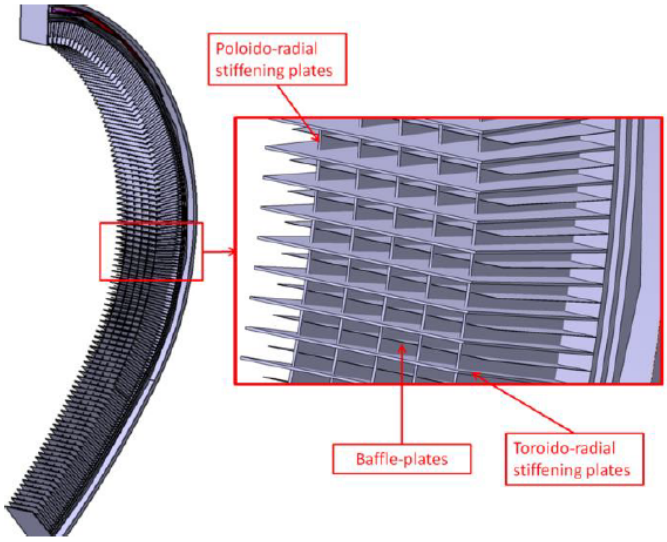

Figure 2.6. WCLL internal structural elements [22]

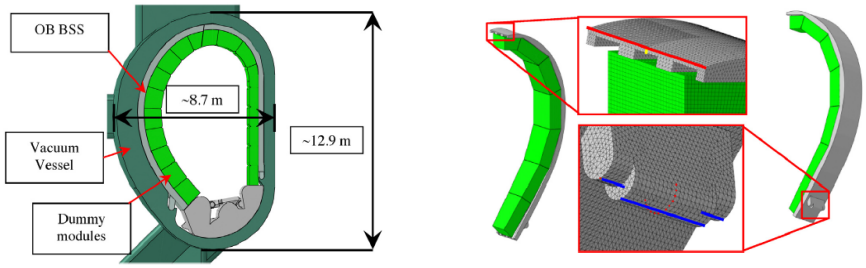

Figure 2.7. Outboard Blanket (OB) back supporting structure (BSS). Left: position with respect to blanket and vacuum vessel, right: detail of blanket attachment [24]

function, are placed in between the horizontal stiffening plates to delimit the inlet and outlet PbLi path in the breeding cell.

The back supporting structure (BSS) is attached at the back plate and sustains the weight of the blanket segment, providing the connection with the VV. In Figure 2.7, its position with regard to the reactor and the attachment points are shown. Due to the intense loads that it needs to withstand, the BSS is the thickest structural component at ≈ 200mm [22, 24].

A narrow temperature window is available for the safe operation of the structural components since under irradiation Eurofer undergoes brittle transition for T$\leq$ 350 °C and severe degradation of thermo-mechanical properties for $T \geq 550\,°C$ [25]. Therefore, limiting the PbLi temperature to accommodate these requirements is one of the most important goals of the blanket cooling system. The structural components must be able to withstand all the mechanical loads derived by pressure, thermal and electromagnetic stresses. This latter load is distinguished into the contribution from self-induced currents in the ferro-magnetic material during magnetic field transients (Lorentz forces) and the interaction with the quasi-static magnetic field (Maxwell forces). Assessment of structural components is conducted according to

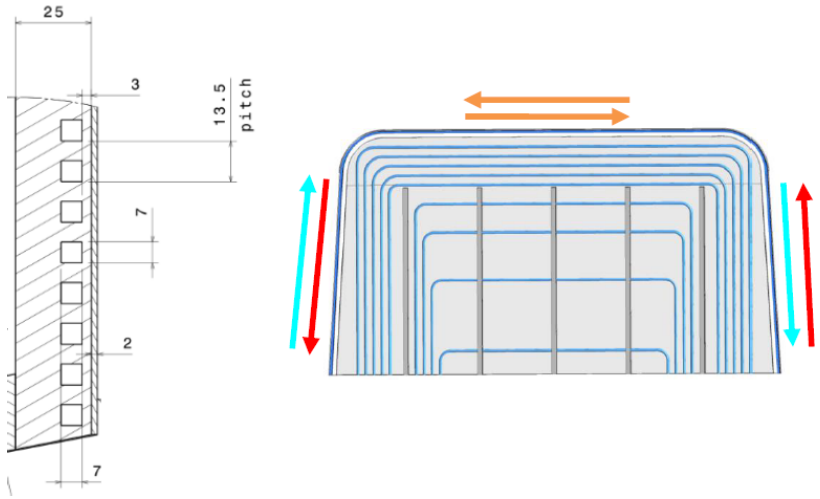

Figure 2.8. First wall cooling system. Left: detail of the square channel layout and first wall cross-section, right: "counter-current" flow path in adjacent channels [21].

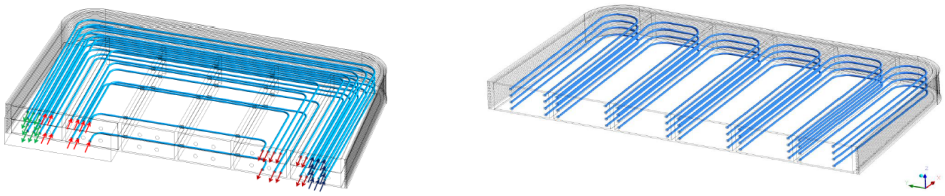

(a) C-pipe layout. **(b)** U-pipe layout.

Figure 2.9. Breeding zone cooling system with two proposed pipe layout: C-pipe and U-pipe [21]

the RCC-MRx standard [26].

2.5.2 Cooling system

The coolant is employed for the refrigeration of both the first wall and the breeder. It is operated with parameters nearly identical to the ones characteristic for a pressurized light water fission reactor (PWR): nominal pressure at 15.5 MPa, inlet temperature equal to 295 °C, and outlet at 328 °C.

Regarding the first wall cooling system, square channels ($l = 7$ mm) built inside the structural material carry the coolant and extend for all the linear extension of the plasma-facing component. Channels are separated by $p = 13.5$ mm and the water flows in opposite directions in adjacent conduits. A graphical representation of the first wall cooling system is available in Figure 2.8.

Breeder refrigeration is ensured by pipes that are immersed in the liquid metal. To minimize the risk of pipe rupture with consequent ingress of water into the breeding zone and violent chemical reactions occurring with the breeder, the coolant pipe is a Double Walled Tube (DWT) with a copper interlayer filling the gap. Several arrangements are possible for the pipes position that, however, must provide a symmetrical temperature in the breeder and the lowest amount of structural

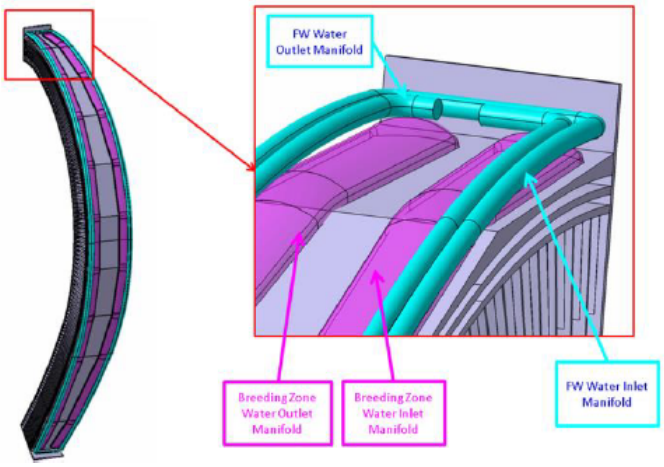

(a) Cooling system manifold position

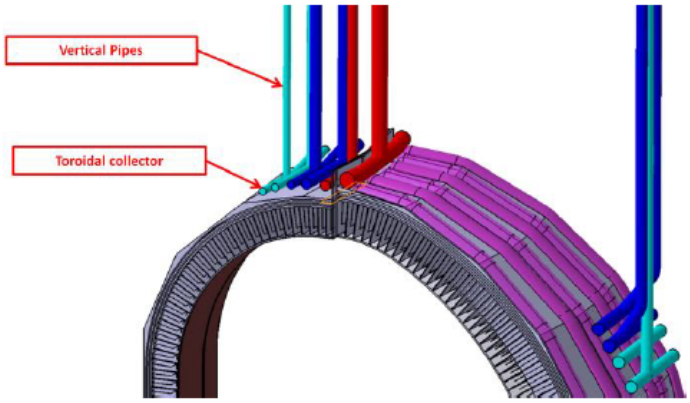

(b) Toroidal collectors and connection with ex-vessel coolant loop

Figure 2.10. Cooling water manifold layout and integration with PHTS [22]

material, to affect the least the TBR.

In Figure 2.9, the U-pipe and C-pipe layouts are presented. The latter follows the same general structure of the first wall cooling system, but it is more difficult to manufacture since pipes must pierce the vertical stiffening plates. To address this issue, the U-pipe configuration has been proposed, which is remarkably easier to construct since the pipe can be inserted into the breeding zone without any interaction with the internal structural elements. Both configuration are currently under study to assess which one will provide the better thermal-hydraulic performance [21, 22, 27].

Both cooling systems are fed by manifolds located in cavities realized in the BSS. In Figure 2.10, the position of the manifolds and the integration with the PHTS is shown. Toroidal collectors are employed to bridge the manifold with the connection pipes.

The main advantage of this concept is that the design of blanket coolant systems can benefit from the wealth of proven technologies and extensive operative experience accumulated in the past 60 years for light water reactors, thus allegedly minimizing

the R&D required for deployment in DEMO. However, open issues still remain about the use of water in a fusion reactor due to concerns about safety and performances: chemical reactivity with lithium, significant tritium permeation in the coolant, low thermal efficiency, and uncertain compatibility with structural materials (copper and Eurofer) are all challenges that must be addressed by the blanket design [28]. To counter the issue of corrosion under irradiation and erosion of the DWT pipes, the coolant velocity is limited to 7 m/s [21].

2.5.3 Breeding zone

The placement of the internal structural elements divides the blanket into ≈ 120 horizontal cells. The elementary cell geometry is modular and it is ideally repeated for all the vertical extension of the segment, allowing for some minor variation to accommodate the reduced width close to the top and bottom cap. The PbLi flow path in the breeding zone, shown in Figure 2.11a, is mostly horizontal: in the inlet channel, the liquid metal flows from the back plate toward the first wall, then turns vertical, and flows back in the outlet channel, which is separated from the inlet by a thin baffle plate. Since the PbLi is only employed as breeding medium and neutron multiplier, its velocity is minimized to avoid large pressure losses and it is ≈ 0.2 mm/s. The elementary cell is divided by the vertical stiffening plates in six conduits that, however, share a common plenum close to the first wall. Horizontal pipes following the C-pipe or U-pipe scheme described in Section 2.5.2 provide the refrigeration.

The PbLi distribution and collection is handled by the manifolds represented in Figure 2.11b. These are narrow rectangular channels clustered in between the back plate and the breeding zone and are divided in two separate arrays: the internal one feeds the breeding zone, whereas the outer one is used for the collection. Blanket flow distribution follows a de-localized scheme where the manifold continuously feeds the elementary cells, which are distributed along the blanket spine. Significantly higher velocities are foreseen in this component ($\approx 1 \div 2$ cm/s).

Additional separate collectors, not represented in Figure 2.11, are necessary to distribute and collect the PbLi from the manifolds depicted in Figure 2.11b, and to ensure the hydraulic connection with the ex-vessel PbLi loop. However, in the current design configuration these components, as well as the routing scheme of the blanket PbLi feeding and draining pipe, have not been clearly defined yet. Indeed, one of the objectives of this study is to address this issue by analyzing in detail several PbLi in-vessel loop configurations to compare their respective advantages and drawbacks, selecting the most promising for further optimization.

2.5.4 Alternative configurations

The low maturity state of the PbLi in-vessel loop design warranted an extensive investigation of possible alternative solution in order to select a configuration with the best potential. Ideally, the PbLi in-vessel flow path should fulfill these requirements:

- Low MHD pressure drop, to minimize stress on structural elements and pumping power required

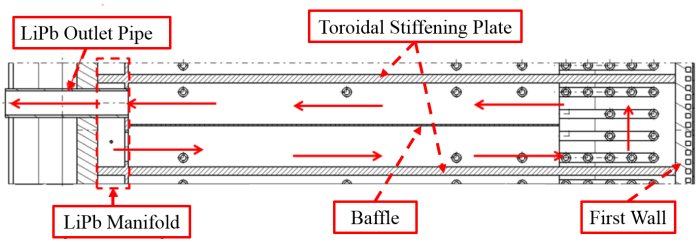

(a) PbLi flow path

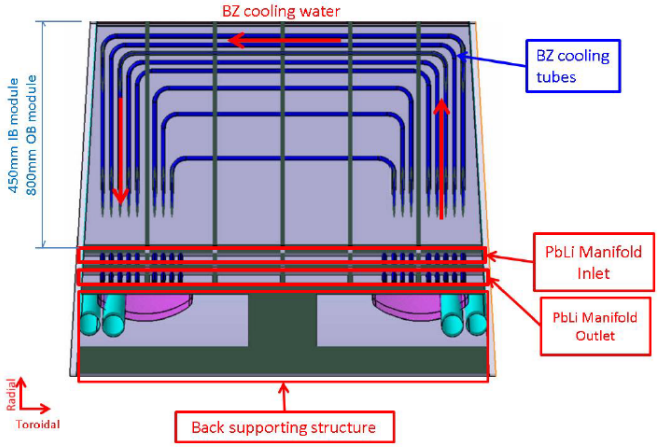

(b) Elementary cell and PbLi manifolds

Figure 2.11. Breeding zone elementary cell with C-pipe layout: PbLi flow path and connection with the distribution and collection manifold [21, 29]

- Uniform flow distribution, to easily predict the PbLi blanket residence time and avoid tritium build-up in stagnant regions
- Ease of integration with the other DEMO systems, in particular the PbLi ex-vessel loop
- Compliance with remote maintenance specifics

A wide campaign was launched to analyze various combination of stiffening plate arrangement, flow distribution scheme, pipe routing from/to PbLi ex-vessel loop, cooling system layout, etc and four baseline configurations were selected to perform a comparative analysis, which is the subject of Part II of this dissertation.

2.6 Summary

In this Section, the principles of fusion energy and tokamak reactor technologies are briefly reviewed with particular attention devoted to the breeding blanket system and the specific design considered in this dissertation, the Water-Cooled Lithium Lead (WCLL).

Despite the continuous research in the past 60 years, no fusion reactor has yet managed to create a self-sustaining plasma that is able to burn for long periods of time and generate much more energy than the one required to start the nuclear

reactions. This objective is expected to be achieved by 2035 by the experimental reactor ITER, that should be able to demonstrate high power plasma regimes and the generation of large energy amounts in several minutes long pulses. The main goal of the R&D activities coordinate by the EUROfusion Consortium is to break the ground and prepare the next incremental step in the fusion reactor development by constructing a demonstrative power plant (DEMO) by 2050. However still not a full-fledged commercial power plant, DEMO should demonstrate the feasibility of electrical power generation by fusion energy and approach quasi-steady operation.

The realization of a closed fuel cycle and the plant tritium self-sufficiency will be instrumental in achieving the DEMO stated goals or, in other and maybe more frank words, it is a non-negotiable condition for successfully operating a fusion power plant. In this framework, the development of a consistent and efficient breeding blanket is of paramount importance. Both solid and liquid breeder concepts have been investigated in recent years with the European efforts focusing on two candidate designs representative of these research lines: the Helium Cooled Pebble Bed (HCPB) and Water-Cooled Lithium Lead (WCLL). Both concepts are scheduled to be tested in ITER in the context of the TBM experimental campaign.

The WCLL design is briefly described by highlighting its main functional areas. Still in the pre-conceptual phase, many open issues must still be addressed in the blanket design. One of the most important is the definition of the PbLi in-vessel flow path and the assessment of the MHD effects on pressure drop and heat transfer. A comparative analysis of four proposed PbLi flow path configuration is conducted in Part II, whereas the heat transfer problem is partially addressed in Part III.

Chapter 3

Liquid Metal Magnetohydrodynamics

3.1 Introduction

Magnetohydrodynamics (MHD) is the branch of fluid-dynamics that involves the study of the motion and evolution of electro-conductive fluids in the presence of electro-magnetic fields. Liquid metals, molten salts and ionized gases are only some of the fluids of industrial interest whose behavior can be described by the application of the magneto-hydrodynamic governing equations. The non-linear coupling between the velocity and electro-magnetic field that characterizes the MHD flows requires the combination of the Navier-Stokes and Maxwell equations to derive a comprehensive and self-consistent set of physical laws. In this chapter, a brief overview of these laws is given for the particular case of an incompressible fluid and some fundamental phenomena of interest for the design of fusion reactor blankets are described. Complete reviews on the general topic of magnetohydrodynamics can be found in Ref. [30–32], whereas a detailed discussion of the phenomena interesting liquid metal MHD can be found in Ref. [33].

3.2 General assumptions

For the purpose of this PhD thesis, the fluid of interest is a liquid metal (like the eutectic alloy PbLi) and, thus, simplifying assumptions that are applicable to this

class of fluids will be employed in the derivation of the MHD governing equations. Namely, we are assuming that the fluid is:

- continuous
- incompressible
- electrically conductive
- Newtonian
- homogeneous and isotropic, with regard to its physical properties
- characterized by temperature-independent physical properties

First, we are going to derive the MHD governing equations for the particular case of an isothermal magneto-hydraulic flow, and then we are going to extend the discussion to a non-isotherm case, introducing the energy equation to completely describe a flow involving buoyancy forces and magneto-convective phenomena. The fundamental concepts discussed in this Section are mainly taken from Ref. [33].

3.3 Magneto-hydraulics

Consider a fluid for which the assumptions previously formulated are valid. For an isothermal flow, the Navier-Stokes equations are reduced to the continuity equation and the linear momentum equation, which are obtained, respectively, from the mass conservation principle and the Newton's second law of motion. For a more complete derivation of these equations, we refer to Ref. [34]. These equations take the form:

$$\nabla \cdot \mathbf{v} = 0 \tag{3.1}$$

$$\frac{\partial \mathbf{v}}{\partial t} + (\mathbf{v} \cdot \nabla)\mathbf{v} = -\frac{1}{\rho}\nabla p + \nu \nabla^2 \mathbf{v} + \frac{1}{\rho}\mathbf{F}_b \tag{3.2}$$

where the symbols $\mathbf{v}$, t, ρ, p, ν and $\mathbf{F}_b$ stand for velocity, time, density, pressure, kinematic viscosity and volumetric body force. The interpretation of eq. (3.2) is straightforward with the left side representing the momentum transport with a time-dependent and convective term, and the right side representing the forces acting on the fluid particle, subdivided into surface (pressure and viscous term) and body ones. In particular, the body force term includes the electromagnetic force ($\mathbf{F}_L$)and, for a non-isothermal flow, the buoyancy force.

Focusing the attention on the former, the electromagnetic force (or Lorentz force) acting on an infinitesimal volume of the fluid containing a charge (q) and seeing a current density ($\mathbf{J}$) pass by can be written with the expression

$$\mathbf{F}_L = q\mathbf{E} + \mathbf{J} \times \mathbf{B} \tag{3.3}$$

where the symbols $\mathbf{E}$ and $\mathbf{B}$ represent the electric and magnetic field. Therefore, the Lorentz force can be divided into a electrostatic component, usually called *Coulomb force*, and one that accounts for the effect of the magnetic field[1].

[1] In some texts, the second right-hand term in eq. (3.3) is called magnetic Lorentz force or Laplace force.

To solve eq. (3.2), it is necessary to introduce additional equations that are able to describe the relationship between the electromagnetic quantities presented in eq. (3.3). These are the Maxwell's equations and, under the simplifying assumptions outlined previously, they take the following form:

$$\nabla \cdot \mathbf{E} = \frac{\rho_e}{\epsilon} \tag{3.4}$$

$$\nabla \cdot \mathbf{B} = 0 \tag{3.5}$$

$$\nabla \times \mathbf{E} = -\frac{\partial \mathbf{B}}{\partial t} \tag{3.6}$$

$$\nabla \times \mathbf{B} = \mu \mathbf{J} + \mu\epsilon \frac{\partial \mathbf{E}}{\partial t} \tag{3.7}$$

where the symbols ρ_e, ϵ and μ represent the charge density, electric permittivity and magnetic permeability. Eq. (3.4) is the Gauss's law that dictates how a distribution of electric charges generates a static electric field. Eq. (3.5) is the Gauss's law for magnetism, which means that the magnetic field is solenoidal, no magnetic monopoles exist and the field lines are always closed. Equation (3.6)) is the Faraday's law of induction, which correlates a time-varying magnetic field with the appearance of an electric field, as well as eq. (3.7) describes the emergence of a magnetic field from a changing electric field or an established current density.

Since the magnetic field $\mathbf{B}$ is a solenoidal field, as stated in eq. (3.5), it can be described through a potential vector $\mathbf{A}$ defined as[2]

$$\mathbf{B} = \nabla \times \mathbf{A} \tag{3.8}$$

Comsequently, if we substitute the identity (3.8) in eq. (3.6), after some algebra, the electric field $\mathbf{E}$ is expressed through the electric (scalar) potential ϕ with the equation

$$\mathbf{E} = -\nabla\phi - \frac{\partial \mathbf{A}}{\partial t} \tag{3.9}$$

If the fluid considered is characterized by an electrical conductivity σ, the current density can be expressed with the general Ohm's law for a moving conductor, which can be written with the expression:

$$\mathbf{J} = \rho_e \mathbf{v} + \sigma(\mathbf{E} + \mathbf{v} \times \mathbf{B}) \tag{3.10}$$

where the terms on the right side represent, respectively, the convection current and the conduction current. To simplify the problem, we further introduce four assumption:

1. The fluid velocity magnitude (u_0) is small compared with the speed of light
2. The charge carriers (i.e. mostly electrons, for liquid metals) velocity is small compared with the fluid velocity
3. The charge carriers are not affected by inertia

[2] $\nabla \cdot (\nabla \times \mathbf{A})$)

4. Thermo-electric effects are negligible

These assumptions imply that the convection current ($\rho_e \mathbf{v}$) in eq. (3.10) is negligible compared to the conduction term, therefore the Ohm's law can be written in the simplified form:

$$\mathbf{J} = \sigma(\mathbf{E} + \mathbf{v} \times \mathbf{B}) \tag{3.11}$$

Accordingly, in eq. (3.7)) the displacement current can be neglected, so the equation reverts to the Ampère's circuital law

$$\nabla \times \mathbf{B} = \mu \mathbf{J} \tag{3.12}$$

By taking the divergence of eq. (3.12), the current density continuity equation is obtained

$$\nabla \cdot \mathbf{J} = 0 \tag{3.13}$$

which states that $\mathbf{J}$ is a solenoidal vector field and that the electric charge is a conservative quantity, i.e. no charge accumulation is observed in conducting materials. Both eq. (3.13) and (3.5) should be theoretically enforced in a CMHD numerical scheme to make it conservative and consistent.

In general, the magnetic field $\mathbf{B}$ will be composed by the sum of an applied, external, magnetic field ($\mathbf{B_0}$) and a self-induced field ($\mathbf{b}$), generated by the induction phenomenon described by eq. (3.6). It is possible to deduce an equation describing the evolution of the total magnetic field by combining the Ohm's law (3.11), Faraday's law (3.6), and Ampére's circuital law (3.7), together with the conditions of solenoidal $\mathbf{B}$ (3.5) and incompressible fluid (3.1)

$$\frac{\partial \mathbf{B}}{\partial t} + (\mathbf{v} \cdot \nabla)\mathbf{B} = \frac{1}{\mu\sigma}\nabla^2 \mathbf{B} + (\mathbf{B} \cdot \nabla)\mathbf{v} \tag{3.14}$$

where the group $\frac{1}{\mu\sigma}$ is the magnetic diffusivity. Equation (3.14) is called the *induction equation*. It states that the evolution in time of the magnetic field is caused by convection (second left-hand term) and diffusion (first right-hand term) of the field lines, together with the field production generated by the mechanical stretching of the field lines by the velocity field (second right-hand term).

Neglecting the electrostatic component in eq. (3.3), the electromagnetic force acting on the fluid is a function only of the magnetic field and is expressed with the relation

$$\mathbf{F}_L = \mathbf{J} \times \mathbf{B} \tag{3.15}$$

It is possible to express the Lorentz force as a function only of the magnetic field by substituting $\mathbf{J}$ with the expression from eq. (3.12)

$$\mathbf{F}_L = \frac{1}{\mu}(\nabla \times \mathbf{B} \times \mathbf{B}) \tag{3.16}$$

Furthermore, employing eq. (3.5) to add the term $(\nabla \cdot \mathbf{B})\mathbf{B}$ and vector identities to eliminate the curl, the Lorentz force takes the form

$$\mathbf{F}_L = \frac{1}{\mu}\left[-\nabla\left(B^2/2\right) + \nabla \cdot (\mathbf{BB})\right] \tag{3.17}$$

where the first right-hand term, the gradient of a scalar, is called *magnetic pressure*, and the second one is a stress term, containing the dyadic product (**BB**). Globally, the Lorentz force can then be expressed as the divergence of a second order tensor, called *Maxwell stress tensor*(**M**), such that $\mathbf{F}_L = -\nabla \cdot \mathbf{M}$.

Introducing eq. (3.17) in eq. (3.2), the only electromagnetic variable of interest for the isothermal magneto-hydraulic problem is the total magnetic field **B** and the fluid evolution is completely described by the solution of the following equation set

$$\nabla \cdot \mathbf{v} = 0 \tag{3.1}$$

$$\frac{\partial \mathbf{v}}{\partial t} + (\mathbf{v} \cdot \nabla)\mathbf{v} = -\frac{1}{\rho}\nabla p + \nu \nabla^2 \mathbf{v} + \frac{1}{\mu\rho}\left(-\nabla\left(B^2/2\right) + \nabla \cdot (\mathbf{BB})\right) \tag{3.2'}$$

$$\frac{\partial \mathbf{B}}{\partial t} + (\mathbf{v} \cdot \nabla)\mathbf{B} = \frac{1}{\mu\sigma}\nabla^2 \mathbf{B} + (\mathbf{B} \cdot \nabla)\mathbf{v} \tag{3.14}$$

$$\nabla \cdot \mathbf{B} = 0 \tag{3.5}$$

Which is composed by 7 equations in 7 variables (**B**, **v**, and p). The addition of eq. (3.5) ensures that **B** is solenoidal[3]. The bi-directional, non-linear, coupling between the magnetic and velocity field is shown in the Lorentz force source term in eq. (3.2)' and in the convection and mechanical stretching term in eq. (3.14). The relative motion of a electro-conductive fluid with regard to a fixed magnetic field results in the self-induction of currents in the fluid that generate an induced magnetic field (**B**) that, added to the applied one, causes the warping of the magnetic field lines, as if they were "dragged" by the fluid. The total magnetic field thus obtained interacts with the induced currents producing a Lorentz force that tends to suppress the relative motion between the fluid and the magnetic field.

3.3.1 Dimensionless groups

To identify the relevant dimensionless groups that play a role in the definition of the MHD flow features, it is useful to derive the dimensionless form of the equation set presented in the previous Section. The quantities $\mathbf{v}, t, \mathbf{B}, \mathbf{J}$ and p are made dimensionless employing the scales: u_0 (characteristic velocity, i.e. mean velocity for the forced convection flow), $t_0 = L/u_0, B_0, J_0 = \sigma u_0 B_0$, and $p_0 = \rho u_0^2$. Moreover, the ∇ operator is scaled by $\nabla_0 = L$. Here, L is the characteristic length, usually chosen as the half-width (i.e. radius) in the magnetic field direction for the flow in a rectangular (circular) duct and for the particular case of unidirectional field. Identifying a dimensionless variable as $\hat{\psi} = \psi/\psi_0$, the rearranged equations take the form:

$$\frac{\partial \hat{v}}{\partial \hat{t}} + (\hat{v} \cdot \nabla)\hat{v} = -\nabla \hat{p} + \frac{1}{Re}\nabla^2 \hat{v} + \frac{N}{Rm}\left(-\nabla \hat{B}^2/2 + \nabla \cdot (\hat{B}\hat{B})\right) \tag{3.18}$$

$$\frac{\partial \hat{B}}{\partial \hat{t}} + (\hat{v} \cdot \nabla)\hat{B} = \frac{1}{Rm}\nabla^2 \hat{B} + (\hat{B} \cdot \nabla)\hat{v} \tag{3.19}$$

where the continuity equations for velocity (Eq. 3.1) and magnetic field (Eq. 3.5) have been omitted for brevity's sake, since they are substantially unchanged compared

[3]Usefully, this condition ensures also that **J** is solenoidal

with the dimensional equations. Three dimensionless groups appear in the equation set so derived: the classical Reynolds number (Re), the interaction parameter (N) and the magnetic Reynolds number (Rm).

Reynolds number

$$Re = \frac{u_0 L}{\nu} \tag{3.20}$$

This well-know group, named after Osborne Reynolds, represents the relative ratio of the inertial to viscous forces and, traditionally, it is related to the transition between the laminar and turbulent flow regime.

Interaction parameter

$$N = \frac{\sigma B_0^2 L}{\rho u_0} \tag{3.21}$$

Sometimes called also Stuart number, the (magnetic) interaction parameter stands for the relative strength of electromagnetic to inertial effects. For $N \ll 1$, the inertial forces dominate the flow and determine the fluid behavior, whereas for large values of B_0 and L, and relatively small u_0, $N \gg 1$ and the flow is regarded as *inertia-less*, i.e. flow features are invariant with respect to Re. This condition is usefully employed for simplified asymptotic studies, since it greatly reduce the complexity of the MHD governing equations [33]. Studies employing this assumption can be found in Bühler [35] and Molokov and Bühler [36].

Magnetic Reynolds number

$$Rm = \mu\sigma u_0 L \tag{3.22}$$

This dimensionless number relates the strength of magnetic advection versus diffusion. For $Rm \ll 1$, the magnetic diffusion is dominant and the field tends to relax quickly, smoothing out any perturbation introduced by the fluid velocity field. Basically, the magnetic field lines are "frozen" in the conductive medium and the influence of the induced magnetic field is, by all means, negligible in the determination of the total field: the flow is regarded as *induction-less*. This is the condition usually encountered for liquid metal MHD flows ($Rm \approx 10^{-2}$ or lower) in the laboratory and fusion reactor blankets, due to the relatively small u_0 and L involved, which results in a very weak coupling between the velocity and magnetic field. Conversely, for $Rm \gg 1$, the magnetic field diffusion is negligible and its time variation is due only to the fluid convection. This is the condition encountered in the molten ferromagnetic Earth core ($Rm \approx 10^4$) and for astrophysical phenomena ($Rm \approx 10^8 \div 10^{10}$). [32].

Hartmann number

In many applications where strong magnetic field are present, the main balance is between the electromagnetic and viscous forces. The relative ratio can be expressed as a function of the interaction parameter and Reynolds number, e.g. $NRe = Ha^2$.

We identify with the symbol Ha the square of this dimensionless group, that we call *Hartmann number* and can be expressed as

$$Ha = B_0 L \left(\frac{\sigma}{\rho \nu} \right)^{0.5} \tag{3.23}$$

Named after Julius Hartmann, it is a measure of the magnetic field intensity and, as such, of the deviation from the ordinary hydrodynamic behavior. If $Ha \gg 1$, the viscous effects are confined to thin boundary layers close to the walls and the flow can be considered *inviscid*. This assumption is often coupled with the inertia-less approximation (for $N \gg 1$) to develop simplified asymptotic analyses [33].

3.3.2 Induction-less approximation

In section 3.3.1, we have introduced the magnetic Reynolds number Rm to characterize the relative ratio between the magnetic advection and diffusion. For $Rm \ll 1$, it was stated how the coupling between the fluid velocity and magnetic field is greatly weakened due to the reduced influence of the self-induced field. If this is so, the magnetic field is no longer a variable of the MHD problem, but it is instead determined only by the boundary conditions that specify the magnitude and orientation of the applied field, since $\mathbf{B} \approx \mathbf{B_0}$. This *induction-less approximation* leads to a great simplification of the governing equations and greatly improves the efficiency of CMHD numerical schemes. Moreover, it is well-suited to treat most LM MHD flows in fusion reactor blankets with the important exception of phenomena occurring during violent plasma-induced transients (e.g major disruptions, vertical displacement events, edge localized modes, etc.) [37].

If a steady applied magnetic field $\mathbf{B}$[4] is considered and assumed to be known, the Lorentz force is expressed with $\mathbf{F}_L = \mathbf{J} \times \mathbf{B}$, where the only variable is the current density distribution. If the magnetic field is time-independent, it follows through from eq. (3.6) that the electric field is irrotational and, therefore, eq. (3.9) is reduced to $\mathbf{E} = -\nabla\phi$. Thus, the Ohm's law takes the form:

$$\mathbf{J} = \sigma(-\nabla\phi + \mathbf{v} \times \mathbf{B}) \tag{3.24}$$

If we combine eq. (3.24) with the charge conservation eq. (3.13), we obtain a Poisson equation for the electric potential that can be solved to obtain its distribution and then, through eq. (3.24), the current density.

$$\nabla \cdot \mathbf{v} = 0 \tag{3.1}$$

$$\frac{\partial \mathbf{v}}{\partial t} + (\mathbf{v} \cdot \nabla)\mathbf{v} = -\frac{1}{\rho}\nabla p + \nu \nabla^2 \mathbf{v} + \frac{1}{\rho}\mathbf{J} \times \mathbf{B} \tag{3.25}$$

$$\nabla^2 \phi = \nabla \cdot (\mathbf{v} \times \mathbf{B}) \tag{3.26}$$

$$\mathbf{J} = \sigma(-\nabla\phi + \mathbf{v} \times \mathbf{B}) \tag{3.24'}$$

Since the fundamental electromagnetic variable is the electric potential, this formulation of the MHD governing equations in the induction-less approximation is

[4] In the following, we assume that $\mathbf{B} \approx \mathbf{B_0}$, and, therefore, the subscript is dropped

dubbed ϕ-formulation. Other formulations are possible by swapping the fundamental electromagnetic variable (e.g. **B** or **J**), but the ϕ-formulation is usually the one implemented in most numerical codes used to analyze LM MHD flows in fusion reactor blankets, due to the great advantage of solving the scalar equation eq. (3.26) in terms of computational speed.

To find the dimensionless form, we apply the same scales defined in section 3.3.1, with the exception of the pressure scale, now defined as $p_0 = \sigma u_0 B_0^2 L$, and the addition of $\phi_0 = u_0 B_0 L$. The dimensionless MHD governing equations for the low Rm case take the form:

$$\frac{1}{N}\left[\frac{\partial \hat{v}}{\partial \hat{t}} + (\hat{v}\cdot\nabla)\hat{v}\right] = -\nabla\hat{p} + \frac{1}{Ha^2}\nabla^2\hat{v} + \hat{J}\times\hat{B} \tag{3.27}$$

$$\hat{J} = (-\nabla\hat{\phi} + \hat{v}\times\hat{B})$$

where the dimensionless eq. (3.1) and eq. (3.26) have been omitted for brevity's sake, since they are substantially unchanged compared with the dimensional equations. It should be noted that, conversely to what is the case for the full MHD governing equations, the simplified equation set obtained through the induction-less assumption does not feature eq. (3.5) therein and, therefore, it does not explicitly require for **B**, and neither **J**, to be divergence-free. Particular care must be taken for the implementation of these equations in numerical schemes since they could lead to the calculation of unphysical current fields. For instance, the non-conservative implementation of the Lorentz force as a source term in eq. (3.25) is prone to generate significant numerical errors for high magnetic field intensity. Conservative schemes have been proposed to address this issue, see for instance Ni et al. [38–40].

3.4 Magneto-convection

Considering now a non-isothermal and induction-less MHD flow, the temperature is added as a variable and an equation describing the energy balance in the fluid must be derived to give closure to the equation set. Moreover, the Lorentz force is no longer the only body force present in the momentum equation, since we want to consider the effect of buoyancy forces arising due to density gradients in the fluid. In the energy balance, we neglect any gain or loss due to expansion/contraction work, since the fluid is incompressible, and the Boussinesq hypothesis is employed to neglect the density dependence on the temperature except for the buoyant body force term, where is assumed to be a linear function of it.

Under these assumptions, the equation derived from the energy balance in a fluid volume take the form

$$\rho c_p\left(\frac{\partial T}{\partial t} + (\mathbf{v}\cdot\nabla)T\right) = \kappa\nabla^2 T + \frac{1}{\sigma}\mathbf{J}^2 + \Phi + Q \tag{3.28}$$

where c_p is the specific heat capacity and κ is the thermal conductivity. The interpretation of the terms in eq. (3.28) is straightforward: the time-derivative of the temperature is dependent on the balance of the heat fluxes entering/leaving the volume, both advective (second term left side) and conductive (first term right side), the magnetic energy loss due to Joule dissipation (second term right side), the

kinetic energy loss due to viscous dissipation (Φ) and the volumetric energy release from chemical or nuclear reactions (Q). For liquid metal MHD flows in fusion reactor blankets, both the Joule and viscous dissipation terms are negligible compared with the other ones, and the equation can be simplified to the expression

$$\frac{\partial T}{\partial t} + (\mathbf{v} \cdot \nabla)T = \alpha_t \nabla^2 T + Q \tag{3.29}$$

where $\alpha_t = \kappa/\rho c_p$ is the thermal diffusivity.

Considering now the momentum equation, the density expression to employ for the buoyancy term is written as a linear function of temperature

$$\rho = \rho_0(1 - \beta_0(T - T_0)) \tag{3.30}$$

where ρ_0, β_0 and T_0 are the density, thermal expansion coefficient and temperature for the reference state. If we now introduce in eq. (3.25) the buoyancy body force term $\mathbf{F}_B = \rho\mathbf{g}$, employing the Boussinesq hyphotesis, the momentum equation takes the form

$$\frac{\partial \mathbf{v}}{\partial t} + (\mathbf{v} \cdot \nabla)\mathbf{v} = -\frac{1}{\rho_0}\nabla p_d + \nu\nabla^2\mathbf{v} + \frac{1}{\rho_0}\mathbf{J} \times \mathbf{B} - \beta_0\mathbf{g}(T - T_0) \tag{3.31}$$

where p_d is the dynamic pressure, which is obtained by removing the hydrostatic term from the total pressure. Therefore, the magneto-convection governing equations are constituted by the equation system

$$\nabla \cdot \mathbf{v} = 0 \tag{3.1}$$

$$\frac{\partial \mathbf{v}}{\partial t} + (\mathbf{v} \cdot \nabla)\mathbf{v} = -\frac{1}{\rho_0}\nabla p_d + \nu\nabla^2\mathbf{v} + \frac{1}{\rho_0}\mathbf{J} \times \mathbf{B} - \beta_0\mathbf{g}(T - T_0) \tag{3.31'}$$

$$\nabla^2\phi = \nabla \cdot (\mathbf{v} \times \mathbf{B}) \tag{3.26'}$$

$$\mathbf{J} = \sigma(-\nabla\phi + \mathbf{v} \times \mathbf{B}) \tag{3.24"}$$

$$\frac{\partial T}{\partial t} + (\mathbf{v} \cdot \nabla)T = \alpha_t \nabla^2 T + Q \tag{3.29'}$$

3.4.1 Dimensionless groups

The dimensionless magneto-convection equations are obtained employing the same scaling detailed in section 3.3.1 with the addition of the characteristic temperature difference ΔT_0 to normalize the temperature increase $T - T_0$ and $Q_0 = \frac{\rho c_p u_0 \Delta T_0}{L}$. For a magneto-convection flow, the characteristic velocity u_0 is derived from the balance between the Lorentz and buoyancy forces, which yields

$$\frac{\sigma u_0 B_0^2}{\rho_0} = \beta_0 g_0 \Delta T_0 \quad \rightarrow \quad u_0 = \frac{\rho_0 \beta_0 g_0 \Delta T_0}{\sigma B_0^2} \tag{3.32}$$

Under these assumptions, the dimensionless magneto-convection equations take the form

$$\frac{Gr}{Ha^4}\left(\frac{\partial \hat{v}}{\partial \hat{t}} + (\hat{v} \cdot \nabla)\hat{v}\right) = -\nabla \hat{p}_d + \frac{1}{Ha^2}\nabla^2\hat{v} + \hat{J} \times \hat{B} - \hat{g}\hat{T} \tag{3.33}$$

$$\frac{PrGr}{Ha^2}\left(\frac{\partial \hat{T}}{\partial \hat{t}} + (\hat{v}\cdot\nabla)\hat{T}\right) = \nabla^2\hat{T} + \hat{Q} \tag{3.34}$$

where the dimensionless form of eqs. (3.1), (3.24) and (3.26) has been omitted for brevity's sake, since substantially unchanged. Again, three dimensionless groups in the equation system obtained: the Grashof (Gr), Hartmann and Prandtl (Pr) numbers.

Grashof number

$$Gr = \frac{g\beta\Delta T L^3}{\nu^2} \tag{3.35}$$

Allegedly named after Franz Grashof, this dimensionless group expresses the relative ratio of buoyancy and viscous forces and, as such, it is the analogue of the Reynolds number for free convection flows. For mixed convection flows, the Richardson number ($Ri = Gr/Re^2$) is employed to determine if the forced or natural convection contribution can be neglected in the case treatment, respectively for $Gr/Re^2 \gg 1$ and $Gr/Re^2 \ll 1$.

Prandtl number

$$Pr = \frac{\nu}{\alpha_t} \tag{3.36}$$

Named after Ludwig Prandtl, this dimensioness number stands for the relative ratio between momentum and thermal diffusivity. If $Pr \gg 1$, the momentum diffusivity is dominant and the heat transfer is mainly influenced by the convection mechanism, i.e. the temperature boundary layer has a smaller thickness compared with the velocity one. This is the case for strongly viscous and poorly conducting fluids, i.e. engine oils. Conversely, for $Pr \ll 1$, the thermal diffusivity and the conduction mechanism are dominant, the velocity boundary layer has a smaller thickness compared with the temperature one. Liquid metals are a class of fluids that befall in this condition, since are characterized by small viscosity and high thermal conductivity. The Prandtl number is not a function of the problem geometry.

Lykoudis number

In eq. (3.33), a characteristic ratio between the Grashof and Hartmann number is present and, therefore, it is useful to introduce an additional dimensionless group related to it and that is able to characterize the relative intensity of buoyancy and electromagnetic forces for a magneto-convection flow. Remembering the expression for the characteristic magneto-convective velocity (eq. (3.32)), we can express it as a function of the Grashof and Hartmann number

$$u_{0,MHD} = \frac{Gr}{Ha^2}\frac{\nu}{L} \tag{3.37}$$

Conversely, for an ordinary hydrodynamic free convection flow, the characteristic velocity is obtained by the balance of the buoyancy and viscous forces, according to the relation

$$u_{0,OHD} = Gr^{0.5}\nu/L \tag{3.38}$$

It is possible to combine these expressions to obtain the following dimensionless parameter

$$Ly = \frac{u_{0,OHD}}{u_{0,MHD}} = \frac{Ha^2}{Gr^{0.5}} \tag{3.39}$$

Named after Paul S. Lykoudis, if $Ly \ll 1$, the buoyancy forces are dominant and the flow exhibits a characteristic velocity close to the analogous free-convection case. Conversely, for $Ly \gg 1$ the magnetic dampening is the main force shaping the flow features.

Magneto-convection interaction parameter

It is useful to define an analogue of the interaction parameter N to be employed for characterizing the relative ratio of electromagnetic and inertial forces in magneto-convective problems. This parameter is defined as the Lykoudis number square

$$N_{MC} = Ly^2 = \frac{Ha^4}{Gr} \tag{3.40}$$

This parameter is used in lieu of N to determine if a magneto-convection flow can be considered inertia-less with regard to the momentum equation, an important condition, for instance, for the purpose of asymptotic analyses. One example of such study is available by Bühler for differentially and internally heated vertical tall rectangular ducts [4].

Péclet number

Traditionally, the Péclet number represents the ratio between advective and diffusive transport rate for different class of phenomena. In thermo-hydraulics, it is defined as follows

$$Pe = RePr \tag{3.41}$$

If we employ the identity $Re = Gr/Ha^2$, it is possible to define the Péclet number for magneto-convective flows as follows

$$Pe = \frac{GrPr}{Ha^2} \tag{3.42}$$

where $GrPr = Ra$ is the Rayleigh number. The Péclet number so defined characterizes the influence of inertia effects in eq. (3.34). If $Pe \ll 1$, the flow can be considered inertia-less with regard to the energy balance.

3.5 Boundary conditions

To solve the equations described in Sections 3.3 and 3.4 for a practical engineering problem initial and boundary conditions must be supplied to completely define the problem. A typical case is a fluid volume V that is bounded by solid walls at an interface Γ, but it is connected through some surfaces to a larger, at limit infinite, fluid body, from where there is flow entering and exiting the volume considered. Initial conditions define the status of all the variables at the initial time step

considered throughout the problem domain and boundary conditions are specified to characterize the problem at the interface of the domain.

For a problem described by the magneto-hydraulic equations discussed in Section 3.3, like the flow in a rectangular duct that it is considered in Section 3.6, kinematic and electromagnetic boundary conditions must be defined. The no-slip condition is commonly employed for viscous fluids flowing over solid surfaces

$$\mathbf{v} = 0 \tag{3.43}$$

For problems involving an inlet/outlet to allow the fluid flowing inside/outside the domain, boundary conditions must be specified to characterize the inflow and outflow. A common example is to define a uniform velocity normal to the boundary at the inlet and zero relative pressure at the outlet, but several combinations are possible [41].

Regarding electromagnetic boundary conditions, they differ depending on the main electromagnetic variable chosen in the expression of the governing equations [33]. Let us consider the ϕ-formulation and, for instance, an insulated wall. No current can penetrate the solid boundary Γ from the fluid side, and, therefore, the current density is null at the wall

$$\mathbf{J} \cdot \mathbf{n} = 0 \tag{3.44}$$

where $\mathbf{n}$ is the unit vector normal to the wall in the inward direction. This condition is also used to characterize the external surface of a duct in the case of electro-conductive walls and for the inlet/outlet, where it is assumed that the flow is in fully developed condition and, thus, no current should enter or exit the domain. The condition can be reformulated in terms of electric potential as following

$$\frac{\partial \phi}{\partial n} = 0 \tag{3.45}$$

Considering a perfectly conducting wall, all the current are assumed to cross the boundary surface and the potential therein is uniform. This is equivalent to assume that the wall is at the reference (ground) potential and we can employ the Dirichlet boundary condition

$$\phi = 0 \tag{3.46}$$

For a finite conductivity wall, it is necessary to solve eq. (3.26) in both the fluid and solid domain to obtain the correct potential distribution. A way to characterize this conjugated problem, it is to assume the conservation of current and potential at the interface Γ[5]

$$\mathbf{J} \cdot \mathbf{n} = \mathbf{J}_w \cdot \mathbf{n} \tag{3.47}$$

$$\phi = \phi_w \tag{3.48}$$

If the wall is thin, i.e. $t_w \ll L$, the problem can be simplified assuming that the current entering the wall is discharged uniformly in the tangential direction, or, equivalently, that there is no normal component of the current *inside* the wall. If this

[5]Only valid if the electric contact resistance is negligible

is true, the normal gradient of the potential in the wall vanishes and the boundary condition takes the form

$$\mathbf{J} \cdot \mathbf{n} = -\frac{\partial \phi}{\partial n} = \nabla_T \cdot (c \nabla_T \phi_w) \tag{3.49}$$

where ϕ_w is the wall potential, that can vary only in the tangential direction, and ∇_T is the two-dimensional operator in the tangential direction. The main advantage of this formulation is that allows to model just the fluid-solid interface, not requiring to solve eq. (3.26) in the solid domain even for three-dimensional or time-dependent flows [33].

For magneto-convective flows, suitable thermal boundary conditions must be added for eq. (3.28). Typical examples include the adiabatic, fixed temperature and fixed heat flux conditions

$$\frac{\partial T}{\partial n} = 0 \tag{3.50}$$

$$T = T_w, \quad \text{at} \quad \Gamma \tag{3.51}$$

$$q'' = q_w, \quad \text{at} \quad \Gamma \tag{3.52}$$

3.6 Magneto-hydraulic flow in rectangular ducts

In the present Section and the following ones, we are going to qualitatively describe some basic MHD phenomena to gain further insights on how the equations derived in Sections 3.3 and 3.4 modify the flow behavior with regard to the usual fluid-dynamics.

The MHD flow in a channel of rectangular cross-section is a well-studied case in magneto-hydraulics, with the first paper on the subject probably being the theoretical work by Shercliff [42], and one of practical interest for the design of fusion reactor blankets, where similar conduits are often used to route the liquid metal flow in both the breeding zone and the manifold region. Channel aspect ratio and wall conductivity are geometrical parameters that play a fundamental role in the definition of the flow features.

Consider the case of a laminar fully developed flow in a duct of rectangular cross section, defined by an horizontal $2a$ and vertical $2b$ length, and infinite stream-wise extension, like the one pictured in Figure 3.1. We employ a coordinate system (x, y, z) located in the duct center for the stream-wise, horizontal and vertical direction. The half-width of the duct in the magnetic field direction is taken as length scale ($L = a$). The duct is filled with an electrically conductive fluid, which is driven in the stream-wise direction by a constant pressure gradient and, thus, is characterized by a unidirectional velocity field $\mathbf{v} = u\tilde{x}$, where u_0 is the mean velocity. A uniform magnetic field is applied in the horizontal direction $\mathbf{B} = B\tilde{\mathbf{y}}$. The duct walls at $y = \pm a$ see a perpendicular magnetic field and are called the Hartmann walls, whereas the walls at $z = \pm b$ are parallel to the magnetic field and are called the side (or Shercliff) walls.

The velocity and magnetic field interacts to generate a current density in the flow as per eq. (3.24), i.e. $\mathbf{J} = \sigma(\mathbf{v} \times \mathbf{B}) = -\sigma u_0 B\tilde{\mathbf{z}}$, and, thus, an electric potential difference arises between the side walls to drive the currents. Since the induced currents have to satisfy the charge conservation and the duct has a finite extension

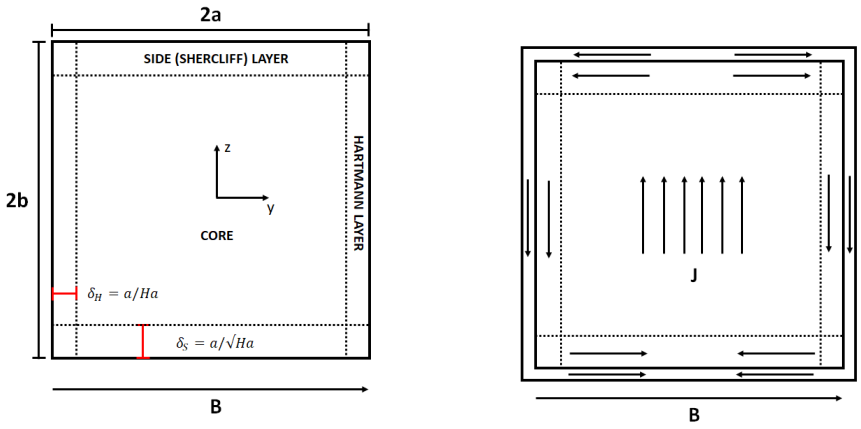

(a) Flow regions and boundary layer scales

(b) Induced currents path

Figure 3.1. MHD flow in rectangular electro-conductive duct with applied transverse magnetic field. The stream-wise direction is entering the picture plane.

in the horizontal direction, the side wall potential is not constant in the tangential direction and will drive the currents to close into the duct walls and the viscous layers attached to them, as it is depicted in Figure 3.1. From the Lorentz force expression (i.e. $\mathbf{F}_L = \mathbf{J} \times \mathbf{B}$), the current components perpendicular to the magnetic field generate a body force. It is possible to distinguish three regions in the duct, depending on the interaction between the Lorentz force and the pressure gradient:

- the *core* region, corresponding to the duct central area, where the Lorentz force is opposed to the driving pressure gradient
- the *Hartmann layers*, attached to the Hartmann walls, where the currents (and the Lorentz force) have the opposite direction compared with core and it is, therefore, aligned with the pressure gradient
- the *side (Shercliff) layers*, attached to the side (Shercliff) walls, where the currents flow parallel to the magnetic field and the Lorentz force has negligible intensity.

In the core, the main force balance is mostly between the Lorentz force and the pressure gradient. Since the former it is directly proportional to the local flow velocity through eq. (3.24), it tends to flatten the velocity profile in this region [33]. In the limit of high magnetic field ($Ha \gg 1$) and low velocity ($N \gg 1$), viscous and inertial forces do not affect the core region, thus the Lorentz force balances the pressure gradient and a slug flow (i.e. flat velocity profile) is observed. Therefore, the electromagnetic forces contribute to the flow pressure drop and, under the assumptions made, the loss due to the "electromagnetic drag" can be several orders of magnitude larger than the viscous one.

In the Hartmann layers, the currents direction is reversed compared with the core and the Lorentz force sustains the pressure gradient, effectively curtailing the region where the viscous forces can exert their influence. The thickness of these layers

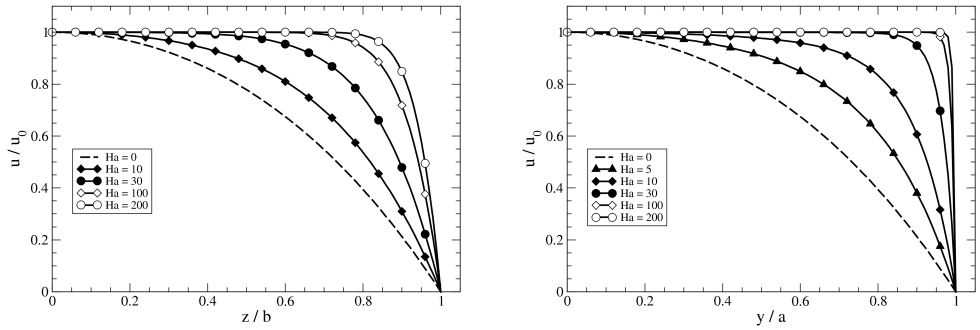

(a) Side wall velocity profile **(b)** Hartmann wall velocity profile

Figure 3.2. Velocity profile across the side and Hartmann walls for the Shercliff flow. Here, u_0 represents the velocity at the duct center.

follows the law $\delta_H = a/Ha$. For $Ha \gg 1$, the layer is very thin and it is characterized by steep velocity gradients and (relatively) high current density. The Hartmann layer is considered an *active* boundary layer, since it does not simply match the no-slip boundary condition at the wall with the core solution but it plays a fundamental role in the definition of the flow features: it is involved in the conservation of the induced currents and it is where most of the drag exerted on the flow is located (together with the Hartmann wall, when this happens to be electro-conductive). Numerical schemes have to accurately resolve the flow solution in the Hartmann layers to achieve acceptable accuracy and, therefore, direct numerical simulation of MHD flows becomes very expensive for $Ha \gg 1$ [43].

In the side layers, the currents are driven by the side wall potential and flow in the tangential direction. Due to the relative orientation of the magnetic field and side wall, no Lorentz force is present and the flow balance is between the pressure gradient and viscous forces only. The layer thickness is greater than for the Hartmann layer and follows the law $\delta_S = a/\sqrt{Ha}$.

The wall conductivity influences the flow behavior and the features appearing in the side layers. To characterize the relative ratio of fluid and wall conductivity, we introduce a dimensionless parameter called *wall conductance ratio*. For a rectangular duct, it can be defined as

$$c = \frac{\sigma_w}{\sigma}\frac{t_w}{a} \tag{3.53}$$

where σ_w and t_w are the wall electrical conductivity and thickness. To illustrate the effect of this parameter on the flow features, we are going to review three fundamental flow conditions: perfectly insulating walls ($c = 0$), perfectly conducting walls ($c = \infty$) and non-uniform wall conductivity.

Shercliff case

The flow in a rectangular duct with perfectly insulating walls ($c = 0$) was first treated by Shercliff [42] who theoretically obtained the exact solution for this problem regarding the velocity and magnetic field. The characteristic velocity profiles across the side and Hartmann walls are represented in Figure 3.2.

If the side walls are not conducting, the currents exiting the core region are forced to close through the viscous side and Hartmann layers. For $Ha \gg 1$ the thickness of these layers is very small and they offer a high resistance path that results in an overall reduced current intensity compared with electro-conductive walls. For constant Re, the pressure gradient is found to be a linear function of Ha or, rather, of the magnetic field intensity through the relation [44]

$$\frac{\partial p}{\partial x} = \lambda \frac{\rho u_0^2}{2a} \tag{3.54}$$

where the pressure coefficient λ is expressed in the form

$$\lambda = \frac{2Ha}{Re}\left(1 - \frac{0.852}{(b/a)Ha^{0.5}} - Ha^{-1}\right)^{-1} \tag{3.55}$$

where Ha/Re is known as the *Hartmann friction term*. In the brackets, it is possible to distinguish the contribution, in order, of the core region, side, and Hartmann layers. In eq. (3.55), the role of the channel aspect ratio b/a in the definition of the electromagnetic drag is evident. For $b/a \to \infty$, the channel is characterized by very long Hartmann walls, the side layer term disappears and the pressure gradient has its maximum value, with all the drag experienced by the flow being generated in the Hartmann layers. Conversely, for $b/a \to 0$ the Hartmann walls are short and, thus, the drag exerted by them is reduced, leading to a correspondingly smaller pressure gradient. Overall, the transition to the MHD regime increases the pressure loss compared with the ordinary hydrodynamic case, and the difference is only widened by a growing magnetic field intensity.

Hunt-I case

We now consider a duct with perfectly conducting walls ($c = \infty$), a scenario for which a comprehensive theoretical solution was first developed by Hunt [45]. Alternative discussions on the same problem were formulated also by Uflyand [46] and Chang and Lundgren [47]. The velocity profile across the side walls is represented in Figure 3.3, the Hartmann velocity profile is the same as the one in Figure 3.2b.

If the side walls are well-conducting, the currents exiting the core region are strongly favored to avoid the more resistive path offered by the thin viscous layers. In the limit of perfectly conducting walls, all the current density generated in the core is flowing through the wall, whereas the boundary layer does not carry any, as it is seen in Figure 3.3a. As a result, the overall current density increases and the pressure loss from the electromagnetic drag is similarly enhanced compared with the insulating case. The pressure gradient takes the form

$$\frac{\partial p}{\partial x} \propto \sigma u_0 B_0^2 \tag{3.56}$$

hence, it becomes a function of Ha^2. Furthermore, close to the side walls, small overshoot regions appear where the velocity is locally higher than in the core ($u/u_0 \approx 1.25$) due to the reduced current density in the viscous layers. However, they do not contribute significantly to the overall channel flow rate.

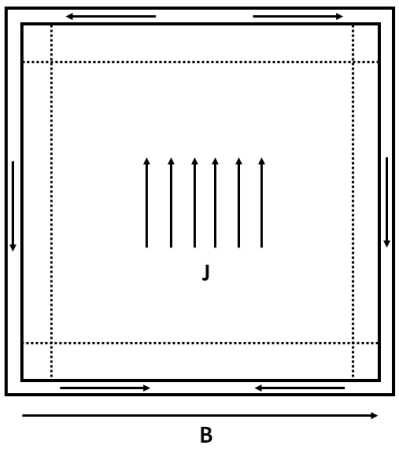

(a) Hunt-I currents path

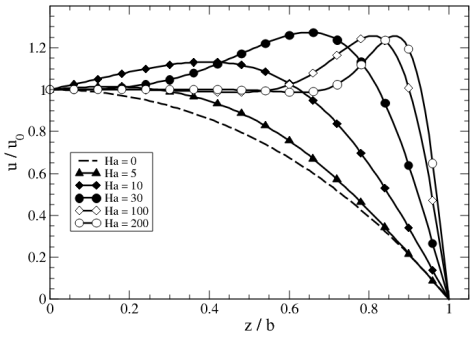

(b) Side wall velocity profile

Figure 3.3. Currents path and velocity profile across the side walls for the Hunt-I flow. Here, u_0 represents the velocity at the duct center.

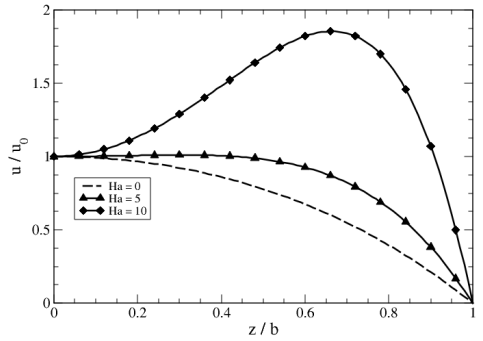

(a) Side wall velocity profile, $Ha = 0 \div 10$

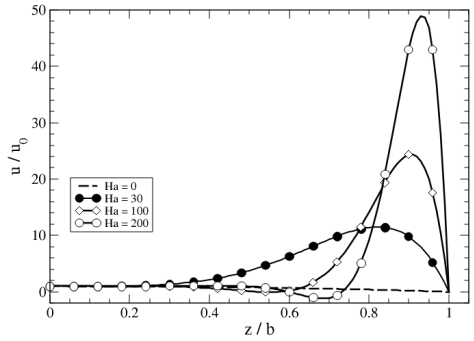

(b) Side wall velocity profile, $Ha = 30 \div 200$

Figure 3.4. Velocity profile across the side walls for the Hunt-II flow. Here, u_0 represents the velocity at the duct center.

Hunt-II case

The second case treated by Hunt considers perfectly conducting ($c_H = \infty$) Hartmann walls and insulating ($c_S = 0$) side walls [45, 48]. The non-uniform wall conductivity has a dramatic impact on the flow features in the side layers. The velocity profile across the side walls is represented in Figure 3.4, the Hartmann velocity profile is the same as the one in Figure 3.2b.

If the side walls are not-conducting, the currents are forbidden to cross the solid-fluid interface and, conversely to what happens in 3.6, the current density is entirely concentrated in the resistive viscous layers. However, since the Hartmann walls are still perfectly conducting, the current density in the core is higher compared to the one from the Shercliff case and, as well, the Lorentz force opposing the fluid movement.

A new phenomenon is observed due to the weak conducting side walls. Since the currents flow parallel to the magnetic field in the boundary layer, the drag exerted

on the flow in these region is significantly reduced compared with the core: the fluid tends to escape the duct center and is redirected in high velocity jets, which flow alongside the insulated walls. Moreover, the maximum velocity in these flow structures is dependent on the magnetic field intensity ($u_{Max}/u_0 \approx \sqrt{Ha/2}$, [33]) and, for $Ha \gg 1$, these jets carry the bulk of the flow rate, whereas the fluid in the core can be considered stagnant. The jet magnitude is further increased for poorly conducting side walls.

It is interesting to note that, for this last case, the velocity profile in the side layers is characterized by both a steep gradient and an inflection point, located at the interface between the jet and the core. These features are related to the arise of flow instabilities in the side layers that, under the right conditions, can trigger the laminar/turbulent regime transition, as it was experimentally observed by Burr et al. [49]. For $Ha \to \infty$, inverse flow regions are observed between the core and the side jet. Intuitively, the pressure gradient for the Hunt-II case is higher than for the Shercliff case, but still lower than the one experienced by a duct with perfectly conducting walls.

For the specular case featuring perfectly conducting ($c_S = \infty$) side walls and insulated ($c_H = 0$) Hartmann walls, the side layers do not feature these peculiar flow structures and, overall, the velocity profile is mostly akin to the Shercliff case, see for instance Hunt and Stewartson [48]. More in general, for walls of non-uniform conductivity the flow is promoted closer to the less conducting wall, whereas the fluid tends to avoid the area surrounding the more conducting wall, resulting in corresponding lower local velocity. Recently, analytical solutions have been developed for asymmetrical walls of arbitrary conductivity by Tao and Ni [50].

3.7 Magneto-convection in differentially heated rectangular duct

Magneto-convective flows are of practical interest for the blankets where the liquid metal is employed exclusively as tritium breeder and carrier, since the fluid velocity is minimized to reduce as much as possible the pressure loss from MHD effects and, therefore, the buoyancy forces can significantly affect the flow features. In this section, we are going to describe the main features for a laminar fully developed flow in a rectangular duct of infinite vertical extension. This case is the magneto-convective analogue of the case treated in section 3.6 for the forced convection and it was first studied asymptotically by Bühler for electro-conductive walls [4], whereas a solution for insulated walls was lately presented by Blosseville et al. [51]. Another important case for blanket engineering, the magneto-convection generated by volumetric power generation, is going to be presented in section 9.9.

Consider the case of a differentially heated duct, like the one presented in Figure 3.5, where a temperature gradient is imposed across one wall pair, whereas the opposite wall pair is adiabatic. We define a coordinate system (x, y, z) for, respectively, the duct axis direction and the two wall directions, with its origin in the duct center. No volumetric power source is present and the fluid is assumed to have excellent thermal conductivity. In particular, we make the hypothesis that inertial effects can be neglected both in the momentum (eq. (3.33)) and energy

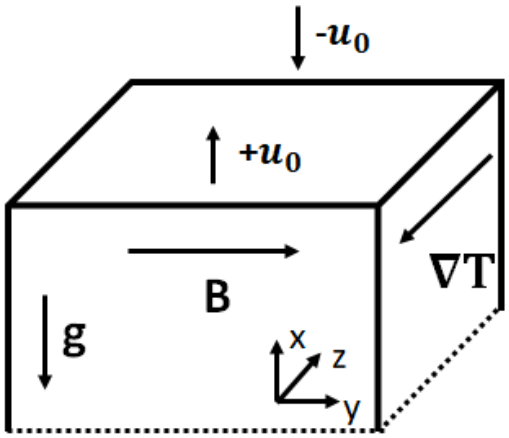

Figure 3.5. Magneto-convection in differentially heated rectangular duct. The velocity scale is $u_0 = \nu Gr/aHa^2$.

(eq. (3.34)) equation, i.e. $Ha^4/Gr \gg 1$[6] and $Pe \ll 1$. Under these assumptions, the energy equation reduces to the Laplace equation $\nabla^2\hat{T} = 0$, and the dimensionless temperature profile can be expressed as a linear function of the wall coordinate. We consider the case for the temperature gradient (i.e. $\hat{T} = z$) perpendicular to the applied magnetic field (i.e. $\hat{B} = y$).

Similarly to what happens in the pressure-driven case, the flow can be divided in a core region and two classes of boundary layers depending on the wall they are attached to. In the core, the main momentum balance is between the pressure gradient, the Lorentz force and the buoyancy force. The temperature gradient between the side walls triggers the appearance of a rotational cell, with the fluid moving upward in the half-duct close to the hot side wall ($z > 0$) and, conversely, downward for $z < 0$. As a result, the induced currents flow in opposite directions and, to respect the charge conservation, are forced to bend in the $y-$direction to close through the side layer/wall and Hartmann layer/wall, thus forming four current loops. The wall conductivity then determines the flow features.

Electro-conductive walls

If the walls are perfectly conductive ($c = \infty$), the velocity in the core is linear and independent by the Hartmann number ($u \approx z$), but in the side layers the fluid is accelerated by jets with velocity $O(\sqrt{Ha})$. This is a feature not found in the pressure-driven case, where high velocity jets are observed only for non-uniform wall conductivity and, for the uniform case, in poorly conducting walls ($Ha^{-0.5} \ll c \ll 1$). For the magneto-convective flow, jets are present in the side layers regardless of the wall conductivity and their velocity is further enhanced for $c \ll 1$ compared

[6] It should be noted that for a flow characterized by high velocity jet, i.e. $O(\sqrt{Ha})$ or O(1), the momentum inertia-less condition is more stringent and it can be written as $Ha^4 \gg Gr(\mathbf{v}\cdot\nabla)\mathbf{v}$. Nevertheless, it is usually met in fusion reactor blankets [4]

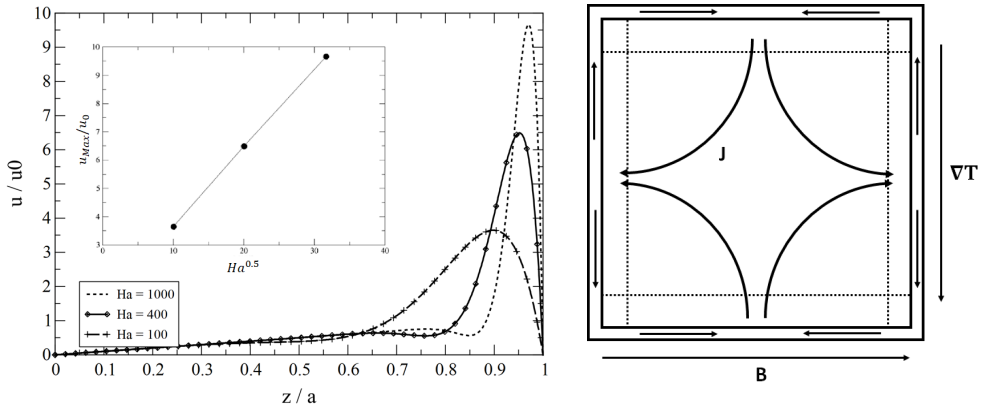

(a) Side wall velocity profile, $Ha = 100 \div 1000$ **(b)** Induced currents path

Figure 3.6. Velocity profile across the side walls for electro-conductive walls and induced currents path. Inside Figure 3.6a, the jet velocity is scaled with $\sqrt{Ha}$.

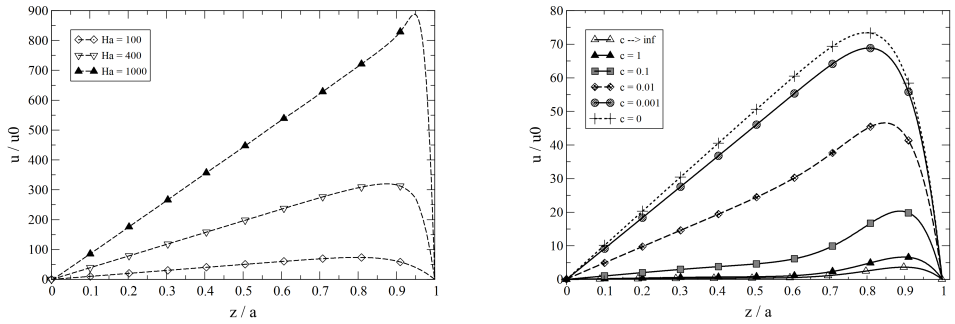

(a) Side wall velocity profile, $Ha = 100 \div 1000$ **(b)** Side wall velocity profile for $Ha = 100$ and $c = 0 \div \infty$

Figure 3.7. Velocity profile across the side walls for perfeclty insulated walls in the range $Ha = 100 \div 1000$ and for several wall conductivity at $Ha = 100$.

with $c = \infty$. The side wall velocity profile and induced currents path for $c = \infty$ are presented in Figure 3.6.

Insulated walls

If the walls are perfectly insulated ($c = 0$), the core velocity takes the form $u = Ha * z$ and jets are no longer observed in the side layers, where the no-slip boundary condition at the wall is directly matched by the core solution. The side wall velocity profile for perfectly insulating duct is presented in Figure 3.7a, whereas in Figure 3.7b the transition from insulated to electro-conductive wall is presented.

For non-uniform wall conductivity the general behavior is quite similar to what already described for the forced convection case. For a Hunt-II scenario, where the side walls are insulated and the Hartmann walls are conducting, the peak velocity is enhanced and its magnitude is O(Ha), whereas the core is found to be almost

stagnant. For $Ha \to \infty$, limited flow reversals are observed in the interface region that connects the jet and the core [52].

Another important case of practical interest for blanket design, not described here, it is for a duct where ∇T is aligned with $\mathbf{B}$. In this situation, the current pattern is rearranged in a single loop and the jets are restricted to the duct corners, which carry most of the flow rate, whereas the core flow is very weak [4, 51]. Due to this phenomenon, for the sameΔT, the $\nabla T \parallel \mathbf{B}$ case features smaller peak velocities compared with $\nabla T \perp \mathbf{B}$ [51].

3.8 Summary

In this Chapter, the governing equations for pressure-driven and magneto-convective MHD flows have been derived from the combination of the Navier-Stokes and Maxwell equations. The quasi-static and induction-less approximations have been employed to simplify the complexity of the problem by decoupling the magnetic field from the fluid velocity. The principal dimensionless groups that influence the flow and their physical meaning have been discussed and suitable kinematic, thermal and electromagnetic boundary conditions have been presented for modeling purposes.

The main phenomena have been exposed discussing the flow in rectangular ducts of arbitrary wall conductivity for both pressure-driven and magneto-convective conditions. For the magneto-hydraulic problem, three relevant situations are described: the flow in an insulated duct (Shercliff case), a perfectly conducting one (Hunt-I case), and a channel with walls of non-uniform conductivity (Hunt-II case). The pressure loss is found to be a function of the magnetic field intensity through Ha and it is generally much higher than the one due to the viscous forces. For $Ha \gg 1$, the viscous term can be neglected entirely, and the pressure loss is approximated only by the Lorentz force term. The viscous forces are confined to thin boundary layers close to the wall, their thickness depending on the relative orientation between the wall normal and the applied magnetic field. The wall conductivity plays a fundamental role by shaping the current paths and it is responsible for the appearance of characteristic feature like the high intensity velocity jets for the Hunt-II case.

For the magneto-convective problem, a vertical differentially heated duct has been considered for insulated and electro-conductive walls. The general features already encountered in the pressure-driven case are found, namely the partitioning of the flow in an inviscid core and thin viscous boundary layers. The temperature gradient leads to a more complex current distribution and to a velocity field dominated by jets for every wall conductivity. The relative orientation of temperature gradient and magnetic field is an important parameter to consider since it affects the fluid velocity field.

Other relevant phenomena for the blanket design, that have not been discussed in this Chapter for brevity's sake, are the MHD effect on turbulence, heat transfer, and mass transport, particularly involving tritium and corrosion.

Part II

Blanket configuration comparative analysis

Chapter 4

Comparative analysis rationale and methodology

4.1 Introduction

One of the most important effects caused by the transition to the magnetohydrodynamic regime for the liquid metal flow in the blanket is the increase in pressure drop due to the retarding action exerted on the fluid by Lorentz forces. For the magnetic field intensity foreseen in a power plant reactor like DEMO, where $Ha = O(10^4)$, the electromagnetic drag is so massive that completely dominates the blanket pressure balance and marginalizes the effect of inertial and viscous forces. An accurate estimate of the MHD pressure drop is of paramount importance to identify the critical points in the PbLi flow path and to guide the design optimization process. Although correlations have been developed since many years to predict the amount of the pressure losses for fully developed flows in ducts with arbitrary wall conductivity, a comprehensive understanding of the MHD phenomena concerning more complex (but very common) geometrical elements is still lacking and the known relations are either too general or have a too narrow range of applicability. Other important phenomena expected to significantly affect the blanket performances, like mixed convection flows, boundary layer instabilities, and coupling between nearby electro-conductive channels, just to cite the most relevant, are still under active research from the MHD scientific community.

Despite these limitations, in this chapter the available correlations are applied to the Water-Cooled Lithium Lead (WCLL) concept to perform a qualitative assessment of the MHD pressure losses in the PbLi hydraulic path for the outboard blanket segment. Four alternative WCLL models are considered, employing different configurations for the Breeding Zone (BZ) elementary cell, fluid distribution layout, and

Table 4.1. WCLL configuration system-level features

	T01.A	T01.B	T02	T03
BZ flow path preferential direction	Radial-poloidal	Radial-poloidal	Poloidal	Poloidal (Upward-Downward)
Typical BZ velocity BZ channel length	< 1 mm/s 1 m	10 mm/s > 50 m	2 mm/s 15 m	4 mm/s 30 m
Cooling pipe layout	Horizontal C-pipes	Horizontal C-pipes	Horizontal U-pipes	Vertical
Flow distribution	Distributed	Localized	Localized	Localized
Feeding pipe routing Draining pipe routing	Bottom Top	Bottom Top	Bottom Top	Top Top

interfaces with the external PbLi loop. A detailed analysis of the PbLi path for each configuration is carried over, identifying possible critical elements and investigating alternative strategies to minimize the pressure drop for the liquid metal evolution. The results of CFD studies performed in the framework of this work were integrated in the qualitative assessment, thus providing useful insights for the discussion of WCLL-specific phenomena. In Chapter 11, the fluid dynamics and heat transfer for the BZ channel of configuration T02 is discussed, whereas in Chapter 10 the BZ flow of configuration T01.A is analyzed in the context of the forced convection flow around a refrigerating pipe transverse to the stream-wise direction.

4.2 Rationale and configuration comparison

The main objective of this study is to estimate the amount of pressure drop due to MHD effects in the PbLi hydraulic path of the WCLL breeding blanket design. Although being in development in the framework of the Work Package Breeding Blanket (WPBB) of the EUROfusion consortium since early 2014, no comprehensive MHD analysis of the WCLL PbLi loop has ever been performed. For the purpose of this study, four alternative configurations are investigated, whose main features are collected in Table 4.1. The principal outcome expected from this analysis is the identification of the blanket configuration that is the most desirable by the point of view of the MHD pressure drop minimization and, in addition, shows the higher potential for being transposed to the inboard and allows the maximum flexibility for alternative feeding/draining schemes.

Configuration T01.A and T01.B share the same BZ flow path, but are radically different regarding the flow distribution concept and this causes a huge difference in the velocity scale expected that, for the latter case, approaches values typical for Dual Coolant breeding blankets. The distributed flow distribution of configuration T01.A involves the use of narrow rectangular channels running along the blanket spine that continuously feed the BZ cells stacked in the poloidal direction. The other WCLL configuration resorts instead to a more classical flow distribution scheme, where a manifold tank directly feeds all the BZ channels.

Configuration T02 and T03 share the BZ and stiffening plate (SP) layout, but

are characterized by a different orientation of the cooling pipes that completely alters the thermal-hydraulic blanket behavior. For the latter, the PbLi is going to flow downward in the back channels and upward in the front channels. To reduce the flow path complexity, this configuration is fed from the top, whereas all the other WCLL models employ as baseline a feeding pipe that is connected to the blanket bottom. The liquid metal egress from the blanket is executed from the top for all the configurations via a draining pipe.

Following the literature consensus, the maximum value of the pressure drop allowed for the outboard blanket is established at 2 MPa [53]. It should be noted that the determination of this figure is intrinsically linked to plant-level energy balance considerations: depending on the efficiency and the head available from the pumps employed to move the liquid metal in the PbLi loop, this limit could be higher or even lower than the one assumed for this study. In general, blanket configurations exceeding the threshold are unlikely to be able to meet the plant design requirements and, moreover, are going to perform even more poorly when translated to the inboard conditions, where the magnetic field intensity is nearly double the one of the outboard blanket (9 T versus 4.5÷5 T).

4.3 Methodology

The analysis is based on the most recent version of the DEMO baseline that was released by the EUROfusion Project Management Unit (PMU) in March 2017 [9]. The coordinates that identify the geometry of the blanket, the pipe connection with the ex-vessel PbLi reactor loop, the toroidal and poloidal field coils are extracted from the report by Maviglia [54] and are combined with the data provided from the WCLL Design Team to define the main parameters of PbLi path subjected to a significant magnetic field for the four configurations analyzed. The available data on geometry are supplemented, where both necessary and unavoidable, by extrapolating the design developed for the 2015 DEMO baseline [55]. Detailed information on the previous WCLL design can be found in Ref. [56–58]. Suitable scale coefficients are employed to account for the different size allocated for the blanket in the two DEMO baseline.

In Figure 4.1, the quasi-toroidal coordinate system employed for this study is presented. First, a quasi-toroidal coordinate system with its origin on the plasma torus center is employed to define the position of components at the tokamak-level scale. In this framework, we define a toroidal (ϕ), vertical (Z), and radial (R) direction. Since the blanket completely surrounds the plasma chamber, a second coordinate system is employed to define position at blanket-level scale with its origin placed in the torus cross-section center. In this case, the toroidal coordinate is shared between the two systems, whereas the radial direction (r) is now defined from the torus cross-section center. A poloidal (θ) direction is added to define the position with respect to the torus horizontal plane. Whenever there is case of ambiguity between R and r, the former is referred to as *global* radial coordinate, whereas the latter as *local* radial coordinate

The DEMO blanket is divided in the toroidal direction into 16 sectors, each corresponding to about 22.5° torus "slice": the inboard blanket is further partitioned

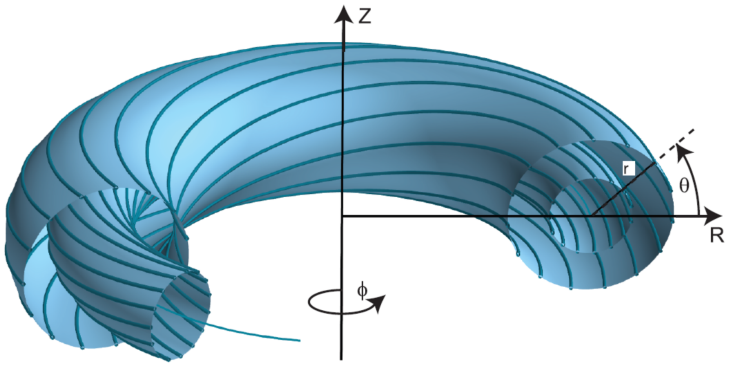

Figure 4.1. Blanket coordinate system with reference to the plasma torus [59]

into two segments, whereas three segments are foreseen for the outboard one (2 lateral segments and 1 central segment). Globally, the DEMO blanket is composed by a total of 32 inboard and 48 (32 lateral, 16 central) outboard segments. Conversely to the inboard, where the two segments share the same geometry and operative parameters, the lateral outboard segment is slightly smaller compared with the central one. The analysis presented in the present chapter is focused on the PbLi hydraulic path for the latter, whereas the lateral outboard and inboard segments are not considered. In Figure 4.2, the blanket sector segmentation and connection with the PbLi loop are presented[1].

The loading of the liquid metal is performed from the VV lower port, whereas the drainage is effectuated through the VV upper port. The layout of the 2017 DEMO baseline is presented in Figure 4.3. The outboard global radial dimension available for the blanket (breeding zone + manifold + supporting structure) is equal to 1 meter [9], as opposed to the $\approx$ 1.3 meter allocated in 2015 [55]. The toroidal width of the blanket segment is not uniform with the vertical (poloidal) coordinate. On the equatorial plane ($z = 0$), the blanket has the maximum toroidal width ($L_{tor} = 1.5$ m), moving upward (or downward) along the vertical (poloidal) coordinate the toroidal width is reduced and reaches its minimum ($L_{tor} \approx 1.05$ m) at the top and bottom blanket caps. Therefore, the cross-section available for the PbLi is a function of the vertical (poloidal) coordinate, even if the elementary fluid cell geometry is mostly unchanged along the blanket height [58].

The PbLi path in the blanket can be divided in four hydraulic regions:

1. **Feeding pipe (FP)**: connection pipe between the PbLi ex-vessel loop and the breeding blanket, its main tasks are the loading, feeding, and emergency draining of the breeding zone. It is usually assumed to be routed through the VV lower port, even if in the context of this study alternative placements are considered. It is characterized by significant velocities ($\approx$ cm/s).

2. **Manifold**: it distributes and collects the PbLi to/from the breeding zone. This region features complex geometrical elements and significant velocities, whereas it occupies a relatively small blanket volume. It is composed by three

[1]Only some of the pipes shown are part of the PbLi circuit, others are dedicated to the routing of the coolant

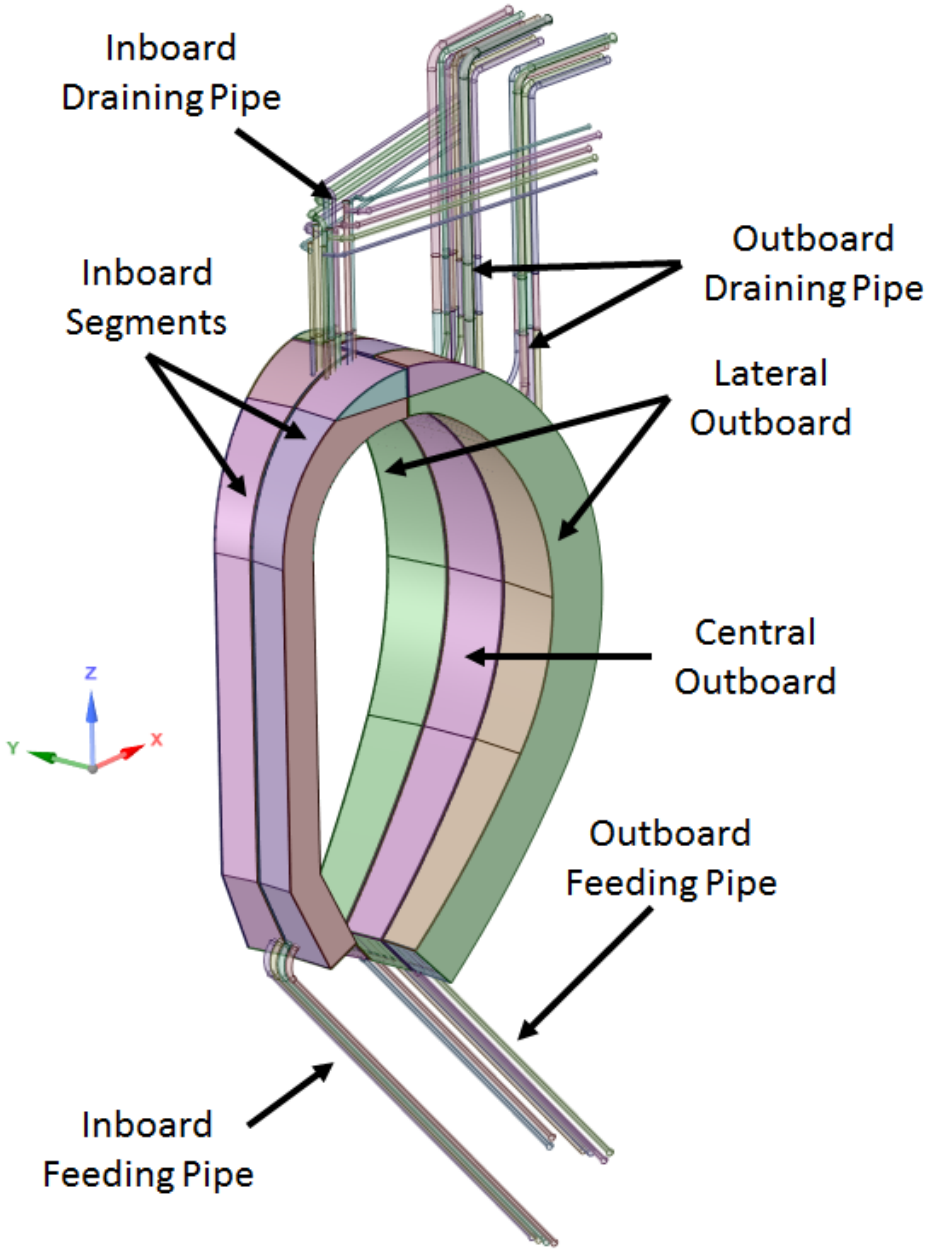

Figure 4.2. DEMO2015 blanket sector and connection pipes with PbLi loop. The DEMO2017 is qualitatively similar.

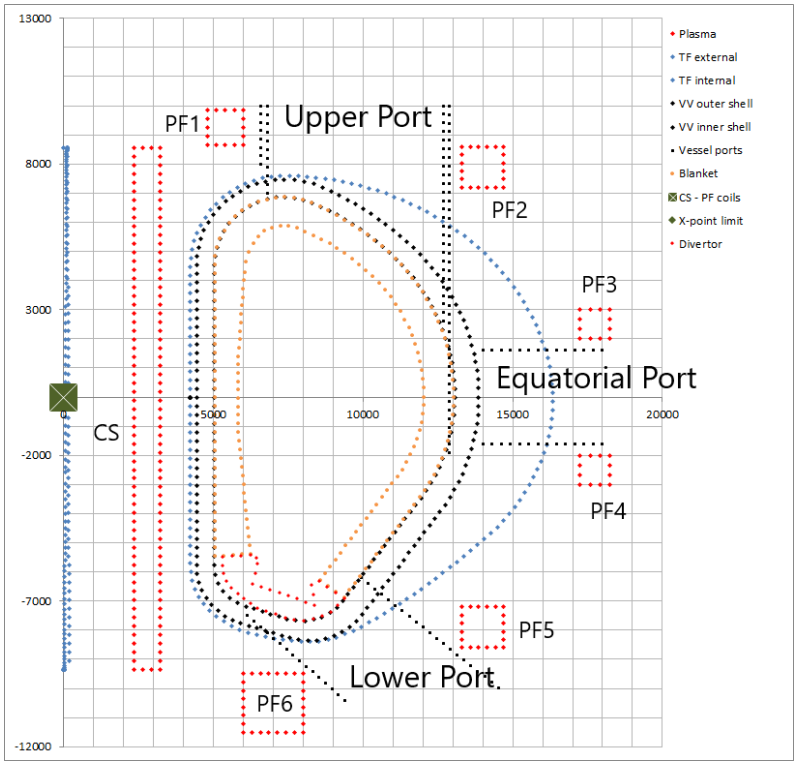

Figure 4.3. DEMO 2017 general layout [54]. The blanket position is indicated by the yellow dots. The abscissa and ordinate axes correspond to the global radial and vertical coordinate.

sub-regions: the Distribution Manifold (DM), the Collection Manifold (CM), and the Spinal Manifold (SM, only for T01.A).

3. **Breeding zone (BZ)**: it occupies the bulk of the blanket volume and it is characterized by relatively simple flow path, mostly aligned with the radial and poloidal direction. Low velocities are expected.

4. **Draining pipe (DP)**: return pipe to the PbLi external loop, its main task is the evacuation of the liquid metal from the blanket. In the design baseline, it is routed through the VV upper port, but in the context of this study, alternative attachment points are considered. It is characterized by significant velocities ($\approx$ cm/s).

The FP and DP regions are common to all the configurations considered, whereas the design of the Manifold and the BZ differs greatly with regard to the geometry, velocity and flow path. Due to the early phase in the design development cycle, only the BZ is characterized by a geometry with a level of detail high enough to allow for a straightforward analysis of the pressure loss in the PbLi path. For the purpose of this study, it is necessary to "bridge the gaps" in the hydraulic layout of the PbLi path and, in particular for the Manifold region, careful conservative assumptions are made to devise the simplest flow path that does not require significant modifications in the structural elements arrangement. Later in the development cycle, it would be

Table 4.2. Physical properties of Lithium-Lead (PbLi) [61] and Eurofer steel [62] at $T = 599$ K.

Property (unit)	Symbol	Value
Lithium-Lead		
Density (kg/m^3)	ρ	9806
Electrical conductivity (S/m)	σ	$7.82{\cdot}10^5$
Kinematic viscosity (m^2/s)	ν	$1.967{\cdot}10^{-7}$
Eurofer		
Electrical conductivity (S/m)	σ_w	$1.145{\cdot}10^6$

Table 4.3. Operative parameters for WCLL PbLi loop [60]

Description	Value	Unit
PbLi Inboard BB Volume	144.9	m^3
PbLi Outboard BB Volume	698.65	m^3
Blanket Total Volume	843.55	m^3
Blanket Total Mass Flow Rate	956.52	kg/s
Number of Inboard Loops	3	
Inboard Loop Mass Flow Rate	56.76	kg/s
Number of Outboard Loops	3	
Outboard Loop Mass Flow Rate	262.08	kg/s
Maximum Temperature	640(367)	K/(C°)
Minimum Temperature	573/(300)	K/(C°)
Average Temperature	599/(326)	K/(C°)

necessary to perform accompanying thermo-mechanical analyses in order to asses the structural stability of the hydraulic components proposed in this study.

The boundary conditions for the interfaces with the PbLi loop are obtained from the report by Utili et al. [60]. The main parameters of the PbLi loop are listed in Table 4.3. The PbLi in the blanket is assumed to be isothermal at the average operative temperature of the PbLi loop, thus any change in the liquid metal physical properties due to the blanket heat load is neglected. These are evaluated according to the correlations obtained by Jauch et al. [61] and are presented in Table 4.2, together with the Eurofer electrical conductivity, which is needed to evaluate c. From the outboard blanket total mass flow rate and the number of outboard segments, assuming uniform flow distribution, it is possible to obtain the PbLi mass flow rate for a central segment as $\Gamma_{OB} = 16.38$ kg/s[2].

4.3.1 Magnetic field

In a tokamak, the main magnetic field components are aligned to the toroidal and poloidal direction and their intensity must be known to evaluate the MHD pressure drop. The magnetic field distribution for the 2017 DEMO baseline is found in the report by Wenninger et al. [63], where it is reported for the equilibrium condition at the Start-of-Flat-Top (SOF) and End-of-Flat-Top (EOF) corresponding, respectively, to the beginning of the tokamak pulse, i.e. after the ramp-up phase, and the end

[2]For reference, the PbLi mass flow rate for an inboard segment is $\Gamma_{IB} = 5.32kg/s$

of the pulse, before the dwell time. For the purpose of this study, the magnetic field is assumed to be time-independent and equal to the SOF value; magnetic field transients are not considered.

The toroidal component is the dominant magnetic field in the blanket, since typically $B_{pol} \approx 0.1 B_{tor}$, and it is employed in the following for the evaluation of the pressure drop, unless otherwise noted. At the reference radial coordinate $R_0 = 8.9316$ m, the toroidal magnetic field has the intensity $B_{tor}(R_0) = 4.8935$ T [63]. In general, the toroidal field component is assumed to be inversely proportional to the radial coordinate inside the boundary delimited by the internal toroidal field coil (TFC) surface (see Figure 4.3) and to be uniform with regard to the poloidal coordinate, i.e. $B_{tor} = f(R)$. The variation law takes the form

$$B_{tor}(R) = B_{tor}(R_0)\frac{R_0}{R} \tag{4.1}$$

Outside of the region defined by the external surface of the TFC, the toroidal field is assumed to be null everywhere ($B_{tor} = 0$). Under these assumptions, we employ two limiting surfaces corresponding, respectively, to the boundary between the plasma and first wall, and between the back supporting structure and vacuum vessel, to identify the outboard blanket region and define the range of the toroidal field therein. In Figure 4.4a, these bounding surfaces are identified by the labels "front" and "back". The plot of the toroidal field on these surfaces is presented versus the vertical coordinate in Figure 4.4. Depending on the position, the toroidal field can vary in the range $B_{tor} = 3.35 \div 5.45$ T: the minimum intensity is found in correspondence of the equatorial plane ($Z = 0$), where the blanket is farthest from the torus center, whereas the maximum is located at the blanket top, in correspondence of the interface with the inboard blanket. Therefore, magnetic field gradients are present for both the poloidal and radial direction that must be considered in the pressure loss calculation for the blanket (see Section 4.3.2).

Regarding the poloidal field component B_{pol}, it is commonly expressed by its projections on the radial (B_r) and vertical (B_z) axis. The field distribution is complex, since it is produced by the interaction of the six poloidal coils and the central solenoid. A snapshot of the topology of the poloidal field component, taken at the SOF equilibrium, can be seen in Figure 4.5. Knowing the poloidal component intensity is very important, especially for the feeding and draining pipe that are crossing the space between two poloidal coils, where the field is at its maximum value, and for channel aligned with the radial direction, like in the configuration T01.A and T01.B, where the magnetic field cannot be considered as simply constituted by its toroidal component.

4.3.2 Pressure drop correlations

The PbLi flow path in the WCLL blanket can be described schematically as a series of pipes, either of rectangular or circular cross-section, bounded by electro-conductive walls, in general of non-uniform thickness, and connected through more complex geometrical elements, i.e. bends, sudden variations of cross-section, etc.

Considering the pressure-driven MHD flow in a duct, for instance rectangular, like the one described in Section 3.6. In the blanket, $Ha \gg 1$ and $N \gg 1$, therefore

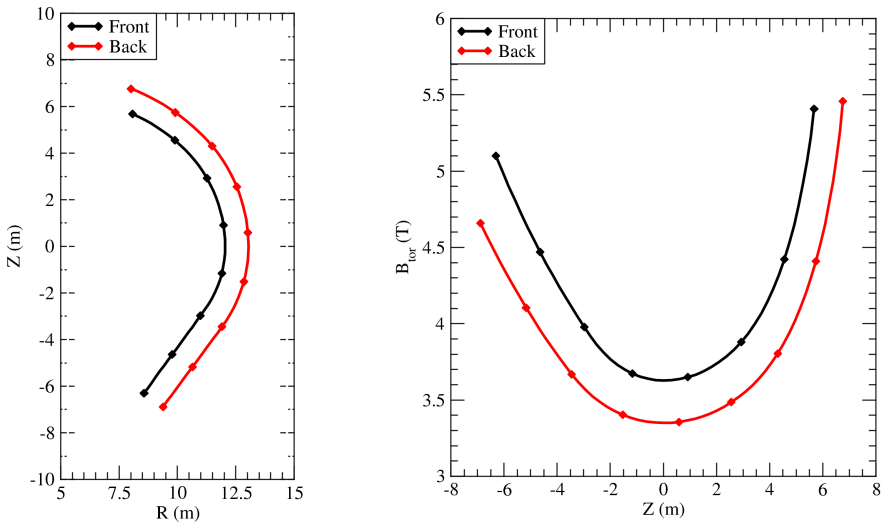

(a) Blanket Boundary **(b)** Toroidal magnetic field

Figure 4.4. The outboard blanket limiting surfaces [54] and the corresponding toroidal magnetic field distribution as a function of the vertical position [63]

the viscous forces are confined to thin boundary layers and the pressure loss occurring in the duct is only due to the retarding effect of the Lorentz Force on the flow, taking the form

$$\Delta p \approx \Delta p_{MHD} = \Delta p_{2D} + \Delta p_{3D} \tag{4.2}$$

The pressure loss due to the Lorentz Force can be split into two terms:

- The **two-dimensional term** (Δp_{2D}) or fully developed flow term is the MHD analogue of the hydrodynamic friction loss. When the flow is fully developed, the only variable with a non-null gradient in the stream-wise direction is the pressure, therefore the currents induced by the relative motion between the fluid and the magnetic field are confined to the duct cross-section. These currents are always present and can be described as an "electromagnetic drag" that dissipates the kinetic energy of the fluid through the Joule effect.

- The **three-dimensional term** (Δp_{3D}) is the MHD analogue of the hydrodynamic concentrated loss. When the flow is characterized by velocity gradients in the stream-wise direction, i.e. it is three-dimensional, the currents are no longer confined to the flow cross-section. The currents that close in the body of the fluid are responsible for additional electromagnetic drag, which is represented by the pressure drop term. 3D MHD flows are observed in complex geometrical elements (i.e. bends, cross-section variation, etc.) or ducts with non-uniform electro-magnetic boundary conditions (i.e. sharp magnetic field gradients, wall conductivity discontinuity, etc.)

More in general, the 3D pressure drop term can be considered as being composed by the sum of three separate contributions [64]

$$\Delta p_{3D} = \Delta p_{\infty} + \Delta p_{v} + \Delta p_{i} \tag{4.3}$$

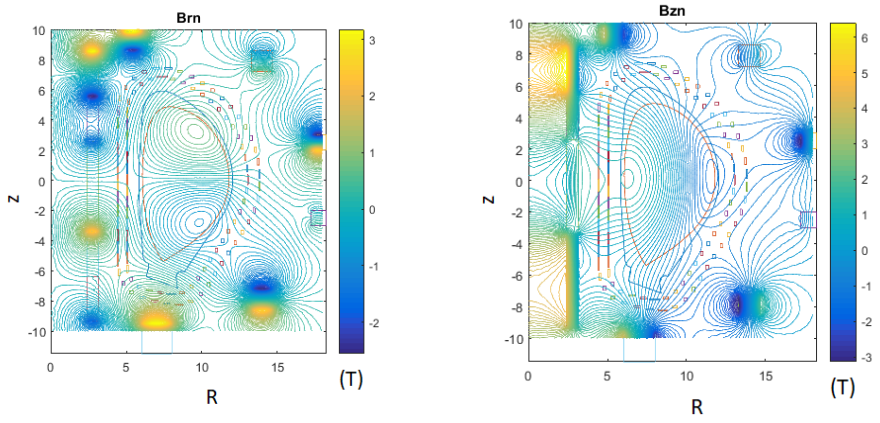

(a) Radial magnetic field component **(b)** Vertical magnetic field component

Figure 4.5. Radial and vertical magnetic field distribution. Magnetic field intensity is expressed in Tesla. SOF equilibrium [63]

where Δp_∞ is the inertia-less/inviscid term for which it is true the condition $\Delta p_{3D} \approx \Delta p_\infty$, if $Ha \gg 1$ and $N \gg 1$. Conversely, if the 3D flow is locally inertial or viscous, the terms Δp_v and Δp_i must be added to account, respectively, for the effects of viscous and inertial forces on the pressure loss.

It should be noted that eq. (4.2) is strictly valid only for a duct immersed in a non electrically conductive medium, i.e. air. In a blanket like the WCLL, the channels where the liquid metal is flowing are not electrically insulated with each other and, therefore, leakage currents can be shared across them. In this situation, it is said that the channels are electromagnetically coupled and this phenomenon leads to global flow rearrangement and, in general, to modified pressure losses compared with a similar, but uncoupled, channel. For a fixed mass flow rate, the electromagnetic coupling increases the pressure losses, or even decrease them, depending on the channel geometry, cross-section shape, relative orientation of channels stack with the magnetic field, etc. In this study, any effect of the electromagnetic coupling on the pressure drop estimate is neglected. A more in-depth analysis should take into account, together with the influence on the overall flow distribution.

Two-dimensional pressure drop estimate

Most of the WCLL PbLi hydraulic path can be described as a long straight channel where, thanks to the high magnetic field intensity, the flow is in the fully developed state and, therefore, $\Delta p \approx \Delta p_{2D}$.

For the fully developed MHD flow in a channel of constant cross-section subject to a transverse and uniform magnetic field, the pressure loss can be obtained as the product of the duct length for the pressure gradient, which can be calculated with the aid of simple correlations available in literature [44].

Limiting the discussion to channels bounded by electro-conductive walls, the pressure gradient takes the form

$$\frac{\partial p}{\partial x} = k_p \sigma u_0 B_0^2 \tag{4.4}$$

where the pressure coefficient k_p depends on the channel cross-section, geometry and wall conductivity. For a rectangular duct defined by a side wall length $2a$ and Hartmann wall length $2b$, the pressure coefficient takes the form proposed by Miyazaki et al. [65]

$$k_p = \frac{c}{1 + c + \frac{a}{3b}} \tag{4.5}$$

where the wall conductance ratio c is expressed through eq. (3.53). For a circular pipe defined by an inner radius r_i and an outer radius r_o, the pressure coefficient is expressed through the relation by Miyazaki et al. [66]

$$k_p = \frac{c}{1 + c} \tag{4.6}$$

where the wall conductance ratio takes the form

$$c = \frac{\sigma_w}{\sigma} \frac{r_o^2 - r_i^2}{r_o^2 + r_i^2} \tag{4.7}$$

if the wall is thin, i.e. $(r_o - r_i)/r_i \ll 1$, then eq. (4.7) reduces to eq. (3.53) with $r_o - r_i = t_w$ and r_i being the characteristic length. For a duct with non-uniform wall conductance ratio, as it is for nearly all the practical applications, the pressure gradient must be calculated according to different correlations. Unfortunately, this case is much less investigated in the literature compared to the more simple uniform conductivity flows, and only a correlation for rectangular duct is available, developed by Hua et al. [67], for the particular case of uniform Hartmann wall conductivity (c_H) and non-uniform side wall conductivity ($c_{S,i}$), which takes the form

$$k_p = \left[1 + c_H^{-1} + \frac{a}{6b}\left(c_{S,1}^{-1} + c_{S,2}^{-1}\right)\right]^{-1} \tag{4.8}$$

No correlation is available for the case of non-uniform Hartmann wall conductivity, i.e. $c_{H,1} \neq c_{H,2}$.

For the purpose of this study, where all the ducts composing the WCLL hydraulic path for the PbLi are bounded by electro-conductive walls, the 2D pressure drop is calculated according to eq. (4.4), employing eqs. (4.5), (4.6) and (4.8) to estimate the value of the pressure coefficient. For the few (rectangular) channels that could not be described with the relations available in literature, the conservative assumption of a uniform wall conductivity assuming the value of the more conductive wall is used. Regarding channels where the applied magnetic field is uniform, but cannot be considered unidirectional, a suitable correction coefficient $\lambda(\alpha)$ is employed to account for the magnetic field inclination [44].

Three-dimensional pressure drop estimate

The evaluation of the 3D pressure drop is much more complicated than the one for the fully developed flow due to its being strongly dependent on the flow geometry and parameters and involving three different terms accounting for electromagnetic, inertial and viscous effects as described in eq. (4.3). Moreover, for 3D MHD flows is often challenging to distinguish axial and cross-sectional currents and, therefore, to

isolate each pressure drop contribution. In the following, it is assumed that every 3D MHD flow occurring in the PbLi hydraulic path is locally inviscid ($Ha \gg 1$) and inertia-less ($N \gg 1$), to neglect all the other terms but the inertia-less/inviscid 3D pressure drop ($\Delta p_{3D} = \Delta p_{\infty}$), and that eq. (4.2) is valid. These are strong assumptions and the first one is not necessarily valid for any kind of flow considered in this study, i.e. in the manifold high velocities are expected in narrow and complex geometrical elements, where inertial effects can conceivably play a significant role. Therefore, the values reported in this study must be taken as a base estimate that should be carefully revised in the future to provide more accurate information for the design.

Conventionally, the 3D pressure drop is expressed with a local MHD resistance coefficient (ζ) that is a function of the interaction parameter N and Hartmann number Ha, other than the problem geometry and magnetic field orientation, and, therefore, represents in an implicit way the increased electromagnetic drag due to the 3D currents [53]. According to this formulation, the inertia-less/inviscid 3D pressure drop takes the form

$$\Delta p_{3D} = \zeta \frac{1}{2} \rho u_0^2 \tag{4.9}$$

where ζ is calculated employing the expression

$$\zeta = kN = k \frac{\sigma B_0^2 L_{3D}}{\rho u_0} \tag{4.10}$$

where L_{3D} is the characteristic length scale for the 3D flow, k is a constant coefficient, and N is the local interaction parameter. A critical point is the determination of the k coefficient that generally has a value in the range $0.25 \leq k \leq 2$, according to the literature consensus, and it is strongly dependent on the flow parameters considered [53]. However, Bühler pointed out how the upper limit assumed for k is usually based on experimental results that were conducted at N and Ha far from actual blanket operative conditions and, since $\zeta = f(Ha, N)$, even larger values could be possible [68]. On the other hand, several references are reporting $k < 0.25$, especially for $N \gg 1$ and flow in bends, therefore care must be taken when determining the value of the k coefficient [44].

In the WCLL design, no insulating element is foreseen to decouple the liquid metal from the electro-conductive walls, therefore the 3D pressure drop must be estimated only for complex geometrical elements and regions with magnetic field gradients. Regarding the former, these elements can be reduced to only two classes of junctions: bends and sudden variation of cross-section.

In general, the 3D pressure drop in these elements is strongly influenced by the relative orientation of the flow and magnetic field [44]. Bends that move the fluid from a plane $\perp \mathbf{B}$ to a plane $\parallel \mathbf{B}$ are characterized by higher pressure drop compared with bends entirely occurring on a plane $\perp \mathbf{B}$. Similarly, for cross-section expansion/contraction in the magnetic field direction the pressure drop is higher than for the same element where the cross-section variation is perpendicular to the magnetic field.

For the present study, 90° bends that move the fluid from/to a plane $\parallel \mathbf{B}$ are characterized by a coefficient k calculated from the theoretical relation that,

according to Reimann et al. [69], takes the form

$$k_{//} = 1.063\frac{c}{4/3 + c} \tag{4.11}$$

This correlation was obtained in the limit $(Ha, N) \to \infty$ for a square duct $(a/b = 1)$ and it has a good agreement with experimental data for both rectangular and circular channels [44]. For ducts with aspect ratio $a/b > 1$, eq. (4.11) is conservative since, noting the similarity with eq. (4.5), it is reasonable to assume that the coefficient will be lower than the theoretical one. Similarly, for ducts with aspect ratio $a/b < 1$, it is reasonable to assume $k_{//} \to 1.063c/(1 + c)$. The $k_{//}$ coefficient calculated through the Reimann correlation can be considered the upper limit for a 90° bend in a rectangular channel that move the fluid in a plane $\perp \mathbf{B}$. In this study, we assume that the coefficient $k_\perp$ for such a bend is related to the Reimann coefficient through the relation

$$k_\perp = 0.33k_{//} \tag{4.12}$$

Since inertial and viscous effects are neglected, 180° bends can be represented by two successive 90° bends and, similarly, for intermediate value opportunely reduced coefficients can be employed, i.e. $k_{60°} = 0.67k_{90°}$. The same approach is employed for bend in circular pipes assuming $k_{//} = 0.125$, as suggested by Kirillov et al. [44].

To describe sudden contraction and expansion, the coefficient $k = 0.5$ is employed regardless of the magnetic field orientation. This value is assumed to be conservative since, as a reference, Bühler reported $k = 0.315$ for an inertia-less, inviscid, sudden expansion in the magnetic field direction for a rectangular duct with large expansion ratio $L_2/L_1 = 4$ and weakly electro-conductive duct walls ($c = 0.028$) [64]. It is reasonable to assume that $k \propto L_2/L_1$ and, following the general trend for three-dimensional pressure losses, $k \to 0$ for progressively more conductive bounding walls $(c \to \infty)$. Therefore, the pressure coefficient for sudden variation of cross-section assumed in this study should be much larger than any actual coefficient for the parameters typical of any cross-section variation found in the WCLL design. Due to the assumption of inertia-less and inviscid regime, given the same geometry parameters there is no difference between the pressure drop in an expansion and in a contraction [64].

For gradual variations, like in the spinal channel of configuration T01.A, the growth or contraction of the cross-section is assumed to be slow enough such that the flow is locally fully developed and that, therefore, for a channel of axial length x_0 the total pressure drop can be calculated with the relation

$$\Delta p = \Delta p_{2D} = \int_{x_0} \nabla p(l)\, dl \tag{4.13}$$

where $\nabla p(l)$ is the pressure gradient for the fully developed flow described in Section 4.3.2, here assumed to be a function of the channel axial length.

A similar condition of local fully developed state can be defined for non-uniform magnetic field if the relative rate of change is small enough in the stream-wise direction [44]. Defining B_0, a, ΔB and x_0 as the reference magnetic field, characteristic length, magnetic field difference and axial length in the region where the magnetic

field is changing, the condition for the local fully developed flow takes the form

$$\partial_x \tilde{B} = \frac{\Delta B}{B_0} \frac{a}{x_0} \ll 1 \tag{4.14}$$

where $\partial_x \tilde{B}$ is the normalized magnetic field gradient. Considering, for instance, the flow in the spinal channel of configuration T01.A from the distribution manifold to the equatorial plane, we have that $\Delta B \approx 2.1$ T, $B_0 = 3.35$ T, $a = 0.12$ m and $x_0 = 8$ m, which gives $\partial_x \tilde{B} \approx 0.01$. Similarly, magnetic field gradients in the BZ for long poloidal (e.g. T02/T03) or radial (e.g. T01.A/T01.B) channels can be assumed to be small enough not to introduce significant 3D effects and the pressure drop can be calculated employing eq. (4.13). However, the local fully developed condition is not satisfied for the fringing field in the TFC where, typically, $\partial_x \tilde{B} = 0.2 \div 0.3$. In general, the pressure drop in a channel with non-uniform magnetic field can be calculated with the relation by Hua et al. [67]

$$\Delta p = \int_{x_0} \nabla p(l)\, dl \; + \; k c^{0.5} p_0 \tag{4.15}$$

where $p_0 = \sigma u_0 B_0^2 x_0$ is the pressure scale. For $c < 0.1$ and $2 \leq x_0/a \leq 5$ in a square duct, it is found that $k \approx 0.1 \div 0.16$ [67]. For the purpose of this study, the pressure drop in the fringing field region is calculated employing eq. (4.6) and assuming both fully developed flow and maximum magnetic field intensity. Comparisons with alternative estimations made with less conservative assumptions are described in section 5.1.

4.4 Chapter summary

In this Chapter, the rationale and methodology for the comparative analysis of the four proposed WCLL configurations are discussed. The study is focused on the estimate of the MHD pressure drop for each configuration and analyzes in detail all the hydraulic regions composing the PbLi in-vessel flow path. Pressure drop correlations available in the literature are used for the estimate of both the two-dimensional and three-dimensional pressure drop term. Inertial, viscous and electromagnetic coupling effects on the pressure drop estimate are neglected.

The results of the analysis are divided for ease of presentation in the following chapters:

- Feeding and Draining pipe (Chapter 5)
- Manifold (Chapter 6)
- Breeding Zone (Chapter 7)

Chapter 5

Feeding and draining pipe

5.1 Feeding pipe

The feeding pipe (FP), as mentioned in Section 4.3, is the connection element between the DEMO PbLi loop and the breeding blanket and its main task is the feeding of the latter with fresh PbLi, hence the name. In the WCLL Design 2016 [22, 58], the FP is characterized by a relatively simple geometry since, as it is possible to see in Figure 5.1, it is composed of a long straight circular pipe that it is routed from the PbLi loop through the VV lower port and into the blanket segment, where it feeds the distribution manifold, not considered in the present section.

The lower port routing of the FP is required for two practical reasons: feeding the PbLi from the bottom simplifies the liquid metal hydraulic path in the blanket and, during planned maintenance or in accidental conditions, it can be used to passively drain the component by gravity. However, these advantages are counterbalanced by the challenging integration with other DEMO systems that are using the lower port for their operation, the most notable example being the divertor and its ancillary systems. Due to the intensive schedule of maintenance required by this component, remote maintenance (RM) requirements for the lower port are quite stringent and impose severe limitations for the blanket FP nominal diameter, wall thickness and general layout [70]. For the purpose of this study, we are going to at first neglect this limitations by assuming that the WCLL blanket could be fed through the lower port by two DN150 pipes. This assumption would be removed in Section 5.1.3, where we are going to consider how RM requirements affect the FP pressure drop by performing a parametric analysis involving the FP outer diameter and wall thickness. In Section 5.1.4, alternative FP routing paths through the VV upper port are considered to partially address these limitations.

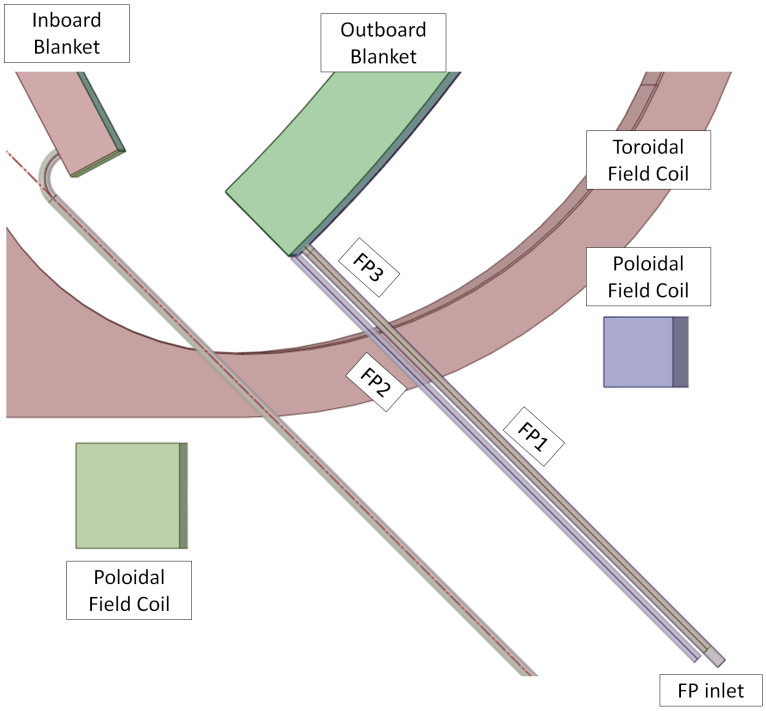

Figure 5.1. Feeding pipe layout and flow sections

The basic MHD flow in the FP is relatively simple, since it is essentially modeled with a 2D flow in an electro-conductive duct of circular cross-section, whose pressure gradient is described by eqs. (4.4) and (4.6). It is possible to divide the FP layout in three sections, for the purpose of the pressure drop estimation, by the relative position of the FP and the TFC:

- **Section FP1**, it considers the FP tract that lies outside of the TFC. The flow is assumed to be in fully developed condition at the FP inlet (see Figure 5.1). The dominant magnetic field component is B_{pol}.

- **Section FP2**, it describes the flow in the FP section passing through the TFC, where B_{tor} is strongly non uniform (fringing magnetic field). B_{pol} influence on the flow is neglected.

- **Section FP3**, it refers to the FP tract from the internal TFC surface to the distribution manifold. The flow is assumed to be in fully developed condition at the exit from the TFC. The dominant magnetic field component is B_{tor}, which is assumed to be uniform and equal to its average value in this section.

For the initial pressure drop estimation, we assume that the central outboard segment is fed by two identical FPs, whose geometry is depicted in Figure 5.1. The main input parameters of the FP are reported in Table 5.1.

Table 5.1. Reference feeding pipe input parameters, section lengths and applied magnetic field

General FP parameters		
Parameter	Value	Unit
FP pipes per segment	2	
Nominal Diameter (DN)	150	mm
Mass flow rate ($\Gamma_{OB}/2$)	8.19	kg/s
PbLi loop design pressure [60]	5	MPa
Temperature	600	K
FP section	Axial length x_i (m)	B (T)
Section FP1	1.5	1.4
Section FP2	1	0÷4.28
Section FP3	6.2	4.52

Table 5.2. Reference feeding pipe data, DN150

Parameter	Symbol	Value	Unit
Outer radius	r_o	84	mm
Inner radius	r_i	75.2	mm
Wall thickness	t_w	8.8	mm
t_w/r_i		0.117	
c (eq. (4.7))		0.163	
k_p (eq. (4.6))		0.14	
Cross-section	A	177.7	cm^2
Mean velocity	u_0	47	mm/s

5.1.1 Pipe dimensioning

The FP dimensioning is done according to the input parameters listed in Table 5.1. The wall thickness is calculated using the well-known relation by Barlow

$$t_w = s_f \frac{PD_o}{2S} \tag{5.1}$$

where P is the design pressure, D_o is the outer diameter and S is the maximum allowable stress [71]. A safety factor $s_f = 2$ is assumed. Considering an operative temperature $T = 600$ K, the maximum allowable stress is chosen as $S = 100$ MPa [71]. Accordingly, $D_o = 0.168$ m [72]. The actual wall thickness is then obtained from Ref. [73] selecting the value closer to the one calculated through eq. (5.1) that meets the BB-RM interface requirements. Currently, the nominal pipe diameter is limited to the range DN = [80,200], whereas the minimum and maximum allowed wall thickness are, respectively, $t_w = 5$ mm and $t_w = 15$ mm [70]. For the reference FP thus dimensioned, the main parameters are collected in Table 5.2.

As a final note, it should be highlighted how the design pressure employed for the feeding pipe dimensioning is higher than the actual PbLi loop design pressure, that was assumed to be $P = 4.6$ MPa considering the maximum hydrostatic head and the contribution from the cover gas pressure and pumping system [60]. However, the PbLi loop design pressure could be subjected to revision, since it neglects both the significant pressure loss in the blanket due to the electromagnetic drag and the PbLi

over-pressurization for an in-box Loss Of Coolant Accident (LOCA). Preliminary studies suggest that during the accident transient PbLi pressure in the blanket can reach up to 3.6 MPa in just 5 seconds and stabilizes at 15.1 MPa around 120 seconds [74]. These phenomena must be carefully addressed since they directly impact the feeding pipe design and, thus, the pressure drop estimate, which is very sensitive to the pipe wall thickness through the wall conductance ratio parameter (c), as it is discussed in Section 5.2.3.

5.1.2 Pressure drop estimate for the reference Feeding Pipe

As discussed previously, the FP flow can be divided into three sections depending on the position with respect to the TFC. In this Section, we are going to estimate the pressure drop for each section and discuss the main assumptions associated to the evaluation.

Feeding pipe outside of the Toroidal Field Coil (FP1)

In the section FP1, the FP is outside of the TFC, therefore $B_{tor} = 0$ and the magnetic field applied to the PbLi is the poloidal component B_{pol}. In Table 5.1, it is stated that this region is characterized by the axial length $x_1 = 6.5$ m and the uniform magnetic field $B = 1.4$ T, moreover, the flow can be considered in fully developed state at what is assumed to be the FP inlet.

The most important assumption made is the uniformity of the poloidal magnetic field. Recalling Figures 4.5a and 4.5b, the real poloidal field distribution is far from being uniform, even in a region so restricted in size as the feeding pipe, with the intensity and orientation of the magnetic field that are, in general, a function of the pipe axial coordinate. It is obvious that the pressure gradient for such a complex flow can hardly be modeled with eq. (4.4), which is only valid for a 2D fully developed flow, even neglecting any inertial and viscous effects on the pressure loss.

Furthermore, the data available on the poloidal field distribution do not cover all the feeding pipe axial extension. Employing as reference the results by Maviglia [63], the information on the poloidal field is limited to the tokamak region $R = (0, 18) \times Z = (-10, 10)$. In Figure 5.2, the poloidal field intensity is plotted against the vertical coordinate for the feeding pipe region [75]. For the section FP1, which roughly starts at $Z = -9$, it is possible to extrapolate the field gradient $\nabla B \approx -0.2$ T/m that will give a range $B_{pol} = 0.2 \div 1.45$ T, for the whole axial extension of the FP outside of the TFC.

Neglecting the variable field orientation, the non-uniform poloidal field satisfies the local fully developed condition eq. (4.14) and it could be treated, as a first approximation, by using eq. (4.13). Nevertheless, uncertainties about the real poloidal field distribution and the complexity of the flow discussed suggest a more conservative approach, therefore $B_{pol} = 1.4$ T is assumed for section FP1. According to eqs. (4.4) and (4.6), the pressure gradient in FP1 can be estimated as

$$\nabla p_1 = 10.125 \text{ kPa/m} \tag{5.2}$$

and it follows that the pressure drop has the value

$$\Delta p_1 = \nabla p_1 x_1 = 62.776 \text{ kPa} \tag{5.3}$$

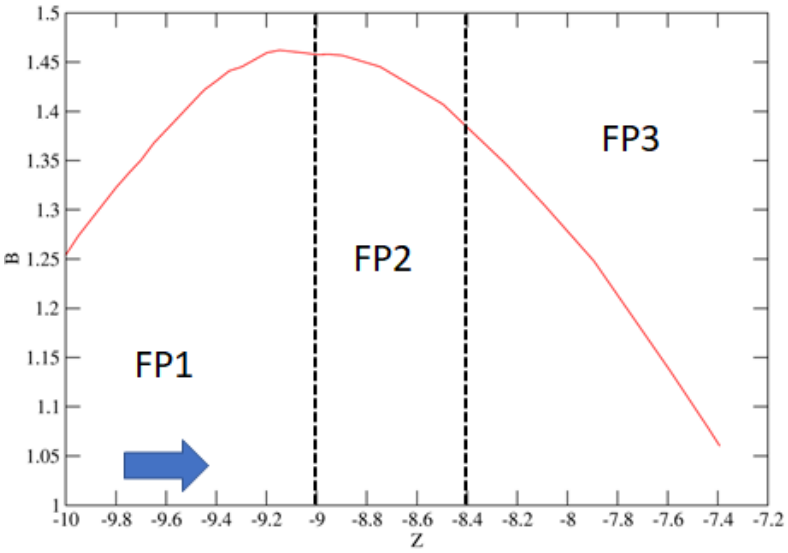

Figure 5.2. Poloidal magnetic field in the feeding pipe region [75], obtained from the data reported by Maviglia [63]. Blue arrow identifies flow direction.

It should be noted that in this study we assume that the poloidal magnetic field is so weak before what we consider as the FP inlet that, in fact, the flow upstream can be treated with the usual relations for non electrically conductive fluid. However, this assumption should be challenged in a more in-depth analysis since a significant penetration of the poloidal field in the tokamak building cannot be ruled off with the data presently available. Indeed, if this is the case, the MHD pressure drop estimate should be extended to account for the interested sections of the ex-vessel PbLi loop.

Feeding pipe in the Toroidal Field Coil thickness (FP2)

In the section FP2, the flow is passing through the TFC. The toroidal magnetic field is strongly non-uniform in this region, ramping up from null to $B_{tor} = 4.28$ T in a length $x_2 = 1$ m. The normalized magnetic field gradient $\partial_x \tilde{B} \approx 0.16$, and the flow cannot be treated assuming local fully developed condition. However, it is not possible to apply in a straightforward way eq. (4.15), since the coefficients reported have been obtained through the best-fit of data for a flow which is quite far from the parameters considered in this study, since it characterizes a square pipe and weakly conducting walls($c < 0.1$).

Considering $B_{tor} = 4.28$ T in the whole FP2, it is possible to obtain a conservative value for the pressure drop. According to eqs. (4.4) and (4.6), the pressure gradient can be estimated as

$$\nabla p_2 = 94.63 \text{ kPa/m} \tag{5.4}$$

and it follows that the pressure drop has the value

$$\Delta p_2 = \nabla p_2 x_2 = 94.63 \text{ kPa} \tag{5.5}$$

Applying eq. (4.15), it is possible to obtain an arguably less conservative estimate

for the pressure drop. If the magnetic field[1] in the TFC thickness can be described with the law

$$B(x) = 0.5 \cdot \left(1 - \tanh\left[0.45 \cdot \left(\frac{-x_2}{2r_i} + 0.4\right)\right]\right) \tag{5.6}$$

the two-dimensional pressure drop for the local fully developed flow takes the value

$$\Delta p_{2,a} = \int_{x_2} \nabla p(l)\, dl = k_p \sigma u_0 \int_{x_2} B(l)^2\, dl = 45.712 \text{ kPa} \tag{5.7}$$

and the three-dimensional term can be estimated with the expression

$$\Delta p_{2,b} = \sigma u_0 B_2^2 x_2 \cdot kc^{0.5} = 12.25 \text{ kPa} \tag{5.8}$$

where $B_2 = 2.14$ T is the average magnetic field in FP2, and the coefficient is assumed as $k = 0.18$, only value reported for a round pipe with $c = 0.027$ by Kirillov [44]. It follows that the total pressure drop estimated according to this less conservative formula is equal to

$$\Delta p_2^{'} = \Delta p_{2,a} + \Delta p_{2,b} = 57.962 \text{ kPa} \tag{5.9}$$

The pressure drop obtained with the Hua relation is approximately 60% of the conservative estimate. Moreover, it should be noted that the data reported for rectangular duct showed that the coefficient k was influenced by the characteristic fringing length x_0/a and that, for progressively less steep magnetic field gradients, the three-dimensional pressure drop term gradually decreased. For $x_0/a = 2$, the 3D pressure coefficient was measured as $k = 0.158$ and it was already reduced to $k = 0.105$ for double the fringing length ($x_0/a = 4$) [44]. For the present configuration, where $x_0/a \approx 8$, and accounting for the reduced intensity of the three-dimensional pressure drop term for thicker and better conducting walls than the one featured in the reported experiment, it is reasonable to assume that $k < 0.1$ and, therefore, the actual pressure drop in FP2 could be even lower than the eq. (5.9) estimate. Nevertheless, in the following the conservative estimation technique is always applied for fringing magnetic field regions.

Feeding pipe inside the Toroidal Field Coil (FP3)

In section FP3, no relevant assumptions must be made in order to reduce the actual flow to a fully developed flow in a pipe with electro-conductive walls. Equation (4.4) can be applied quite straightforwardly considering the average magnetic field $B_{tor} = 4.52$ T

$$\nabla p_3 = 105.54 \text{ kPa/m} \tag{5.10}$$

and it follows that the pressure drop has the value

$$\Delta p_3 = \nabla p_3 x_3 = 158.311 \text{ kPa} \tag{5.11}$$

and the total pressure drop in the feeding pipe

$$\Delta p = \Sigma \Delta p_i = 315.718 \text{ kPa} \tag{5.12}$$

[1] The subscript *tor* has been omitted for clarity

Table 5.3. Reference feeding pipe (DN150x2) pressure drop

Path section	B (T)	x_i (m)	Δp (kPa)	$\Delta p_i/\Delta p$ (%)
FP1	1.4	6.2	62.776	19.9
FP2	4.28	1	94.63	30.0
FP3	4.52	1.5	158.311	50.1
Feeding pipe		8.7	315.718	100

Table 5.4. Feeding pipe pressure drop for several nominal diameters. DN150(x2) refers to the reference FP layout considered in Section 5.1.2.

Nominal diameter	300	250	200	150(x2)	150	125	100	80
r_i (mm)	144.45	122.3	98.6	75.2		62.75	50.85	39.45
t_w (mm)	17.5	14.2	11	8.8		7.1	6.3	5
c	0.169	0.162	0.156	0.163		0.158	0.172	0.176
A (cm^2)	655.5	470	305	355.4	177.7	123.7	81	48.9
u_0 (cm/s)	2.55	3.55	5.5	4.7	9.4	13.5	20.6	34.2
N_1	890	538	281	250	125	73	39	18
N_3	9200	5605	2900	2600	1300	750	400	188
Δp (kPa)	176	237.2	353.8	315.72	627.9	882.5	1446	2446
$\Delta p/\Delta p_{Ref}$	0.558	0.751	1.12	1	1.99	2.80	4.58	7.75

A summary of the pressure drop estimate for the reference feeding pipe is available in Table 5.3. The bulk of the pressure drop ($\approx 80\%$) is localized in the flow path inside the TFC, which accounts for only 30 % of the total feeding pipe axial length. This result is not surprising, since the toroidal field is much more intense than the poloidal one, and the imbalance could be even greater with more realistic assumptions for FP1. On the other hand, the flow is far from being totally inertia-less in FP1, i.e. $N \approx 250$, and the complexity of the magnetic field topology could conceivably result in a pressure drop higher than the present estimate.

The FP layout considered in this Section allows to carry the outboard segment PbLi flow rate with relatively low velocity, but it requires the use of two DN150 round pipes, and is quite demanding in terms of occupied space in the lower port. Indeed, a layout with a single feeding pipe is usually considered as the reference for the blanket design [58]. In section 5.1.3, we are going to analyze how the pressure drop estimate is affected when a single feeding pipe is considered and the influence of the pipe diameter.

5.1.3 Feeding Pipe pressure loss sensitivity on nominal diameter

To characterize the effect of the feeding pipe size on the pressure drop estimate, we have considered seven nominal diameters for a single pipe layout to be compared with the reference case discussed in Section 5.1.2: DN80, DN100, DN125, DN150, DN200, DN250, DN300. The lower diameter (DN80) is currently the smallest size envisioned for the blanket feeding pipe to comply with the RM requirements in the VV lower port, whereas DN125 is considered the upper size limit that could be

achieved reasonably, if the lower port geometry would be revised to allow for a larger dedicated space to the PbLi feeding pipes. Nominal diameters larger than DN150 are considered for comparison's sake: their use is incompatible with the lower port integration but, as will be discussed in Section 5.1.4, are an option for the FP routing through the upper port. Interface requirements currently forbid the use of pipes with DN > 200 and $t_w > 15$ mm even for the upper port, since they are currently incompatible with the state-of-the-art of remotely controlled cut and weld tools, but they have nevertheless been included to provide an outlook for "optimistic" pressure loss in the FP. The results of the parametric study are collected in Table 5.4.

The wall conductance ratio does not vary in a wide range for this analysis ($c = 0.156 \div 0.176$) due to the assumption of constant design pressure ($P = 5$ MPa), therefore the pressure drop estimate is affected only by the mean velocity in the pipe (u_0), itself a function of the pipe diameter. Smaller pipes result in higher flow velocity for $\Gamma_{OB} = const.$ and the increase in pressure drop for DN < 150 is quite remarkable with $\Delta p_{80} = 2446$ kPa being above the blanket design threshold ($\Delta p = 2000$kPa) just by its own and near eight times the pressure drop in the reference FP. The necessity to account also for the pressure losses in the other PbLi path regions under the same limit makes the use of feeding pipe with DN < 150 rather unfeasible.

Conversely, for DN > 150, the velocity is reduced compared with the reference case and the pressure drop is correspondingly curtailed. Indeed, taking into account just blanket requirements, the DN300 pipe is very desirable and not only because of the limited pressure drop, but also for the inherent accuracy of the estimate. Larger pipes are characterized by stronger interaction parameters and they satisfy more easily the assumption of inertia-less flow that is employed in this study. It is reasonable to assume that DN300 would be the pipe least affected by the error in pressure drop estimate introduced by neglecting the inertial effects. Conversely, pipes with DN < 150 are characterized by smaller interaction parameters and, for the limiting case of DN80, it is not unreasonable to assume that the inertial regime will extend for the whole pipe extension, thus significantly affecting the pressure drop estimate. These considerations must be reviewed together with RM and reactor integration requirements in order to establish a consolidate feeding pipe design for the lower port routing path.

5.1.4 Feeding Pipe pressure loss sensitivity on routing scheme

In Section 5.1.3, it was discussed how a large diameter feeding pipe should be preferred due to the lower pressure drop, but that its integration with the other DEMO systems could be tricky. The purpose of this section is to assess the pressure drop estimate for alternative routing schemes from the VV upper port, where RM and reactor integration requirements are less stringent and can allow up to DN200 for the blanket feeding pipe [70]. Moreover, the upper port routing for the FP is the reference layout for the breeding zone of configuration T03 where, as described in Section 7.5, the PbLi flows downward in the blanket back through long poloidal channels.

Two routing schemes are considered using as a model those described in Section 5.2. The feeding pipe layout among these schemes differs essentially with regard to the attachment point to the distribution manifold:

Table 5.5. Reference upper port feeding pipe (DN200), pressure drop for top-point scheme. About the pressure drop estimation methodology and the path section labeling, refer to Section 5.2.1.

Path section	B (T)	x_i (m)	∇p (kPa/m)	Δp (kPa)	$\Delta p_i/\Delta p$ (%)
DPA7	0.483	2.3	1.353	3.112	0.82
DPA6	0.909	0.63	4.791	3.083	0.81
DPA5	0.909	5.34	4.791	25.582	6.74
DPA4	0.909	0.46	4.791	2.152	0.57
DPA3	0.314	0.3	0.572	0.171	0.05
DPA2	5.46	1	172.845	172.845	45.51
DPA1	5.46	1	172.845	172.845	45.51
Draining pipe		9.93		379.792	100

- The **mid-point** routing scheme, shown in Figure 5.4, mirrors the draining pipe layout that is considered for the WCLL Design 2016, where the attachment is foreseen roughly at two-third of the blanket poloidal height [22, 58].
- The **top-point** routing scheme, shown in Figure 5.3, allows an easier integration with the BZ hydraulic path of configuration T03, where the attachment is foreseen at the top of the blanket. The pipe layout mirrors the inboard segment draining pipe scheme (for reference, see Figure 4.2)

The main advantage of the mid-point scheme is the ease of integration with other DEMO systems, since the feeding pipe is placed in a region that is already completely dedicated to the outboard segment piping. Conversely, the manifold placement and BZ hydraulic path is made more complex and it becomes rather problematic, especially for configurations T02 and T03. In general, a bypass channel located along the blanket BSS is required to bring the PbLi from the feeding pipe to the breeding zone, a component that is susceptible to be characterized by intense pressure losses. This issue, very similar to the one faced by the draining pipe, is discussed more in-depth in Section 5.2.2.

The top-point scheme has similar features regarding the integration with other DEMO systems and the blanket, not featuring any clear-cut advantage compared with the mid-point attachment. However, this scheme is the preferred option for the T03 layout, since it greatly simplifies the BZ hydraulic path, and it is therefore considered here. Both these schemes are described in more detail in Section 5.2, where they are employed in reverse for the routing of the draining pipe, whereas in the Section we will limit to the presentation of the results obtained.

The reference FP considered for the upper port routing is a single DN200 pipe, whose parameters are analogous to the one reported in Table 5.4 for the lower port FP. Furthermore, the top-point attachment for the feeding pipe is considered as the reference layout for the T03 blanket. The results for the top-point and mid-point schemes are reported in Tables 5.5 and 5.6.

The bulk of the pressure drop is again localized in the flow path inside the TFC, therefore the total pressure drop is strongly influenced by the pipe length in this region and by the attachment point. The mid-point scheme benefits from the connection with the manifold location being further away from the central solenoid

Table 5.6. Reference upper port feeding pipe (DN200), pressure drop for mid-point scheme. About the pressure drop estimation methodology and the path section labeling, refer to Section 5.2.2.

Path section	B (T)	x_i (m)	∇p (kPa/m)	Δp (kPa)	$\Delta p_i/\Delta p$ (%)
DPB7	0.483	2.30	1.35	3.115	1.23
DPB6	0.909	0.63	4.79	3.228	1.28
DPB5	0.284	3.95	0.47	1.843	0.73
DPB4	3.513	1.20	71.56	85.874	33.94
DPB3	3.513	1.07	71.56	76.435	30.21
DPB2	3.513	0.52	71.56	38.193	15.10
DPB1	3.716	0.55	80.06	44.300	17.51
Draining pipe		10.22		252.989	100

($R \approx 13$ m) compared with the top-point scheme ($R \approx 8$ m): the toroidal magnetic field is correspondingly lower, 3.716 T versus 5.45 T, and the total pressure drop is reduced. This effect is partially counterbalanced by the top-point scheme featuring a shorter pipe length inside the TFC ($\approx 2m$) versus 3.34 m for the mid-point scheme.

Compared with the results for the lower port DN200, the mid-point scheme allows a 15% reduction of the feeding pressure drop, whereas an increase of 30% is found with regard to the top-point scheme. However, the pressure loss reduction for both the upper port schemes is substantial if compared with a realistic dimension for the lower port FP, i.e. DN100, and it has the potential to be even higher employing FP with DN $>$ 200. This is undoubtedly an advantage for the T03 and, in a minor way, T01.A blankets, whose breeding zone are already envisioned (or well suited to be adapted for) an upper port PbLi feeding. Conversely, for the T01.B and T02 blankets the BZ hydraulic path cannot be modified in a straightforward way to allow the feeding from the upper port.

As a final note, it should be highlighted that, although the routing of the feeding pipe from the upper port provides some benefits concerning reactor systems integration and pressure drop, it introduces safety concerns about the PbLi drainage from the blanket during accidental transients. Due to the feeding pipe being unable to execute this function, specific pipes must be designed and operated in such a way to allow the PbLi drainage whenever necessary. Since these pipes must be filled with PbLi and are located close enough to the plasma, they will accumulate tritium that, not being directly connected to the PbLi hydraulic circuit, it could be difficult to efficiently circulate, causing an unwanted tritium inventory build-up. Moreover, a dedicated heating system must be foreseen in order to avoid the solidification of the PbLi, introducing an additional safety-relevant system to an already very complex machine. The consolidated FP layout should address these issues in order to allow the upper port routing of the feeding pipe.

5.2 Draining pipe

The draining pipe (DP), as mentioned in Section 4.3, is the other connection element between the blanket and the PbLi loop that is tasked with the removal from the breeding zone of the liquid metal containing tritium. The DP geometry is quite simple

and it can be reduced to the MHD flow in a circular duct with electro-conductive walls. However, as opposed to what happens for the FP, the DP layout cannot be described as a straight duct, since the routing from the upper port involves the introduction of more complex geometrical elements. Two routing schemes, already partially described in Section 5.1.4 with regard to the FP, are considered: the mid-point scheme foresees the attachment to the blanket at around two-third of the poloidal height, whereas the top-point scheme allows the collection of the depleted PbLi from the blanket top, close to the interface with the inboard blanket.

The top-point scheme, shown in Figure 5.4, has the advantage of being relatively easy to integrate with all the blanket configurations, but it is located in a region closer to the central solenoid and, therefore, it will be characterized by higher pressure losses. Moreover, the pipe routing can be difficult due to the limited size available in the top of the blanket, where the inboard segment draining pipes and coolant piping are envisioned. The mid-point attachment, shown in Figure 5.3, has been the DP reference layout in the WCLL Design 2016 and it is the scheme that provides the easier integration with the reactor system. This advantage is compensated by the necessity to design a bypass channel to bring the depleted liquid metal from the blanket top to the DP or otherwise alter the BZ layout to allow for an efficient collection of the liquid metal. These requirements, even if limited only to the upper part of the breeding zone, are going to affect negatively the overall blanket pressure drop compared with the top-point attachment.

For the purpose of this study, the top-point routing scheme is assumed as the reference for the DP layout. In Section 5.2.1, the flow path is described and the overall pressure loss is calculated for the reference scheme, whereas in Section 5.2.2 the alternative scheme is discussed. For both the routing schemes, the reference DP considered is a single DN200 pipe, whose parameters are analogous to the one reported in Table 5.4 for the lower port FP analysis.

5.2.1 Top-point draining scheme

For this routing scheme, the PbLi flow path in the DP can be divided into seven sections due to the relevant geometrical elements, the orientation with regard to the TFC and the main magnetic field component. The DP flow path is shown in Figure 5.3 and can be described by the following hydraulic sections

- **Section DPA1**, it is the vertical straight DP tract that connects the collection manifold with the internal TFC surface. It lies entirely inside the TFC. The flow is assumed to be in fully developed condition at the DP inlet.

- **Section DPA2**, it corresponds to the flow in the DP section passing through the TFC where B_{tor} is strongly non uniform (fringing magnetic field). B_{pol} influence on the flow is neglected.

- **Section DPA3**, it is a vertical straight pipe that connects the external TFC surface with the first bend. The flow is assumed to be in fully developed condition at the exit from the TFC. It lies entirely outside the TFC, therefore the dominant magnetic field component is B_{pol} but, since the pipe is aligned with the vertical axis, only the radial component B_r is considered.

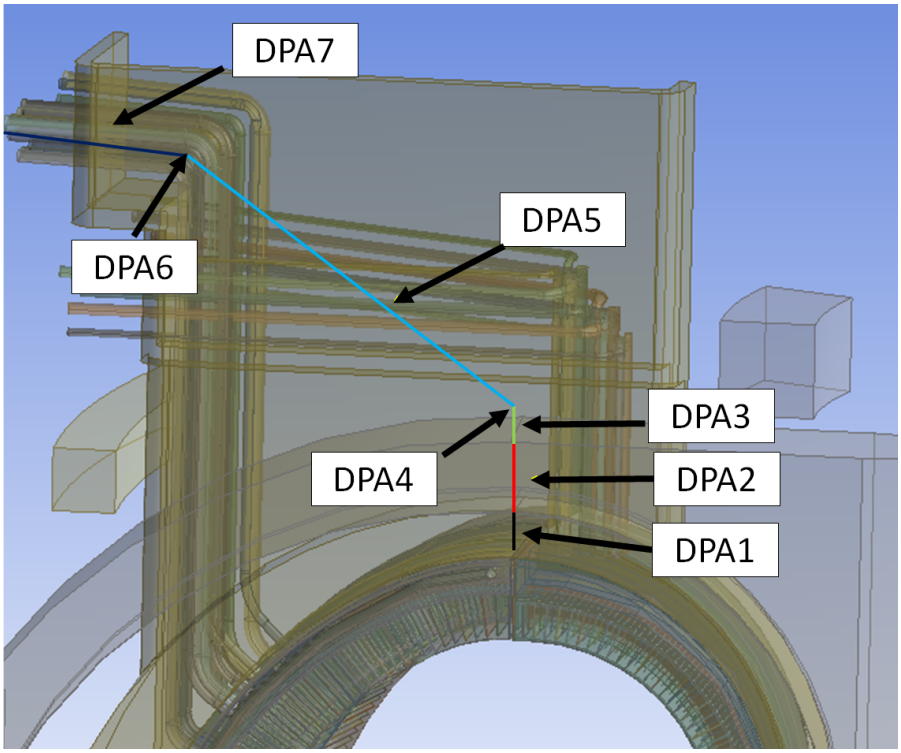

Figure 5.3. Draining pipe layout for the top-point attachment routing scheme and flow sections

- **Section DPA4**, it is a 60° smooth bend with curvature radius $R = 0.4$ m. It lies entirely outside the TFC, therefore the dominant magnetic field component is B_{pol} and the bend is considered parallel to the applied magnetic field .

- **Section DPA5**, it is a straight pipe that connects the first and second bend. It lies entirely outside the TFC, therefore the dominant magnetic field component is B_{pol}.

- **Section DPA6**, it is a 30° smooth bend with curvature radius $R = 0.4$ m. It lies entirely outside the TFC, therefore the dominant magnetic field component is B_{pol} and the bend is considered parallel to the applied magnetic field .

- **Section DPA7**, it is a radial straight pipe that connects to the second bend with the DP outlet and the external PbLi loop. The dominant magnetic field component is B_{pol} but, since the pipe is aligned with the radial axis, only the vertical component B_z is considered.

The reference data for the mid-point DP layout are reported in Table 5.7. The top-point routing scheme is considerably less developed than the other one and the feasibility of some of the path sections envisioned in this study, most notably section DPA5, need to be assessed in the framework of the DEMO integration requirements.

Table 5.7. Reference draining pipe (DN200) section lengths and applied magnetic field for the top-point routing scheme

DP section	Axial length x_i (m)	B (T)
DPA1	1	5.46
DPA2	1	5.46
DPA3	0.3	0.314
DPA4	0.42	0.909
DPA5	5.34	0.909
DPA6	0.63	0.909
DPA7	2.30	0.483

Section DPA1

The section DPA1 is composed of a vertical straight electro-conductive pipe that connects the distribution manifold and the internal TFC surface. Since it is entirely comprised in the TFC, the main magnetic field component is B_{tor} and, due to the orientation of the pipe, the intensity of the field can be assumed as constant. Assuming that at the DP inlet the flow is in fully developed state, the pressure gradient can be calculated employing eq. (4.4)

$$\nabla p_1 = 172.845 \text{ kPa/m} \tag{5.13}$$

and it follows that the pressure drop has the value

$$\Delta p_1 = \nabla p_1 x_1 = 172.845 \text{ kPa} \tag{5.14}$$

Section DPA2

In the section DPA2, the pipe is passing through the TFC. The toroidal magnetic field is strongly non-uniform in this region, ramping down from $B_{tor} = 5.46$ T to null in a length $x_2 = 1$ m. The normalized magnetic field gradient $\partial_x \tilde{B} \approx 0.197$, and the flow cannot be treated assuming local fully developed condition. The same methodology described in Section 5.1.2 is applied to obtain a conservative estimate of the pressure drop in this section.

Considering $B_{tor} = 5.46$ T in the whole DPA2, the pressure gradient takes the same value as in DPA1

$$\nabla p_2 = \nabla p_1 = 172.845 \text{ kPa/m} \tag{5.15}$$

and it follows that the pressure drop has the value

$$\Delta p_2 = \nabla p_2 x_2 = 172.845 \text{ kPa} \tag{5.16}$$

Following the assumptions detailed in Section 5.1.2, it is possible to obtain a less conservative estimate employing the Hua relation. The inertia-less/inviscid term is obtained by the integration of the pressure drop term on the duct section according to the magnetic field variation law

$$\Delta p_{2,a} = \int_{x_2} \nabla p(l)\, dl = k_p \sigma u_0 \int_{x_2} B(l)^2\, dl = 83.31 \text{ kPa} \tag{5.17}$$

and the three-dimensional term can be estimated with the expression

$$\Delta p_{2,b} = \sigma u_0 B_2^2 x_2 \cdot kc^{0.5} = 22.83 \text{ kPa} \tag{5.18}$$

where $B_2 = 2.73$ T is the average magnetic field in DPA2, and the coefficient is assumed as $k = 0.18$. It follows that the total pressure drop

$$\Delta p_2^{'} = \Delta p_{2,a} + \Delta p_{2,b} = 106.14 \text{ kPa} \tag{5.19}$$

That, again, shows how the pressure drop obtained with the Hua relation is approximately 60% of the conservative estimate. The more intense estimate is assumed in the following as reference pressure drop in section DPA2.

Section DPA3

In the section DPA3, the vertical straight pipe is outside of the TFC, therefore the dominant magnetic field is B_{pol}. Due to the pipe orientation, only the radial component (B_r) is transverse to the liquid metal flow and is responsible for pressure losses. From the data reported by Maviglia [63], the maximum radial magnetic field $B_r = 0.314$ T in the region is assumed for this calculation.

Since the magnetic field is uniform and the flow is assumed in fully developed state at the TFC exit, the pressure gradient can be calculated employing eq. (4.4) and it takes the value

$$\nabla p_3 = 0.572 \text{ kPa/m} \tag{5.20}$$

and it follows that the pressure drop has the value

$$\Delta p_3 = \nabla p_3 x_3 = 0.171 \text{ kPa} \tag{5.21}$$

Section DPA4

In the section DPA4, the pipe describes a 60° smooth bend with curvature radius $R = 0.4$ m. Since the pipe lies outside of the TFC, the dominant magnetic field is B_{pol}. The bend is assumed to be parallel to the magnetic field, that is assumed at its maximum value in the region $B = 0.909$ T, according to the data reported by Maviglia [63].

The pressure drop in this section can be described with the sum of a two-dimensional and three-dimensional term. For the former, the pressure gradient can be calculated employing eq. (4.4)

$$\nabla p_4 = 4.79 \text{ kPa/m} \tag{5.22}$$

and it follows that the 2D pressure drop has the value

$$\Delta p_{4,2D} = \nabla p_4 x_4 = 2.01 \text{ kPa} \tag{5.23}$$

For the bend $//\mathbf{B}$ in a circular pipe, it is assumed from Section 4.3.2 that $k_{//} = 0.125$. For a 60° bend , it follows

$$k_4 = \frac{60}{90} k = 0.0833 \tag{5.24}$$

Assuming the pipe radius $r_i = 98.6$ mm as length scale of the 3D effect, the local interaction parameter can be calculated as

$$N_4 = 118.43 \tag{5.25}$$

and the local resistance coefficient

$$\zeta = k_4 N_4 = 9.87 \tag{5.26}$$

Finally, the 3D pressure drop takes the value

$$\Delta p_{4,3D} = \frac{1}{2}\zeta \rho u_0^2 = 0.1453 \text{ kPa} \tag{5.27}$$

The overall pressure drop in this flow section can be calculated as

$$\Delta p_4 = \Delta p_{4,2D} + \Delta p_{4,3D} = 2.152 \text{ kPa} \tag{5.28}$$

where the 3D pressure drop accounts for $\approx 7\%$.

Section DPA5

In section DPA5, the pipe is no longer aligned with any axis and, therefore the full poloidal field B_{pol} must be employed for the pressure drop estimate. The section brings the draining pipe from the region immediately above the blanket top to the larger outboard piping system ensemble located at the far end of the upper port (see Figure 5.3 for reference).

The pressure gradient is calculated employing eq. (4.4), and it takes the value

$$\nabla p_5 = 4.791 \text{ kPa/m} \tag{5.29}$$

and it follows that the pressure drop has the value

$$\Delta p_5 = \nabla p_5 x_5 = 25.582 \text{ kPa} \tag{5.30}$$

This flow section can be considered "conservative", since it allows the full application of the poloidal field for an extensive length. Alternative pipe routing could minimize the pressure drop in this section by aligning the pipe with either the radial or vertical direction.

Section DPA6

In section DPA6, the pipe describes a 30° smooth bend with curvature radius $R = 0.4$ m. The bend is assumed to be parallel to the magnetic field, that is assumed at its maximum value in the region $B = 0.909$ T, according to the data reported by Maviglia [63].

The pressure drop in this section can be described with the sum of a two-dimensional and three-dimensional term. For the former, the pressure gradient has the same value of the one calculated for section DPA5

$$\nabla p_6 = \nabla p_5 = 4.791 \text{ kPa/m} \tag{5.31}$$

and it follows that the 2D pressure drop has the value

$$\Delta p_{6,2D} = \nabla p_6 x_6 = 3.01 \text{ kPa} \tag{5.32}$$

For the bend //**B** in a circular pipe, it is assumed from Section 4.3.2 that $k_{//} = 0.125$. For a 30° bend , it follows

$$k_6 = \frac{30}{90} k = 0.042 \tag{5.33}$$

Assuming the pipe radius $r_i = 98.6$ mm as length scale of the 3D effect, the local interaction parameter is equal to the one for section DPA4

$$N_6 = N_4 = 118.43 \tag{5.34}$$

and the local resistance coefficient follows

$$\zeta = k_6 N_6 = 4.93 \tag{5.35}$$

Finally, the 3D pressure drop takes the value

$$\Delta p_{6,3D} = \frac{1}{2} \zeta \rho u_0^2 = 0.0727 \text{ kPa} \tag{5.36}$$

The overall pressure drop in this flow section can be calculated as

$$\Delta p_6 = \Delta p_{6,2D} + \Delta p_{6,3D} = 3.083 \text{ kPa} \tag{5.37}$$

where the 3D pressure drop accounts for $\approx 2\%$.

Section DPA7

In the section DPA7, the pipe is outside the TFC and it is aligned with the radial axis. For this reason, only the vertical component of the poloidal magnetic field is considered for the pressure drop estimate. For $z = 10$ m and for $R = 15 \div 18$ m, the maximum vertical magnetic field is considered $B_z = 0.483$ T.

The pressure gradient is calculated employing eq. (4.4) and it takes the value

$$\nabla p_7 = 1.353 \text{ kPa/m} \tag{5.38}$$

and it follows that the pressure drop has the value

$$\Delta p_7 = \nabla p_7 x_7 = 3.112 \text{ kPa} \tag{5.39}$$

The total pressure drop in the draining pipe

$$\Delta p = \Sigma \Delta p_i = 379.789 \text{ kPa} \tag{5.40}$$

A summary of the pressure drop estimate for the top-point draining pipe is available in Table 5.5. The same considerations discussed in Section 5.1.4 for the upper port routing of the feeding pipe applies for the top-point attachment of the draining pipe.

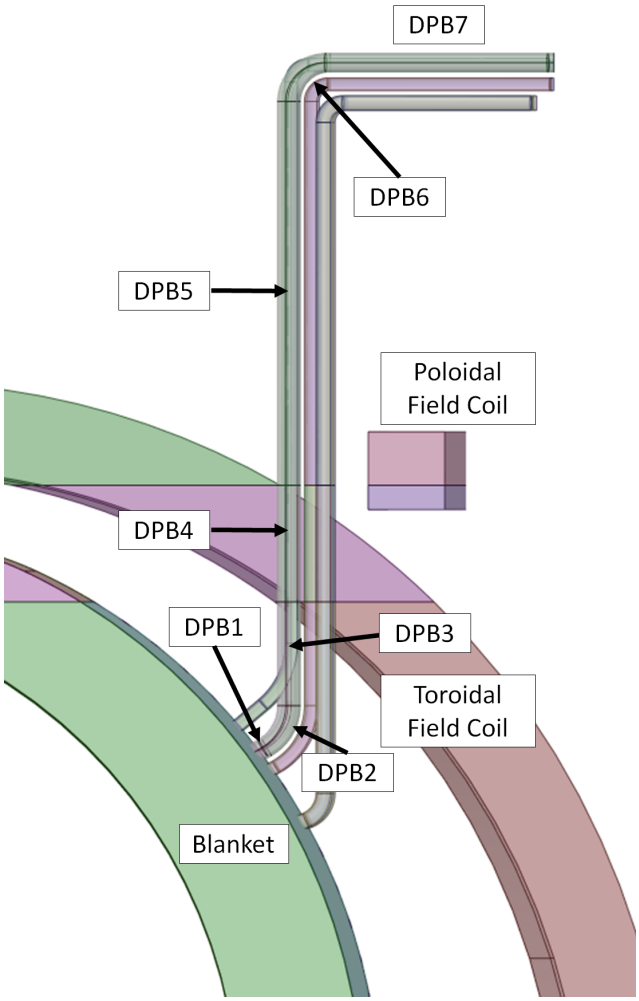

Figure 5.4. Draining pipe layout for the mid-point attachment routing scheme and flow sections

5.2.2 Mid-point draining scheme

For this routing scheme, the PbLi flow path in the DP can be divided in seven sections due to the relevant geometrical elements, the orientation with regard to the TFC and the main magnetic field component. The DP flow path is shown in Figure 5.4 can be described as following

- **Section DPB1**, it is the straight DP tract that connects the collection manifold with the first bend. It lies entirely inside the TFC. The flow is assumed to be in fully developed condition at the DP inlet.
- **Section DPB2**, it is a 60° smooth bend with curvature radius $R = 0.5$ m. It lies entirely inside the TFC, therefore the dominant magnetic field component is B_{tor} and the bend is $\perp \mathbf{B}$.
- **Section DPB3**, it is a vertical straight pipe that connects the first bend with the internal TFC surface. It lies entirely inside the TFC.

Table 5.8. Reference draining pipe (DN200) section lengths and applied magnetic field for the mid-point routing scheme

DP section	Axial length x_i (m)	B (T)
DPB1	0.55	3.716
DPB2	0.52	3.513
DPB3	1.07	3.513
DPB4	1.20	3.513
DPB5	3.95	0.284
DPB6	0.63	0.909
DPB7	2.30	0.483

- **Section DPB4**, it corresponds to the flow in the DP section passing through the TFC where B_{tor} is strongly non uniform (fringing magnetic field). B_{pol} influence on the flow is neglected.
- **Section DPB5**, it is a vertical straight pipe that connects the external TFC surface with the second bend. The flow is assumed to be in fully developed condition at the exit from the TFC. It lies entirely outside the TFC, therefore the dominant magnetic field component is B_{pol} but, since the pipe is aligned with the vertical axis, only the radial component B_r is considered.
- **Section DPB6**, it is a 90° smooth bend with curvature radius $R = 0.5$ m. The dominant magnetic field component is B_{pol} and the bend is $//\mathbf{B}$.
- **Section DPB7**, it is a radial straight pipe that connects to the second bend with the DP outlet and the external PbLi loop. The dominant magnetic field component is B_{pol} but, since the pipe is aligned with the radial axis, only the vertical component B_z is considered.

The reference data for the mid-point DP layout are reported in Table 5.8.

Section DPB1

In the section DPB1, the pipe is inside the TFC and the dominant magnetic field is B_{tor}. Assuming that at the DP inlet the flow is in fully developed state, the pressure gradient can be calculated employing eq. (4.4)

$$\nabla p_1 = 80.064 \text{ kPa/m} \tag{5.41}$$

and it follows that the pressure drop has the value

$$\Delta p_1 = \nabla p_1 x_1 = 44.3 \text{ kPa} \tag{5.42}$$

Section DPB2

In the section DPB2, the PbLi flows inside a 60° smooth bend with curvature radius $R = 0.5$ m. The bend is assumed to be perpendicular to the toroidal magnetic field. The pressure drop in this section can be described with the sum of a two-dimensional

and three-dimensional term. For the former, the pressure gradient can be calculated employing eq. (4.4)

$$\nabla p_2 = 71.56 \text{ kPa/m} \tag{5.43}$$

and it follows that the 2D pressure drop has the value

$$\Delta p_{2,2D} = \nabla p_2 x_2 = 37.47 \text{ kPa} \tag{5.44}$$

For the bend $//\mathbf{B}$ in a circular pipe, it is assumed from Section 4.3.2 that $k_{//} = 0.125$. For a 60° bend perpendicular to the magnetic field, it follows

$$k_2 = \frac{1}{3} \cdot \frac{60}{90} k = 0.0278 \tag{5.45}$$

Assuming the pipe radius $r_i = 98.6$ mm as length scale of the 3D effect, the local interaction parameter can be calculated as

$$N_2 = 1769 \tag{5.46}$$

and the local resistance coefficient

$$\zeta = k_2 N_2 = 49.14 \tag{5.47}$$

Finally, the 3D pressure drop takes the value

$$\Delta p_{2,3D} = \frac{1}{2} \zeta \rho u_0^2 = 0.724 \text{ kPa} \tag{5.48}$$

The overall pressure drop in this flow section can be calculated as

$$\Delta p_2 = \Delta p_{2,2D} + \Delta p_{2,3D} = 38.193 \text{ kPa} \tag{5.49}$$

where the 3D pressure drop accounts for $\approx 2\%$.

Section DPB3

In the section DPB3, the pipe is inside the TFC and the dominant magnetic field is B_{tor}. The pressure gradient can be calculated employing eq. (4.4) and it has the same value calculated in Section 5.2.2

$$\nabla p_3 = \nabla p_2 = 71.56 \text{ kPa/m} \tag{5.50}$$

and it follows that the pressure drop has the value

$$\Delta p_3 = \nabla p_3 x_3 = 76.435 \text{ kPa} \tag{5.51}$$

Section DPB4

In the section DPB4, the pipe is passing through the TFC. The toroidal magnetic field is strongly non-uniform in this region, ramping down from $B_{tor} = 3.513$ T in a length $x_4 = 1.2$ m. The normalized magnetic field gradient $\partial_x \tilde{B} \approx 0.164$, and the flow cannot be treated assuming local fully developed condition. The same

methodology described in Section 5.1.2 is applied to obtain a conservative estimate of the pressure drop in this section.

Considering $B_{tor} = 3.513$ T in the whole DPB4, according to eqs. (4.4) and (4.6) the pressure gradient in DPB4 can be estimated as

$$\nabla p_4 = 71.56 \text{ kPa/m} \tag{5.52}$$

and it follows that the pressure drop has the value

$$\Delta p_4 = \nabla p_4 x_4 = 85.874 \text{ kPa} \tag{5.53}$$

Section DPB5

In the section DPB5, the pipe is outside the TFC and it is aligned with the vertical axis. For this reason, only the radial component of the poloidal magnetic field is considered for the pressure drop estimate. For $R = 12.441$ m, the maximum radial magnetic field is considered $B_r = 0.2837$ T.

The pressure gradient can be calculated employing eq. (4.4) and it takes the value

$$\nabla p_5 = 0.467 \text{ kPa/m} \tag{5.54}$$

and it follows that the pressure drop has the value

$$\Delta p_5 = \nabla p_5 x_5 = 1.843 \text{ kPa} \tag{5.55}$$

Section DPB6

In the section DPB6, the PbLi flows inside a 90° smooth bend with curvature radius $R = 0.4$ m. The bend is assumed to be parallel to the poloidal magnetic field. The pressure drop in this section can be described with the sum of a two-dimensional and three-dimensional term. For the former, the pressure gradient can be calculated employing eq. (4.4)

$$\nabla p_6 = 4.791 \text{ kPa/m} \tag{5.56}$$

and it follows that the 2D pressure drop has the value

$$\Delta p_{6,2D} = \nabla p_6 x_6 = 3.01 \text{ kPa} \tag{5.57}$$

For the bend $//\mathbf{B}$ in a circular pipe, it is assumed from Section 4.3.2 that $k_{//} = k_6 = 0.125$. Assuming the pipe radius $r_i = 98.6$ mm as length scale of the 3D effect, the local interaction parameter can be calculated as

$$N_6 = 118.43 \tag{5.58}$$

and the local resistance coefficient

$$\zeta = k_6 N_6 = 14.80 \tag{5.59}$$

Finally, the 3D pressure drop takes the value

$$\Delta p_{6,3D} = \frac{1}{2}\zeta \rho u_0^2 = 0.218 \text{ kPa} \tag{5.60}$$

The overall pressure drop in this flow section can be calculated as

$$\Delta p_6 = \Delta p_{6,2D} + \Delta p_{6,3D} = 3.228 \text{ kPa} \tag{5.61}$$

where the 3D pressure drop accounts for $\approx 3\%$.

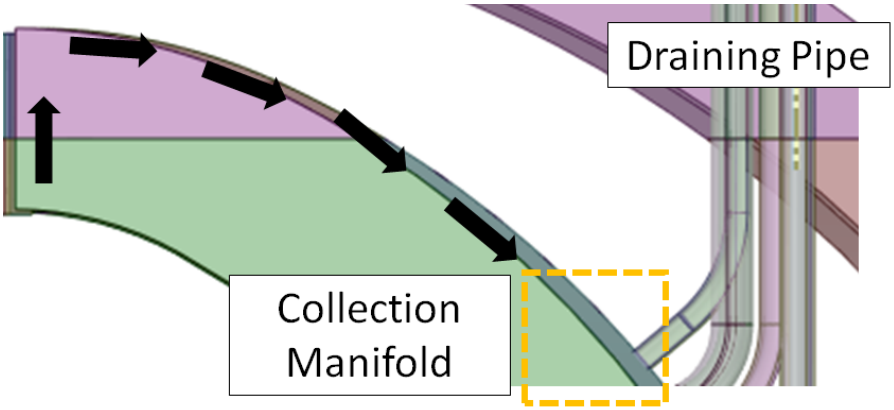

Figure 5.5. Bypass channel layout and connection with the draining pipe

Section DPB7

In the section DPB7, the pipe is outside the TFC and it is aligned with the radial axis. For this reason, only the vertical component of the poloidal magnetic field is considered for the pressure drop estimate. For $z = 10$ m and for $R = 15 \div 18$ m, the maximum vertical magnetic field is considered $B_z = 0.483$ T.

The pressure gradient can be calculated employing eq. (4.4) and it takes the value

$$\nabla p_7 = 1.353 \text{ kPa/m} \tag{5.62}$$

and it follows that the pressure drop has the value

$$\Delta p_7 = \nabla p_7 x_7 = 3.115 \text{ kPa} \tag{5.63}$$

The total pressure drop in the draining pipe

$$\Delta p = \Sigma \Delta p_i = 252.989 \text{ kPa} \tag{5.64}$$

A summary of the pressure drop estimate for the mid-point draining pipe is available in Table 5.6. The same considerations discussed in Section 5.1.4 for the upper port routing of the feeding pipe applies for the mid-point attachment of the draining pipe.

Bypass channel

For the mid-point routing scheme, to bring the depleted PbLi to the draining pipe it is necessary to envision a hydraulic path that connects the breeding zone with the attachment point. The specific geometry of such a bypass channel depends on the WCLL configuration, in this section we are going to take as a reference the configuration T01.A to discuss the effect of this channel on the overall pressure drop of the draining pipe.

The proposed layout for the bypass channel is shown in Figure 5.5: the channel starts at the end of the Spinal Manifold collection leg, located at the blanket topmost, it makes a sharp 180° bend and goes downward to reach the mid-point attachment point, where the Collection Manifold is located. The bypass channel is essentially an

Table 5.9. Bypass channel, configuration T01.A. The lower end of the mean velocity refers to the central channel. For more details about the Spinal Manifold, please see Section 6.2

Parameter	Symbol	Value	Unit
Toroidal length	$2a$	240	mm
Radial length	$2b$	50	mm
Poloidal length	L	5180	mm
Bend length	z_b	240	mm
Cross-section	A	1200	cm^2
Mean velocity	u_0	$3.6 \div 5.1$	cm/s
Wall ratio (Radial-Poloidal SP)	c_1	0.1	
Wall ratio (Toroidal-Poloidal SP)	c_2	0.187	
Aspect ratio	a/b	6	
Pressure coefficient (eq. (4.8))	k_p	0.046	

extension of the terminal part of Spinal Manifold duct, whose geometrical parameters are reported in Table 5.9.

The 180° bend is described in the inertia-less/inviscid regime, as discussed in Section 4.3.2, as the sum of two 90° bend. In this case, the main magnetic field is B_{tor} and, since the flow moves from the poloidal to the vertical and back again to the poloidal direction, the bend is $\perp \mathbf{B}$. Considering a sharp bend, the 2D pressure drop term is limited to the flow in the vertical direction (z_b). From eqs. (4.4) and (4.8) and considering the maximum velocity in Table 5.9, the pressure gradient takes the value

$$\nabla p_1 = 55.13 \text{ kPa/m} \tag{5.65}$$

and the two-dimensional pressure drop is calculated as

$$\Delta p_{1,2D} = \nabla p_1 z_b = 13.22 \text{ kPa} \tag{5.66}$$

The three-dimensional coefficient for the sharp bend $//\mathbf{B}$ in a square duct can be calculated with eq. (4.11). Neglecting the (favorable) aspect ratio of the bypass ratio, from eq. (4.11) and the bypass channel parameters we obtain

$$k_{//} = 1.063 \frac{c_2}{4/3 + c_2} \approx 0.131 \tag{5.67}$$

where c_2 has been considered as uniform wall conductance ratio. For a bend $\perp \mathbf{B}$, we have

$$k_{\perp} = \frac{k_{//}}{3} = 0.0436 \tag{5.68}$$

Consequently, the local interaction parameter and MHD resistance can be expressed as

$$N_1 = 1914 \tag{5.69}$$

$$\zeta = 79.78 \tag{5.70}$$

and the three-dimensional pressure drop term is calculated as

$$\Delta p_{1,3D} = \zeta \rho u_0^2 = 2.07 \text{ kPa} \tag{5.71}$$

where the term is doubled to account for the 180° bend. The overall pressure drop is

$$\Delta p_1 = \Delta p_{1,2D} + \Delta p_{1,3D} = 15.29 \text{ kPa} \tag{5.72}$$

with the 3D term accounting for $\approx 13\%$.

The flow along the blanket back is described by the same relations employed for the 2D pressure drop term employed for the previous section. Assuming the average value for the magnetic field across the path $B = 4.4$ T as uniform, the pressure drop is

$$\Delta p_2 = \nabla p_1 L = 185.61 \text{ kPa} \tag{5.73}$$

and the overall bypass channel pressure drop is equal to

$$\Delta p = \Delta p_1 + \Delta p_2 \approx 201 \text{ kPa} \tag{5.74}$$

The pressure drop in the bypass channel is relatively high and, when it is added to the draining pipe, results in a total pressure loss $\Delta p = 454$ kPa for the mid-point routing scheme, around 20% than the top-point scheme pressure drop. Although this drawback is partially recovered by the repositioning of the collection manifold in a region of weaker magnetic field (see Section 6.2.3), the mid-point draining pipe is strongly penalized by the necessity to provide a connection between the blanket top and the drainage point. Moreover, it should be noted how the bypass channel layout described herein is somehow "optimistic", since the integration of such component in the back supporting structure is challenging, and that the top-point routing scheme could be favored even more without any significant restructuring of the BZ hydraulic path aimed to favor the mid-point attachment.

5.2.3 Influence of wall thickness on pressure loss estimate

To conclude the discussion over the pressure drop estimate for the feeding and draining pipe, a final note must be made about the assumption made in Section 5.1.1 regarding the design pressure for these elements. Taking into account the in-box LOCA accidental sequence, we want to design the connection pipes between the blanket and the PbLi loop such that they are able to withstand 110% of the maximum pressure expected during the transient. Under this assumption, $P = 18$ MPa and keeping the same design criteria described in Section 5.1.1, for the reference DN200 draining pipe this causes an increase in the wall thickness from $t_w = 11$ mm to $t_w = 40$ mm[2]. Correspondingly, $c = 0.163 \rightarrow 0.63$ and the mean velocity in the pipe reaches up to 11 cm/s.

For both the draining pipe schemes, the larger wall thickness results in a dramatic increase of the pressure drop estimate. For the top-point draining pipe, the change in design requirements makes the routing scheme utter unfeasible, since $\Delta p_{top} \approx$ 2180 kPa, well above the design criterion even assuming less conservative assumptions for the pressure drop calculation. The situation is not much better for the mid-point draining pipe, where $\Delta p_{mid} \approx 1447$ kPa, over a six times increase compared with the earlier estimate. Applying the new design pressure to the reference FP selected for

[2]Moreover, such a pipe will not comply with the remote maintenance requirements, since at the moment the cutting tool is limited to a wall thickness $t_w = 15$ mm

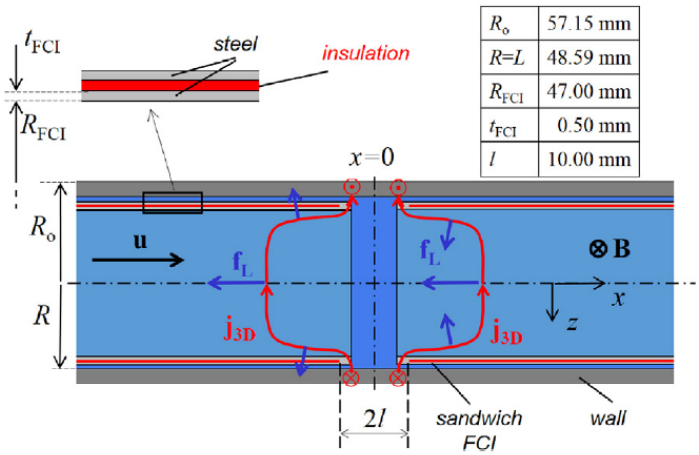

Figure 5.6. "Sandwich" flow channel insert placed inside a circular pipe. The discontinuity in electrical insulation allows currents in the liquid metal to close through the thick conductive wall [76]

the WCLL bottom feeding scheme (i.e. two DN150 pipes), the update pressure drop for the FP is calculated as $\Delta p_{fp} \approx 1858$ kPa. It is clear from these estimates how a tightening of the pressure requirements on the PbLi loop will require the adoption of different strategies for the design of the feeding and draining pipe. Indeed, the introduction of insulating elements seems an unavoidable necessity to keep the total blanket pressure drop below 2000 kPa in such a scenario.

5.3 Pressure loss estimate for Feeding Pipe with electrical insulation

To reduce the pressure losses in a MHD channel flow, one of the possible strategies is to reduce the electrical conductivity of the bounding walls in order to hamper, or even totally prevent, the shortcut of the induced currents. For the limiting case of perfectly insulated circular pipe, the pressure gradient can be expressed with eq. (3.54), originally derived for an insulating rectangular duct in Section 3.6, with the pressure coefficient λ that takes the form [44]

$$\lambda = \frac{3\pi}{4}\frac{Ha}{Re}\left(1 - \frac{3\pi}{2Ha}\right)^{-1} \tag{5.75}$$

It is straightforward to observe that, due to the structure of the pressure coefficient, in this case the pressure losses are greatly reduced compared with the electro-conductive duct, since $\partial p/\partial x \propto B$ cf. $\partial p/\partial x \propto B^2$. Even for the latter case, weakly conducting walls are favored over more conductive ones due to the parameter c_w directly affecting the pressure coefficient k_p through eq. (4.6). All the other parameters being constant, a lower c_w results in a reduction of the resistive electromagnetic force experienced by the flow.

Since the use of dielectric structural materials is mostly impossible in the blanket due to other requirements, thin insulating coatings or loosely fitted flow channel

Table 5.10. Pressure drop for naked (Δp) and electrically insulated feeding pipe (Δp_{FCI})

Nominal diameter	200	150	125	80	80(x4)
r_0 (mm)	69.55	52.15	41.85	29.45	
r_1 (mm)	68.05	50.65	40.35	27.95	
t_w (mm)	40.00	32.00	28.00	15.00	
c_w	0.6311	0.6601	0.6997	0.5784	
c_{FCI}	0.0214	0.0288	0.0361	0.0522	
$\Delta\hat{p}_{\mathrm{gap}}$	0.2315	0.1802	0.1522	0.0871	
u_0 (cm/s)	10.99	19.55	30.36	61.31	15.33
u_1 (cm/s)	11.48	20.73	32.66	68.06	17.02
Δp (kPa)	2032.6	3715.5	5972.9	10736.2	2684.1
Δp_{FCI} (kPa)	189.2	352.5	620.4	1652.9	413.2
• Δp_{2D} (kPa)	113.1	272.3	534.9	1584.7	396.2
• Δp_{3D} (kPa)	76.1	80.1	85.6	71.9	18.0
η (%)	90.7	90.5	89.6	84.6	
η_c (%)	94.4	92.3	91.1	85.2	
η_{eff} (%)	96.0	97.7	98.4	99.2	
$\Delta p_{3D}/\Delta p_{\mathrm{FCI}}$ (%)	40.2	22.7	13.8	4.3	

inserts (FCI) have been proposed to avoid the electrical coupling between the flowing liquid metal and the well-conducting wall. In the European fusion programme, the latter approach is considered as the baseline for MHD pressure drop mitigation in the DCLL design, whereas R&D activities on coatings are mostly performed on the topic of anti-corrosion and anti-permeation barriers [11, 77]. One possible FCI design is the so called "sandwich" concept that is composed by a thin layer of alumina ($t = 0.1$ mm) included between two protective sheets of Eurofer ($t = 0.5$ mm) that, welded together, are then fitted inside a rectangular or circular pipe, leaving a small gap (≈ 1 mm) where the liquid metal is allowed to flow between FCI and wall. It is not possible to achieve complete electrical insulation with this design, due to both the liquid metal flowing in the gap and Eurofer sheets providing a path for the currents closure. Numerical analyses have highlighted that, even accounting for these phenomena, the FCI is able to greatly curtail the channel pressure losses to $\approx$5% of the one estimated for the naked pipe [78]. However, many key issues must still be addressed to demonstrate the FCI effectiveness in operative conditions, just to cite a few: the alumina physical properties evolution under irradiation, pressure difference between the gap and main flow (and associated stresses on the FCI), high wall corrosion rate due to jet in the gap, etc.

In addition to these issues, the relative poor maturity and complexity of the manufacturing techniques involved are currently limiting the maximum length for the realization of continuous flow channel inserts to $S \approx 0.5$ m. It is reasonable to assume that discontinuities in the electrical insulation will be present in the blanket that, even for straight channels, will allow leakage currents from the liquid metal to flow through the thick conductive wall, causing enhanced pressure drop due to 3D effects. Recently, this problem has extensively been studied for circular pipes with the aid of numerical analyses and experimental activities. The results have suggested that the 3D pressure drop is roughly proportional to the conductance relative ratio between the naked wall (c_w) and the FCI (c_{FCI}), as well as the gap

axial length ($2l$) [76, 77, 79, 80].

Assuming a design pressure $P = 18$ MPa, like the one used in Section 5.2.3, it is relatively simple to estimate the pressure drop for a FP, analogous to the one described in section 5.1, which has been electrically insulated through the use of discrete length, finite conductivity, sandwich FCIs. As it was discussed in Section 5.2.3, deployment of FCI could be desirable for the WCLL to minimize the pressure drop in the massive pipes required to withstand the blanket over-pressurization during accidental transients.

In Figure 5.6, it is shown a sketch of the insulated feeding pipe geometry. The effective pipe inner radius is assumed as $r_1 = r_0 - t_{\mathrm{FCI}}$, where r_0 is the inner pipe radius calculated according to the chosen design pressure P (using the relations described in Section 5.1.1) and $t_{\mathrm{FCI}} = 15$ mm is the FCI equivalent thickness, which includes both the insert and the gap depth. The gap has been neglected for the pressure drop estimation, but for the effective pipe cross-section reduction. Nevertheless, both the insert Eurofer sheets are assumed to be in electrical contact with the liquid metal and, to estimate the equivalent wall conductance ratio, they are considered as bundled in a single metal strip characterized by thickness $t'_{\mathrm{FCI}} = 10$ mm, so that

$$c_{\mathrm{FCI}} = \frac{\sigma_w}{\sigma} \frac{t'_{\mathrm{FCI}}}{r_1} \tag{5.76}$$

where the effective inner radius r_1 is chosen as the problem length scale. We assume that each FCI segment is long $S = 1$ m and the discontinuity between insulating elements is constant throughout the pipe extension and equal to $2l = 20$ mm. To simplify the problem, it is assumed that the insulation is continuous over the TFC thickness (section FP2, see section 5.1.2) and that $n = 8$ insulation gaps are present along the pipe: respectively, $n_1 = 6$ in FP1 and $n_3 = 2$ in FP3.

The two-dimensional pressure drop in the insulated pipe is straightforwardly calculated in the three sections, applying the procedure previously described in section 5.1, using the effective liquid metal velocity in the pipe (u_1) and wall conductance ratio (c_{FCI})

$$\Delta p_{2\mathrm{D}} = \Sigma \Delta p_i \tag{5.77}$$

for which the pipe axial length used in eq. (5.77) is calculated subtracting the total discontinuity, $n \cdot 2l$.

To obtain the total pressure drop in the pipe, the contribution from the insulation gaps must be added. The pressure drop due to the leakage currents is characterized by a dimensionless coefficient ($\Delta\hat{p}_{\mathrm{gap}}$), proportional to the ratio between the wall and FCI conductance parameter

$$\Delta\hat{p}_{\mathrm{gap}} = 7.86 \cdot 10^{-3} \frac{c_w}{c_{\mathrm{FCI}}} \tag{5.78}$$

where a correction factor is applied to account for the gap length, extrapolating from the numerical results and experimental data presented for a similar configuration in Refs. [76, 80]. Equation (5.78) reproduces quite well the available data in the range $1 \leq c_w/c_{\mathrm{FCI}} \leq 30$, but it is strictly valid only for the chosen gap length and becomes unreliable for $c_{\mathrm{FCI}} \to 0$, where eq. (5.78) predicts $\Delta\hat{p}_{3D} \to \infty$, instead of approaching the asymptotic value predicted by the theory for $c_w = \infty$ and

$c_{\mathrm{FCI}} = 0$ [79, 80]. Moreover, it should be noted that formally eq. (5.78) has been obtained for inertia-less ($N \gg 1$) and inviscid ($Ha \gg 1$) flows; the former condition is not always satisfied for the pipe tract upstream from the TFC.

The absolute pressure drop for the insulation gap is obtained by the relation

$$\Delta p_{\mathrm{gap}} = \Delta \hat{p}_{\mathrm{gap}} \cdot \sigma u_0 B^2 r_1 \tag{5.79}$$

where u_0 is the mean velocity in the naked pipe. The overall pressure drop in the pipe due to insulation gaps is calculated then simply by

$$\Delta p_{3D} = n \cdot \Delta p_{\mathrm{gap}} \tag{5.80}$$

and, consequently, the total pressure drop in the insulated pipe

$$\Delta p_{\mathrm{FCI}} = \Delta p_{2\mathrm{D}} + \Delta p_{3D} \tag{5.81}$$

In Table 5.10, the pressure drop for the naked pipe and the insulated pipe for 4 nominal diameters (DN80, DN125, DN150 and DN200) are presented. The "sandwich" FCI is very efficient in decoupling the liquid metal from the wall and significantly reduces the pressure losses experienced by the FP, despite the relative high conductivity of the insert ($\approx 10^{-2}$) and the average flow velocity increase due to the cross-section contraction. We can define the discontinuous FCI efficiency

$$\eta = 1 - \frac{\Delta p_{\mathrm{FCI}}}{\Delta p} \tag{5.82}$$

For larger pipes, η is higher than for smaller pipes: the insert is proportionally less conductive, since its thickness is constant but $c_{\mathrm{FCI}} \propto t'_{\mathrm{FCI}}/r_1$, and u_1 is less sensitive to the contracted cross-section, amounting to 11% increase with regard to u_0 for DN80 and just 4% for DN200. However, $\Delta p_{\mathrm{gap}} \propto c_{\mathrm{FCI}}^{-1} r_1$ and, being c_w mostly uniform in the range considered, it increases with the nominal diameter: the pressure drop due to the insulation discontinuity is almost constant for all the cases considered and the total pressure loss becomes increasingly dominated by the 3D pressure drop term, which reaches up to 40% for DN200. Neglecting the discontinuity length, we can confound Δp_{2D} for the total pressure drop in a pipe with continuous insulation and define the related pressure loss reduction efficiency

$$\eta_c = 1 - \frac{\Delta p_{2\mathrm{D}}}{\Delta p} \tag{5.83}$$

and the overall normalized efficiency for a discontinuous insulation takes the form

$$\eta_{\mathrm{eff}} = \eta / \eta_c \tag{5.84}$$

Increasing the nominal diameter, η_{eff} slightly decreases but its value remains very high, which means that the pressure drop reduction is still significant compared with the naked pipe, despite the relative increase of the three-dimensional term. This result is not really surprising when we remember that the we assumed an optimistic maximum insert length $S = 1$ m, resulting in nearly 98% of the pipe extension being insulated. If we modify this assumption by decreasing the maximum insert length,

the normalized efficiency is negatively affected in turn. For instance, considering the DN200 pipe and $S = 0.1$ m, we calculate $\eta_{\text{eff}} = 0.53$, which corresponds to about 1 MPa, nearly five times the value computed for $S = 1$ m, even if the insulation is still covering ≈80% of the pipe length. Conversely, for the same reduction in the DN80 pipe insulation, we found that $\eta_{\text{eff}} = 0.94$ corresponding to a relative small 30% increase in the pressure drop. We can conclude that for smaller pipes, it is possible to tolerate wider discontinuities in the pipe insulation without significantly worsen the FCI efficiency.

Among the FPs reported in Table 5.10, only the DN80 is complying to both the RM specification on the wall thickness ($t_w \leq 15$ mm) and the maximum pressure foreseen for the in-box LOCA transient, but its pressure drop is still unacceptable. Splitting the flow rate in four DN80 pipes, it allows to obtain a feasible value for the pressure drop in the FP ($\Delta p \approx 410$ kPa) with an equivalent cross section of a single DN150. Assuming that the available cross-section in the VV lower port is approximately equal to a DN125 pipe, three insulated DN80 pipes occupy about the same space with a still acceptable $\Delta p \approx 550$ kPa.

5.4 Summary

In this Chapter, the pressure drop for the connection pipes between the blanket and the PbLi ex-vessel loop is estimated. Different routing schemes, pipe diameter and pipe number are considered to show each parameter influence. For all the configurations, except T03, the lower port routing scheme is preferable since it simplifies the integration with the blanket part of the PbLi hydraulic loop. However, stringent remote maintenance requirements in the lower port do not allow the pipe size required to achieve acceptable pressure losses and, thus, routing schemes from the upper port are still worth of consideration. Configuration T01.A is potentially adaptable to the less size demanding mid-point routing scheme, an advantage that is not shared by the other WCLL models.

Finally, the feeding and draining pipe dimensioning should take into account the over-pressurization scenario due to an in-box LOCA. Currently, the ex-vessel PbLi loop is dimensioned only for a maximum pressure of 4.6 MPa and, for consistency's sake, a similar assumption is made in this study, but more demanding pressure requirements will warrant an analysis revision and could very well result in unacceptable pressure losses for naked electro-conductive pipes. In this case, a possible mitigation strategy is the introduction of low-conductivity FCI or coating to decouple the fluid from the feeding and draining pipe wall.

Chapter 6

Manifold

6.1 Introduction

In this chapter, the pressure drop for the manifold region into the four configurations is estimated. Due to similarities in BZ hydraulic path and, thus, geometry to achieve flow distribution, the study is divided in two sections: the manifold of configuration T01.A and T01.B is discussed in Section 6.3, whereas the layout of T02 and T03 is going to be treated in Section 6.3.

6.2 Manifold for configuration T01.A and T0.1B

Following the analysis results discussed in Sections 5.1 and 5.2, the feeding pipe is assumed to be composed of two identical DN150 pipes, which are routed through the VV lower port and are attached to the blanket close to the divertor/blanket boundary interface (see Figure 4.3). Similarly, the draining pipe is constituted by a single DN200 pipe that is routed through the VV upper port following the top-point scheme and it is connected to the blanket close to the outboard/inboard boundary interface. This layout greatly simplifies the integration with the BZ hydraulic path, especially for the T01.B configuration, and it is characterized by relatively low pressure drop.

The manifold general layout is divided into three components: Distribution Manifold (DM), Collection Manifold (DM) and Spinal Manifold (SM). The first two components are shared between the two configurations and are very similar, whereas the SM is a feature present only in configuration T01.A.

- The **Distribution Manifold** receives the PbLi exiting the feeding pipe and it is located in the bottom part of the blanket. In configuration T01.B, the

manifold supplies directly the liquid metal to the BZ channels, whereas in T01.A its function is limited to convey the flow to the Spinal Manifold channels (Supply Leg).

- The **Spinal Manifold** is an "intermediate" component that is needed in configuration T01.A to distribute the PbLi among the poloidally stacked BZ cells. It is composed of two parallel arrays of rectangular channels running for all the segment poloidal height and contained in a narrow gap between the BZ and the back supporting structure. The interior array, called Supply Leg, transports upward the PbLi from the DM and gradually feeds the BZ cells, whereas the external array, called Recovery Leg, retrieves the depleted PbLi from the BZ and it finally delivers the fluid to the Collection Manifold.

- The **Collection Manifold** is located in the top part of the blanket and it conveys the fluid to the draining pipe. Similarly to what said for the DM, this component is directly fed by the BZ only for T01.B, whereas the Recovery Leg channels of the SM play this role for T01.A

The manifold layout for T01.B is relatively straightforward compared with the one devised for T01.A and it can be considered as a simplified solution. For this reason, we will first focus the study on the T01.A manifold and, then, the differences with the T01.B structure will be discussed and analyzed.

6.2.1 Distribution manifold T01.A

The layout of the T01.A distribution manifold is presented in Figure 6.1. The DM is composed of four narrow rectangular channels, of which only two are shown in Figure 6.1, that are also belonging to the Supply Leg of the Spinal Manifold and constitute its initial length. The feeding pipes are attached at the center of the manifold lateral channels and need to cross both the back supporting structure and the lateral channels of the Spinal Manifold Recovery Leg, which are mirroring the layout of the DM.

The attachment of the feeding pipe is chosen to address concerns about flow distribution due to the asymmetry in the BZ caused by the increasing toroidal width of the BZ, which enlarges from ≈ 1 m of the blanket bottom to the 1.5 m observed at the equatorial plane. To follow this transition, the BZ channels are progressively enlarged and, after ≈ 4 m of linear length, the lateral channels split in two sub-channels, thus that on the equatorial plane the BZ elementary cell is composed of six channels of approximatively equal toroidal width [22, 58]. Under the assumption of uniform flow distribution, the lateral channels of the DM (which belong also to the SM) will have to carry a larger flow rate than the central ones, thus generating a pressure imbalance that will tend to shift the fluid toward the central channels, resulting in the likely overfeed of these ones. The lateral attachment of the feeding pipes allow to better control this imbalance by hindering the fluid movement to the central channel.

The DM geometrical parameters are reported in Table 6.1. At the feeding pipe/manifold connection, the PbLi flow is assumed to be aligned with the radial direction and, therefore, we define an elementary toroidal-poloidal DM channel

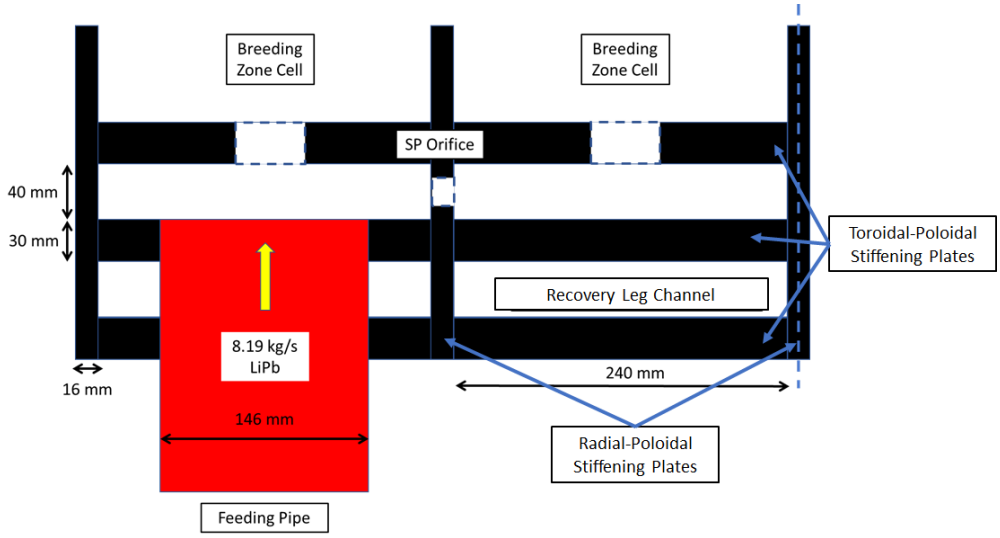

Figure 6.1. WCLL T01.A distribution manifold, radial-toroidal view. Dashed line identifies symmetry axis. Lateral channel is on the left, central channel on the right. For clarity's sake, breeding zone/recovery leg connection and water pipes are not shown.

where the flow incoming from the pipe expands. Since this channel is just the initial part of the SM channel, which can be considered as being infinitely extended in the poloidal direction with regard to the feeding pipe, the poloidal height is taken as the equivalent dimension of a BZ cell, i.e. 135 mm (see, for reference, Section 7.2).

The hydraulic path in the DM lateral channel can be outlined as follow

1. **Sudden expansion** from feeding pipe to toroidal-poloidal manifold channel
2. **90° sharp bend** from radial to poloidal direction ($\perp$ **B**)
3. **Sudden contraction** from toroidal-poloidal to toroidal-radial manifold channel

Similarly, the hydraulic path in the DM central channel can be summarized with these geometrical elements

1. **Sudden expansion** from feeding pipe to toroidal-poloidal manifold channel
2. **Sudden contraction** from toroidal-poloidal to poloidal-radial manifold channel
3. **90° sharp bend** from radial to toroidal direction (//**B**)
4. **Toroidal flow** from lateral to central channel, assumed as fully developed
5. **Sudden contraction and expansion** through Stiffening Plate Orifice (SPO) connecting the lateral and central channel
6. **Sudden expansion** from poloidal-radial to toroidal-radial manifold channel
7. **90° sharp bend** from toroidal to poloidal direction (//**B**)

Table 6.1. Distribution manifold channel, configuration T01.A. The wall conductance ratios reported use the toroidal half-width as length scale. For the flow aligned with the toroidal direction, the poloidal half-width is adopted.

Channel parameters			
Toroidal length	$2a$	240	mm
Radial length	$2b$	40	mm
Poloidal length	L_{pol}	135	mm
Toroidal-Poloidal Cross Section	$A_{t,p}$	324	cm^2
Poloidal-Radial Cross Section	$A_{p,r}$	54	cm^2
Radial-Toroidal Cross Section	$A_{r,t}$	96	cm^2
Wall parameters			
Radial-Poloidal Stiffening Plate	$2t_{r,p}$	16	mm
Toroidal-Poloidal Stiffening Plate	$2t_{t,p}$	30	mm
Wall ratio (Radial-Poloidal SP)	c_1	0.099	
Wall ratio (Toroidal-Poloidal SP)	c_2	0.186	

The first element is in common for both flow paths. The pressure drop can be calculated according to the methodology outlined in Section 4.3.2. The magnetic field is assumed uniform and aligned with the toroidal direction ($B_{tor} = 4.76$ T), except in the radial-poloidal channel where it is substituted by the poloidal field ($B_{pol} = 1.4$ T).

Lateral channel

(#1) Sudden expansion The flow exiting the feeding pipe pours out in the toroidal-poloidal manifold channel, where it undergoes a sudden expansion. Around 41% of the total mass flow rate ($\Gamma_1 = 3.358$ kg/s) is assumed to be redirected toward the central channel path, whereas the remaining 59% ($\Gamma_2 = 4.832$ kg/s) executes a sharp right turn to the poloidal direction and sudden contraction to the toroidal-radial manifold channel.

Neglecting the 2D pressure drop term, the sudden expansion from the feeding pipe is characterized by the coefficient $k = 0.5$ and the local interaction parameter $N_1 = 2911$, where the FP inner radius ($r_i = 75$ mm) is assumed as length scale and $u_{FP} = 4.7$ cm/s as velocity scale [68]. Under these assumptions, the local resistance coefficient is $\zeta = kN = 1456$ and the pressure drop can be estimated as

$$\Delta p_1 = 1.2\zeta \frac{1}{2}\rho u_{FP}^2 = 18.779 \text{ kPa} \tag{6.1}$$

where a correction factor 1.2 is employed to account for the combined expansion in the direction $//\mathbf{B}$ and $\perp \mathbf{B}$. The mean velocity in the toroidal-poloidal channel is $u_{t,p} = u_{FP}A_{FP}/A_{t,p} = 2.57$ cm/s.

(#2) 90° sharp bend To calculate the pressure drop in the 90° sharp bend from the radial to the poloidal direction, we define a reduced toroidal-poloidal channel equivalent to the 59% of the overall cross section of the original channel to account for the partitioning of the flow rate among the two flow paths. The reduced channel is characterized by $L_{tor} = 0.59 \cdot (2a) = 141$ mm and the same poloidal height as the

original channel. The characteristic length of the bend is defined as the equivalent hydraulic radius

$$r_2 = D_h/2 = \frac{2 \cdot (A'_{t,p})}{2L_{tor} + 2L_{pol}} = 56.87 \text{ mm} \tag{6.2}$$

where $A'_{t,p} = L_{tor}L_{pol}$. For a right sharp bend $\perp \mathbf{B}$ in a rectangular channel with $c = c_2$, we found $k = k_{//}/3 = 0.04331$ where $k_{//}$ is calculated from eq. (4.11). Employing r_2 as length scale the local interaction parameter is $N_2 = 3986$ and $\zeta = 172.65$, the bend pressure drop is estimated as

$$\Delta p_{l,2} = 0.564 \text{ kPa} \tag{6.3}$$

(#3) Sudden contraction The contemporary variation of cross section due to the flow passing from the toroidal-poloidal to the radial-toroidal channel causes an increase in the mean velocity $u_{t,r} = u_{t,p}A'_{t,p}/A_{t,r} = 5.14$ cm/s. The characteristic length of the contraction is defined as the equivalent hydraulic radius of the radial-toroidal channel

$$r_{r,t} = D_h/2 = \frac{2 \cdot (A_{r,t})}{4a + 4b} = 34.28 \text{ mm} \tag{6.4}$$

the sudden contraction is characterized by the coefficient $k = 0.5$. Employing $r_{r,t}$ as length scale, the local interaction parameter is $N_3 = 1207$ and $\zeta = 603$. The pressure drop can be estimated as

$$\Delta p_{l,3} = 1.2\zeta \frac{1}{2} \rho u_{r,t}^2 = 9.3777 \text{ kPa} \tag{6.5}$$

where a correction factor 1.2 is employed to account for the combined variation of cross section in the direction $//\mathbf{B}$ and $\perp \mathbf{B}$.

Total lateral path The overall pressure drop for the lateral channel can be calculated as following

$$\Delta p_l = \Sigma \Delta p_{l,i} = 28.273 \text{ kPa} \tag{6.6}$$

Central channel

(#1) Sudden expansion After the flow undergoes the sudden expansion from the feeding pipe to the receiving channel, around 41% of the total mass flow rate is conveyed to the central channel through an orifice realized in the radial-poloidal stiffening plate. Therefore, the pressure drop term due to this expansion is shared between the two hydraulic paths and it is represented by eq. (6.1).

(#2) Sudden contraction and (#3) 90° sharp bend The central channel flow rate is assumed to occupy 41% of the toroidal-poloidal manifold channel and, similarly to what is done for the lateral channel flow path, it is possible to define this reduced channel through an equivalent toroidal length $L'_{tor} = 0.41 \cdot (2a) = 98.27$ mm, whereas the poloidal height is kept unchanged ($L_{pol} = 135$ mm) with regard to the original channel. To convey the PbLi toward the stiffening plate, the flow executes a sharp right bend from the radial to the toroidal direction, that it is $//\mathbf{B}$. In doing

so, the flow enters the radial-poloidal channel, whose parameters are reported in Table 6.1. Since this channel is characterized by a smaller cross-section compared with the (equivalent) toroidal-poloidal one, the flow undergoes a sudden contraction and it is accelerated to a mean velocity

$$u_{r,p} = u_{t,p}\frac{A_{t_p}^{''}}{A_{r,p}} = 6.34 \text{ cm/s} \tag{6.7}$$

where $u_{t,p} = 2.57$ cm/s, as it was derived for the lateral channel hydraulic path, and $A_{t_p}^{''} = L_{tor}^{'} \cdot L_{pol} = 132$ cm^2 is the cross section of the equivalent toroidal-poloidal channel. The hydraulic radius of the radial-poloidal channel, calculated as following

$$r_2 = D_h/2 = \frac{2 \cdot (A_{r,p})}{4b + 2L_{pol}} = 30.85 \text{ mm} \tag{6.8}$$

it is employed as characteristic length scale for the contraction pressure drop calculation, obtaining $N_2 = 880.38$ and $\zeta = 440.19$ from the assumption $k = 0.5$. The pressure drop is estimated as

$$\Delta p_{c,2} = 1.2\zeta\frac{1}{2}\rho u_{r,p}^2 = 10.415 \text{ kPa} \tag{6.9}$$

where a correction factor 1.2 is employed to account for the combined variation of cross section in the direction $//\mathbf{B}$ and $\perp \mathbf{B}$.

The pressure drop coefficient in the bend is calculated assuming $c = 0.186$ and, according to eq. (4.11), it is estimated as $k_{//} = 0.13$. Employing r_2 from eq. (6.8) as length scale and $u_{r,p}$ as characteristic velocity, the local interaction parameter is $N_3 = 880.38$ and the local resistance factor $\zeta = 114.39$. Consequently, the pressure drop is calculated as

$$\Delta p_{c,3} = 2.255 \text{ kPa} \tag{6.10}$$

(#4) Toroidal flow and (#5) Sudden contraction and expansion To reach the central channel, the fluid must pass through the stiffening plate that it is obstructing the radial-poloidal manifold channel. To allow this crossing, the structural element must be pierced to create a Stiffening Plate Orifice (SPO), whose dimension is going to impact both the PbLi pressure drop and the mechanical stability of the plate. In general, the flow through the orifice can be divided into a 2D pressure drop, due to the fluid transfer from lateral to central channel along the toroidal direction, and a combined sudden contraction/expansion modeling the transition through the orifice. The former term is not affected, to the first order term, by the aperture geometry, whereas the latter term is strongly dependent on it, in particular the available cross-section. In other words, the 2D term can be considered the pressure loss that will occur in the channel devoid of any obstacles, i.e. when the orifice opening is equal to the channel cross-section.

First, let us consider the toroidal flow. If a fully developed flow is assumed, the pressure gradient can be calculated according to the classical relation defined in eq. (4.4). The stream-wise length of the radial-poloidal channel is obtained by the sum $L_{SPO} = 2a + 2t_{r,p} = 256$ mm. Since the flow is aligned with the toroidal direction, the poloidal field component $B_{pol} = 1.4$ T is the one exerting the resistive

action on the fluid. The half-width of the channel in the poloidal direction ($L_{pol}/2$) is chosen as length scale. The radial-poloidal channel is bounded by the bottom cap plate, assumed to have $2t_{BC} = 25$ mm, and the toroidal-poloidal stiffening plates. The upper part of the channel is not bounded by a solid wall but it is connected to the SM channel that, due to its approximatively infinite extension in the poloidal direction compared with the one examined, is assumed to be delimited by a wall as conductive as the liquid metal, i.e. having $c = 1$. The wall conductance ratio for the bottom cap and the toroidal-poloidal stiffening plate take the form

$$c_{BC} = \frac{\sigma_w}{\sigma}\frac{t_{BC}}{b} = 0.275 \tag{6.11}$$

$$c_2^{'} = \frac{\sigma_w}{\sigma}\frac{t_{t,p}}{b} = 0.330 \tag{6.12}$$

The pressure coefficient k_p is estimated with eq. (4.8) adopting the average wall conductance ratio $c_H = (c_{BC} + 1)/2$ between the bottom cap and the fluid surface for the Hartmann wall. Considering $L_{pol}/2$ as length scale and $u_{r,p}$ as characteristic velocity, it follows that the pressure gradient is

$$\nabla p_4 = 16.27 \text{ kPa/m} \tag{6.13}$$

and the 2D pressure drop term for the SPO flow is calculated as

$$\Delta p_{c,4} = 4.160 \text{ kPa} \tag{6.14}$$

From what exposed previously about the physical meaning of this pressure drop term, the value obtained from eq. (6.14) must be considered as the lowest estimate for the SPO pressure drop, corresponding to when the orifice opening is equal to the channel cross-section.

Consider now the pressure drop term due to the sudden contraction and expansion as the fluid flows through the orifice. The orifice cross-section and shape are some of the parameters influencing the pressure drop. For the purpose of this study, we assume that the orifice is rectangular and that, compared with the upstream radial-poloidal channel, its poloidal width is kept unchanged ($L_{p,SPO} = L_{pol}$), whereas the radial width is halved ($L_{r,SPO} = b$). Under these assumptions, the orifice area is half of the upstream/downstream channel and the only cross-section variation is in the radial direction, thus being perpendicular to both B_{tor} and B_{pol}. The SPO parameters are reported in Table 6.2.

Assuming r_{SPO} and u_{SPO} as the scales for length and velocity, the local interaction parameter is calculated adopting the poloidal magnetic field intensity, $N_{pol} = 21.495$, and, thus $\zeta = 0.5N_{pol} = 10.748$. For the purpose of this estimate, the toroidal field component is supposed not to influence the pressure loss in the contraction and is neglected. However, this assumption may not be particularly conservative, since the toroidal field is perpendicular to the contraction direction, even if it is aligned with the stream-wise direction. To the best knowledge of the author, the only study reported in the literature considering a sudden variation in the cross-section involving a bi-directional magnetic field with one component aligned with the stream-wise direction did not address the influence of the magnetic field inclination on the pressure drop [81]. Under the assumptions made, the head

Table 6.2. Geometrical parameters for the flow through Stiffening Plate Orifice (SPO)

Upstream/downstream radial-poloidal manifold channel			
Radial width	$2b$	40	mm
Poloidal width	L_{pol}	135	mm
Cross Section	$A_{p,r}$	54	cm^2
Mean velocity	$u_{p,r}$	6.34	cm/s
Stiffening Plate Orifice			
Stream-wise length	$s = 2t_{r,p}$	16	mm
Radial width	$L_{r,SPO}$	20	mm
Poloidal width	$L_{p,SPO}$	135	mm
Hydraulic radius	r_{SPO}	34.84	mm
Cross Section	A_{SPO}	27	cm^2
Mean velocity	u_{SPO}	12.68	cm/s

loss in the contraction and expansion from the orifice can be described as the same phenomenon in reverse order. The total pressure drop in the orifice is calculated with the relation

$$\Delta p_{c,5} = \Delta p_C + \Delta p_E = \zeta \rho u_{SPO}^2 = 1.695 \text{ kPa} \tag{6.15}$$

It should be noted that the intense velocity in the orifice is likely to produce relevant inertial effects, which are currently neglected, and that are likely to influence the estimate even more for a smaller available cross-section than the one presently considered.

(#6) Sudden expansion and (#7) 90° sharp bend After crossing the SPO the fluid enters the DM central channel, where it executes a sharp 90° bend from the toroidal to the poloidal direction and undergoes a contemporary sudden expansion from the radial-poloidal to the toroidal-radial channel. Regarding the latter, characteristic length and velocity of the smaller channel ($u_{r,p}$ and r_2) are employed as scales for the pressure drop calculation and, therefore, we estimate

$$\Delta p_{c,6} = \Delta p_{c,2} = 10.415 \text{ kPa} \tag{6.16}$$

The mean velocity in the enlarged channel takes the value $u'_{t,r} = u_{p,r} A_{p,r} / A_{r,t} = 3.572$ cm/s. From the channel cross-section $A_{r,t}$ and other parameters reported in Table 6.1, it is possible to calculate the hydraulic radius $r_{r,t} = D_h/2 = \frac{2 \cdot (A_{r,t})}{4b+4a} = 34.28$ mm and, since the pressure drop coefficient in the bend is calculated assuming $c = 0.186$, we have $k_{//} = 0.13$. Employing $r_{r,t}$ as length scale and $u'_{t,r}$ as characteristic velocity, the local interaction parameter is $N_7 = 1736$ and, consequently, the pressure drop is calculated as

$$\Delta p_{c,7} = 1.411 \text{ kPa} \tag{6.17}$$

Total central Finally, the overall pressure drop in the central channel hydraulic path is obtained through the sum of all the contributions

$$\Delta p_c = \Sigma \Delta p_{c,i} = 49.130 \text{ kPa} \tag{6.18}$$

Table 6.3. Pressure loss in the distribution manifold channels for reference feeding pipe (DN150 x2)

	Lateral channel	Central channel	
Δp_1	18.779		kPa
$\Delta p_{i,2}$	0.564	10.415	kPa
$\Delta p_{i,3}$	9.378	2.255	kPa
$\Delta p_{i,4}$		4.160	kPa
$\Delta p_{i,5}$		1.695	kPa
$\Delta p_{i,6}$		10.415	kPa
$\Delta p_{i,7}$		1.411	kPa
Δp_i	28.720	49.130	kPa

where the loss in the SPO, neglecting the toroidal flow, is $\approx 3.5\%$ of the total pressure drop. An overview of the pressure drop for the two hydraulic paths is reported in Table 6.3.

Ensuring uniform flow distribution is a big concern for the T01.A manifold. Although the central channel features $\approx 170\%$ of the head loss calculated for the lateral path, the flow rate for this hydraulic path is expected to increase substantially compared with the value considered for this estimate since, as we are going to discuss in Sections 6.2.2 and 6.2.3, it is characterized by significantly lower pressure losses in the other portions of the manifold. To equalize the overall pressure imbalance, a possible strategy could involve the SPO cross-section reduction and the insertion of additional obstacles in the central spinal manifold channel.

Single feeding pipe

For a single pipe that feeds the distribution manifold, a different flow layout must be adopted, which features the pipe attachment moved to the blanket segment center and the shortening of the toroidal-poloidal stiffening plate to create a larger space for the fluid expansion and allow for an easier pipe welding. Due to the particular symmetry of the distribution manifold layout, the same procedure described previously can be applied to estimate the pressure losses in the new configuration by just swapping the central and lateral path hydraulic elements. Unfortunately, the use of a single feeding pipe further exacerbates the pressure imbalance between the lateral and central flow path since in this case the channel featuring the higher pressure losses is the former rather than the latter, as it is possible to see in Table 6.4, where an overview of the pressure drop is reported assuming a DN200 feeding pipe, whose parameters where calculated in Section 5.1.3. For the case considered $\Delta p_l / \Delta p_c = 3.23$ that, added to the further imbalance observed in the other manifold sections, it is going to severely underfeed the BZ lateral channels.

It should be noted that the diameter of the feeding pipe directly affects the estimate of Δp_1, since a smaller pipe will lead to higher expansion ratio with regard to the toroidal-poloidal channel, and vice versa, as it is possible to see comparing the results from Tables 6.3 and 6.4. For the limiting case of a DN80 feeding pipe, $\Delta p_1 = 28.26$ kPa and, since the other pressure loss terms are unaffected by the pipe diameter, the pressure drop ratio between the channels is reduced to $\Delta p_l / \Delta p_c = 2.17$.

Table 6.4. Pressure loss in distribution manifold channels for single DN200 feeding pipe

	Lateral channel	Central channel	
Δp_1	11.515		kPa
$\Delta p_{i,2}$	14.987	0.564	kPa
$\Delta p_{i,3}$	3.246	6.517	kPa
$\Delta p_{i,4}$	5.986		kPa
$\Delta p_{i,5}$	2.440		kPa
$\Delta p_{i,6}$	14.987		kPa
$\Delta p_{i,7}$	6.935		kPa
Δp_i	60.096	18.596	kPa

6.2.2 Spinal manifold

The Spinal Manifold (SM) is the largest component by volume of the manifold hydraulic region. Its main function is to distribute uniformly the PbLi flow rate into the cells composing the breeding zone. It is constituted by two arrays of rectangular channels nested between the BZ and BSS: the internal array, called Supply Leg (SL), distributes continuously the liquid metal among the cells, whereas the external one, called Recovery Leg (RL), collects and conveys the tritium-rich PbLi to the collection manifold. The radial-poloidal layout of the SM channels is outlined in Figure 6.2, whereas the toroidal-radial one is shown in Figure 6.1 for the SM lower section, which is coincident with the distribution manifold.

Both the RL and SL are co-flowing in the upward poloidal direction and have nearly identical geometries. In the SL, the mass flow rate in its channel is gradually decreasing moving upward due to the continuous feeding of the elementary cells. The opposite phenomenon happens in the RL, where the mass flow rate ramps from null at the bottom to its maximum value right at the top of the blanket. Moreover, due to the widening toroidal width of the blanket from the bottom to the equatorial plane, SL and RL channels do not have a uniform cross-section. This variation is mostly evident for the lateral channel that branches in two at $S \approx 4$ m and merges again at $S \approx 12$ m, whereas the central channel is mostly unchanged for the whole SM length. For this reason, similarly to what was done for the distribution manifold analysis, a central and lateral channel hydraulic path are defined to estimate the pressure losses in this component. For all channels, the radial width is constant at 40 mm, whereas the toroidal width is a function of the blanket spine linear length (S), as outlined in Table 6.5. The variable cross-section of the central channel will be neglected in the following.

Neglecting any effects due to the electromagnetic coupling through leakage currents and assuming that the flow rate variation is continuous, the flow in the SM channels can be approximated as locally fully developed and, therefore, the pressure drop can be obtained from the gradient linear integral, calculated according to eqs. (4.4) and (4.8). The toroidal magnetic field variation is obtained from eq. (4.1), whereas the mean velocity law in the channel is approximated with a linear law, which assumes that half of the mass flow rate is distributed at the equatorial plane. According to the results obtained in Section 6.2.1, the maximum velocity for both the lateral and central channel is located at the DM outlet and it amounts, respectively,

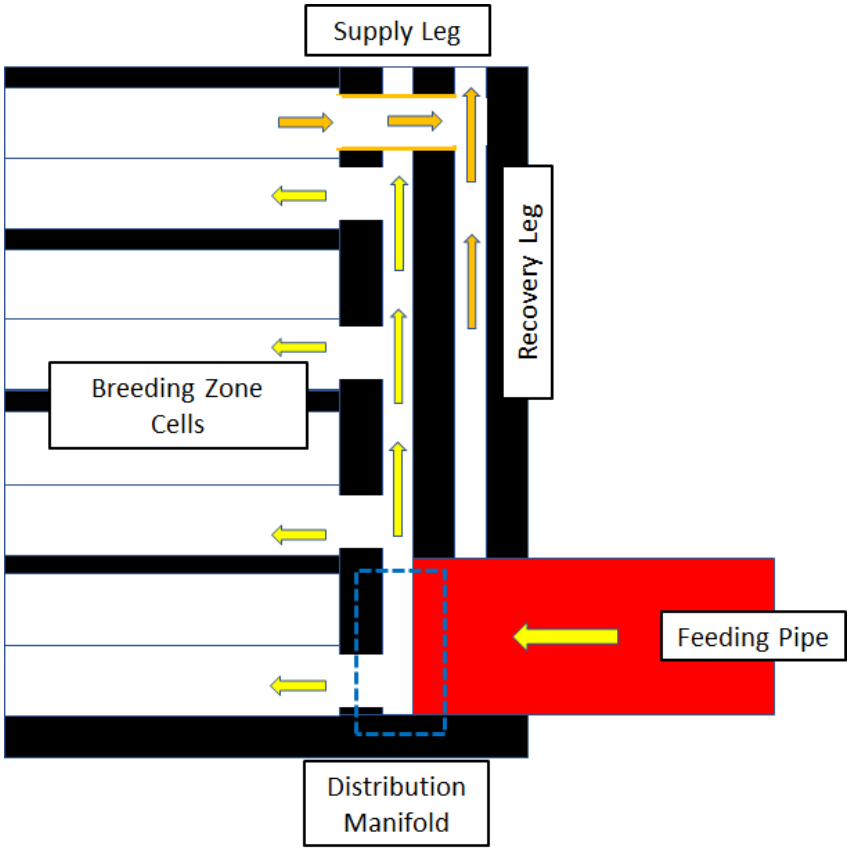

Figure 6.2. Detail of the bottom part of the WCLL T01.A spinal manifold, radial-poloidal view. Dashed box marks the position of the distribution manifold. For clarity's sake, the connection with the recovery leg is shown only for the topmost cell.

to $u_l = u_{t,r} = 5.14$ cm/s for the former, and to $u_c = u'_{t,r} = 3.572$ cm/s for the latter.

Central channel

In Figure 6.3, the pressure gradient for the SL and RL of the SM central channel is plotted against the manifold linear length. The intersection point identifies the position of the BZ cell for which half of the flow rate is distributed (or collected, referring to the RL), which is located slightly above the equatorial plane at $Z = 0.583$ m. Recalling Figure 4.4, the higher magnetic field in the top half of the blanket causes higher pressure losses in the corresponding RL tract, where the flow rate is increasing while moving toward the blanket top. Consequently, the pressure drop in the SM for a certain BZ cell is a function of its position along the blanket spine. For an arbitrary BZ cell located at a certain linear length S_i on the blanket spine, it is possible to calculate the associated SL and RL pressure loss by integrating the relative gradient curve for $S \leq S_i$ and $S \geq S_i$. The total pressure loss can be obtained by the sum of these two contributions. In Figure 6.4, the overall pressure drop for an arbitrary BZ cell fed by the SM central channel is plotted against the cell position: the cells located close to the top and bottom of the blanket are

Table 6.5. Toroidal width of SM channels as function of the blanket spine linear length. The external channel is a branch of the lateral channel existing in the range $S = 4 \div 11.76$.

S (m)	Lateral channel	(External channel)	Central channel	
0	240		240	mm
4	336		234	mm
4.1	234	(86)	234	mm
8.55	234	(217)	234	mm
11.75	234	(86)	234	mm
11.76	336		234	mm
16.93	240		240	mm

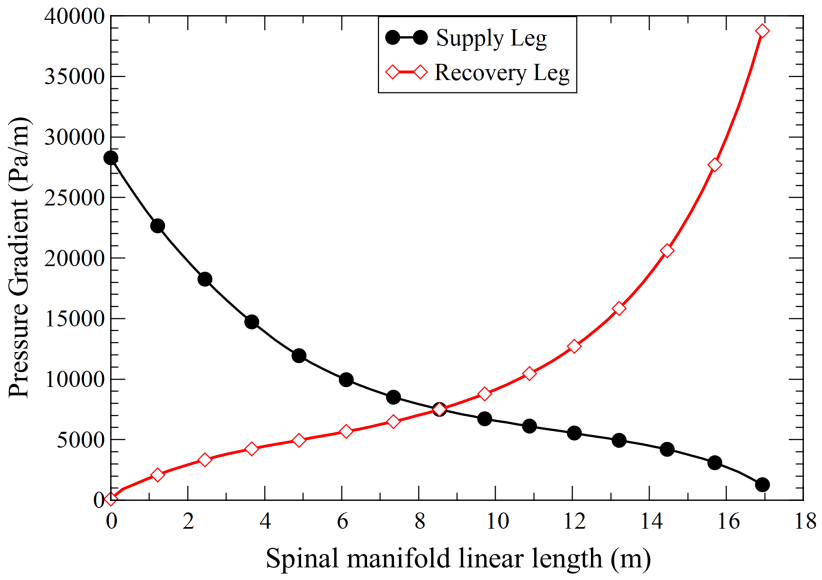

Figure 6.3. Pressure gradient for SM central channel Supply and Recovery Leg

characterized by lower pressure loss compared with those located near the equatorial plane. The maximum pressure loss in the SM central channel is observed for the cell located at $S = 8.55$ m, for which $\Delta p_c = 269.74$ kPa.

Lateral and external channel

For the SM lateral channel, the same methodology described for the central one can be applied to calculate the pressure drop. However, conversely to what occurs there, the cross-section of this flow element cannot be considered invariant with the spinal length, since its toroidal width increase to follow the blanket enlargement moving toward the equatorial plane. As a consequence, the toroidal width of the lateral channel increases from $2a = 240$ m at $S = 0$ m to $2a^{'} \approx 336$ m at $S \approx 4$ m. The pressure gradient decreases rapidly due to combined effect of the increased cross-section and diminished pressure coefficient, since $k_p \propto b/a$. In Figure 6.5, the

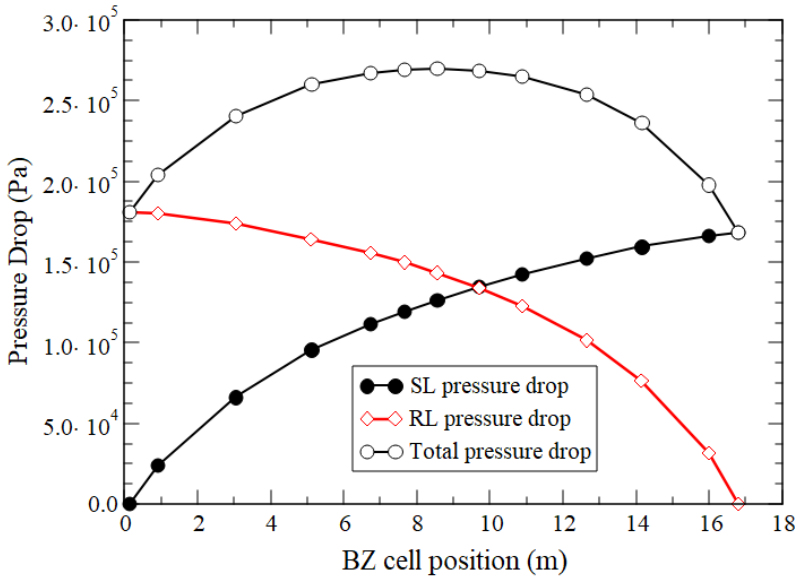

Figure 6.4. Supply leg, recovery leg and total pressure drop for an arbitrary BZ cell fed by the SM central channel

pressure gradient for the BZ cell experiencing the maximum head loss in the SM is shown for both the lateral and central flow path, which is quite representative of the plot for an arbitrary BZ cell. It can be seen how the lateral channel gradient falls below the other flow path value, even if the lateral one is carrying around 40% more flow rate. At $S \approx 4$ m, the channel is so wide that it branches in two: a main channel, which keeps the *lateral channel* name in our framework, and whose geometry is identical to the central one, and a smaller conduit, called *external channel*. The toroidal width of the latter duct continues to be a function of the linear length and increases moving toward the equatorial plane, whereas the former has a mostly invariant cross-section. In Figure 6.5, the flow distribution at the lateral channel branching is assumed to be completely described by the classical continuity equation. If Γ_L is the flow rate in the lateral channel before the branching, the flow rate in the daughter channels is

$$\Gamma_L^{'} = \Gamma_L \frac{A_L^{'}}{A_L^{'} + A_E} \tag{6.19}$$

$$\Gamma_E = \Gamma_L \frac{A_E}{A_L^{'} + A_E} \tag{6.20}$$

Due to this assumption and because of its small toroidal width, the pressure gradient of the external channel is about five times the one calculated for the lateral duct. This difference reduces with the spinal length due to the increasing toroidal width of the external channel and, at $S = 8.55$ m, $\nabla p_E \approx \nabla p_L$. Due to this phenomenon, a significant discrepancy is observed for the maximum pressure drop in this two elements, where the lateral channel features $\Delta p_L \approx 285$ kPa, whereas for the external

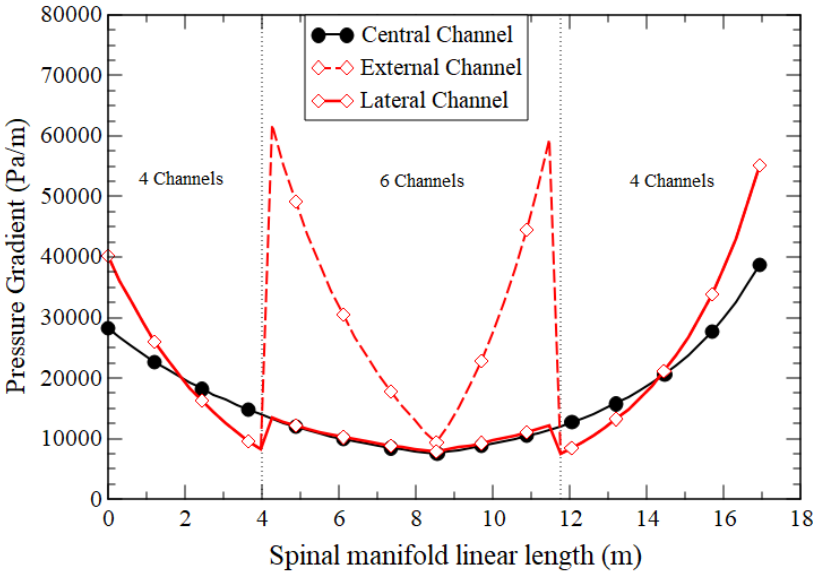

Figure 6.5. Pressure gradient for the SM central, lateral and external channel. The plots are obtained for the maximum pressure drop flow path (BZ cell at $S = 8.55$ m).

duct we have $\Delta p_E \approx 442$ kPa. An overfeeding of the lateral channel is expected to compensate the pressure drop imbalance between the two channels, which stabilizes at around $\Delta p \approx 340$ kPa. It is not clear how much the electromagnetic coupling is going to affect the flow distribution for this element: since lateral and external channels are stacked in the magnetic field direction the coupling is expected to equalize the flow rate and slightly decrease the pressure drop compared with the uncoupled channels [82]. However, the significant asymmetry between the ducts makes difficult to formulate reliable predictions following the results reported in the literature, which mostly refers to the simpler case of symmetric channels. In the following, $\Delta p = 340$ kPa is the estimate figure used to characterize the pressure loss in both the lateral and external channel.

Flow around obstacles in the Supply Leg

In Figure 6.2, it is shown how the PbLi exiting the BZ is transported to the RL through a pipe that crosses the SL channel. Since this pipe can have a considerable diameter, as it is going to be discussed in Section 7.2, the SL channel blockage is not negligible and neither the 3D pressure loss generated by the velocity gradients around the obstacle. Assuming a pipe diameter $d = 50$ mm, the blockage ratio is defined as $\beta = d/2a$, where $2a$ is the channel toroidal width. Considering what is reported in Table 6.5, the blockage ratio can range from $\beta \approx 0.21$ for the central channel to $\beta \approx 0.58$ for the external one for its minimum cross-section value, close to the branching point. In the present section, we are going to estimate the pressure drop related to the flow around these obstacles for the central and lateral flow paths,

for which we are going to neglect the cross-section variation. It should be noted how the tube connecting BZ and RL is not the only obstacle that crosses the SL channel: the coolant pipes pass through it as well and, for the lateral channels, contribute to increase the channel blockage ratio significantly. However, since the coolant pipe penetration is restricted to the external channels, their effect is going to be neglected in the present analysis[1].

Considering the BZ cell at $S = 8.55$ m, if the poloidal extension of the BZ elementary cell is equal to $L_{pol} = 0.135$ mm, we can calculate the number of cells that are passed by the SL channel before reaching the chosen blanket spine length as $n = S/L_{pol} \approx 64$. Consequently, the PbLi moving in the SL channel must flow around n successive obstacles to reach this particular BZ cell. To have a first estimate, the 3D pressure due to a single obstacle can be calculated with the correlation developed in Chapter 10 for the flow around an obstacle subjected to bi-directional magnetic field. According to eq. (10.14), the 3D pressure drop can be expressed in the form

$$\Delta p_{3D} = 0.09665\, \sigma u_0 B_0^{1.73} d \tag{6.21}$$

For the central channel, if we assume an average velocity $u_0 = 2.7$ cm/s and magnetic field $B = 3.79$ T, the average 3D obstacle pressure drop is estimated as

$$\Delta p_{3D,c} = 1022.56 \text{ Pa} \tag{6.22}$$

and the overall 3D pressure drop due to the flow around obstacles in the SL channel is calculated as

$$\Delta p_{o,c} = n \cdot \Delta p_{3D,c} = 65.444 \text{ kPa} \tag{6.23}$$

For the lateral channel, if we consider an average velocity $u_0 = 3.1$ cm/s and magnetic field $B = 3.79$ T, the average 3D obstacle pressure drop is estimated as

$$\Delta p_{3D,l} = 1175.75 \text{ Pa} \tag{6.24}$$

and the overall 3D pressure drop due to the flow around obstacles in the SL channel is calculated as

$$\Delta p_{o,l} = n \cdot \Delta p_{3D,l} = 75.248 \text{ kPa} \tag{6.25}$$

where $\Delta p_{o,l}/\Delta p_{o,c} \approx 1.15$. The pressure drop estimate for the SM channels can be updated accordingly

$$\Delta p_c = 335.184 \text{ kPa} \tag{6.26}$$

$$\Delta p_l = 415.284 \text{ kPa} \tag{6.27}$$

The pressure losses from the flow around the BZ outlet pipe are quite considerable, since they account for about $18.1 \div 19.5\%$ of the overall pressure drop for, respectively, the lateral and central flow path. The obstacle weight on the overall pressure loss is expected to further increase when considering also the effect of the cooling pipes and, moreover, it could be particularly high for the external channel. Under the assumptions made, the obstacle loss affects only the SL channel and this phenomenon

[1]The coolant pipes partially block also the RL lateral channels, since they need to penetrate the whole radial width of the SM to reach the BZ from their manifolds, which are located close to the BSS

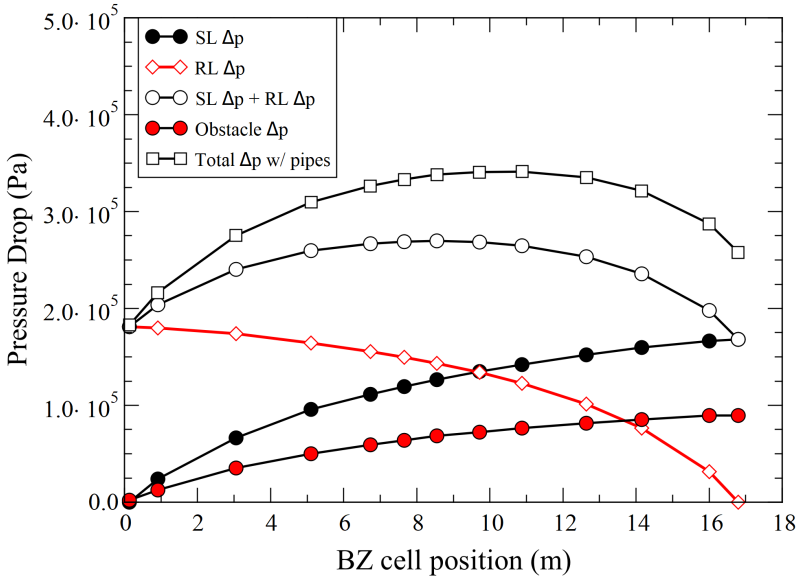

Figure 6.6. Effect of obstacles in the SL for the pressure drop of an arbitrary BZ cell fed by the SM central channel

causes the shift to $S \approx 10.8$ m for the position of BZ cell for which the maximum SM pressure drop is observed. However, as it is possible to see in Figure 6.6, the maximum pressure loss for the central channel is $\Delta p_c \approx 341$ kPa, which is quite close to our current estimate.

It should be noted that the PbLi flowing in the connection pipe is in electrical contact with the wall and such tube is immersed, in turn, in the upward flow happening in the SL manifold channel. Therefore, it is reasonable to assume that the pipe and the larger duct are electromagnetically coupled through mutual leakage currents. To the best knowledge of the author, such a cross-flow coupled case has never been investigated in the literature and could have unforeseen consequences on the pressure drop estimate and even on the mechanical stability of the connection pipe, therefore a more detailed investigation is deemed necessary to assess the influence of this phenomenon. However, since the BZ outlet pipe has no structural function it could be feasible to electrically insulate it and avoid any unintended consequences.

6.2.3 Collection manifold T01.A

The Collection Manifold (CM) layout, which is shown in Figure 6.7, is coincident with the spinal manifold end and, thus, is very similar to the distribution manifold geometry, being constituted by 2 lateral and 2 central channels, which are symmetrical with respect to the blanket segment midline. Due to the assumption of a singular DN200 draining pipe, the flow paths in the CM are identical to the one described for the case of the DM fed by a singular feeding pipe, with the only exception that they

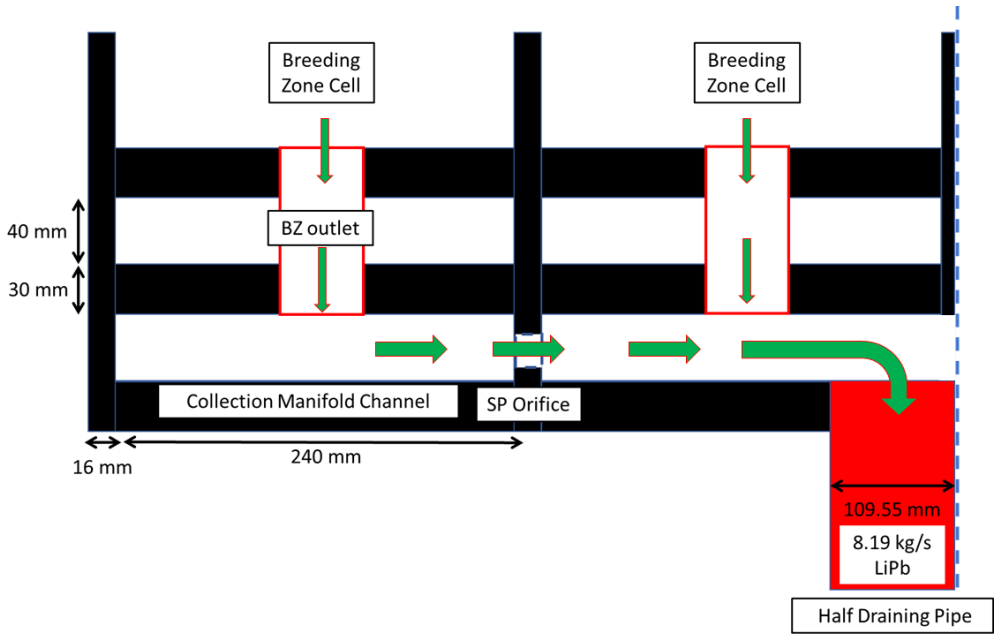

Figure 6.7. WCLL T01.A collection manifold, radial-toroidal view. Dashed line identifies symmetry axis. Lateral channel is on the left, central channel on the right. For clarity's sake, water pipes are not shown.

occur in reverse order. The inlet velocity for the CM lateral and central channel is, respectively, $u_l = u_{t,r} = 5.14$ cm/s and $u_c = u'_{t,r} = 3.572$ cm/s, equal to the DM outlet velocity and SM maximum velocity.

Two different positions for the CM are considered. The first layout postulates the adoption of the top-point draining scheme for the draining pipe, therefore the CM is located at the blanket top-most position. Consequently, the magnetic field intensity employed to estimate the pressure drop is $B_{tor} = 5.46$ T and $B_{pol} = 0.909$ T, with consistent assumptions regarding the DP estimate described in Section 5.2.1. Accordingly, the alternative layout follows the mid-point draining scheme and the CM is located at about 2/3 of the blanket poloidal height. The magnetic field intensity employed to estimate the pressure drop for this layout is $B_{tor} = 3.64$ T and $B_{pol} = 0.909$ T. The top CM results are reported in Table 6.6, whereas the one for the mid CM layout can be found in Table 6.7.

The pressure losses for the mid-point CM are lower than the one expected for the top CM due to the lower magnetic field intensity in this region. However, how it was discussed in Section 5.2.2, it is necessary to foresee a bypass channel array to transport the PbLi from the blanket top to the draining point to adopt such layout. This component effectively amounts to an extension of the SM channel and it is characterized by intense pressure losses ($\Delta p \approx 200$ kPa), other than being very challenging to integrate with the back supporting structure and the water manifold. These issues completely negate every advantage of the CM mid-point location and, therefore, the top-point draining scheme is preferred. In the following, the results presented in Table 6.6 are taken as reference for the T01.A CM pressure loss.

Table 6.6. Pressure loss in the collection manifold channels for the top-point draining scheme. For details about the calculation methodology, refer to Section 6.2.1

	Lateral channel	Central channel	
$\Delta p_{i,7}$	2.670		kPa
$\Delta p_{i,6}$	19.703		kPa
$\Delta p_{i,5}$	1.024		kPa
$\Delta p_{i,4}$	2.523		kPa
$\Delta p_{i,3}$	4.267	8.567	kPa
$\Delta p_{i,2}$	19.703	0.742	kPa
Δp_1	15.061		kPa
Δp_i	64.926	24.370	kPa

Table 6.7. Pressure loss in the collection manifold channels for the mid-point draining scheme. For details about the calculation methodology, refer to Section 6.2.1

	Lateral channel	Central channel	
$\Delta p_{i,7}$	1.118		kPa
$\Delta p_{i,6}$	8.769		kPa
$\Delta p_{i,5}$	1.024		kPa
$\Delta p_{i,4}$	2.523		kPa
$\Delta p_{i,3}$	1.899	3.813	kPa
$\Delta p_{i,2}$	8.769	0.318	kPa
Δp_1	6.703		kPa
Δp_i	30.879	10.833	kPa

6.2.4 Overall pressure loss for T01.A manifold

The analysis results are summarized in Table 6.8. For the distribution manifold, a feeding scheme that uses two DN150 feeding pipes attached at the lateral channels center is assumed. For the spinal manifold, the pressure losses are calculated for the distribution/collection flow path to the BZ cell at $S = 8.55$m, where the maximum 2D pressure drop in the supply and recovery leg is foreseen, and assuming no pressure imbalance between the lateral and external channel. Finally, the collection manifold is assumed to be located at the top of the blanket and to be drained by a singular DN200 draining pipe.

The spinal channel is the most critical component of the manifold region where nearly 82% of the overall pressure drop is located due to the long poloidal extension needed to distribute the flow rate to the stacked BZ cells. The analysis of the flow in this component is further complicated by the different size of the central, lateral and external channel, the non-uniform cross-section and the presence of numerous obstacles that cross the channels, perturbing the fluid and causing significant 3D pressure losses. Flow imbalance between the central and the lateral channels is another important issue, since it could lead to severe underfeeding of the external elements of the breeding zone, a problem that could be further exacerbate by the effect of the electromagnetic coupling between the channels. However, it is challenging to envision a way to optimize and simplify the PbLi flow path in the spinal channel due to the requirements of the BZ layout for configuration T01.A

Table 6.8. Overall pressure loss in the manifold hydraulic region for configuration T01.A, broken down by component contribution. The external channel is assumed to have the same pressure drop of the lateral channel.

	Lateral channel	Central channel		$\Delta p_i/\Delta p$ (%)
Distribution	28.720	49.130	kPa	5.56/12
Spinal			kPa	
• 2D flow (SL+RL)	340	269.74	kPa	66.8/66
• Obstacle	75.248	65.444	kPa	14.8/16
Collection	64.926	24.370	kPa	12.8/6
Total Manifold	508.894	408.684	kPa	100/100

and the complexity of its integration with the coolant manifolds, which occupy a significant share of the space available between the BZ and the BSS. Moreover, it should be noted that a significant pressure imbalance is present between the BZ cells on the equatorial plane, which are characterized by the higher SM pressure drop, and the cells located close to the blanket bottom. Since the head loss in the BZ is mostly negligible compared with the manifold, as it will be demonstrated in Section 7.2, mitigation strategies in the manifold area must be adopted to obtain an uniform flow distribution in the BZ.

6.2.5 Manifold for configuration T01.B

In configuration T01.B, the spinal manifold is no longer present and this hydraulic region is composed only by the distribution and collection components. The flow partitioning scheme is drastically simplified, since the whole PbLi mass flow rate is directly fed to the BZ, meaning that the continuous poloidal distribution envisioned for T01.A is not necessary anymore. The distribution (and collection) manifold layout is modeled after the one discussed for T01.A: the supply and recovery leg channels of the spinal manifold are merged, the toroidal-poloidal SP is removed, whereas a toroidal-radial SP is extended toward the back supporting structure to create an enclosure. In Figures 6.8 and 6.9, the radial-toroidal and radial-poloidal views of the T01.B manifold are presented. Recalling Figure 6.2, it can be highlighted how the region that was designated to host the spinal manifold in T01.A is instead integrated in the BZ for configuration T01.B, where is employed to route the PbLi to the successive cell in the poloidal stack, as it will be described in Section 7.3.

The principal geometrical parameters of the manifold are reported in Table 6.9. It is possible to distinguish a lateral and central flow path depending on channel position, as it was done for the T01.A manifold in Section 6.2.1, and the feeding pipe is assumed to be attached at the lateral channel center. Due to the similarities between T01.A and T01.B layout, the DM flow paths share most hydraulic elements. Notable exceptions are the lack of any flow orientation change toward the poloidal direction and the addition of a sudden contraction/expansion through the Breeding Zone Orifice (BZO), that connects the manifold with the BZ cell. The hydraulic path in the DM lateral channel is described by these elements

1. **Sudden expansion** from feeding pipe to toroidal-poloidal manifold channel

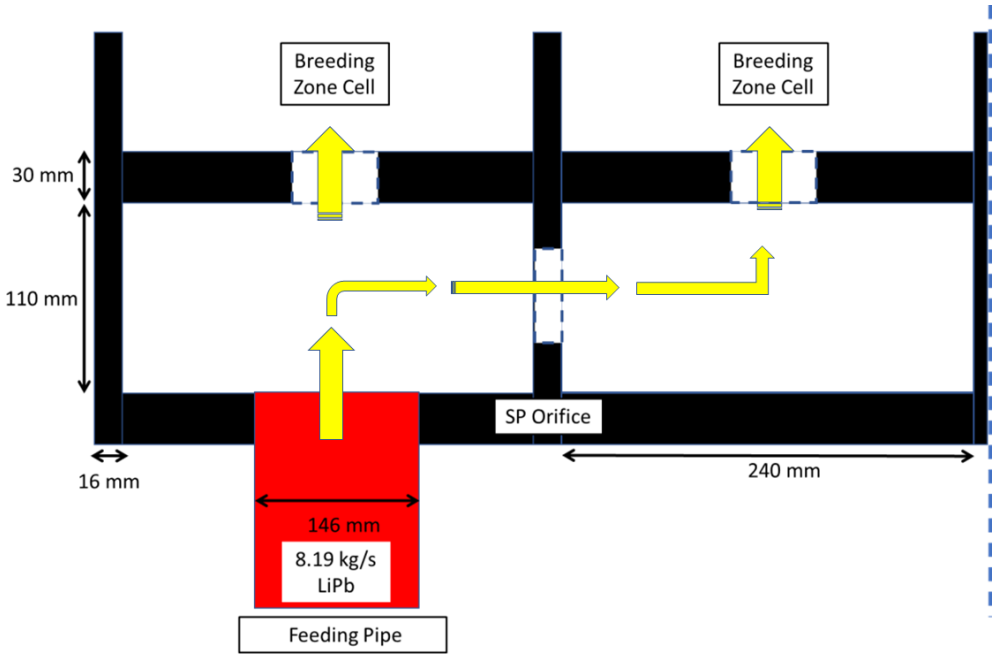

Figure 6.8. WCLL T01.B distribution manifold, radial-toroidal view. Dashed line identifies symmetry axis. Lateral channel is on the left, central channel on the right. For clarity's sake, water pipes are not shown.

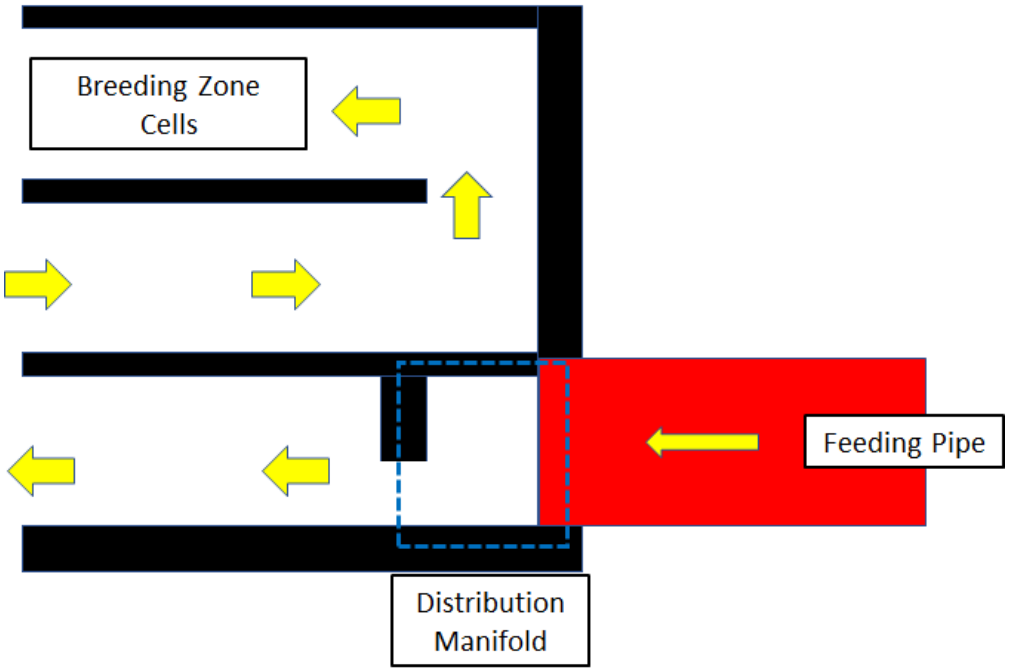

Figure 6.9. WCLL T01.B distribution manifold and BZ cells, radial-poloidal view.

2. ***Sudden contraction and expansion*** through the BZO connecting lateral channel and BZ

Similarly, the hydraulic path in the DM central channel can be summarized as follows

1. **Sudden expansion** from feeding pipe to toroidal-poloidal manifold channel
2. **90° sharp bend** from radial to toroidal direction (//**B**)
3. **Sudden contraction** from toroidal-poloidal to poloidal-radial manifold channel
4. **Toroidal flow** from lateral to central channel, assumed as fully developed
5. **Sudden contraction and expansion** through the Stiffening Plate Orifice (SPO) connecting lateral and central channel
6. **Sudden expansion** from poloidal-radial to toroidal-poloidal manifold channel
7. ***90° sharp bend*** from toroidal to radial direction (//**B**)
8. ***Sudden contraction and expansion*** through the BZO connecting lateral channel and BZ

where the first element is in common between the flow paths. The italicized components are specific for the T01.B manifold. Regarding the lateral channel, the pressure drop estimate for the sudden contraction and expansion through the BZO is analogous to the one employed to assess the SPO: we assumed the orifice to be circular with $d_{BZO} = 100$ mm. Regarding the central channel, the element no. 6 and 7 are equivalent respectively to no. 3 and 2, and the flow through BZO can be treated in the same way adopted for the lateral channel. The same flow rate partitioning of the T01.A manifold is assumed with 41% of the flow rate allocated to the central channel and 59% to the lateral one. Pressure drop estimate for each hydraulic element is detailed in Table 6.10.

Compared with the T01.A results (see Table 6.3), the pressure drop is increased for both channels due to the intense loss caused by the cross-section variation in the BZO, respectively 46% and 27% for the lateral and central flow path. To reduce the overall pressure drop it is possible to enlarge the orifice diameter, whereas employing different size for the two flow paths can help to achieve the desired flow distribution.

The pressure drop estimate in the collection manifold follows the same methodology outlined for configuration T01.A. Similarly to what was done in Section 6.2.3, the manifold is drained by a singular DN200 pipe that it is positioned at the blanket segment center. Pressure loss in lateral and central flow paths can be estimated using the relations defined for the distribution manifold hydraulic elements in reverse order. Consequently, the pressure drop in the lateral channel is $\Delta p_{l,CM} = 92.443$ kPa, whereas for the central channel we have $\Delta p_{c,CM} = 68.28$ kPa. Compared with the T01.A results (see Table 6.6), a twofold increase is observed for the pressure loss in the T01.B central channel due to both the relative simplicity of the flow path in the T01.A configuration and heavy pressure drop in the BZO.

Table 6.9. Distribution manifold channel, configuration T01.B. The wall conductance ratios reported use the toroidal half-width as length scale. For the flow aligned with the toroidal direction, the poloidal half-width is adopted.

Channel parameters			
Toroidal length	$2a$	240	mm
Radial length	$2b$	110	mm
Poloidal length	L_{pol}	135	mm
Toroidal-Poloidal Cross Section	$A_{t,p}$	324	cm^2
Poloidal-Radial Cross Section	$A_{p,r}$	148.5	cm^2
Wall parameters			
Radial-Poloidal Stiffening Plate	$2t_{r,p}$	16	mm
Toroidal-Poloidal Stiffening Plate	$2t_{t,p}$	30	mm
Wall ratio (Radial-Poloidal SP)	c_1	0.099	
Wall ratio (Toroidal-Poloidal SP)	c_2	0.186	

Table 6.10. Pressure losses for hydraulic element in the the T01.B distribution manifold channels according to the reference feeding scheme (DN150 x2)

	Lateral channel	Central channel	
Δp_1	18.779		kPa
$\Delta p_{i,2}$	23.166	1.611	kPa
$\Delta p_{i,3}$		7.439	kPa
$\Delta p_{i,4}$		1.538	kPa
$\Delta p_{i,5}$		1.383	kPa
$\Delta p_{i,6}$		7.439	kPa
$\Delta p_{i,7}$		0.887	kPa
$\Delta p_{i,8}$		23.166	kPa
Δp_i	41.945	62.192	kPa

6.2.6 Summary for T01.A and T01.B manifolds

For each manifold component of configuration T01.A and T01.B, it is possible to define the average value from the lateral and central flow path as a representative value of the pressure drop. A comparison between the results of these configurations is outlined in Table 6.11, where it can be seen how the elimination of the spinal manifold greatly enhances the performance of T01.B, which is characterized by roughly a fourth of the pressure drop calculated for T01.A. However, the simplification of the manifold layout does not results in an overall reduced pressure drop for the blanket, as it is discussed in Section 7.3, since it forces the adoption of a convoluted flow path for the BZ.

6.3 Manifold for configuration T02 and T03

These configurations share a similar BZ layout based on long poloidal ducts where the PbLi flows only upward (i.e. T02) or downward for the back channels and then upward in the one close to the FW (i.e. T03). Consequently, the manifold layout does not vary much between the two configurations and, in particular, it

Table 6.11. Overall pressure loss in the manifold hydraulic region for configuration T01.A and T01.B, broken down by averaged component contribution.

	T01.A	T01.B	
Distribution	38.925	52.069	kPa
Spinal			kPa
• 2D flow (SL+RL)	304.87		kPa
• Obstacle	70.346		kPa
Collection	44.333	80.362	kPa
Total Manifold	458.474	132.431	kPa

is considerably simpler than the one envisioned for the configurations adopting a mostly radial BZ flow path.

In the following, the calculation methodology outlined in Section 4.3 is applied to estimate the pressure drop in T02 and T03 manifold. For the purpose of this study, two general layouts, shown in Figure 6.10 using the T02 distribution manifold as reference, are considered: a manifold tank, where a space devoid of any obstacles is created for the purpose of flow distribution (respectively, collection), and a "conservative" manifold, for which SPs divide the tank in separate channels, mirroring the BZ geometry, that requires the introduction of orifices to allow the flow distribution (respectively, collection). For each manifold model, the influence of the feeding scheme adopted (single or double pipe) is investigated to assess the more favorable configuration. In this Section, for brevity's sake the pressure drop estimate for configuration T02 is presented in an abridged version: a more detailed discussion, including the calculation procedure, can be found in Ref. [75].

6.3.1 Distribution Manifold Tank T02

Consider the distribution manifold for configuration T02, it is assumed that the stiffening plates, which define the BZ channel arrangement, can be shortened and anchored to a thick Bottom Supporting Plate (BSP) at a distance $H = 242$ mm from the blanket bottom cap. The region contained between these plates, mostly devoid of obstacles[2], is designated as the Distribution Manifold Tank (DMT). Furthermore, it is assumed that the BSP can be penetrated to create suitable orifices for the connection between BZ poloidal channels and DMT. Under these assumptions, the radial-poloidal DMT layout is described by Figure 6.10a. The BSP orifices arrangement strictly follows the BZ channel layout, which is presented in Figure 6.11. The geometrical parameters are reported in Table 6.12.

The flow path in the manifold tank depends on the specific BZ channel that it is fed. In general, the flow path can be divided in these hydraulic elements

1. **Sudden expansion** from feeding pipe to manifold tank: calculation is performed with eqs. (4.9) and (4.10) assuming k = 0.5.

2. **Two-dimensional flow in the tank**: pressure drop is calculated with

[2]No assumptions are made regarding the cooling pipe arrangement which are required for the manifold refrigeration

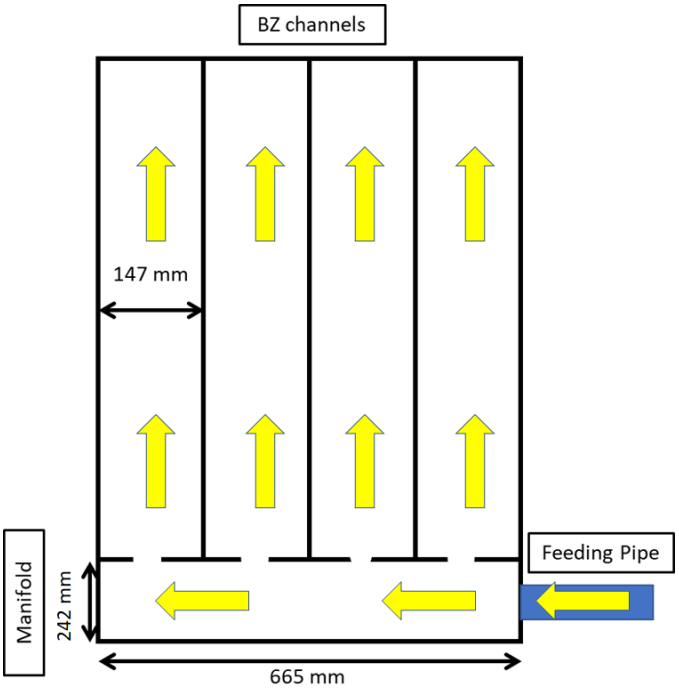

(a) Manifold Tank

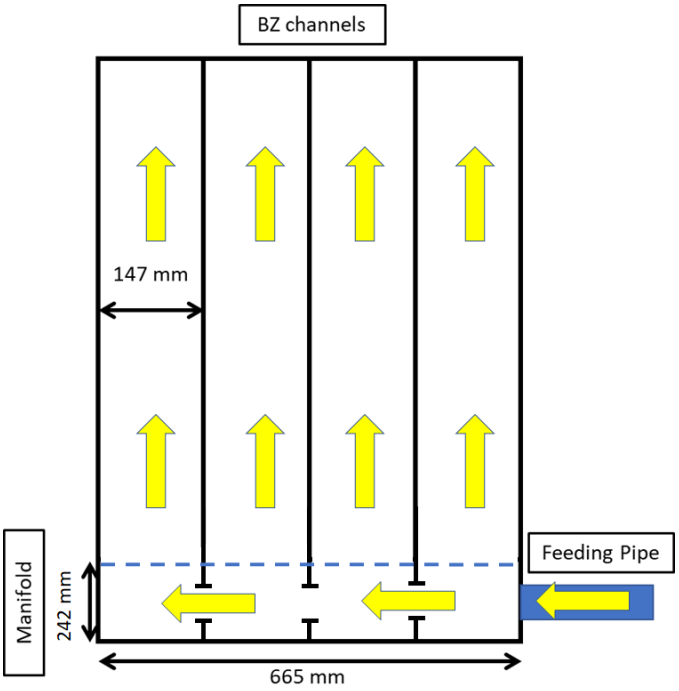

(b) Manifold with Orifices

Figure 6.10. T02 manifold layouts, radial-poloidal view. The dashed line in Figure 6.10b marks the end of the manifold region and the arrows identify the flow path

Table 6.12. T02 manifold geometrical parameters. The wall thickness for the SPs are referred to the configuration with orifices, see Section 6.3.2.

Channel parameters			
Lateral channel toroidal width	L_4	120	mm
Central channel toroidal width	$L_1/L_2/L_3$	110	mm
Poloidal height	H	242	mm
Back channel radial width	R_1	167	mm
Front channel radial width	$R_2/R_3/R_4$	147	mm
Wall parameters			
Radial-Poloidal Stiffening Plate	$t_{r,p}$	16	mm
Toroidal-Poloidal Stiffening Plate	$t_{t,p}$	19	mm
First Wall/Bottom Supporting Plate		25	mm

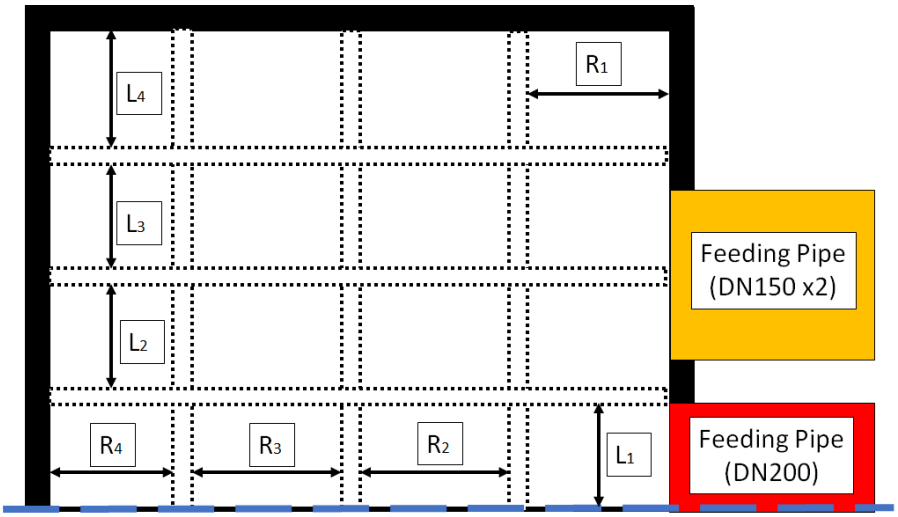

Figure 6.11. T02 manifold tank layout, radial-toroidal view. The dotted lines mark the SPs position in the BZ, i.e. above the BSP. Dashed line identifies a symmetry axis. DN200 feeding pipe refers to the single feeding scheme, DN150x2 to the double one. Dimensions reported in Table 6.12.

eqs. (4.4) and (4.8) and, depending on channel position, it includes contributions from both *toroidal* and *radial*-aligned fully developed flow

3. **90° sharp bend** from manifold tank to poloidal direction ($\perp$ **B**)

4. **Sudden contraction** from equivalent toroidal-poloidal manifold channel to BZ channel

5. **Sudden contraction and expansion** through the BSP orifice connecting manifold tank and associated BZ channel; the orifice is circular and has a diameter such that its cross-section in 50% of the BZ channel.

For the arbitrary BZ channel $C_{i,j}$, it should be noted that hydraulic element no. 1, 3, 4, and 5 are not dependent by the specific BZ channel considered (i.e they are invariant with the distribution flow path), as opposed as what happens for no.

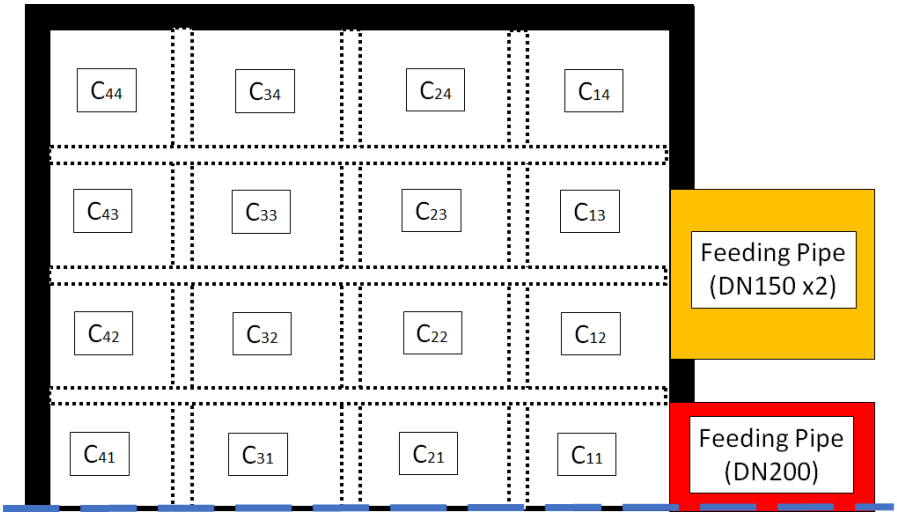

Figure 6.12. Calculation grid for pressure drop estimate due to the flow distribution in the T02 manifold tank. For the generic channel $C_{i,j}$, the index i refers to the grid (i.e. toroidal position) column and j to the grid row (i.e. radial position). Channel dimensions are reported in Table 6.12.

2, which is determined by the channel position in the calculation grid presented in Figure 6.12. Consequently, the pressure drop for an arbitrary channel will be composed of a fixed term and a variable term

$$\Delta p_i = \Delta p_f + \Delta p_{2D} \tag{6.28}$$

where the fixed term can be expressed as $\Delta p_f = \Delta p_1 + \Delta p_3 + \Delta p_4 + \Delta p_5$, for which the determination of each term is straightforward employing the relations described in Section 4.3.2.

Conversely, the determination of the variable pressure drop term is more complicated. The channel-dependent two-dimensional pressure drop can be described by the relation

$$\Delta p_{2D} = \nabla p_T \cdot \Sigma_i L_i + \nabla p_R \cdot \Sigma_i R_i \tag{6.29}$$

with ∇p_T and ∇p_R being the pressure gradient for, respectively, the toroidal and radial-aligned flow taking place in suitably oriented manifold equivalent channels, whereas $\Sigma_i L_i$ and $\Sigma_i R_i$ stand for total flow length in the toroidal and radial direction that the flow must travel to reach the BZ channel position.

In general, the pressure gradient is not uniform but rather a function of the stream-wise position, since it is evident that when the flow advances along the toroidal (or radial) length a part of the mass flow rate is redirected toward the BZ poloidal channels, thus resulting in a reduced mean velocity in the equivalent channel and, in turn, pressure gradient. For the single pipe feeding scheme, the flow rate variation in the toroidal direction for the equivalent radial-poloidal manifold

Table 6.13. Fixed pressure drop term, broken down for each hydraulic element contribution, of the T02 manifold tank. Please note, that the term due to the sudden expansion from the feeding pipe to tank depends by the feeding scheme adopted.

Δp_i	kPa	
	Single FP	Double FP
1: Expansion to Tank	25.144	16.388
3: 90°bend $\perp$ **B**	0.163	
4: Contraction to BZ channel	0.942	
5: BSP Orifice	3.037	
Δp_f	29.287	20.531

tank channel can be approximated with the step-like function

$$\Gamma(L) = \begin{cases} \Gamma_{OB}/2 & \text{for } L \leq L_1/2 \\ \Gamma_{OB}/2 \cdot 3/4 & \text{for } L_1/2 \leq L \leq 3/2L_1 \\ \Gamma_{OB}/2 \cdot 1/2 & \text{for } 3/2L_1 \leq L \leq 5/2L_1 \\ \Gamma_{OB}/2 \cdot 1/4 & \text{for } 5/2L_1 \leq L \leq 3L_1 + L_4/2 \end{cases}$$

where the toroidal length L is the independent variable and, to simplify the notation, $L_1 = L_2 = L_3$ (see Table 6.12). The law for the flow rate variation in the radial direction for the equivalent toroidal-poloidal manifold tank channel can be obtained by substituting R with L in the relation presented and remembering that $R_2 = R_3 = R_4$ (see Table 6.12). Similar relations can be written also for the double pipe feeding scheme: for instance, the toroidal flow rate law is going to be composed by only two terms, neglecting the different cross-section of the upper and lower flow path. Finally, to calculate the pressure gradient, a proper equivalent duct must be defined: for the toroidal-aligned flow we assume $2a = H$ and $2b = R_1 + 3R_2 + 3t_{t,p}$, whereas for the radial-oriented one we will have $2a = 3L_1 + L_4 + 3t_{r,p}$ and $2b = H$. A uniform wall thickness, $t = 25$ mm, is assumed to determine the wall conductance ratio with eq. (4.5). The 3D pressure drop for the sudden expansion from the feeding pipe, the bend toward the poloidal direction, and the flow in the BSP orifice are calculated according to the procedure detailed in Section 4.3.2.

Assuming the average toroidal field intensity $B_{tor} = 4.87$ T and the maximum for the poloidal component $B_{pol} = 1.4$ T, the manifold tank pressure drop estimates for both the single and double feeding pipe scheme are collected in Tables 6.13 and 6.14. The pressure drop for the BZ channel $C_{i,j}$, which belongs to the toroidal i-column and radial j-row in Figure 6.12, is obtained through the reformulation of eq. (6.28)

$$\Delta p(C_{i,j}) = \Delta p_f + \Delta p_{i,j} \tag{6.30}$$

For both the single and double feeding pipe scheme, the invariant pressure drop term is the dominant one, accounting from 80% to 96% of the total pressure drop. In particular, the higher pressure drop contribution is from the feeding pipe expansion; a phenomenon that it is not likely to change even for more accurate estimations and that accounts for all the difference in the pressure drop estimate between the two feeding schemes. For the single feeding pipe the channel pressure drop is in the

Table 6.14. Two-dimensional pressure drop estimate (expressed in kPa) for the T02 manifold tank calculated with eqs. (4.4) and (4.5). The radial flow term S_i is equivalent for each BZ channel placed on the i-column in Figure 6.12, and, similarly, for the toroidal flow term regarding the channel on the j-row.

Radial flow (S_i)	S_1		S_2		S_3	S_4
	1.211		1.439		0.959	0.452
	Single FP				Double FP	
Toroidal flow (T_j)	T_1	T_2	T_3	T_4	$T_{1\div4}$	
	0.092	0.157	0.105	0.055	0.052	
$\Delta p_{i,j}$	$\sum_{i=1}^{i} S_i + \sum_{j=1}^{j} T_j$					

range $\Delta p(C_{i,j}) = 30.56 \div 34.70$ kPa, whereas for the double feeding pipe falls in the range $\Delta p(C_{i,j}) = 21.794 \div 25.638$ kPa. For the former scheme, C_{11} and C_{44} are the channels featuring, respectively, the minimum and maximum pressure loss. For the double feeding pipe a small reduction of the pressure imbalance among the channels is observed due to the feeding scheme reducing the toroidal length traversed: the minimum pressure loss is found at C_{12} and C_{13}, whereas the maximum is calculated in C_{41} and C_{44}.

This manifold configuration is characterized by relatively small pressure losses due to the large size of the proposed tank and, in turn, of the equivalent channels employed for the estimation of the 2D pressure drop term. Even the sudden contraction/expansion through the BSP orifice is not particularly expensive: since the opening is sized assuming that it covers 50% of the BZ poloidal channel cross-section, which results in $d \approx 100$ mm, around 38% of the BSP surface is available for the flow. A reduced cross-section for the orifice (i.e. $\approx 20\%$ of BZ channel cross-section) will increase the mechanical stability of the BSP at the price of slightly increased pressure drop ($5 \div 8\%$).

Setting aside the BSP penetration problem, the practical realization of the proposed manifold tank must assess two more pressing issues. First, the mechanical stability of the blanket must be ensured for the in-box LOCA, which means that the bottom cap must withstand an over-pressurization scenario for 18 MPa. At the current state of the design, it is not clear if the weakening of the bottom structure of the blanket due to the shortening of the stiffening plates can be compensated by an opportunely cap reinforcement and, thus, detailed thermo-mechanical analyses involving dynamic and static simulations are required to assess the feasibility of the proposed configuration.

The second important issue is related to the extension of the manifold region close to the first wall: the intense neutronic heating in this region cannot be underestimated and, therefore, the BZ cooling system must ensure also the manifold refrigeration. Coupled thermal-hydraulics/MHD analyses, like the one performed for the T02 BZ in Chapter 11, are required to investigate this problem, which is a daunting task due to the manifold complexity, even when the heat transfer phenomena are not considered. Moreover, the cooling system layout will introduce several obstacles in the tank, curtailing the free space available for the flow distribution and, possibly,

sensibly increasing the total channel pressure drop even from the quite conservative figure presented in this Section.

6.3.2 Distribution Manifold with Orifices T02

If the stiffening plate arrangement must be preserved in the manifold to ensure the mechanical stability of the blanket, suitable orifices must be envisioned on the SPs to allow the flow distribution to the BZ poloidal channels. Compared with the layout discussed in Section 6.3.1, the flow path to distribute the PbLi to each BZ channel is more straightforward, since it is clearly guided by the structural elements, as it can be seen in Figure 6.13, where the flow map for the two feeding schemes considered is presented. The manifold geometric parameters are unchanged and reported in Table 6.12, for which the poloidal height H does not anymore specify a solid boundary, but it is the fictitious height of the manifold channels that, otherwise, could be considered infinitely extended in the poloidal direction, since they are coincident with the bottom section of the BZ channels. The toroidal and poloidal magnetic field intensity are $B_{tor} = 4.87$ T and $B_{pol} = 1.4$ T.

For the arbitrary channel $C_{i,j}$ (defined in the same way as described in Section 6.3.1), the flow in the manifold is composed by several hydraulic elements

1. **Sudden expansion** from feeding pipe to manifold tank: calculation is performed with eqs. (4.9) and (4.10) assuming k = 0.5.

2. **Two-dimensional flow in the tank**: pressure drop is calculated with eqs. (4.4) and (4.8) and, depending on channel position, it includes contributions from both *toroidal* and *radial*-aligned fully developed flow

3. **90° sharp bend** from manifold to poloidal direction ($\perp$ **B**)

4. **Sudden contraction** from equivalent toroidal-poloidal manifold channel to BZ channel

5. **Sudden contraction and expansion** through n orifices on the Radial-Poloidal SP

6. **Sudden contraction and expansion** through m orifices on the Toroidal-Poloidal SP.

7. **90° bend** from radial to toroidal direction (//**B**)

8. **90° bend** from toroidal to radial direction (//**B**)

The hydraulic elements no. 1, 2, 3, and 4 are analogous to the one discussed for the manifold tank and can be estimated according to the methodology presented in Section 6.3.1, whereas no. 5, 6, 7, and 8 are specific for the present configuration. Following the reasoning employed for the manifold tank, the pressure drop for the arbitrary channel can be split in a term invariant with position (i.e. flow path) and two variable ones

$$\Delta p(C_{i,j}) = \Delta p_f + \Delta p_A(C_{i,j}) + \Delta p_B(C_{i,j}) \tag{6.31}$$

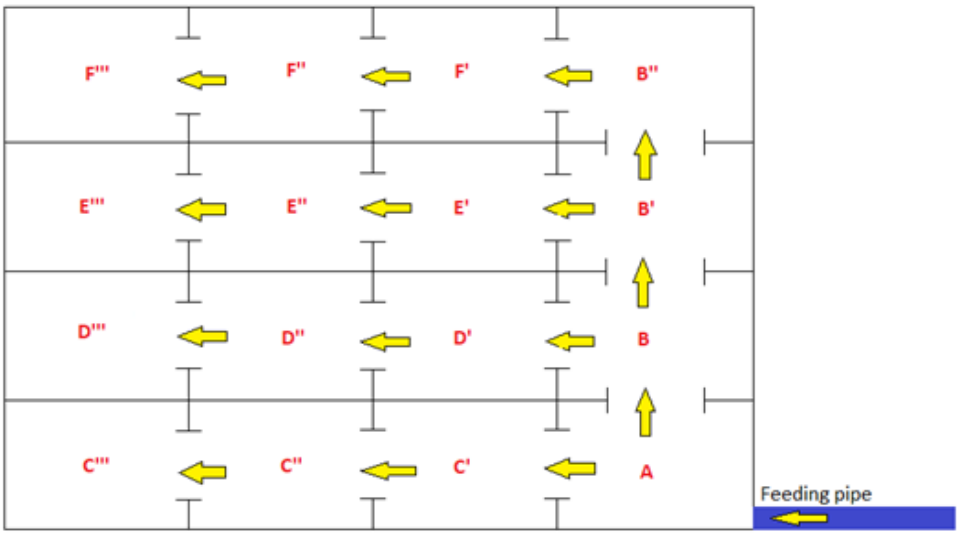

(a) Single feeding pipe

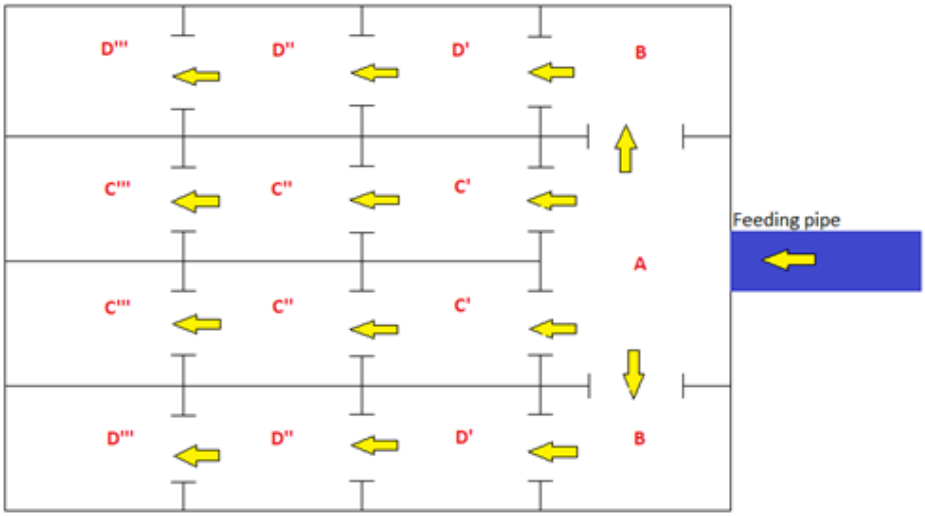

(b) Double feeding pipe

Figure 6.13. T02 manifold with orifices layout, radial-toroidal view [75]. Channel dimensions and other geometrical parameters reported in Table 6.12 apply also for this configuration

Table 6.15. Two-dimensional pressure drop estimate in T02 manifold with orifices (in kPa) calculated with eqs. (4.4) and (4.5). Radial flow term S_i is equivalent for each BZ channel placed on the i-column in Figure 6.13, and, similarly, for the toroidal flow term regarding the channel on the j-row.

Radial flow (S_i)	S_1 1.564		S_2 2.473		S_3 1.649	S_4 0.778
	Single FP				Double FP	
Toroidal flow (T_j)	T_1 0.298	T_2 0.513	T_3 0.342	T_4 0.178	$T_{1\div4}$ 0.171	
$\Delta p_A(C_{i,j})$	$\sum_{i=1}^{i} S_i + \sum_{j=1}^{j} T_j$					

The invariant term Δp_f is completely analogous to the one calculated for the manifold tank, with the exception of the term due to the orifice between the tank and the BZ channel. Referring to the estimates and labeling reported in Table 6.13, the invariant term can be computed according to the expression

$$\Delta p_f = \Delta p_1 + \Delta p_3 + \Delta p_4 \tag{6.32}$$

which, of course, it is still dependent on the feeding scheme considered through the pressure loss for the expansion from the feeding pipe (Δp_1).

The variable term $\Delta p_A(C_{i,j})$ is related to the fully developed flow in toroidally and radially aligned manifold channels and is very similar to the analogous term computed for the manifold tank, the main difference being in the geometric parameters for the ducts that carry the flow. Referring to Table 6.12, the duct considered for the toroidally aligned flow has $2a = H$ and $2b = R_1$, whereas the duct for the radially aligned flow is characterized by $2a = L_1$ and $2b = H$. For the former, a uniform wall thickness $t = 25$ mm is considered to estimate the wall conductance ratio with eq. (4.5), whereas for the latter is assumed $t = 9.5$ mm. Under these assumptions, this pressure drop term can be calculated for the arbitrary channel $C_{i,j}$ employing the data collected in Table 6.15.

The channel-dependent term $\Delta p_B(C_{i,j})$ is related to the 3D pressure drop due to the flow through SP orifices and bends in the plane of the magnetic field B_{tor}. Regarding the orifice piercing the toroidal-poloidal SP (labeled OR), the opening is assumed to have a cross-section equal to 25% of the toroidal-poloidal channel. Similarly, for the orifice on the radial-poloidal SP (called OT), the opening is assumed to have a cross-section equal to 40% of the radial-poloidal channel. Under these assumptions, this pressure drop term can be calculated for the arbitrary channel $C_{i,j}$ employing the data collected in Table 6.16.

Finally, the pressure drop associated to the flow distribution to every $C_{i,j}$ channel is obtained from eq. (6.31). For the single feeding pipe, the pressure drop range is $28.113 \div 64.988$ kPa, whereas for the double feeding pipe we have $19.228 \div 47.765$ kPa. The channels associated with the minimum and maximum pressure loss are the same identified in Section 6.3.1 for the manifold tank due to the very similar flow map.

The double feeding pipe scheme simplifies the flow distribution and it is associated with lower pressure losses compared with the single pipe scheme: similarly to what

Table 6.16. Orifice and bend pressure drop terms in T02 manifold with orifices (expressed in kPa). Flow paths for each BZ channel $C_{i,j}$ are presented in Figure 6.13. OR_i refers to the orifice on the toroidal-poloidal SP (transverse to the radial direction), OT_j to the orifice on the radial-poloidal SP (transverse to the toroidal direction).

Toroidal-Poloidal SP (OR_i)	OR_1	OR_2	OR_3	OR_4
	0	10.043	6.696	3.348
Radial-Poloidal SP (OT_j)	Single FP			Double FP			
	OT_1	OT_2	OT_3	OT_4	OT_1	OT_2	OT_3	OT_4
	0	2.130	1.420	0.710	0.710	0		0.710
	If $j = 1$	If $j \neq 1$	If $j = 1, 4$	If $j = 2, 3$
Bend (radial→toroidal) (BT_j)	0	5.892	1.964	0
Bend (toroidal→radial) (BR_j)	0	0.705	0.705	0
$\Delta p_B(C_{i,j})$	$\sum_{i=1}^{i} OR_i + \sum_{j=1}^{j} OT_j + BR_j + BT_j$			

was observed for the manifold tank case, the latter is characterized on average by 40% pressure drop increment. The passage through orifices is very expensive, especially for the toroidal-poloidal SPs, and the invariant pressure drop term has a lower incidence on the channels far from the manifold inlet ($\approx 30 \div 40\%$) compared with the ones close to it ($\approx 90\%$). This phenomenon leads to relevant pressure imbalance among the channels that must be counteracted to ensure a uniform flow distribution. Of course, this issue can be solved by iterating on the manifold design to achieve the optimized distribution of orifice sizes to meet the flow distribution requirement, but uncertainties about the pressure drop estimate for small orifices, i.e. dominated by the inertial regime, and the effect of the electromagnetic coupling among the channels suggest that extensive 3D CMHD simulations will be required. Regarding the manifold cooling issue, this configuration does not seem to bring any significant advantage compared with the tank. Conversely, the pipe layout is further complicated due to the necessity of working around the SP arrangement instead of in a space devoid of obstacles. The pressure drop increase from the flow around obstacles may be even higher than in the manifold tank since it is reasonable to foresee that, to avoid further weakening of the SP from additional penetrations, the cooling pipes will be routed through the orifices already envisioned for the PbLi flow distribution. In conclusion if the SP arrangement is preserved, the T02 distribution manifold performances are degraded due to more uneven flow distribution and a pressure drop 40% average increase. Pending the thermo-mechanical assessment of the layout structural stability, the tank configuration with the double feeding pipe scheme is assumed as T02 distribution manifold reference for the analysis purpose.

6.3.3 Collection Manifold Tank T02

According to the top-point draining scheme, the T02 Collection Manifold is placed at the blanket top, close to the boundary with the inboard blanket, and the PbLi is removed from it by a single DN200 pipe. The manifold is modeled according to the tank approach described in Section 6.3.1. Due to the assumptions made to estimate the pressure drop in the distribution manifold, the pressure loss in this component

can be calculated employing the same procedure outlined in Section 6.3.1 just by reversing the order of the flow hydraulic elements in eq. (6.30). It should be noted that the same reasoning is applicable for a manifold where the SP arrangement is preserved: for brevity's sake, only the results for the reference case are going to be reported in this Section.

To account for the placement in the blanket top part, the intensity of the toroidal and poloidal magnetic field are taken as $B_{tor} = 5.46$ T and $B_{pol} = 0.909$ T. The pressure drop range in the manifold is $38.374 \div 43.274$ kPa, where the position of the minimum and maximum pressure loss channels is analogous to the one for the distribution manifold.

6.3.4 Manifold T03

The configurations T02 and T03 share the same SP arrangement and, therefore, BZ channel layout. This design choice allows to treat the pressure drop in the manifold region employing the same procedure described in Section 6.3.1 with only some small modifications to account for the differences between the configurations. The most characteristic feature of the T03 configuration is found in the BZ, where the PbLi flows downward in the back channels, executes a 180° turn at the blanket bottom and proceeds upward in the channels close to the FW. This flow path allows to realize a compact manifold region at the blanket top in which the distribution and collection tanks are integrated with each other, as it is possible to see in Figure 6.14a, where the T03 manifold region is depicted. For the purpose of this analysis, the study will be limited to a manifold region adopting the tank approach but, due to the substantial similarities with the T02 configuration, the discussion detailed in Section 6.3.2 could be extended straightforwardly for T03. The effect of the cooling pipes on the flow features and pressure drop is neglected, consistently with the methodology employed in Sections 6.2, 6.3.1 and 6.3.2.

Distribution Manifold T03

The distribution manifold layout is shown in Figure 6.14b for the radial-toroidal cross-section. Recalling Figures 6.11 and 6.12, it is evident how the T03 distribution manifold can be imagined as the analogous T02 component, for which it is forbidden to distribute the flow to the channels close to the FW with the introduction of a toroidal-poloidal SP. Each BZ channel will be forced to carry a mass flow rate doubled compared with the T02 configuration and the equivalent radial-poloidal tank channel, employed to calculate the contribution from the radially aligned fully developed flow, will be shortened. Despite these modifications, the general hydraulic elements composing the flow path described by the PbLi to reach the arbitrary channel $C_{i,j}$ are equal to the one employed for the T02 manifold tank case in Section 6.3.1, as well as the geometrical parameters collected in Table 6.12.

Regarding the flow rate variation, the radial manifold channel law for the single feeding pipe scheme can be updated to the following expression

$$\Gamma(R) = \begin{cases} \Gamma_{OB}/2 & \text{for } R \leq R_1/2 \\ \Gamma_{OB}/2 \cdot 1/2 & \text{for } R_1/2 \leq R \leq R_1 + R_2/2 \end{cases}$$

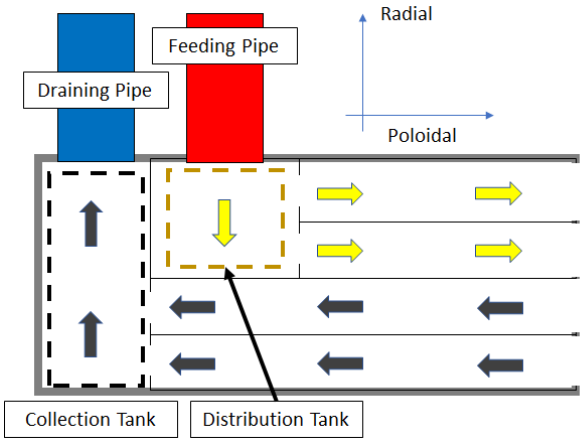

(a) Manifold layout and connection with feeding/draining pipe, radial-poloidal view

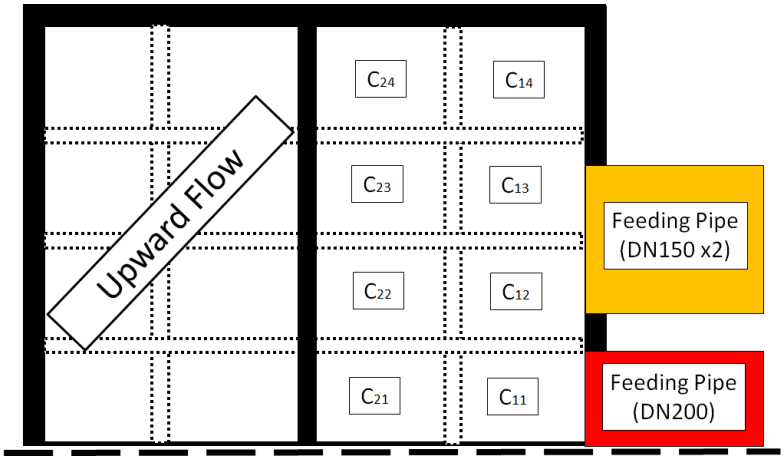

(b) Distribution manifold, radial-toroidal view

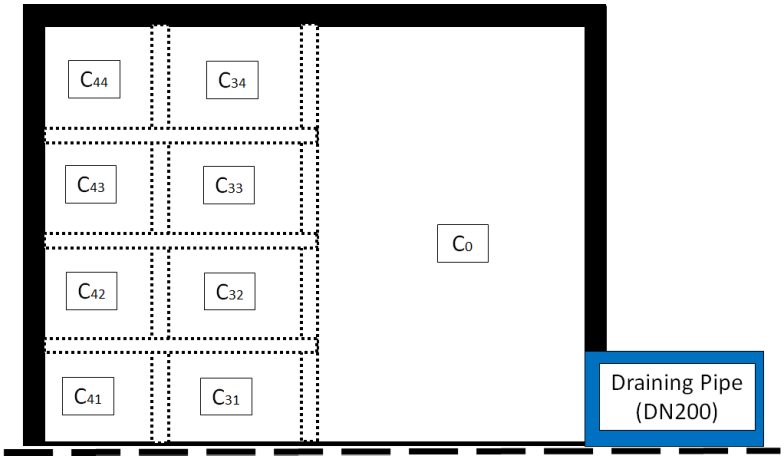

(c) Collection manifold, radial-toroidal view

Figure 6.14. T03 manifold hydraulic region. Channel dimensions and other geometrical parameters reported in Table 6.12 apply also for this configuration

Table 6.17. Fixed pressure drop term, broken down for each hydraulic element contribution, of the T03 distribution manifold. Please note, that the term due to the sudden expansion from the feeding pipe to tank depends by the feeding scheme adopted.

Δp_i	kPa	
	Single FP	Double FP
1: Expansion to Tank	31.606	20.559
3: 90°bend $\perp$ **B**	0.411	
4: Contraction to BZ channel	2.368	
5: BSP Orifice	7.636	
Δp_f	42.020	31.014

Table 6.18. Two-dimensional pressure drop estimate (expressed in kPa) for the T03 manifold tank calculated with eqs. (4.4) and (4.5). The radial flow term S_i is equivalent for each BZ channel placed on the i-column in Figure 6.14b, and, similarly, for the toroidal flow term regarding the channel on the j-row.

Radial flow (S_i)	S_1 1.522				S_2 1.604
	Single FP				Double FP
Toroidal flow (T_j)	T_1	T_2	T_3	T_4	$T_{1\div4}$
	0.069	0.120	0.080	0.041	0.040
$\Delta p_{i,j}$	$\sum_{i=1}^{i} S_i + \sum_{j=1}^{j} T_j$				

whereas the toroidal law for both feeding pipe scheme is unchanged compared with the one described in Section 6.3.1. Similarly, the equivalent radial-poloidal channel dimension is adapted to $2b = R_1 + R_2 + t_{t,p}$. Since the manifold is placed in the blanket top part, the magnetic field intensity used for the pressure drop estimate is equal to the one used for the T02 collection manifold discussed in Section 6.3.3. The pressure loss for the arbitrary BZ channel $C_{i,j}$, which belongs to the toroidal i-column and radial j-row in Figure 6.14b, is obtained through the expression

$$\Delta p(C_{i,j}) = \Delta p_f + \Delta p_{i,j} \tag{6.30'}$$

where Δp_f and $\Delta p_{i,j}$ can be calculated from the value reported in Tables 6.17 and 6.18.

For the single feeding pipe, the pressure drop range is $43.612 \div 47.812$ kPa, whereas for the double feeding pipe we have $32.575 \div 36.579$ kPa. The channels associated with the minimum are the same identified in Section 6.3.1 for both the feeding pipe schemes, whereas the maximum is located in C_{24} and C_{21}, the latter just for the double pipe. The component is characterized by the same general behavior observed for the T02 manifold tank, however the invariant pressure drop term constitutes a higher portion of the overall loss, being compromised between 87% and 97% because of the higher magnetic field and reduced contribution from the radially aligned fully developed flow. Employing a double pipe feeding scheme is also slightly less efficient since the pressure loss gain is reduced to around 32%

compared with the 38% for configuration T02.

Collection Manifold T03

The collection manifold layout is shown in Figure 6.14c and its geometrical parameters are completely analogous to the DM, listed in Table 6.12. To describe the behavior of the liquid metal in this component the only change that must be made to the distribution manifold model regards the radial law for the flow rate variation, that is updated to account for the region labeled with C_0 in Figure 6.14c

$$\Gamma(R) = \begin{cases} \Gamma_{OB}/2 \cdot 1/2 & \text{for } R \leq 3/2R_2 \\ \Gamma_{OB}/2 & \text{for } 3/2R_2 \leq R \leq R_1 + 5/2R_2 \end{cases}$$

which means that after the channel C_3j, the full flow rate is carried by the toroidal-poloidal equivalent channel. The pressure drop for the arbitrary channel can now be calculated with eq. (6.30) employing the data reported in Tables 6.17 and 6.18 with the only exception of $S_4 = 0.756$ kPa and $S_3 = 3.878$ kPa describing the radially aligned flow term.

The pressure drop range in the manifold is $45.968 \div 50.842$ kPa. C_{31} and C_{44} features the minimum and maximum pressure drop.

It should be noted how for the configuration T03 the feasibility of the manifold tank approach is probably more reasonable to assume than for configuration T02: the placement of both manifolds in the upper part of the blanket lessen the requirements for the mechanical stability of these components since the upper cap is not subjected to the whole hydrostatic pressure load of the blanket like the bottom one and could, in principle, better tolerate the enhanced stress due to the shortening of the SP. Nevertheless, thermo-mechanical analyses are required to refine the upper cap design and demonstrate the feasibility of the tank approach. For the T03 configuration, only the collection manifold is subjected to significant neutronic heating and must be refrigerated. This requirement has been partially addressed already by the blanket design, since the vertical cooling pipes required for the BZ refrigeration are going to cross the manifold region and can conceivably provide also the manifold cooling. However, the complexity of the coupled thermal-hydraulics/MHD analyses required to analyze the PbLi flow in the manifold is enhanced, even compared with the intricate problem posed by the T02 layout, due to the huge number and convoluted geometry of the cooling pipes.

6.3.5 Summary for T02 and T03 manifolds

For each manifold component of configuration T02 and T03, it is possible to define the average channel pressure drop as a representative value. A comparison between the results of these configurations is outlined in Table 6.19. The higher magnetic field intensity for the DM and the enhanced mass flow rate in the channels penalizes the performance of configuration T03, which even when compared with the T02 SP manifold, is characterized by $\approx +12\%$ in overall pressure drop. This drawback is partially compensated by less demanding assumptions for the blanket mechanical stability thanks to the less strained upper cap but even this advantage could be unreliable, if the SP manifold would be required also for T03. However, the pressure

Table 6.19. Overall pressure loss in the manifold hydraulic region for configuration T02 and T03 (single and double feeding pipe scheme), broken down by averaged component contribution. In brackets, the overall T02 pressure drop for a DM manifold with preserved SP arrangement; the same results are provided also regarding T03 for comparison.

	T02	T03 (DFP)	T03 (SFP)	
Distribution	23.716	34.577	45.712	kPa
• Distribution w/SP	33.497	41.384		kPa
Collection	40.824	48.405		kPa
Total Manifold (w/SP)	64.54 (74.321)	82.982 (89.809)	94.117	kPa

drop estimates presented in this Section neglect the cooling pipe contribution that, since the manifold requires refrigeration and for T03 is crossed by the bulk of the BZ cooling system, could sensibly affect the result.

6.4 Chapter summary

The manifold hydraulic region of T01.A shows considerable differences compared with the other configurations and is characterized by the highest pressure drop. The culprit for this behavior is the spinal manifold where high flow rate and long channel extension combine in creating unfavorable pressure losses. However, the continuous distribution scheme provides great flexibility and, in principle, could be easily adapted to different feeding schemes. Aside from the spinal manifold, configuration T01.A and T01.B share a similar configuration characterized by a compact geometry that is slightly penalizing compared with the larger and simpler T02 and T03 manifold. In turn, these configurations can be further hampered by the necessity to preserve the stiffening plate arrangement, which increases the overall pressure drop. Moreover, the estimate is affected by significant uncertainty due to the large number of orifices and inertial effects likely to manifest therein. In conclusion, even if manifold pressure loss is not the most important contribution, detailed analyses are still required to assess the flow distribution and the effect of electromagnetic coupling.

Chapter 7

Breeding zone

7.1 Introduction

The PbLi flow path in the BZ for each WCLL configuration is analyzed in this Section. In T01.A and T01.B, the PbLi flows mostly in the radial direction, but part of its path is aligned with the poloidal axis to connect regions of the same elementary cell (i.e. T01.A) or to ferry the liquid metal toward the successive one (i.e. T01.B). In T02, the flow path is aligned throughout the blanket with the poloidal axis and the PbLi creeps upward in square channels. In T03, the BZ layout is the same but the back channels carry the flow downward and a 180° bend at the blanket bottom is employed to convey the fluid to the front channels, where it flows upward. Almost everywhere, the PbLi motion in the BZ is characterized by small mean velocity ($\leq 1\ cm/s$) and it can be treated with the classic relations for the fully developed flow in electro-conductive rectangular ducts (eq. (4.4)): for T02 and T03, the poloidal magnetic field can be neglected thanks to the flow orientation, whereas in the other configurations the motion happens mostly in the radial direction and a correction factor must be specified to account for the bi-directional magnetic field. 3D effects play an important role for the determination of the overall pressure drop and are assessed as well.

7.2 Configuration T01.A

In Figure 7.1, the layout for configuration T01.A is presented. The breeding zone is formed by an elementary cell that covers the blanket segment toroidal width and is divided into six elementary channels, each one fed separately by the spinal

Table 7.1. T01.A central elementary channel geometrical parameters

Central elementary channel			
Toroidal width	$2a$	234	mm
Poloidal width	$2b$	60.5	mm
Cell poloidal height	H	135	mm
Radial length	R_1	400	mm
Bend length	R_2	150	mm
DWT diameter	d	13.5	mm
Cooling pipes number		21	
Wall parameters			
Radial-Poloidal Stiffening Plate	$2t_{r,p}$	19	mm
Toroidal-Radial Stiffening Plate	$2t_{r,t}$	12	mm
Baffle Plate	$2t_b$	2	mm
First Wall	$2t_{Fw}$	25	mm

manifold (see Section 6.2). Due to the variable width of the blanket with the poloidal coordinate, the breeding zone layout undergoes modifications in its structure very similar to the one discussed for the spinal manifold. For the purpose of this analysis, we will focus on the equatorial plane layout, which is shown in Figure 7.1a, and, in particular, on the central channel PbLi path, which is represented in Figure 7.1b. For these channels, the cooling elements are transverse to the stream-wise direction, as it is shown in Figure 7.1c, and the flow around them can be treated as discussed in Section 6.2.2[1].

The flow rate in the central channel can estimated from the total number of elementary cells in the blanket segment. If the cell poloidal height is defined as $H = 4b + 2t_b + 2t_{r,t} = 0.135$ m, the number of cells can be calculated from the blanket linear length at the first wall ($S_{fw} = 14.67$ m)

$$N_{cell} = S_{fw}/H \approx 109 \tag{7.1}$$

Since we are interested in the flow rate of the central channel in the equatorial plane cell, we can assume that the number of channels for each cell is $n = 6$ without introducing any significant error, even if in general this condition is not respected for the bottom and top blanket cells. The flow rate is expressed through the relation

$$\Gamma = \frac{\Gamma_{OB}}{n \cdot N_{cell}} \approx 0.025 \text{ kg/s} \tag{7.2}$$

From the parameters listed in Table 7.1, the average velocity in the channel is $u_0 \approx 0.18$ mm/s.

The PbLi flow path in the BZ channel can be outlined with ten hydraulic elements

1. **Sudden contraction** from SM supply leg channel to BZ Inlet Opening
2. **90° sharp bend** from poloidal to radial direction ($\perp \mathbf{B}$)
3. **Sudden expansion** from BZ Inlet Opening to channel

[1]This treatment is not valid for the lateral and external channel in where the cooling pipe are, at least partially, aligned with the flow direction.

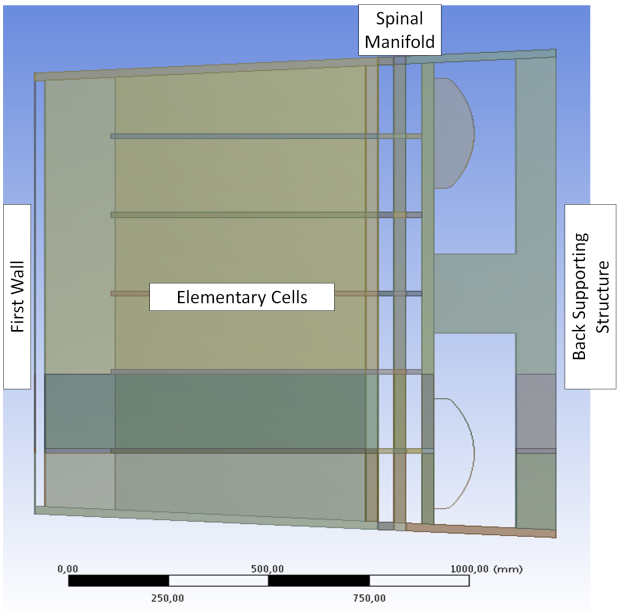

(a) Equatorial plane breeding zone, toroidal-radial view

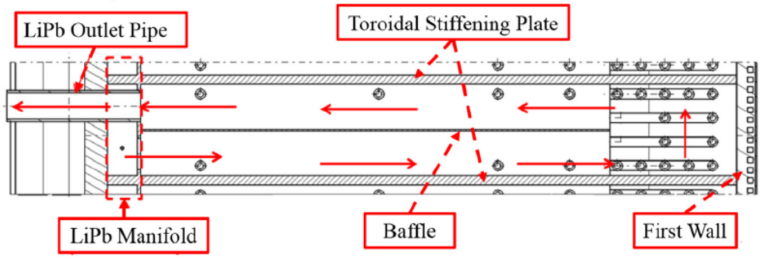

(b) Central elementary channel with PbLi highlighted, radial-poloidal view [29]

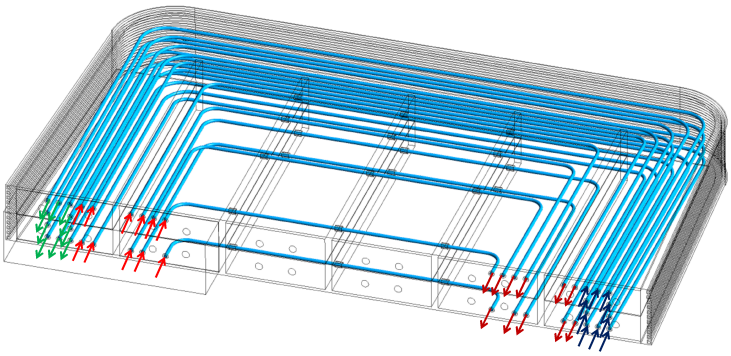

(c) Elementary cell cooling elements arrangement [22]

Figure 7.1. T01.A breeding zone layout. Channel dimensions and other geometrical parameters are reported in Table 7.1. The pipe arrangement in Figure 7.1b is not representative of the other elementary channels.

4. **Fully developed flow** in channel: this component includes also the poloidal flow in the 180° bend
5. **Flow around obstacles**: transverse to the stream-wise direction and offset from the centerline, discussed in detail in Chapter 10. The average flow path crosses 13 pipes.
6. **180° sharp bend** from radial to poloidal to radial ($\perp \mathbf{B}$)
7. **Sudden contraction** from channel to BZ Outlet Pipe
8. **Fully developed flow** in Outlet Pipe
9. **90° sharp bend** from radial to poloidal direction ($\perp \mathbf{B}$)
10. **Sudden expansion** from BZ Outlet Pipe to SM recovery leg channel

The first and last components are the ones characterized by the most intensive pressure losses due to the high expansion/contraction ratio with the SM channels. In the following, the cooling pipes influence on the flow features is assumed to be restricted to their pressure drop penalty, i.e. the flow is assumed to regain its fully developed state instantaneously after crossing the pipe. This assumption is justified by the combined effect of low velocity and strong magnetic field intensity in the channel.

Fully developed flow in the BZ channel

The MHD flow in the T01.A BZ channel was the subject of a CFD study in Ref. [29] and more details about the fluid dynamics are reported in Section 10.3.1 in the framework of the flow around obstacles. For the purpose of this study, just the main features and results will be described. The T01.A channel is characterized by walls of non-uniform thickness, therefore the liquid metal tends to reorganize on the duct cross-section in order to promote the flow features close to the least conductive wall (i.e. the baffle plate), whereas the motion close to other walls is suppressed. Moreover, the skewed magnetic field provokes the boundary layer jets detachment from the walls parallel to the magnetic field.

The problem complexity means that it cannot be easily treated employing the relations presented in Section 4.3.2. Starting from the results reported in Ref. [29], it is possible to extrapolate the pressure gradient for the BZ channel accounting for the differences in velocity and magnetic field intensity with the present case. For the channel on the equatorial plane, it is obtained that

$$\nabla p_{2D} \approx 0.150 \text{ kPa/m} \tag{7.3}$$

We can define the average flow path in the channel with the equivalent length $L = 2 \cdot (R1_1 + R_2/2) + (2b + 2t_b) \approx 1.02$ m, where the second right hand term describes the poloidal flow in the channel bend. It follows that the pressure loss term due to the fully developed flow takes the form

$$\Delta p_{2D} = \nabla p_{2D} \cdot L \approx 0.157 \text{ kPa} \tag{7.4}$$

Thanks to the PbLi abysmal velocity, this term is very small and, therefore, does not contribute significantly to the pressure balance between the BZ cells.

Connection with the Spinal Manifold

The BZ channel interface with the manifold region is composed of two connecting elements: the Inlet Opening, linked to the SM supply leg, and the Outlet Pipe, that it is connected with the SM recovery leg and, thus, crosses the other SM channel.

The Outlet Pipe is characterized by an outer diameter $d_o = 50$ mm, as it was discussed in Section 6.2.2, and, if a standard wall thickness $t_w = 3.68$ mm is employed, an inner diameter $d_i \approx 43mm$. Due to the crossing of the SM supply leg, the pipe has also a non-negligible axial length ($L = 100$ mm) and the flow inside it can be considered in fully developed state, assuming that the pipe wall is not in electrically contact with the surrounding toroidal-poloidal plate.

The Inlet Opening is basically a round orifice drilled in the toroidal-poloidal plate that separates the BZ from the SM and it can be seen in Figure 6.1. Its diameter is assumed to be equal to the internal diameter of the Outlet Pipe, i.e. $d_i \approx 43$ mm.

The sudden cross-section variation from the SM manifold to the connecting elements is the main pressure drop contribution for the T01.A BZ and can be calculated assuming as velocity and length scale the parameters of the SM channel ($u_0 = 2.23$ cm/s and $L = 3.42$ cm). Employing eq. (4.9), it follows that $\Delta p = 1.817$ kPa, a term that is valid for both the inlet opening and the outlet pipe. Similarly, it is possible to calculate the pressure drop term due to the 90° bend as $\Delta p = 0.151$ kPa.

Conversely, the cross-section variation from the connecting element to the BZ channel is less pressure loss intensive and can be calculated with eq. (4.9) assuming as velocity and length scale the average velocity ($u_{pipe} = 0.179$ cm/s) and radius of the connecting element ($u_0 = 0.18$ cm/s). Employing eq. (4.9), it follows that $\Delta p = 0.091$ kPa, a term that is valid for both the inlet opening and the outlet pipe.

Finally, the fully developed flow in the outlet pipe is calculated with eqs. (4.4) and (4.6), where $c = 0.234$, and $\Delta p_{2D,pipe} = 0.323$ kPa. It should be noted that this estimate is not necessarily conservative: 60% of the outlet pipe length is inside the toroidal-poloidal SP, which can be assumed as a perfectly conductive wall, and the rest is immersed in the SM channel, electrically coupled to a cross-flow. It is unclear how the latter will affect the estimate, but if no electrical insulation is foreseen between the toroidal-poloidal SP and the outlet pipe, the two-dimensional pressure drop term increases nearly ten times to $\Delta p'_{2D} = 2.290$ kPa.

Summary

The determination of the pressure losses in the other BZ channel hydraulic elements is relatively straightforward employing the relations discussed in the previous section and it is therefore omitted. The overall pressure drop in the central channel for the BZ equatorial plane cell is presented in Table 7.2, broken down by each element contribution.

The very low velocity in the BZ channel causes limited pressure losses in this hydraulic region. Indeed, they could be neglected without significantly altering the pressure drop estimate for the whole configuration since they amount to ≈1% of the manifold pressure drop. This is not a surprising outcome, because this layout was purposefully designed to achieve the lowest possible pressure drop. BZ cells located

Table 7.2. BZ T01.A pressure loss, broken down for each hydraulic element contribution and expressed in kPa.

Δp_i		$\Delta p_i/\Delta p(\%)$
SM→Inlet Opening	1.968	42.3
• XS variation	1.817	
• Bend	0.151	
Inlet Opening→Channel	0.091	1.95
BZ channel	0.226	4.84
• 2D flow	0.157	
• Bend	0.044	
• Pipes	0.025	
Channel→Outlet Pipe	0.091	1.95
Outlet Pipe→SM	2.291	49.1
• 2D flow	0.323	
• Bend	0.151	
• XS variation	1.817	
Δp_{BZ}	4.667	100

toward the bottom and top of the blanket segment are exposed to a stronger magnetic field intensity but, even in their case, the maximum pressure drop $\Delta p_{BZ} \approx 11.5$ kPa never exceeds the 3% of the manifold pressure drop. Electromagnetic coupling effects should not affect this estimate, but could cause the appearance of localized flow reversals in the corner bordering two adjacent counter-flowing channels [83]. Since no significant imbalance can be attributed to the BZ flow path, it is even more important to carefully regulate the SM manifold pressure losses to achieve an uniform flow distribution.

7.3 Configuration T01.B

The breeding zone of configuration T01.B is an updated version of T01.A where the elementary cells are interconnected and the PbLi has to flow through all of them, being distributed at the bottom and collected at the top of the blanket thanks to the elimination of the spinal manifold. Due to this design change, T01.B is composed of continuous channels that wind through the whole blanket linear length, which causes a huge increase in the channel mean velocity compared with T01.A in addition, of course, to the length of the PbLi hydraulic part.

To estimate the pressure drop in the T01.B breeding zone, the following assumptions are made with regard to T01.A

- The baffle plate, separating the inlet and outlet duct, is removed from the T01.A channel to form a continuous duct, which is the T01.B baseline channel

- Every other toroidal-radial SP is shortened to leave a connection between contiguous channel close to the first wall and equal in width to the T01.A bend. Those two interconnected channels constitute the T01.B elementary cell

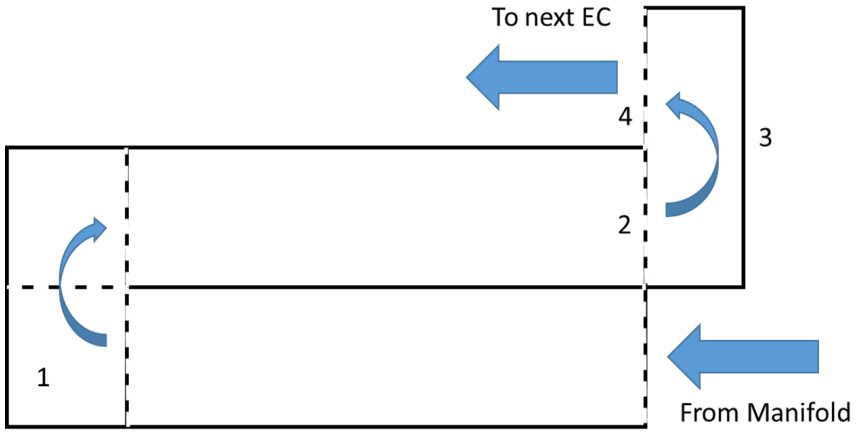

Figure 7.2. T01.B breeding zone, hydraulic element outline. Radial-poloidal view

- The spinal manifold region is employed as the connection element (turn-back) between successive elementary cells
- The pipe layout is maintained without any modifications

The general layout of the T01.B breeding zone is presented in Figure 7.2, whereas the geometrical parameters are listed in Table 7.3. Due to the updated cell poloidal height, the number of cells composing the blanket is reduced from 109 in T01.A to 54 in T01.B. If we assume that the BZ is composed of six channels for all its extension, the flow rate in the channel would be $\Gamma_i = \Gamma_{OB}/6 = 2.73$ kg/s. From the channel geometrical parameters, it follows that the channel average velocity would be $u_0 = 9.7$ mm/s, which is more than fifty times the value for configuration T01.A. Since the blanket toroidal width is not uniform, the BZ is actually composed of four channels in the bottom: two lateral and two central, characterized by a flow rate equal to, respectively, 59% and 41% to the inlet one; mirroring the manifold structure described in Section 6.2.2. The lateral channel branch in two at ≈ 4 m of the blanket linear length and the six-channel layout is maintained until 11.76 m when the later channels merge again. It follows that the average velocity for the lateral and central channel at the BZ inlet is, respectively, $u_l = 1.67$ cm/s and $u_c = 1.16$ cm/s.

Beside the fully developed flow, the PbLi flow path in the BZ channel can be described with 5 hydraulic elements

1. **180° sharp bend** from radial to poloidal to radial
2. **Sudden contraction** from BZ channel to turn-back channel
3. **180° sharp bend** from radial to poloidal to radial
4. **Sudden expansion** from turn-back channel to BZ channel
5. **Flow around obstacles**: transverse to the stream-wise direction and offset from the centerline, discussed in detail in Chapter 10. The average flow path crosses 26 pipes.

Table 7.3. T01.B central elementary channel geometrical parameters.

Elementary channel			
Toroidal width	$2a$	234	mm
Poloidal width	$2b$	123	mm
Cell poloidal height	H	270	mm
Radial length	R_1	400	mm
Bend length	R_2	150	mm
Turn-back length	R_3	110	mm
DWT diameter	d	13.5	mm
Cooling pipes number		42	
Wall parameters			
Radial-Poloidal Stiffening Plate	$2t_{r,p}$	19	mm
Toroidal-Radial Stiffening Plate	$2t_{r,t}$	12	mm
First Wall	$2t_{Fw}$	25	mm

The cooling pipes influence on the flow features is assumed to be restricted to their pressure drop penalty, i.e. the flow is assumed to regain its fully developed state instantaneously after crossing the pipe. This assumption is justified by the strong magnetic field intensity in the channel.

Fully developed flow in the BZ channel

The BZ channel for configuration T01.B is characterized by two pair of walls of different thickness: the radial-poloidal stiffening plates, across the toroidal direction, and the toroidal-radial ones across the poloidal direction. The simplified channel layout allows to apply eq. (4.8) to calculate the pressure coefficient in eq. (4.4). A correction factor $\lambda_\alpha = 1.7$ is employed to account for the bi-directional magnetic field, which for the equatorial plane has an inclination $\alpha = 16°$, as suggested by Kirillov et al. [44]. The corrected pressure coefficient takes the form

$$k_p = \lambda_\alpha \cdot \left[1 + c_{r,p}^{-1} + \frac{a}{6b}\left(2c_{r,t}^{-1}\right)\right]^{-1} \tag{7.5}$$

where $c_{r,p} = 0.1$ and $c_{r,t} = 0.075$. Since the BZ channel is extended for all the blanket poloidal length, the gradient for the fully developed flow is not uniform but must be discussed with the same procedure outlined for the spinal manifold channel in Section 6.2.2. As it is possible to see in Figure 7.3, the pressure gradient trend is very similar to the one for the spinal manifold channel. The average pressure gradient in the breeding zone is calculated as $\nabla\bar{p}_c = 12.394$ kPa and $\nabla\bar{p}_l = 15.951$ kPa. Defining the average flow path in the BZ cell as $L = 2 * R_1 + R_2 + R_3 + H = 1.34$ m, the overall 2D pressure drop for the BZ channel is

$$\Delta p_{c,2D} = \nabla\bar{p}_c \cdot L \cdot N = 896.5 \text{ kPa} \tag{7.6}$$

$$\Delta p_{l,2D} = \nabla\bar{p}_l \cdot L \cdot N = 1154 \text{ kPa} \tag{7.7}$$

where N = 54 is the number of BZ elementary cells. The impact of the channel windy path inside the BZ is already evident by the baseline pressure drop term, which for the lateral channel already exceeds 1 MPa.

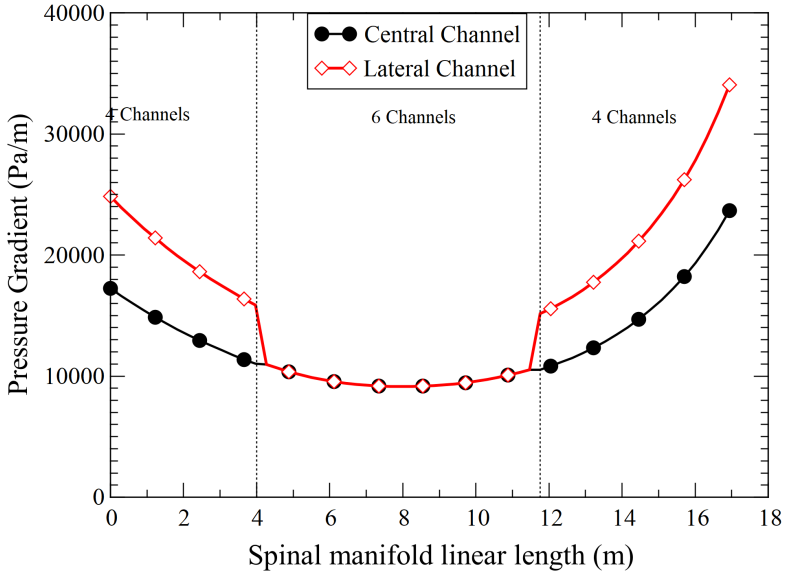

Figure 7.3. Pressure gradient in the T01.B BZ channels plotted versus the blanket spine coordinate

3D pressure drop

To estimate the pressure drop in the other elements of the PbLi hydraulic path in the BZ channel, we are going to focus the attention on the central channel elementary cell, for which the 2D pressure gradient is equal to the average one. In this cell, we consider the toroidal field as equal to the average value for the first wall area (B_{tor} = 4.19 T) for the calculation of the first 180° sharp bend, whereas for the other elements we consider the average value for the back supporting structure B_{tor} = 3.91 T. Contribution from the cooling pipes is obtained through the application of eq. (10.14), whereas the bends and sudden variation in the cross-section are estimated according to the relations described in Section 4.3.2.

For the first 180° sharp bend, velocity and length scale are $u_0 = 1.19$ cm/s and $L = 8.06$ cm, thus $\Delta p = 0.549$ kPa. Cross-section variations between the BZ channel and the turn-back channels are equivalent and estimated employing $u_0 = 1.33$ cm/s and $L = 7.48$ cm. From eq. (4.9), it follows that $\Delta p = 3.577$ kPa. Regarding the second 180° sharp bend, velocity and length scale are the same, thus $\Delta p = 0.497$ kPa. The pipe pressure penalty is $\Delta p = 3.365$ kPa.

The overall pressure drop from 3D effects is $\Delta p_{3D} = 11.565$ kPa that, compared with the average cell 2D pressure drop $\Delta p_{2D} = 17.318$ kPa, gives a relative ratio $\psi = \Delta p_{3D}/\Delta p_{2D} = 0.67$. This parameter describes the relative importance of the 3D effects for the "average cell" and, since this cell is characterized by the average magnetic field value, it can be taken as a representative value for the 3D pressure drop on the whole channel extension. Indeed, since 3D pressure drop tends to have a weaker dependence on the magnetic field intensity compared with the fully developed

term this ratio can be considered as conservative with regard to the elementary cells close to the bottom and top part of the blanket.

Summary for T01.B breeding zone

Since we have established the relative ratio between three-dimensional and two-dimensional pressure drop and we know the value of the latter, it is possible to calculate the overall pressure drop for the T01.B BZ channel

$$\Delta p_c = \Delta p_{c,2D} + \psi \cdot \Delta p_{c,2D} = 1545 \text{ kPa} \tag{7.8}$$

$$\Delta p_l = \Delta p_{l,2D} + \psi \cdot \Delta p_{l,2D} = 1985 \text{ kPa} \tag{7.9}$$

Conversely to the other blanket configurations, T01.B is characterized by a very high pressure drop in the breeding zone, mostly because of the tortuous hydraulic path ($L > 70$ m) described by the liquid metal. Accounting for the pressure losses in the manifold, the lateral channel is above the maximum allowable pressure drop (2000 kPa) and even the central channel is close to that limit. A possible strategy to limit the pressure drop for this configuration is to reduce the velocity in the BZ channel by further merging together adjacent channels. However, this could have the drawback of affecting the mechanical stability of the blanket.

7.4 Configuration T02

The breeding zone layout for configuration T02 is shown in Figure 7.4. The BZ channels are long poloidal duct, where the PbLi flows upward, and no complex geometrical elements, such as bends or variation of cross-section, are present, therefore they can be treated as electro-conductive ducts where the flow is fully developed according to eqs. (4.4) and (4.5). Since the ducts are aligned with the poloidal direction, only the toroidal field is transverse to the flow and must be considered for the pressure drop estimate. In general, the magnetic field is not uniform and a gradient is present among the back and front channels, where the field is strongest. However, the gradient is quite small (i.e.$\partial_x \tilde{B} \ll 1$) and is compensated by the different linear length and cross-section of the channels, with both parameters recording higher values for the back channels. Under these assumptions, the only 3D flow contribution to the pressure drop is from the flow around the horizontal U-pipes employed for the BZ refrigeration: this case is discussed in more detail in Chapter 11, where the mixed convection flow around the cooling element for the FW channel is analyzed.

The mass flow rate is assumed to be uniformly distributed across the BZ channels, which is a hypothesis that is backed up by the contained pressure drop range observed for the manifold tank approach. For the generic channel defined by the toroidal dimension $2a = 164$ mm and radial dimension $2b = 147$ mm, the flow rate is estimated as

$$\Gamma_i = \frac{\Gamma_{OB}}{32} = 0.512 \text{ kg/s} \tag{7.10}$$

From the channel cross-section $A = 2a \times 2b = 0.024$ m^2, the mean velocity $u_0 = 2.17$ mm/s is obtained. Adopting an uniform wall conductance ratio equivalent to

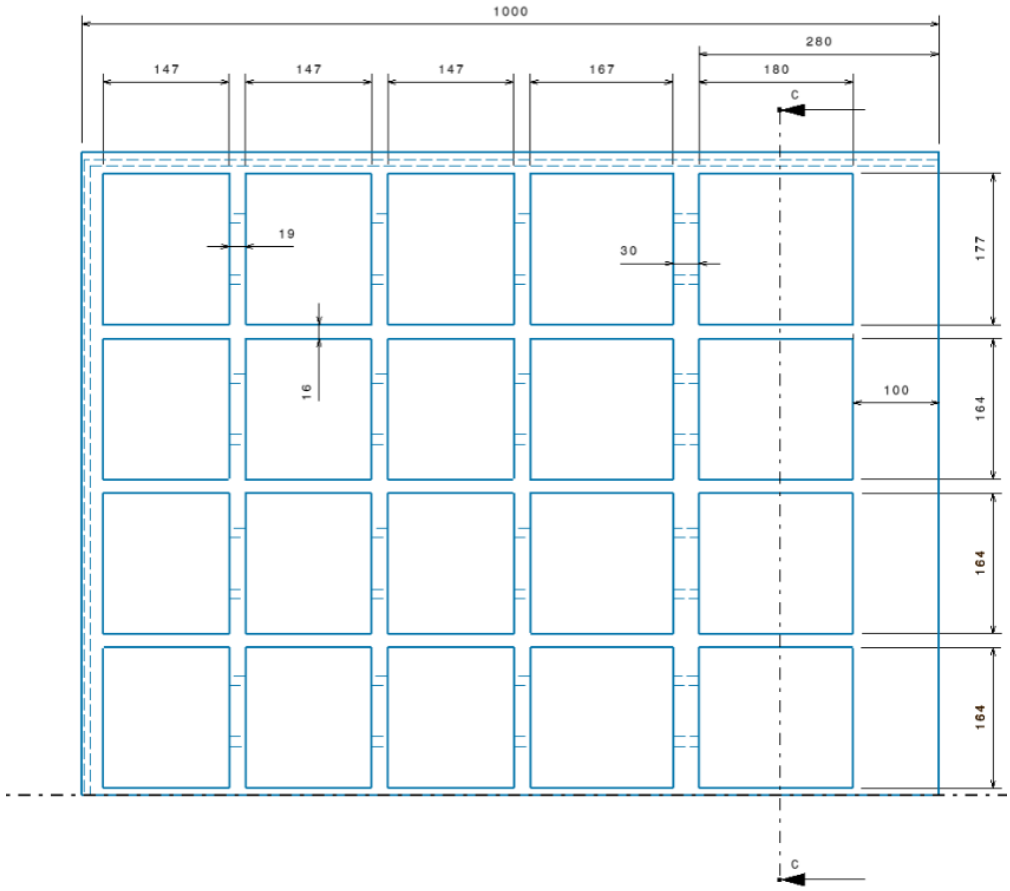

Figure 7.4. T02 and T03 breeding zone layout. Radial-toroidal view, first wall on the left. Dashed line on the bottom identifies the BZ symmetry line [84].

the wall thickness of the toroidal-poloidal SP, i.e. $c = 0.0169$, and the average value of the magnetic field at the first wall $B_{tor} = 4.19$ T, the pressure gradient takes the form

$$\nabla p_{fw} = 3.255 \text{ kPa/m} \tag{7.11}$$

If the channel length is equal to the blanket linear length at the first wall, i.e. $L_{fw} = 14.67$ m, the two-dimensional pressure drop for the first wall channel is estimated as

$$\Delta p_{fw,2D} = \nabla p_{fw} \cdot L_{fw} = 47.74 \text{ kPa} \tag{7.12}$$

The same analysis can be repeated for a channel close to the BSS, for which $2a = 164$ mm and $2b = 167$, to establish the pressure drop range in the breeding zone. Assuming the mass flow rate is unchanged due to the uniform flow distribution assumption then $u_0 = 1.91$ mm/s, the pressure gradient is evaluated according to the average field on the BSS ($B_{tor} = 3.91$T)

$$\nabla p_{bss} = 2.450 \text{ kPa/m} \tag{7.13}$$

and it follows from the blanket linear length at the BSS, i.e. $L_{bss} = 16.94$ m, that

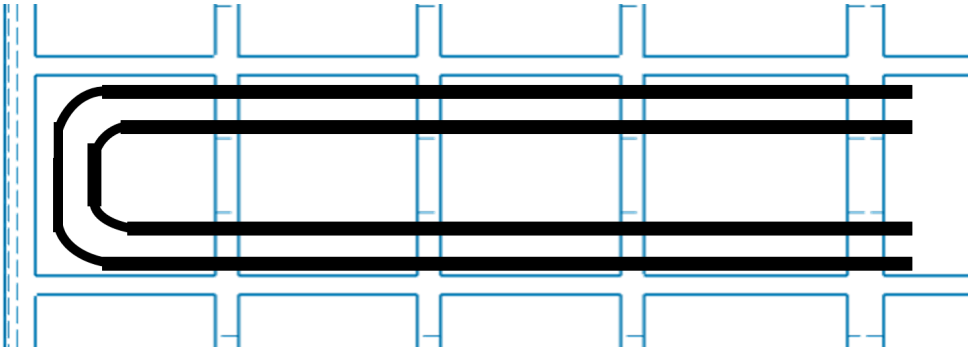

Figure 7.5. T02 BZ cooling element layout. Radial-toroidal view, first wall on the left [84].

the two-dimensional pressure drop amounts to

$$\Delta p_{bss,2D} = \nabla p_{bss} \cdot L_{bss} = 42.34 \text{ kPa} \tag{7.14}$$

The pressure drop for the BSS channel is very close to the previous estimate, being $\approx 89\%$ of the one calculated for the FW channel, and it backs up our assumption that the mass flow rate in the blanket it is likely to be evenly distributed among the channels, neglecting the electro-coupling phenomena.

The cooling element is composed of two nested DWT U-pipes. The pipes are inserted from the BSS and cross the toroidal-poloidal SP through rectangular openings drilled for this purpose. In Figure 7.5, it can be seen how the cooling pipes are tasked to refrigerate all the four channel on the same radial row. To estimate the 3D pressure drop contribution due to the flow around the nested U-pipes, it is possible to extrapolate the results discussed in Chapter 11 for the elementary cell of the FW channel, which is characterized by a poloidal pitch between the pipes equal to $p_v = 60$ mm. The CFD model makes the assumption of perfectly conductive surface for both the duct walls and cooling pipes: for $B_{tor} = 4.4$ T and a mean flow velocity $u_0 = 1.825$ mm/s, the total pressure drop computed in the channel is equal to $\Delta p_{cfd} = 2010$ Pa.

For these parameters, the theoretical pressure gradient in the perfectly conducting wall can be obtained assuming $k_p = 1$

$$\nabla p_{fw,\infty} = 27.665 \text{ kPa/m} \tag{7.15}$$

and the theoretical pressure drop in the channel is calculated as

$$\Delta p_{th} = \nabla p_{fw,\infty} \cdot p_v = 1660 \text{ Pa} \tag{7.16}$$

The pressure drop due to the obstacle can be estimated by the difference between the calculated and theoretical channel pressure drop

$$\Delta p_o = \Delta p_{cfd} - \Delta p_{th} = 350.1 \text{ Pa/pipe} \tag{7.17}$$

It should be noted that this estimate is not necessarily representative of the actual BZ channel behavior since the cooling pipes are, in general, characterized by a finite conductivity, and the same it is true for the duct bounding walls. Nevertheless, it has

been observed that for $Ha \to \infty$ the three-dimensional pressure drop term due to the presence of an obstacle does no longer depends on the obstacle conductivity [85]. In any case, the present estimate can be considered conservative with regard to the obstacle pressure drop.

Assuming that $\Delta p_o \propto u_0 B^2$, the obstacle pressure drop can be re-scaled to account for the different conditions employed in this analysis for the FW channel.

$$\Delta p_{o,fw} = 376.2 \text{ Pa} \tag{7.18}$$

From the results of the CFD analysis performed in Chapter 11, the poloidal pitch between cooling elements that can effectively refrigerate the FW channel is found to be $\tilde{p}_v = 40$ mm. From the blanket linear length at the FW, it follows that the number of pipes $n_p = L_{fw}/\tilde{p}_v \approx 367$. The cooling pipes pressure penalty is estimated as

$$\Delta p_o = \Delta p_{o,fw} \cdot n_p = 138.1 \text{ kPa} \tag{7.19}$$

and the overall BZ channel pressure drop is calculated as

$$\Delta p = \Delta p_o + \Delta p_{fw,2D} = 185.81 \text{ kPa} \tag{7.20}$$

The obstacle contribution has a fundamental impact on the BZ pressure drop estimate, since it constitutes $\approx 75\%$ of the pressure loss calculated for the FW channel. It should be noted that this estimate is most probably very conservative, but it is undeniable that the large number of cooling elements required to cool the T02 BZ are for sure going to significantly affect the pressure loss in the channel. Similar estimations cannot be done for the channels not immediately adjacent to the FW, since there the cooling pipes are straight and characterized by a lower blockage ratio compared with the nested U-pipes envisioned for the analyzed channel. Despite this, it is reasonable to assume that the obstacles are going to have a lesser impact on the pressure drop estimate for the back channels, at least because their number is, of course, invariant and they would be more evenly distributed over the channel length.

7.5 Configuration T03

Configuration T03 preserves the SP arrangement described for T02 and, therefore, its BZ layout is analogous to the one presented in Figure 7.4. In Figure 7.6, it can be seen how the main variation compared with T02 regards the cooling system, which it is modified to route the pipes in the BZ. Different number of pipes are required to refrigerate the channels along the BZ radial row: the maximum density of pipes is foreseen for the FW channel, where $n_{fw} = 17$ are envisioned, whereas for the BSS channel $n_{bss} = 2$ are enough to limit the PbLi temperature under the Eurofer operation threshold ($T \leq 823$ K) [86]. Since the PbLi flows downward in the back part and upward in the front part of the blanket, two channels can be defined for the BZ radial row: the duct "I", constituted by the BSS (i.e. Ia) and FW (i.e. Ib) channel studied in Section 7.4 for configuration T02, and the conduit "II", composed by the two internal channels (i.e. IIa and IIb).

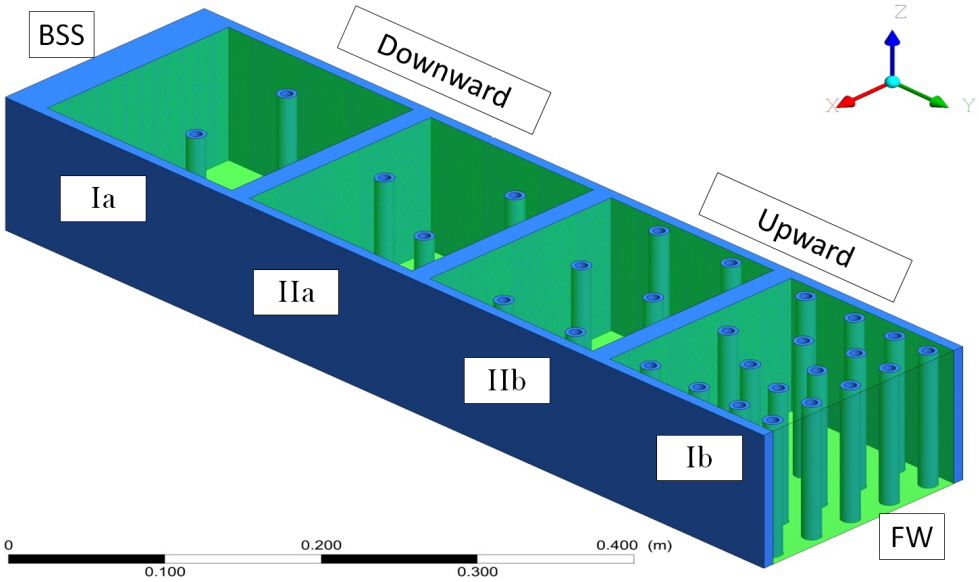

Figure 7.6. T03 BZ layout and vertical cooling pipes arrangement. Radial-toroidal view [86].

Table 7.4. T03 BZ channel equivalent cross section and fully developed flow pressure gradient. For channel labeling refers to Figure 7.6, unmodified cross-section A is derived from the T02 BZ layout data (see Figure 7.4).

Channel	Number of pipes [86]	$A(\mathrm{m}^2)$	$\hat{A}(\mathrm{m}^2)$	$\hat{A}/A$	u_0(mm/s)	B_{tor}(T)	∇p_{2D}(kPa/m)
Ia (BSS)	2	0.02739	0.02710	0.990	3.85	3.91	5.052
IIa	3	0.02411	0.02368	0.982	4.41	3.91	5.783
IIb	6	0.02411	0.02325	0.964	4.49	4.19	6.750
Ib (FW)	17	0.02411	0.02168	0.899	4.82	4.19	7.241

Very few MHD study have been published regarding forced convection flows in the presence of obstacles aligned with the stream-wise direction. The most notable work to date is most probably the one presented by Bühler and Mistrangelo where the forced and natural convection flow around a electrically insulated single vertical pipe was investigated [87]. For the former case, it was found that at $Ha = 1000$ the velocity profile is constant along magnetic field lines with the appearance of two core regions, called inner and outer core, separated by internal layers tangent to the cooling pipe. In particular, the inner core region is characterized by lower velocity, being more dampened by the magnetic field compared with the outer core. Regrettably, no information were reported by the authors about a variation in the pressure gradient compared with the empty duct. No similar study for an electro-conductive pipe or a channel with several pipes has been reported in the literature, to the best of the author's knowledge.

For the purpose of this study, the cooling pipes are assumed to do not introduce a significant effect on the pressure gradient except for the reduced cross-section available for the PbLi flow. Under this assumption, the reduced cross-section for a

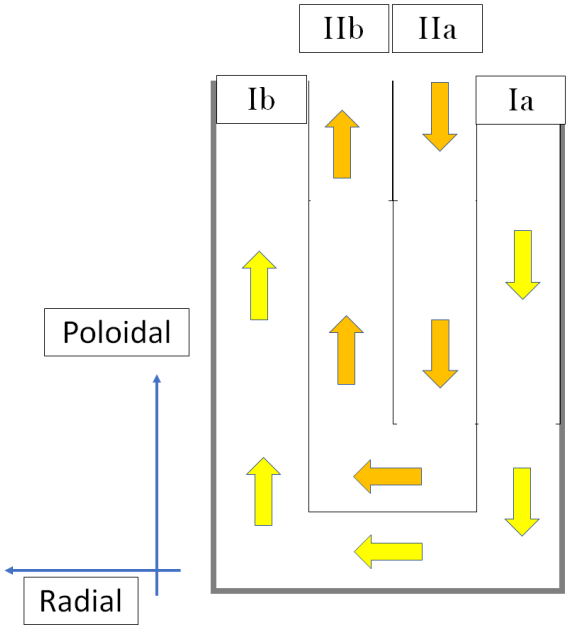

Figure 7.7. T03 BZ first and second leg connection. Radial-poroidal view.

channel crossed by n cooling pipes can be expressed as

$$\hat{A} = A - n \cdot \pi(d/2)^2 \tag{7.21}$$

where the pipe diameter is $d = 0.0135$ m. The mass flow rate is assumed to be evenly distributed such that $\Gamma = 1.024$ kg/s for every BZ channel. Neglecting the buoyancy forces and taking $c = 0.169$ as the uniform wall conductance ratio, the pressure gradient for each channel is estimated according to eqs. (4.4) and (4.5). The results are collected in Table 7.4. The channel Ib is the one most affected by the cross-section reduction, registering a 25% velocity increase compared with Ia.

Expressing the linear length of the first ("a") and second leg ("b") of the channel with L_{bss} and L_{fw}, the two-dimensional pressure drop in the defined channel is calculated as

$$\Delta p_I = \Delta p_{Ia} + \Delta p_{Ib} = 191.77 \text{ kPa} \tag{7.22}$$

$$\Delta p_{II} = \Delta p_{IIa} + \Delta p_{IIb} = 196.95 \text{ kPa} \tag{7.23}$$

where a discrepancy of $\approx 3\%$ is found between the two flow paths.

The connection between the first and second leg of the BZ channels is constituted by a 180° bend at the blanket bottom, where the elbow channel is assumed to have the same width of the "a" duct. Moreover, the poloidal height is equal to the radial length of the "a" channel. The general layout is shown in Figure 7.6.

For the duct II, the variation of cross-section in the elbow, due to the cross-section difference between the first and second leg channel, can be neglected and the pressure drop can be estimated as the sum of the 2D fully developed flow in the connection and the two 90° rectangular bends that, employing eq. (4.11), are characterized by $k_\perp = 0.0398$. The elbow radial length for the channel II is $L_{II} = 166$ mm. Since the

average magnetic field is $B_{tor} = 4.87$ at the blanket bottom, it follows that

$$\Delta p_{II,e} = \Delta p_{2D} + 2 \cdot \Delta p_{90} = 1.494 + 0.253 = 1.747 \text{ kPa} \tag{7.24}$$

where the velocity in the first leg is assumed as scale velocity for the pressure drop estimate.

A similar reasoning can be employed for the duct I where, however, the cross section variation between the first and second leg cannot be neglected. The elbow radial length for the channel I is $L_I = 508$ mm. It follows that

$$\Delta p_{I,e} = \Delta p_{2D} + 2 \cdot \Delta p_{90} + \Delta p_{xs} = 3.994 + 0.236 + 1.738 = 5.968 \text{ kPa} \tag{7.25}$$

where the velocity in the first leg is assumed as scale velocity for the pressure drop estimate, except for the cross-section variation, for which the second leg parameters are employed.

Accounting for the connection, the overall pressure drop in the BZ flow paths can be updated to a more accurate estimate

$$\Delta p_I = \Delta p_{Ia} + \Delta p_{Ib} + \Delta p_{I,e} = 197.738 \text{ kPa} \tag{7.26}$$

$$\Delta p_{II} = \Delta p_{IIa} + \Delta p_{IIb} \Delta p_{II,e} = 198.697 \text{ kPa} \tag{7.27}$$

where the deviation between the flow paths becomes negligible. As a final note, the likelihood of flow re-circulation in channel Ia and IIa is believed to be very high due to the combination of significant volumetric heating, downward flow, and considerable axial length [88]. Further studies aiming to characterize the downward mixed convection flow in channel with vertical obstacles are deemed necessary if, when, and to what extent the reverse flow appears.

7.6 Chapter summary

In this Chapter, the pressure drop is estimated for the breeding zone part of the PbLi hydraulic path in the four configurations. Negligible velocity and relatively short length in T01.A results in very small pressure losses, whereas the opposite is true for T01.B that alone nearly exceeds the design limit. In fact, the pressure loss in the T01.B BZ is so high that it makes the configuration utterly unfeasible when combined with the other hydraulic regions. The other two configurations are both characterized by medium velocity and long channel length, therefore the BZ contribution to the overall pressure loss is significant. Uncertainties affect the T03 estimate to a great extent, since it is likely characterized by intense re-circulation in its downward channels and it is not clear if the correlations employed for this study will be representative of mixed convection with vertical internal obstacles. Electromagnetic coupling is thought to play an important role in the flow distribution for T01.A, T02, and T03. Regarding the first configuration, flow re-circulation appearing at the interface to counter-flowing cells is highly probable and it has been previously observed in numerical simulations carried over for the HCLL design [83].

Chapter 8

Comparative analysis conclusions

The overall pressure drop for each configuration is reported in Table 8.1, where it is broken down for the contribution of each hydraulic region. Configuration T01.A, T01.B and T02 employs the double feeding DN150 pipe scheme and the routing from the VV lower port, whereas configuration T03 is fed from the upper port and adopts the top-point attachment. The same draining pipe is employed for all the four configurations: a DN200 single pipe attached at the top of the blanket. For the manifold and breeding zone, the contribution averaged on all the flow paths is reported and the manifold tank approach is employed for configurations T02 and T03.

Recalling the design pressure drop limit defined in Section 4.2, it is immediately evident how the combination of high velocity and long BZ channels does not allow T01.B to fall below the threshold. The other three configurations have similar performances with their pressure drop comprised between 0.95 and 1.16 MPa. This is not surprising, since the contribution from the feeding and draining pipe is shared among them and amounts from a minimum of 60% for T01.A to the 73.5% registered for T02. The importance of the feeding and draining pipe on the overall pressure drop cannot be overstated and, nevertheless, the design of these elements has so far being neglected, probably since they are not involved in the blanket thermal-hydraulics and are considered simple connection elements with the external PbLi loop. The optimization of feeding and draining pipe layout can be considered a relatively

Table 8.1. Overall pressure drop in the four WCLL configurations (expressed in kPa), broken down by hydraulic region

Hydraulic region	T01.A	T01.B	T02	T03
Feeding pipe		315.718		379.792
Manifold	458.474	132.431	64.54	94.117
Breeding zone	4.667	1765	185.81	198.218
Draining pipe		379.789		
Overall pressure drop	1158.65	2592.34	945.86	1051.92

straightforward strategy to reduce the overall blanket pressure drop. Larger feeding pipes minimize the PbLi velocity but are difficult to integrate with the strict remote maintenance requirements for the size available in the lower port. On the other hand, alternative routing schemes are susceptible to raise the pressure drop estimate in the manifold and BZ, other than not being compatible with all the configurations. The adoption of insulating coating limited to these elements could be a possible solution, but their reliability and the impact of discontinuous insulation should be carefully assessed.

The good performance of configuration T02 is a product of the simple PbLi flow path and rational flow distribution scheme. However, this layout has significant uncertainties regarding the mechanical stability and the capacity of the cooling system to refrigerate it. The latter issue is discussed in more detail in Chapter 11 in the framework of the FW breeding zone channel, whereas the mechanical stability of the blanket is strictly related to the capacity of the bottom and upper cap to resist to the pressure transients envisioned for the in-box LOCA and other design basis accidents. If this cannot be ensured, the flow distribution is considerably complicated by the necessity to preserve the SP arrangement and the manifold performances are degraded. Other thermo-mechanical issues revolve around the high percentage of the toroidal-poloidal SPs, that must be perforated to allow the passage of the cooling pipes and the absence of any structural element connecting the FW and the BSS. In conclusion, even if it seems to be the most desirable from the point of view of MHD pressure losses, the feasibility of the WCLL T02 configuration is hamstrung by several uncertainties.

The second best configuration, T03, has advantages and drawbacks similar to the one discussed for T02. Moreover, it is not clear if the vertical pipe layout will be able to effectively refrigerate the BZ: preliminary results for hydrodynamic conditions have shown that an unfeasible number of pipes is required to both keep the maximum PbLi temperature below the Eurofer operational limit and to maintain the water velocity below 7 m/s [86]. Moreover, the scarcity of results published in the literature about forced convection around vertical pipes introduces a significant uncertainty on the reliability of the present study. Flow reversals are also likely to appear in the back of the blanket, where the liquid metal flows downward in a long channel and is subjected to a relevant volumetric power heating, which are a significant drawback for the blanket tritium control, both in terms of overall inventory and permeation toward the coolant [88].

The third best configuration, T01.A, has been the subject of extensive thermo-mechanical and thermal-hydraulics in the past years and its behavior is relatively well understood. The main advantage is the abysmal velocity of the PbLi in the breeding zone channel, which results in negligible pressure drop in this region. Conversely, the flow distribution relies on a very complicated layout composed of co-flowing arrays of narrow rectangular ducts that are extended for the whole blanket length. Ensuring the correct flow distribution of the liquid metal in the blanket is foreseen to be very challenging due to the relevant pressure imbalance between the spinal manifold flow paths and tortuous connection with the BZ. Moreover, extending this design to inboard conditions could prove to be difficult since there the spinal manifold will be located in the blanket region with the highest magnetic field, as opposed as what happens for the outboard. However, the great flexibility of this layout

that, for instance, allows a relative straightforward integration with the mid-point feeding/draining routing scheme, it is a decisive advantage and suggests a wider room for optimization compared with the other configurations.

An open issue that has been neglected in the present study is the electromagnetic coupling between the WCLL ducts that, being in electrical contact with each other, are likely to share massive amounts of leakage currents. Even if its impact on the pressure drop estimate could be limited, especially for configuration T01.A, the electromagnetic coupling is expected to significantly alter the flow features in the BZ. For instance, some consequences documented in literature are the appearance of flow reversals at the interface between counter-flowing channels (T01.A) [83] and the suppression of the flow rate in channels at the center of an array stacked perpendicularly to the magnetic field direction (T02) [82].Flow distribution is another aspect that is going to be significantly affected by this phenomenon, since mass flow rate imbalance among coupled channels tends to be lower compared with the uncoupled case, at the expanse of an increase in the overall configuration pressure losses. The WCLL layout complexity (i.e. obstacles, asymmetrical ducts, etc.) and the lack in the literature of studies concerning similar geometries make difficult to accurately predict how much the coupling phenomena are going to modify the pressure drop figures presented in this study. In the next years, extensive MHD analyses should be devoted to characterizing these important issues.

As a final remark, the pressure loss figures presented in this study for the four alternative WCLL configurations, even if relatively low compared with the design threshold imposed, should be considered an initial step from which to proceed for the stream-lining and simplification of the blanket design. Extrapolating the discussed configurations to the inboard conditions ($B \approx 8$ T, $\Gamma_{\mathrm{IB}} = 5.32$ kg/s, $R \approx 0.4$ m, and toroidal width $L \approx 1$m), it is expected for the pressure loss figure to increase by a factor $\approx$3.5, which, of course, will not allow any configuration to remain below the design threshold. In particular, the most affected one is going to be configuration T01.A: if the SM is located for the outboard segment in the blanket back (i.e. the region that experiences the lower magnetic field), the situation is reversed for the inboard segment, where the SM is exposed to the maximum field, which will probably lead to a significant performance degradation compared with the other configurations. Mitigation strategies should be implemented to decrease the overall MHD pressure loss in the outboard blanket to about 0.4$\div$0.5 MPa; a figure for which the design extrapolation to the inboard segment leads to $\Delta p_{\mathrm{IB}} \leq 2$ MPa.

Part III

Numerical modeling

Chapter 9

ANSYS CFX validation for incompressible MHD flows

9.1 Introduction

In this Chapter, the electromagnetic model integrated in the commercial CFD code ANSYS CFX is validated against some selected incompressible magnetohydrodynamics benchmarks regarding forced convection, magneto-convection and free surface flows. ANSYS CFX is a finite volume CFD code that employs a parallel implicitly coupled multi-grid solver engine [89]. Since 2009, the code includes in its distribution an electromagnetic model that allows the treatment of MHD flows. The objective of this Section is to assess the boundaries of the code capabilities and to determine if and to what extent CFX can be considered an useful tool to simulate incompressible MHD phenomena.

9.2 Rationale

The effects generated by the interaction between liquid metal and magnetic field are multiple, subtle, and directly impact the blanket design. Full understanding of the

MHD phenomena happening in the blanket is an unavoidable requirement to devise a component able to fulfill the stringent specifics required to operate in the harsh fusion reactor environment. In this framework, accurate and efficient Computational Magnetohydrodynamics (CMHD) codes are in high demand to both support the LM blanket design and to provide system-level predictive capabilities for integration in multi-physics platforms.

The ideal CMHD code for fusion applications should be a numerical tool able to simulate complex and large-scale 3D geometries employing multi-material computational domains. The code should be able to model steady and unsteady MHD flows and the regime transition, handle non-uniform magnetic field and electric boundary conditions, provide support for Q2D and full MHD turbulence, and coupled heat/mass transfer capabilities, in particular for the tritium and corrosion models. Moreover, all these capabilities should be demonstrated for a parameter range consistent with a fusion reactor: $Ha \approx 10^4$, $Re \approx 10^4$, $Gr \approx 10^{12}$, and finite wall conductance ratio [1, 90].

Although considerable efforts have been spent in the past 30 years by the fusion community, no CMHD code is currently able to fulfill all these demanding requirements. In particular, the Hartmann number currently achievable for complex 3D calculations is at least an order of magnitude below the $Ha = 10^4$ stated goal. General complexity of the governing equations, necessity to resolve simultaneously phenomena happening in a wide range of length scales, consistent numerical schemes able to enforce the charge conservation and divergence-free/curl-free conditions for the magnetic field are some of the most notable obstacles that need to be overcome in order to develop a CMHD code that will fully answer the blanket modeling needs. Intensive code testing and the creation of a benchmark database are also required.

On the route to the ideal CMHD code, existing CFD engines like CFX can provide useful if preliminary information about fundamental MHD phenomena that can then be studied in further detail with the aid of experimental activities and more advanced numerical tools. Quality control and improvements of the existing models is also an important goal and can be obtained only through extensive code testing and thorough validation protocols against theoretical solutions and code-to-code bench-marking.

9.3 State-of-the-art for CMHD codes

Although a dedicated CMHD code able to simulate all the phenomena involved in a liquid metal blanket is still not available, the fusion community has spent considerable efforts toward this goal and, during the years, a substantial number of numerical methods and computational tools have been developed.

The application of computational methods to the resolution of liquid metal MHD problems dates back at least to the 70s when pioneering analyses on straight pipes were performed by Butsenieks and Shcherbinin [91]. Successively, Aitov et al. employed the fractional steps method to extend the study to more complex geometries like curved channel and sudden variation of cross-section [92, 93]. Expensive requirements in term of computational storage and the rudimentary tools available at the time limited these studies to 2D geometry and low magnetic field intensity

($Ha \approx 20$).

For fusion applications, where $N \gg 1$, $Ha \gg 1$, asymptotic techniques taking into account only the dominant effects were usually preferred due to their capability to provide fast and cheap analyses in parameter range inaccessible to more sophisticated numerical methods [94]. In the late 80s and early 90s, semi-numerical methods were developed to overcome some of the limitations of the asymptotic techniques like, for instance, the difficulty in representing developing flows and non-uniform electrical boundary conditions. These models relied on the core flow approximation, i.e. balance restricted to pressure gradient and Lorentz force in the core region, to simplify the governing equations to a two-dimensional set and then used iterative methods to recreate the three-dimensional flow [95]. These codes proved successful in the treatment of non-uniform magnetic field, bend, electrically coupled multiple ducts, and turbulence in strong magnetic fields [35, 96].

The increase in computer power allowed in the 90s to explore full numerical analysis of MHD flows at higher Ha, thus permitting to investigate phenomena pertaining to complex geometrical elements, which are impossible to represent with approximate techniques. The seminal paper published by Sterl in 1990 [97] presented a finite difference scheme able to directly simulate 2D flows up to $Ha = 10^3$ and 3D problems up to $Ha = 10^2$ and it was shortly followed in 1991 by a 3D finite volume scheme developed by Kunugi et al. [98] that was applied to straight channels and bend in rectangular geometries. Throughout the 90s and 00s, the direct numerical approach became gradually more widespread and general-purpose CFD codes started providing incompressible MHD models in their distribution. Computational tools based on the finite element method were also created, mostly tailored for applications in the metallurgy field [99]. The development in 2007 of a numerical scheme based on a conservative formulation of the Lorentz force strongly accelerated the progress in the maximum Ha computationally achievable, reaching $Ha = 10^4$ for simple fully developed flow and several thousands for more complex geometries [1].

Focusing the attention on finite volume CFD codes, the tools available for the modeling of 3D LM MHD flows can be divided into two broad categories: Tailored and General Purpose. A Tailored code is specifically developed for MHD applications, whereas a General Purpose code provides MHD capabilities as an add-on to a core of other CAE functionalities. Only a handful of codes belong to the first category, among the most notable one must cite:

- **HIMAG** is jointly developed by University of California, Los Angeles (UCLA) and the private company HyPerComp, Inc. since the early 00s [100]. It is a parallel, time accurate MHD solver for three- dimensional closed and free surface flows on unstructured and hybrid meshes. Heat and mass transfer and Lagrangian particle tracking are provided through add-on modules. The code is developed to handle multi-material computational domains and it is also able to compute electromagnetic and thermal quantities in solid walls, including the effects of contact resistance, and strongly temperature-dependent properties. It supports both the electric and magnetic induction formulation.

- **MTC** is a parallel C++ code developed by the FDS team from the Hefei Chinese Academy of Science. Two versions of the code have been released: MTC-H 1.0 [101], based on a structured computational grid and MTC-H

2.0, which was extended to employ an unstructured mesh [102]. The original code is able to simulate 2D and 3D pressure-driven flows in simple geometries. Successively, magneto-convection and MHD turbulence capabilities were implemented [103, 104].

- **Anuprahava-1** is a general purpose CFD code developed by the Indian Institute of Technology in Hyderabad. A dedicate MHD module is provided which is capable of handling non-orthogonal, multi-block, structured grids and treats a coupled fluidâĂŞwall (conjugate) modeling to include thermal and electro-magnetic effects in the presence of duct walls and electro-thermally coupled manifolds [105]. Simplified models (2D geometry, fully developed flows, inertia-less, etc.) and a wall-function for near-wall treatment are included in the code distribution for maximum flexibility. The code is currently limited to structured mesh.

In addition, the open source object-oriented Fortran200X scientific software library `FEMPAR` provides support for induction-less incompressible MHD analyses based on the finite element method [106, 107]. The main advantage of a Tailored code is that its development is strongly focused on the MHD treatment and, in principle, could have better performances and a wider selection of dedicated models compared with a General Purpose code. On the other hand, no Tailored code is yet mature and fully validated enough to be made available to the general public, commercially or otherwise, and, therefore, their use is still restricted to the developing institutions.

General Purpose are CFD platforms that are originally developed for a wide range of engineering applications and that include in their distribution models that support MHD computations. Without any pretense to be exhaustive, a list of General Purpose code that fit this description will include Fluent and CFX (part of the ANSYS CFD suite), Fluidyn, COMSOL, STAR-CCM+ and OpenFOAM. Some of these codes provide out-of-the box MHD capability, like Fluent [108] and CFX [109], whereas COMSOL does not distribute a dedicated MHD module, but this functionality can be obtained through the coupling of stand-alone physical models [110]. These codes provide limited possibilities to tweak the numerical model through built-in programming language. This feature was employed in the past to implement the MHD governing equations in platform still lacking this capability, see for example the work of Di Piazza and Bühler [111] and Mistrangelo [112] on CFX, but it is a intricate procedure that still lacks the necessary degree of flexibility since it is not possible for the user to directly modify the source code. Moreover, discretization and other numerical techniques employed by the code are generally not modifiable and described with insufficient details in the product documentation. License costs are also a non-trivial issue, since MHD computations often require the use of High Performance Computing (HPC) systems numbering in the hundreds of processor units.

In the last years, many research groups have moved their activities from traditional codes to the open source library OpenFOAM to overcome these constraints. OpenFOAM is a general purpose object-oriented CFD toolbox distributed by CFD Direct and OpenCFD. The default release includes a MHD solver called `mhdFoam` that relies on the magnetic induction formulation and a PISO-like scheme to enforce the divergence-free condition of the induced field [113]. In addition to not requiring

any licensing fee, the main advantage of OpenFOAM is its excellent extensibility and parallelization. Thanks to this features, several MHD models have been developed in recent years to cover a wide range of phenomena of interest for the blanket design: laminar and Q2D turbulence around obstacles [114], coupled MHD/heat transfer/tritium transport [115], magneto-convection and electrical coupling of multiple domains [116, 117].

The main advantage of General Purpose codes is that they offer user-friendly environments and graphical interfaces that greatly simplify the simulation work-flow. On the other hand, the flexibility of General Purpose proprietary codes tend to be quite limited and, in general, the MHD models distributed by the supplier are not mature and validated as the other engineering modules. On the other hand, open source codes like OpenFOAM provide a more research-oriented solution that forfeits some advantages (i.e. custom support, GUI, etc.) for the possibility to more readily extend and modify the numerical module.

Most of the described codes employ the induction-less approximation and the electric potential formulation in order to reduce the complexity and non-linearity of the governing equations to improve the code performances. Magnetic induction numerical tools are generally more unwieldy and computationally expensive to apply for the treatment of 3D MHD flows in complex geometries, therefore their development has been slower compared with the electric potential solvers. Despite these drawbacks, this class of codes is the only one able to represent blanket phenomena characterized by strongly unsteady magnetic field, i.e. plasma disruptions, and development of numerical methods is currently ongoing for finite magnetic Reynolds number flows [37, 118].

As a final note, it should be noted that the development in direct numerical simulation tools in last years has not been accompanied by an analogous activity in the implementation of MHD capability for system codes. Traditionally employed for the design of fission reactor, system codes are mono-dimensional (or more recently multi-dimensional) numerical tools that exchange the depth and detail of the CFD codes for a simplified treatment of the physical processes that, however, allows to assess the thermal-hydraulic performances on the reactor scale. Typical examples are RELAP and TRACE that, although initially developed for applications in light water reactors, have been extended in the last years to employ other fluids, i.e. liquid metals [119]. Rudimentary MHD correlations relying on modified viscous stress term to account for the electromagnetic drag are implemented in RELAP5-3D [120] and MARS-FR [121], but are limited to straight rectangular/circular ducts and thus do not support any treatment for junctions, manifolds, and any complex geometrical elements. More recently, a novel system code called MHD-SYS has been developed that features correlations for the modeling of multiple coupled ducts and heat transfer for basic layouts, whereas coupling with CFD codes (i.e. `mhdFoam`) is employed to supply the system code with reliable input data for the behavior of the flow in complex geometrical elements [122, 123]. The development of a reliable system code able to model the MHD phenomena is desirable since many blanket elements are amenable to be treated in such a simplified way. Unfortunately, this endeavor is hampered by the lack of high quality experimental data for the fusion reactor parameter range that are severely needed to develop accurate correlations that can be implemented in system code. The next generation of experimental facilities,

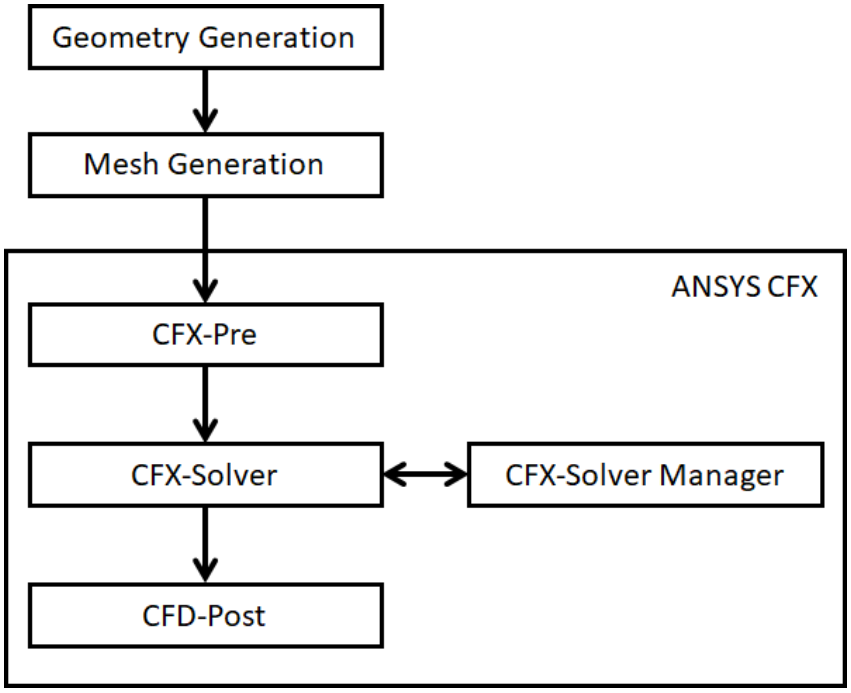

Figure 9.1. CFX simulation workflow

as well as the growing database of numerical results, is expected to promote the development of these numerical tools in the near future [90].

9.4 CFX numerical method and MHD model implementation

ANSYS CFX is a general purpose CFD software suite. It is constituted by four main modules that handle the simulation setup, run, and post-processing:

- **CFX-Pre**: physics pre-processor unit, it is used to define settings and physics conditions for the case studied
- **CFX-Solver**: this module proceeds to the discretization and iterative solutions of the specified governing equations
- **CFX-Solver Manager**: it allows to interact and control with CFX-Solver during the simulation run
- **CFD-Post**: post-processor unit, it is used to visualize, analyze, and process the simulation results

The typical work-flow is depicted in Figure 9.1, geometry and mesh generation steps can be performed inside the ANSYS Workbench platform or using supported external software programs.

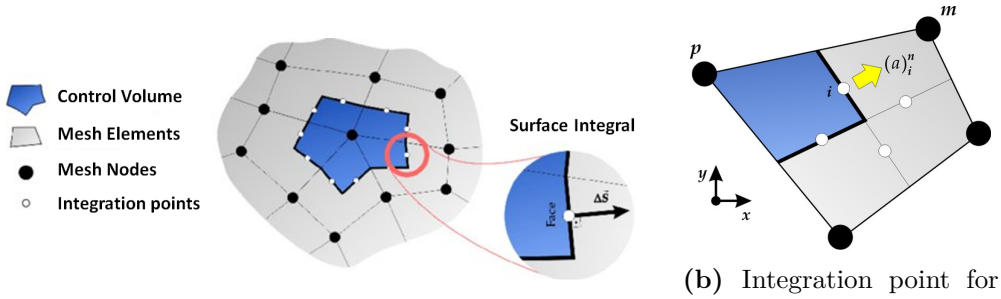

(a) CV main geometrical entities

(b) Integration point for surface integral and neighboring nodes

Figure 9.2. Element-based finite volume method: CV construction and surface integral [124]

9.4.1 Discretization procedure

The Navier-Stokes equations are discretized in CFX using an element-based finite volume method. During the mesh generation step, the problem geometry is divided in several discrete elements and nodes, which are shared among adjacent elements. Control Volumes (CVs), which are used to conserve the problem fundamental quantities, are constructed around each mesh node (called a vertex in the CFX terminology), as it is shown in Figure 9.2a, which means that each CV is composed of several sectors belonging to different mesh elements. The computational grid so obtained is co-located and all the solution variables and fluid properties are stored at the mesh nodes [89].

The partial differential equations describing the fluid behavior are integrated over the CVs, volume and surface integrals are defined to describe respectively source (or accumulation) terms in the element and fluxes sum on the surfaces. These integrals are discretized to obtain a system of algebraic equations that can be solved with an iterative procedure: volume integrals are discretized within each element sector and transferred to the corresponding CV, whereas surface integrals are discretized at the integration points (ip), which are located at the center of each surface segment within a mesh element (i.e. at the interface of neighboring CVs). Surface integrals for CVs sharing an integration point are equal and opposite, therefore they are locally conservative [89].

The discretized integral mass and momentum conservation equations can be written as:

$$V\left(\frac{\rho-\rho^0}{\Delta t}\right)+\sum_{ip}\dot{m}_{ip}=0 \tag{9.1}$$

$$V\left(\frac{\rho\mathbf{v}_i-\rho^0\mathbf{v}_i^0}{\Delta t}\right)+\sum_{ip}\dot{m}_{ip}(\mathbf{v}_i)_{ip}=\sum_{ip}(p\Delta n_i)_{ip}+\sum_{ip}\left(\mu\left(\frac{\partial\mathbf{v}_i}{\partial\mathbf{x}_j}+\frac{\partial\mathbf{v}_j}{\partial\mathbf{x}_i}\right)\Delta n_j\right)+\bar{S_{\mathbf{v}_i}}V \tag{9.2}$$

where $\dot{m}_{ip}=(\rho\mathbf{v}_j\Delta n_j)_{ip}$, V is the control volume, Δt the time step, Δn_j is the discrete outward surface vector, the subscript ip denotes evaluation at an integration point, summations are executed over all the integration points belonging to the control volume, and the superscript ^{0} refers to the old time level.

In Equations (9.1) and (9.2), the transient term is discretized with a First Order

Backward Euler scheme, that is robust, fully implicit, bounded, conservative, and does not have a time step size limitation. A Second Order Backward Euler scheme is also available for selection in the code.

The advection term requires the variable ϕ evaluation at the integration point approximating the neighboring nodal values. The discretization scheme is expressed by the relation:

$$\phi_{ip} = \phi_{up} + \beta \nabla\phi \cdot \Delta\vec{r} \tag{9.3}$$

where ϕ_{up} is the upwind node value, $\vec{r}$ is the vector from the upwind node to the integration point, β is a weight parameter called Blend Factor, and $\nabla\phi$ is the property nodal gradient. Depending on the value assumed by β and $\nabla\phi$, different numerical schemes are used by the code. The Upwind scheme is formally a first order spatially accurate upwind scheme, which corresponds to eq. (9.3) when $\beta = 0$, and it is very robust but prone to numerical diffusion. If $0 < \beta < 1$, the quantity $\beta\nabla\phi \cdot \Delta\vec{r} \neq 0$, called Numerical Advection Correction, is used to reduce the diffusion errors originated by the pure upwind scheme (Specified Blend Factor scheme). For this case, $\nabla\phi$ at the integration point is calculated as the average of the adjacent nodal gradients. If $\beta = 1$ is applied, the Specified Blend Factor scheme is formally second-order spatially accurate, but it is also unbounded, which can lead to the introduction of non-physical oscillations where steep gradients are present. Instead, a High Resolution scheme is employed where the β value is calculated from the property distribution in the adjacent nodes to be as close as possible to 1, while satisfying the boundedness principle. For this scheme, $\nabla\phi$ is taken from the upwind node.

The control volume gradient on a node is evaluated through the relation

$$\nabla\phi = \frac{1}{V} \sum_{ip} (\phi \Delta\vec{n})_{ip} \tag{9.4}$$

where $\Delta\vec{n}$ is the outward surface vector at the integration point. Equation (9.4) requires ϕ to be evaluated at the integration points from the neighboring nodal values. This approximation is done through finite-element shape functions, which describe the property evolution in the mesh element with the expression:

$$\phi = \sum_{i=1}^{k} N_i \phi_i \tag{9.5}$$

where k is the number of nodes for the element shape considered (hexahedron, tetrahedron, wedge, pyramid). The shape function satisfies the condition $\sum_{i=1}^{k} N_i = 1$ and its expression depends on the element shape considered, but it is always linear in terms of the parametric coordinates system (s, t, u), from which the name *tri-linear*. An example for the cases of tetrahedral and hexahedral element is shown in Figure 9.3.

Diffusion and pressure gradient terms are similarly evaluated using tri-linear (or linear) shape functions. For the discrete mass flow rate $\dot{m}_{ip}$, a modified version of the Rhie-Chow interpolation technique is used to ensure the physical pressure-velocity coupling: a momentum-like equation is solved to evaluate $\mathbf{v}_{j,ip}$ with the introduction of a pressure-redistribution term that depends on the mesh resolution and is spatially third-order accurate [89].

$$N_1(s,t,u) = 1 - s - t - u$$
$$N_2(s,t,u) = s$$
$$N_3(s,t,u) = t$$
$$N_4(s,t,u) = u$$

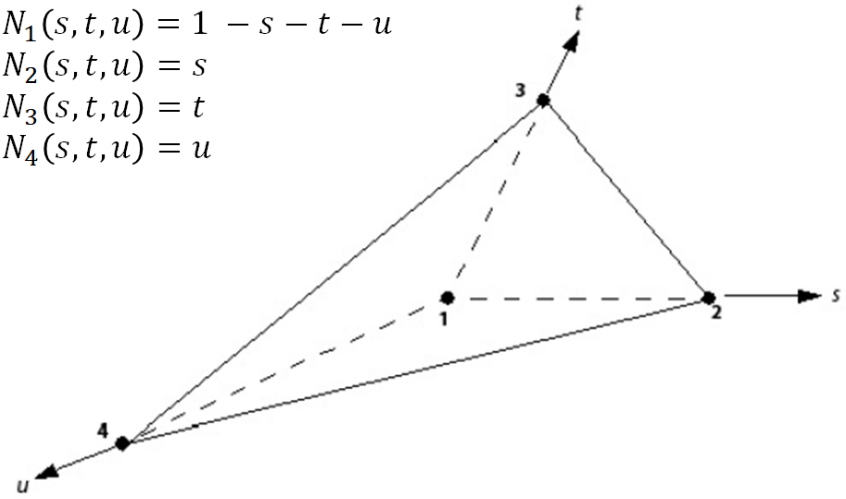

(a) Tetrahedral element

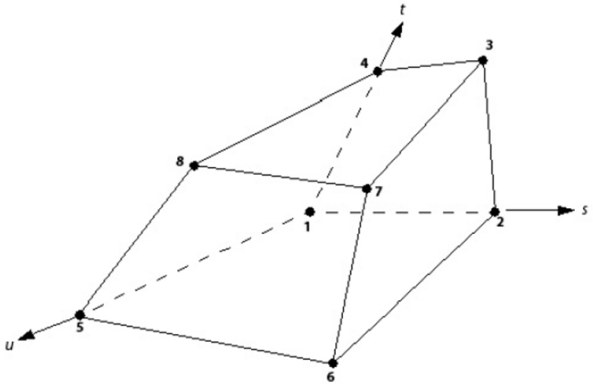

$$N_1(s,t,u) = (1-s)(1-t)(1-u) \qquad N_5(s,t,u) = (1-s)(1-t)\,u$$
$$N_2(s,t,u) = s(1-t)(1-u) \qquad N_6(s,t,u) = s(1-t)\,u$$
$$N_3(s,t,u) = s\,t\,(1-u) \qquad N_7(s,t,u) = s\,t\,u$$
$$N_4(s,t,u) = (1-s)\,t(1-u) \qquad N_8(s,t,u) = (1-s)\,t\,u$$

(b) Hexahedral element

Figure 9.3. Tri-linear shape functions for tetrahedral and hexahedral element [89]

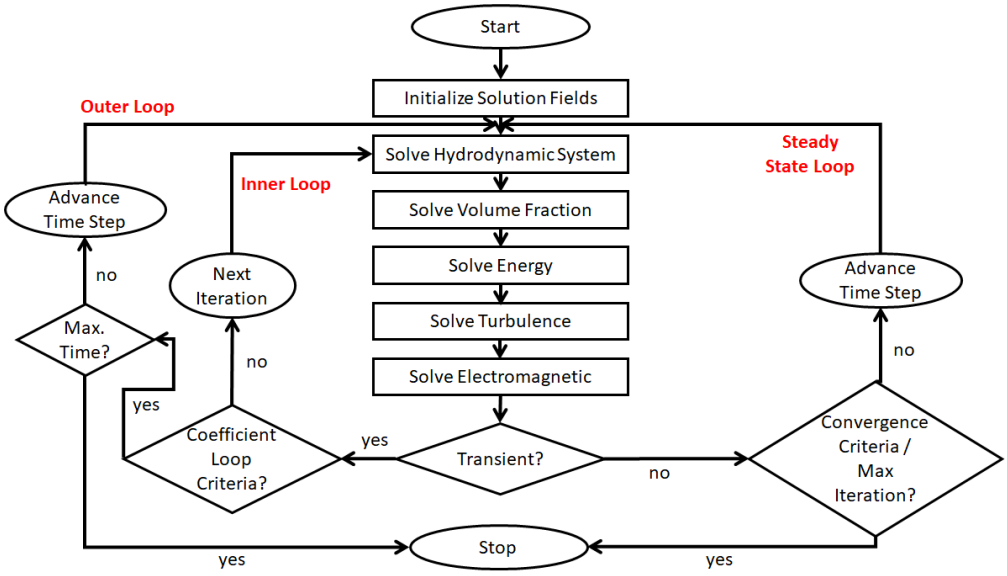

Figure 9.4. CFX solver algorithm

9.4.2 Solver theory

The general solution algorithm in CFX-Solver is presented in Figure 9.4. The numerical method employs a coupled technique, in which the momentum and continuity equations are solved together in a single algebraic system. Both steady-state and transient problems can be solved with this method. For the former, a virtual time-step is defined that can be interpreted as an "under-relaxation factor", which main role is to control the convergence speed, and, for each time step, the code performs a single iteration. Conversely, the code executes multiple iterations within the same time-step (inner loop) during a transient analysis and additional convergence criteria are defined to specify the time step advancement (outer loop). The linearized equations system is solved with a Multigrid (MG) accelerated Incomplete Lower Upper (ILU) factorization technique.

9.4.3 Electromagnetic model

The electromagnetic model in ANSYS CFX allows to study the motion of electrically conducting, electrically charged, and magnetically polarizable fluids through the coupling of standard CFD transport equations and the Maxwell ones, which are required to describe the electromagnetic variables. In Chapter 3, it was discussed how the electromagnetic force effects on the fluid can be represented through the addition of suitable source terms in the Navier-Stokes equations.

The complete equations set for the electromagnetic model is presented below [89]

$$\frac{\partial \rho}{\partial t} + \nabla \cdot (\rho \mathbf{v}) = 0 \tag{9.6}$$

$$\frac{\partial \rho \mathbf{v}}{\partial t} + \nabla \cdot (\rho \mathbf{v} \otimes \mathbf{v}) = -\nabla p + \nabla \cdot \tau + \mathbf{F}_{emag} - \rho_0 \beta (T - T_0) + \mathbf{S}_M \tag{9.7}$$

$$\frac{\partial\left(\rho h_{tot}\right)}{\partial t}-\frac{\partial p}{\partial t}+\nabla\cdot\left(\rho\mathbf{v}h_{tot}\right)=\nabla\cdot\left(\kappa\nabla T\right)+\nabla\cdot\left(\mathbf{v}\cdot\tau\right)+\mathbf{S}_{emag}+\mathbf{S}_{E} \tag{9.8}$$

where eq. (9.8) is the conservation of total energy equation and h_{tot} is the total enthalpy, related to the static enthalpy through $h_{tot}=h+1/2\mathbf{v}^2$. The electromagnetic force source term for an electrically conducting fluid is $\mathbf{F}_{emag}=\mathbf{J}\times\mathbf{B}$. Electric and magnetic vector potential are defined to provide closure for eqs. (9.6) to (9.8), following the relations discussed in chapter 3

$$\mathbf{E}=-\nabla\phi-\frac{\partial\mathbf{A}}{\partial t} \tag{3.9'}$$

$$\mathbf{B}=\nabla\times\mathbf{A} \tag{9.9}$$

The transport equation for the electric potential is obtained assuming conductive media and neglecting the transient terms

$$\nabla\cdot\left(-\sigma\nabla\phi\right)=\nabla\cdot\left(-\sigma(\mathbf{v}\times\mathbf{B})\right) \tag{9.10}$$

A similar equation is obtained for the magnetic vector potential, assuming uniform magnetic permeability and enforcing the Coulomb gauge $\nabla\cdot\mathbf{A}$, that can be written with the expression

$$\nabla\cdot\left(\frac{1}{\mu}\nabla\mathbf{A}\right)=\sigma(\mathbf{E}+\mathbf{v}\times(\nabla\times\mathbf{A})) \tag{9.11}$$

Solving eqs. (9.10) and (9.11) allows to properly calculate the current density in the fluid and, from that, the source terms modeling the MHD effects in eqs. (9.7) and (9.8). The current density can be obtained either from the Ohm's law

$$\mathbf{J}=\sigma(-\nabla\phi+\mathbf{v}\times\mathbf{B}) \tag{9.12}$$

or the Ampere's circuital law

$$\mathbf{J}=\frac{1}{\mu}\nabla\times(\nabla\times\mathbf{A})=-\nabla^2\mathbf{A} \tag{9.13}$$

To activate the electromagnetic model, a fluid material with specified electrical conductivity and magnetic permeability properties must fill the computational domain. The model is composed by two separate modules: the electric one, which adds eq. (9.10), and the magnetic one, which adds eq. (9.11). Regarding the first, it is also possible to define a static electric field to model electrohydrodynamic problems in electrically charged fields, for which no magnetic field can be present. On the other hand, the electric model can be flagged to solve eq. (9.10), which needs a specified magnetic model to work: either a static field, equivalent to the induction-less approximation, or one calculated through eq. (9.11).

Theoretically, it should be possible to use CFX to model MHD flows where the self-induced magnetic field is not negligible employing the magnetic vector potential option, even if this possibility has not been investigated in the framework of this work. Conjugated heat transfer is one of the features offered by ANSYS CFX, which allows to model the heat transfer in a solid domain through the specification of suitable interface boundary conditions, and the same technique is used to solve eq. (9.10) for conjugated electromagnetic calculations.

9.5 Validation Methodology

In this chapter, several benchmarks are performed to assess the capability of ANSYS CFX to simulate and recreate the fundamental features of a wide range of MHD phenomena encountered in water-cooled LM blankets. A rigorous validation methodology is required to establish the reliability of the code results and to judge if and, moreover, to what extent they can be useful to support the blanket design and other reactor systems that may involve LM MHD flows like, for instance, the Plasma-Facing Components (PFCs). Previous validation efforts for this code have been reported in the literature but are either based on outdated versions of the code, where no MHD model was present and the governing equations had to be implemented with user-defined functions [111,112,125], or are rather limited in scope to simple flow cases or low Hartmann number [109, 121].

Forced convection, magneto-convection (buoyancy-driven) and free surface flows are considered as the most important classes of phenomena and are the focus of the validation procedure described in this chapter. Other relevant phenomena such as the magnetic field influence on mass transport and turbulence are currently ignored, but will have to be considered in the future for a more thorough assessment.

Following the recommendations reported in the paper from Smolentesev et al. [1], two forced convection benchmarks are performed covering two-dimensional and three-dimensional laminar MHD flows. Their results are reported in Sections 9.6 and 9.7.

The two-dimensional MHD forced convection benchmark is split in two test cases concerning the flow in rectangular channels of different conductivity. First, the flow in a duct with perfectly insulating walls, also known as Shercliff case, is considered. An analytical solution for this problem has been published in Ref. [42] and its main features are discussed in Section 3.6. The second test case assumes a duct with non-uniform wall conductivity, where the side walls are perfectly insulating and the Hartmann walls are electrically conductive. This problem was first treated and solved theoretically in Ref. [45] and it is also known as Hunt-II flow (or simply Hunt flow). The main features of this case are described in Section 3.6. For the benchmark, a finite conductivity Hartmann wall with $c = 0.01$ is considered [1]. For both test cases, the accuracy with respect to the analytical velocity profile and the dimensionless flow rate $\tilde{Q}$ are the indexes that are employed to assess the results quality.

The three-dimensional MHD forced convection benchmark considers the flow in a finite conductivity pipe where a non-uniform (fringing) magnetic field is applied, causing the appearance of 3D currents that are responsible for an additional pressure drop term. For this test case, the comparison with experimental results is performed with regard to the axial pressure gradient (APG) and transversal pressure difference (TDP) between the pipe wall and center, which can be considered as a local index for the magnitude of the 3D currents [2, 3].

For the magneto-convection problem, the fully developed laminar flow in a infinitely tall rectangular duct is considered as the test case for the code validation. Analytical solutions for this problem have been developed for differentially and internally heated ducts, which are characterized by, respectively, a linear and parabolic temperature profile [4, 51]. For the differentially heated duct, both per-

fectly insulating and conducting walls are considered in the benchmark, whereas the internally heated problem was limited to perfectly conducting walls for the lack of a theoretical solution or reliable numerical results for insulating ducts. To assess the results quality for the magneto-convection benchmark, the numerical velocity profile is compared with the analytical one: an estimate of both local error (peak velocity) and integral error (on the whole duct cross-section) is provided. The results of the magneto-convection benchmarks are presented in Sections 9.8 and 9.9

To validate the code with regard to free surface problems, the case of a fully developed thin-film flow bounded by perfectly insulating walls is considered. In Section 9.10, the code results are validated employing the analytical solution by Shishko et al. [5] and their quality is evaluated by the comparison between the velocity profiles.

9.6 Fully developed laminar steady pressure-driven MHD flow

The geometry of this benchmark is analogous to the one presented in Figure 3.1. A vertical magnetic field is applied to the square channel and the flow is driven by a constant and uniform pressure gradient. Furthermore, the flow is assumed to be in fully developed condition. The duct is filled with isothermal PbLi at $T = 599$ K, which physical properties are evaluated according to the correlations presented by Jauch et al. [61] and are collected in Table 4.2. For the Hunt-II case, the Hartmann wall is made of Eurofer, which electrical conductivity is evaluated from Mergia and Boukos [62].

Periodic boundary conditions at the front and back surfaces of the channel are employed to simulate a duct of infinite axial length. The dimensionless flow rate is defined through the expression

$$\tilde{Q} = \int_{-1}^{1} d\tilde{y} \int_{-1}^{1} \tilde{u}\, d\tilde{z} \tag{9.14}$$

and it is calculated employing the dimensionless axial velocity $\tilde{U}$, which is normalized adopting the following scale

$$\tilde{u} = \frac{u}{\left[\frac{b^2}{\nu\rho}(-\frac{dp}{dx})\right]} \tag{9.15}$$

The axial velocity is obtained from the analytical solutions in Refs. [42] and [45] for, respectively, the Shercliff and Hunt-II case. The pressure gradient in the duct is $-dp/dx$, the cross-sectional coordinates are scaled as $\tilde{z} = z/a$ and $\tilde{y} = y/b$, where z is the direction along the magnetic field and a is the half-width of the duct.

The results reported in this Section are also described in Ref. [29] for the Shercliff case and in Ref. [75] for the Hunt-II case. The Shercliff-Hunt solution reformulated by Ni et al. is employed to validate the velocity profiles [39].

9.6.1 Shercliff case

To simulate the Shercliff case, all the duct walls are modeled with the "zero flux" boundary condition. In Figure 9.5, numerical results for the velocity profile in the

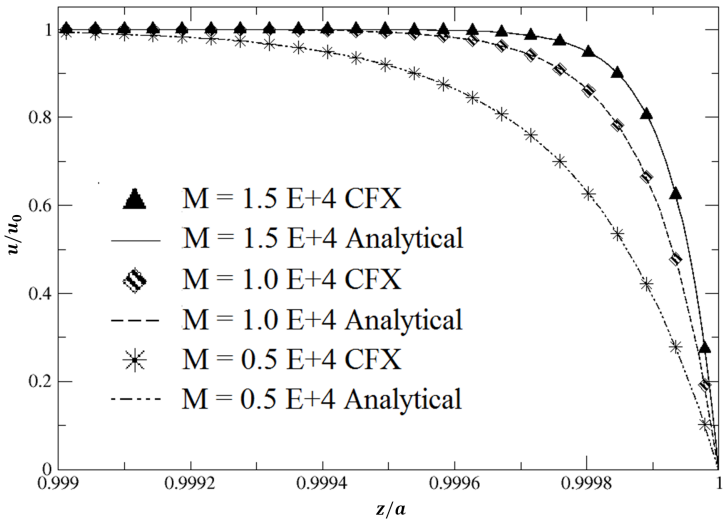

Figure 9.5. Hartmann velocity profile validation for $Ha = 5000,\ 10000,$ and 15000

Table 9.1. Dimensionless mass flow rate validation for the Shercliff case

	$\tilde{Q}$ Analytical [1]	$\tilde{Q}$ Numerical	Error (%)
$Ha = 500$	$7.680 \cdot 10^{-3}$	$7.772 \cdot 10^{-3}$	0.54
$Ha = 5000$	$7.902 \cdot 10^{-4}$	$7.919 \cdot 10^{-4}$	0.21
$Ha = 10000$	$3.965 \cdot 10^{-4}$	$3.965 \cdot 10^{-4}$	0.01
$Ha = 15000$	$2.648 \cdot 10^{-4}$	$2.660 \cdot 10^{-4}$	0.44

Hartmann boundary layer (symbols) are compared with the analytical solution (lines) at $Ha = 5000,\ 10000,$ and 15000, whereas results for the dimensionless flow rate are collected in Table 9.1 for every Ha. The code shows an excellent agreement with the theoretical solution featuring an error $\approx 0.5\%$ for the selected index.

9.6.2 Hunt-II case

To simulate the Hunt-II case, the side walls are modeled with the "zero flux" boundary condition. A solid domain of suitable thickness is employed to model a Hartmann wall with $c = 0.01$ and the electric potential equation is solved in both the conjugated solid and fluid domain. The velocity profile validation is presented in Figure 9.6: the side and Hartmann wall profiles are shown for $Ha = 500$ in Figures 9.6a and 9.6b, whereas the electric potential and side wall velocity profile are presented for $Ha = 15000$ in Figures 9.6c and 9.6d. The results for the dimensionless flow rate are collected in Table 9.2. The code shows an excellent agreement with the theoretical solution for $Ha = 500 \div 10000$, where the error is $\approx 0.5\%$. The code performance for $Ha = 15000$ is slightly worse with the peak velocity in Figure 9.6d being underestimated by $\approx 3\%$, as well as the dimensionless flow rate.

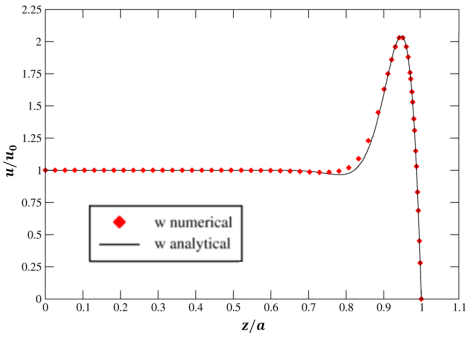

(a) Side velocity profile for $Ha = 500$

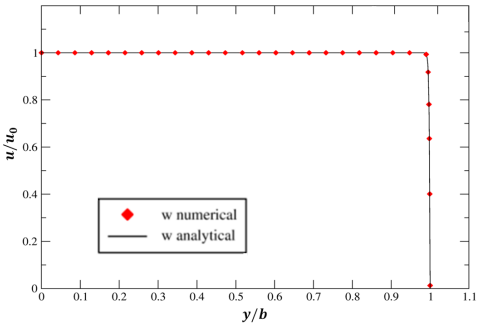

(b) Hartmann velocity profile for $Ha = 500$

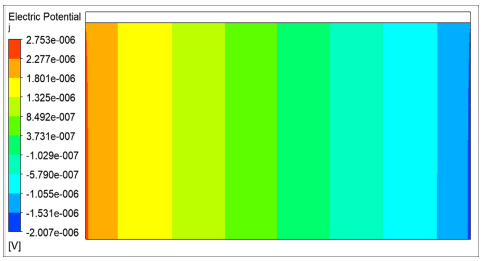

(c) Electric potential for $Ha = 500$

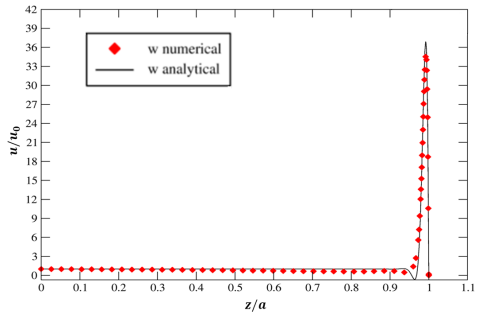

(d) Side velocity profile for $Ha = 15000$

Figure 9.6. Velocity profile and electric potential for the Hunt-II case

Table 9.2. Dimensionless mass flow rate validation for the Hunt-II case

	$\tilde{Q}$ Analytical [1]	$\tilde{Q}$ Numerical	Error (%)
$Ha = 500$	$1.405 \cdot 10^{-3}$	$1.418 \cdot 10^{-3}$	0.59
$Ha = 5000$	$1.907 \cdot 10^{-5}$	$1.897 \cdot 10^{-5}$	0.50
$Ha = 10000$	$5.169 \cdot 10^{-6}$	$5.143 \cdot 10^{-6}$	0.50
$Ha = 15000$	$2.425 \cdot 10^{-6}$	$2.493 \cdot 10^{-6}$	2.80

9.6.3 Summary

Excellent agreement with the analytical solutions was found for both the 2D MHD magneto-hydraulic benchmarks, as it was largely expected for these basic problems. Despite the good performance, the mesh refinement required to minimize the numerical error was very demanding for $Ha \approx 10^4$, since a sufficient number of nodes must be provided to accurately follow the sharp gradients in the jet region, in addition to the well known requirement in the Hartmann boundary layer, thus calling for large stretching factor to match the very refined jet mesh with the wide spacing adopted in the core region.

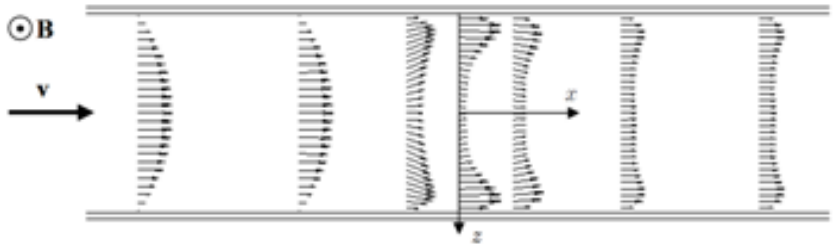

Figure 9.7. Velocity profiles in electro-conductive duct with non-uniform magnetic field [126].

Table 9.3. Dimensionless parameters for Benchmark Problem B1 [1].

	Ha	N	c
Pipe duct	6600	10700	0.027

9.7 3D laminar steady MHD flow in circular pipe with fringing magnetic field

In this Section, the 3D laminar steady flow in a non-uniform (fringing) magnetic field is considered. Such case is representative of the flow crossing a magnet boundary, for instance the TFC discussed in section 5.1.2, where the magnetic field is characterized by significant gradients in the stream-wise direction. This case follows the specifics outlined by Smolentsev et al. for the Benchmark Problem B1, which was presented in Ref. [1]. The results discussed in this Section were part of an activity described in more detail in Ref. [75].

In Figure 9.7, the velocity vectors across the channel are plotted at various axial locations. At the inlet, magnetic field is null and a hydrodynamic profile is observed. Moving along the stream-wise direction, the magnetic field starts to increase and the velocity profile flattens in the core region with jets appearing close to the side walls. Magnetic field variation in the stream-wise direction generates an axial potential difference, which drives currents upstream and downstream of the magnetic field gradient region. The induced axial currents close their path throughout the duct width and these transverse currents are responsible for a additional Lorentz force that opposes the flow movement. The fluid tries to bypass the channel center by flowing close to the lateral walls, where the retarding electromagnetic force is weaker: the velocity is strongly reduced in the core and increased near the walls. The main parameters of the benchmark are collected in Table 9.3.

To assess the quality of the numerical results produced by the code, experimental data produced during the campaign on the ALEX facility are employed. The original publications detailing these results can be found in Refs. [2, 3].

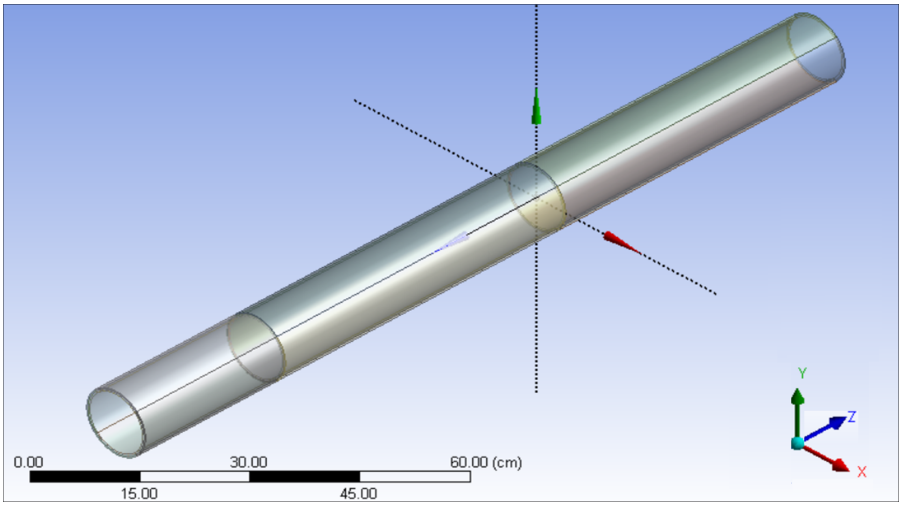

Figure 9.8. Benchmark Problem B1 geometry

Table 9.4. Benchmark Problem B1 parameters

Pipe inner radius	r_i	54.1	mm
Wall thickness	t_w	2.6	mm
Total pipe axial length	L	1352.5	mm
Mean velocity	u_0	7	cm/s
Magnetic field intensity	B_0	2.135	T

9.7.1 Numerical model

Figure 9.8 shows the geometry employed for the simulation of Benchmark Problem B1. The main geometrical and physics parameters are collected in Table 9.4. The fluid flowing in the channel is sodium-potassium alloy (NaK) and it is assumed to be isothermal at $T = 20°C$. Its thermo-physical properties are reported in Table 9.5. For the pipe wall, the only physical property of interest is the electrical conductivity, which is set arbitrarily to obtain $c = 0.027$ according to the pipe geometrical parameters.

The fluid is assumed to enter the duct in fully developed condition at the inlet, for which a suitable velocity profile is obtained through a 2D simulation employing periodic boundary conditions. At the interface between the fluid and pipe wall the no-slip boundary condition is enforced. At the outlet, relative pressure is set to zero.

In the upstream portion of the duct, magnetic field is uniform and constant $B = B_0\hat{y}$. The magnetic field variation along the stream-wise direction in the fringing region is described by the expression

$$\frac{B}{B_0} = 0.5\left[1 - \tanh\left(0.45(z/r_i - 0.4)\right)\right] \tag{9.16}$$

and it is represented in Figure 9.9. Since the pipe wall is characterized by finite wall conductivity, the fluid and solid domain are coupled through an interface in order to properly solve the electric potential equation. The external surface of the pipe wall is assumed to be in contact with a perfect dielectric medium.

Table 9.5. Thermo-physical properties for NaK [127]. For Benchmark Problem B1 the properties for $T = 20°C$ are employed.

T [°C]	ρ [kg m^{-3}]	ν [10^{-6} m^2 s^{-1}]	σ [10^6 S m^{-1}]
20	868.4	1.05	2.88
40	863.2	0.902	2.79
60	858.1	0.834	2.70

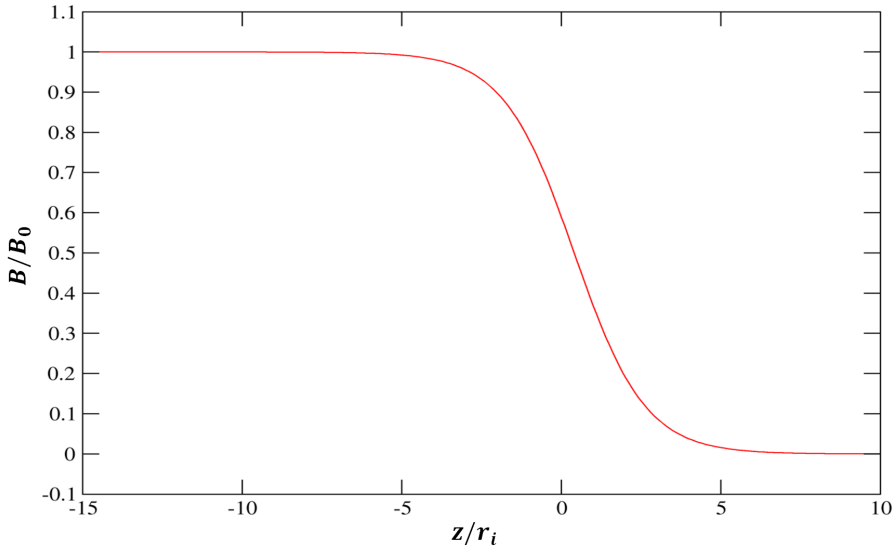

Figure 9.9. Benchmark Problem B1 magnetic field

To validate the numerical results, two quantities are considered: axial pressure gradient (APG) and transverse pressure difference (TPD). In general, both quantities are a function of the stream-wise coordinate due to the non-uniform magnetic field and the transverse pressure difference is defined between the wall and pipe center. It is generally considered to be a reliable indicator of the 3D effects magnitude [3].

The dimensionless APG is defined using the expression

$$\text{APG} = \frac{\partial p}{\partial z} \cdot \frac{1}{\sigma u_0 B_0^2} \tag{9.17}$$

Whereas the transverse pressure difference is expressed as

$$\text{TPD} = \frac{p_c - p_w}{r_i \sigma u_0 B_0^2} \tag{9.18}$$

Where p_c and p_w are the pressure at wall and pipe center.

9.7.2 Benchmark results

In Figures 9.10 and 9.11, validation against the experimental data for the two quantities of interest are presented. For the axial pressure gradient, the code slightly overestimates it in the upstream region but, otherwise, a good agreement with

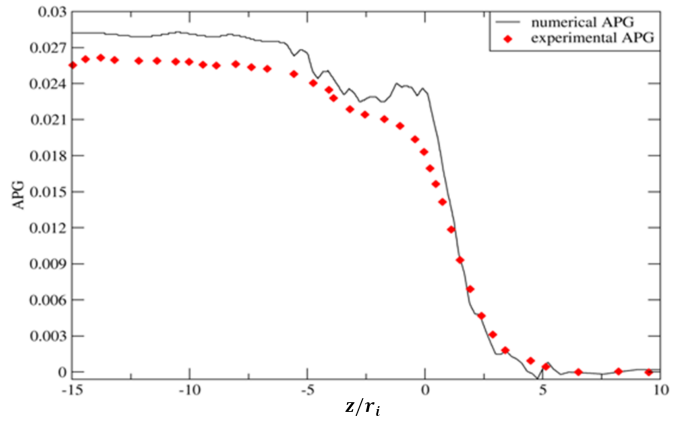

Figure 9.10. Benchmark Problem B1 axial pressure gradient validation

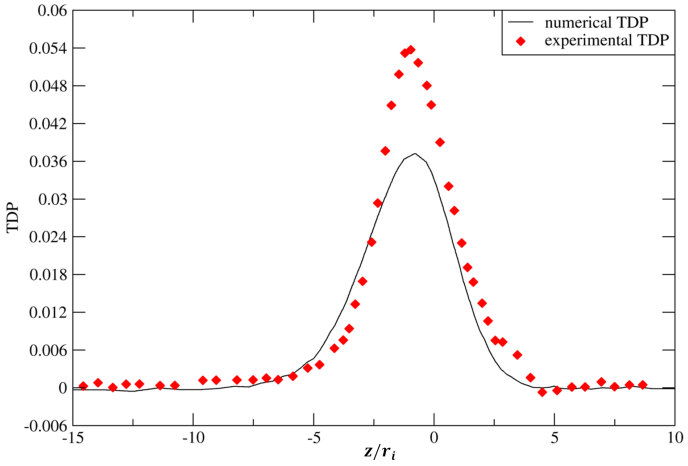

Figure 9.11. Benchmark Problem B1 transverse pressure difference validation

the experimental data is observed. The total integral error for the whole duct is estimated to be about 8%, therefore the code is able to reliably calculate the 2D pressure drop term in the conduit.

Instead, a worse performance is observed for the prediction of the effect caused by the 3D currents, where the code overall underestimates the TDP and, thus, the magnitude of the currents. The maximum error is found at the peak in Figure 9.11 and it is equal to about 31%. Overall, the agreement with the experimental data is acceptable and, if the error on the 3D pressure drop can be assumed to be similar to the TPD integral error, the code is going to underestimate it for about 20%.

However, it should be noted that an error of similar magnitude for the transverse pressure difference estimate in this benchmark has been reported in the literature by Ni et al. [128] for HIMAG, which featured an underestimate $\approx 20\%$, and, more recently, by Gajbhiye et al. [105] for Anuprahava-1 ($\approx 30\%$) that, however, considered the Benchmark Problem B2 featuring a rectangular duct.

Possibly, the TDP underestimate can be related to the numeral strategy adopted

for the modeling of the non-uniform magnetic field. In principle, the magnetic field applied to the pipe must satisfy the divergence-free and curl-free conditions but, in fact, it is represented in the numerical model as being composed by just an unidirectional component. Such a field it is not, in general, consistent with the real 3D magnetic field employed in the experiment and can lead to the inaccurate prediction of the pressure drop in the numerical model. It has been recently demonstrated by Albets-Chico et al. that a refined numerical model employing a 3D magnetic field recreated from the consistent best-fit of the experimental data can significantly improve the transverse pressure difference estimate [129].

Despite this important result, it was pointed out by Gajbhiye et al. that the information provided in the original references [2, 3], used to derive the benchmark specifications, are not sufficient to unequivocally recreate the experimental magnetic field and that, moreover, the issue of the sensitivity of the numerical results to the use of different interpolation techniques has not been addressed. In particular, Gajbhiye et al. demonstrated that a better estimate of the transverse pressure difference can be obtained even with an inconsistent magnetic field by switching from the traditional tangent hyperbolic function (as the one employed in eq. (9.16)) to a 5-parameter logistic fit [105].

In conclusion, a case can be made that the performance of ANSYS CFX in this benchmark, despite being improvable, shows a reasonable agreement with the experimental data and it is consistent with the results presented in the literature for the validation of similar numerical tools.

9.7.3 Summary

The flow in a electro-conductive circular pipe subjected to a non-uniform magnetic field is employed as a benchmark to test the capability of ANSYS CFX to represent laminar steady 3D MHD flows, as it was proposed by Smolentsev et al. [1]. Experimental data, presented in Refs. [2, 3], are employed to validate the numerical results.

The code is found to have a reasonable agreement with the experimental data since it is able to reproduce the pressure gradient and transverse pressure difference trends with the stream-wise direction. A larger error is observed for the estimation of the latter quantity, which is correlated to the intensity of the 3D currents appearing in the pipe. This occurrence is going to lead to the underestimation of the 3D pressure drop and it can probably be related to the numerical strategy adopted for the implementation of the magnetic field in the numerical model. However, similar errors have been reported in the literature for other CMHD code and the CFX performance can be considered as consistent with the average accuracy. A more refined implementation of the fringing magnetic field and/or the adoption of a variation law more akin to the actual experimental conditions could further improve the code performances.

In the future, the rectangular duct benchmark for a fringing magnetic field, described in Ref. [1] as Benchmark Problem B2, will be performed to better validate the capability of CFX to simulate laminar 3D MHD flows in non-uniform magnetic fields.

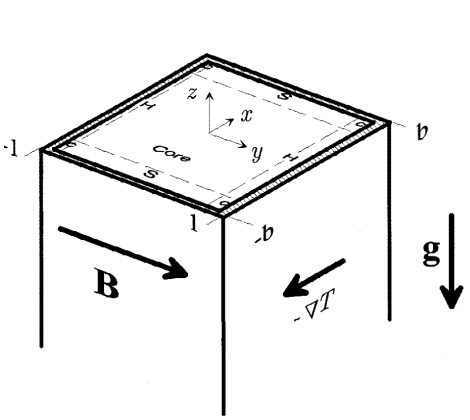

(a) Duct geometry

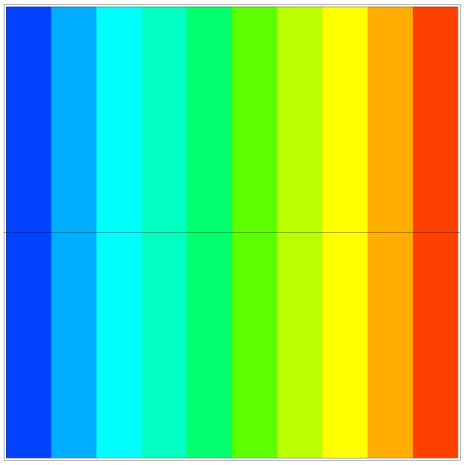

(b) Temperature contour

Figure 9.12. Benchmark geometry [4] and temperature distribution in the duct

9.8 Magneto-convection in differentially heated duct

The benchmark geometry is represented in Figure 9.12a. A constant linear temperature gradient is applied to the flow such that $\nabla T = \hat{x}$. The side walls are kept at a constant temperature, whereas the Hartmann walls are adiabatic. The magnetic field is transverse to the flow and perpendicular to the temperature gradient, whereas the gravity vector is aligned with the duct axis. Fluid physical properties are assumed to be constant in the temperature range observed in the duct and are evaluated at the reference temperature $T_0 = 599$ K (see Table 4.2).

The analytical solution employed to validate the numerical results assumes that inertial effects in both the momentum and energy equation can be neglected, i.e. $Gr/Ha^4 \ll 1$ and $Pe \ll 1$ [4]. Given the value of Ha, the characteristic temperature difference in the duct is obtained from Gr that satisfies the inertia-less condition. The analytical solution is valid only for electro-conductive walls, i.e. $c_s \gg Ha^{-1/2}$, therefore for insulating walls the numerical results presented in Refs. [52, 111] are used for the validation purpose[1]. Validation involves the estimate of a local (peak velocity) and integral (on the whole-cross section) error: for the perfectly conducting case, direct comparison is presented between the numerical and theoretical velocity profile across the side walls. Velocity in the duct is scaled accordingly to the magneto-convection characteristic velocity $w_0 = \nu Gr/Ha^2 L$, where L is the characteristic length that, in this case, corresponds to the half-width of the channels. The results presented in this Section have been previously published in Ref. [130].

9.8.1 Perfectly insulating duct

To simulate the perfectly insulating case, all the walls are modeled with the "zero flux" option for the electric potential model that basically enforces a Neumann boundary

[1] At the time, we did not know that an analytical solution was obtained by Blosseville et al. for this case [51]

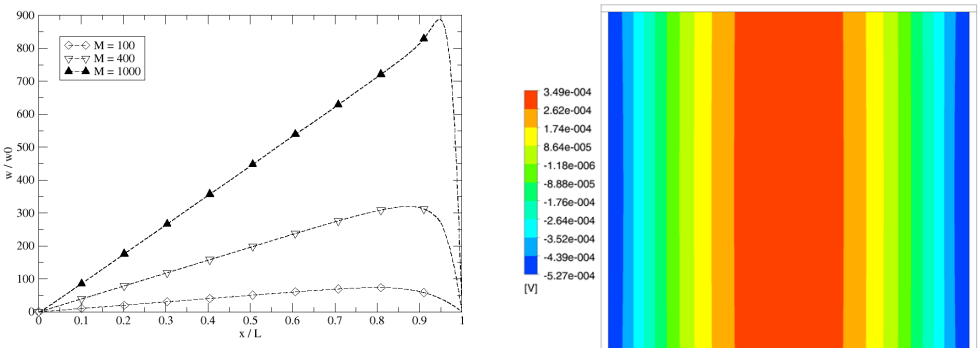

(a) Side velocity profile for $Ha = 100$, $Ha = 400$, and $Ha = 1000$.

(b) Electric potential contour

Figure 9.13. Velocity profile and electric potential contour for the differentially heated perfectly insulating case. The velocity profile refers to the half of the duct close to the hot wall [130]

condition ($\partial\phi/\partial n = 0$). The velocity profile is presented in Figure 9.13a and the electric potential contour in Figure 9.13b. In the insulating duct, the currents cannot penetrate the bounding walls and are forced to close through the boundary layers. Due to the opposite movement of the jets appearing close to the hot and cold wall, the currents appearing in the side layers are reversed with regard to each other and four current path loops are formed centered on the duct corners (see Figure 3.6a). The velocity in the core takes the form $w \approx Ha \cdot x$ and the almost linear velocity profile is correctly represented by the code, as it can be seen in Figure 9.13a. For this case, the integral error was not computed due to the lack of an analytical solution since, when the study was performed, we were not aware of Ref. [51].

The results for the peak error are collected in Table 9.6. The code is able to represent all the significant flow features and shows an acceptable agreement with the numerical results presented in the literature. Maximum error for the peak velocity does not exceed 5%.

9.8.2 Perfectly conducting duct

To simulate the perfectly conducting case, all the walls are modeled with the "ground" option for the electric potential model that basically applies a Dirichlet boundary condition ($\phi = 0$). The validation of velocity profiles against the theoretical solution is presented in Figure 9.14, whereas the peak and integral errors are collected in Table 9.6.

For perfectly conducting walls, the electric potential contour is presented in Figure 9.14d. The potential is significantly different than for the insulated case: the core potential is constant perpendicular to magnetic field lines, whereas it exhibits a parabolic distribution in the direction parallel to them. Consequently, the velocity in the core is linear and independent by the Hartmann number. However, this results in a steep potential gradient in the side layer that drives the flow from the duct center to the side walls. Similarly to what is observed for the insulating duct, jets aligned in opposite direction appear close to the hot and cold wall but, in this case,

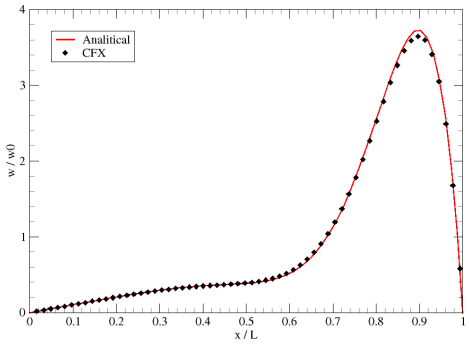

(a) Side velocity profile for $Ha = 100$

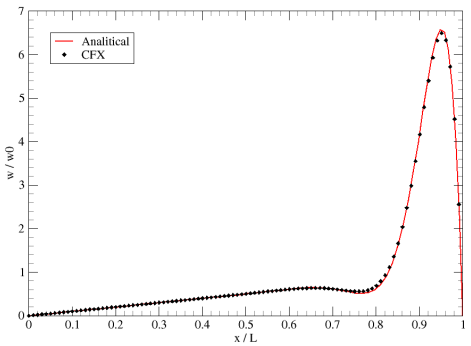

(b) Side velocity profile for $Ha = 400$

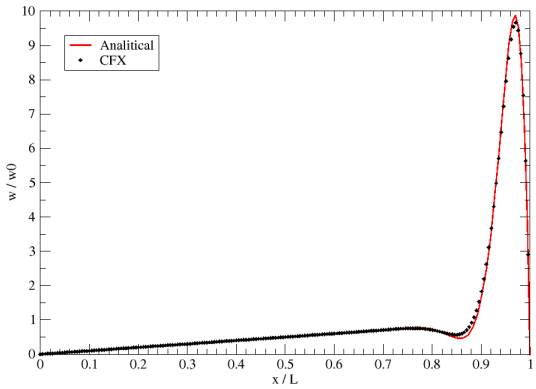

(c) Side velocity profile for $Ha = 1000$

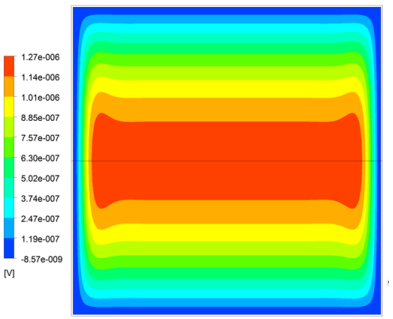

(d) Electric potential contour

Figure 9.14. Velocity profile and electric potential contour for the differentially heated perfectly conducting case. The velocity profile refers to the half of the duct close to the hot wall [130]

they overshoot significantly the velocity scale in the core. All these features are properly represented by the code.

The peak velocity error for all the cases considered is $\approx 2\%$, whereas the error on the velocity profile error is even smaller, being $\approx 1.5\%$. The code performances for this benchmark are in excellent agreement with the theoretical solution.

9.8.3 Summary

In this benchmark, the magneto-convection in a differentially heated duct is studied considering the limiting cases of perfectly conducting and insulating walls. The performances of the code are validated employing the analytical solution by Bühler for the former case [4] and numerical results in Refs. [52,111] for the latter. CFX has shown excellent performances in the prediction of flow features and the capability to model finite conductivity cases was demonstrated in Ref. [130]. However, the validation process has been limited to relatively low magnetic field intensity ($Ha \leq 1000$) and in the future it would be desirable to extend the benchmark to a parameter range closer to blanket conditions.

Table 9.6. Validation results for the differentially heated duct benchmark according to peak (p.e.) and integral error (i.e.)

c	Ha	p.e.[%]	i.e.[%]
0	100	0.68	n.a.
	400	4.08	
	1000	2.08	
∞	100	2.01	0.79
	400	1.26	1.49
	1000	2.20	1.46

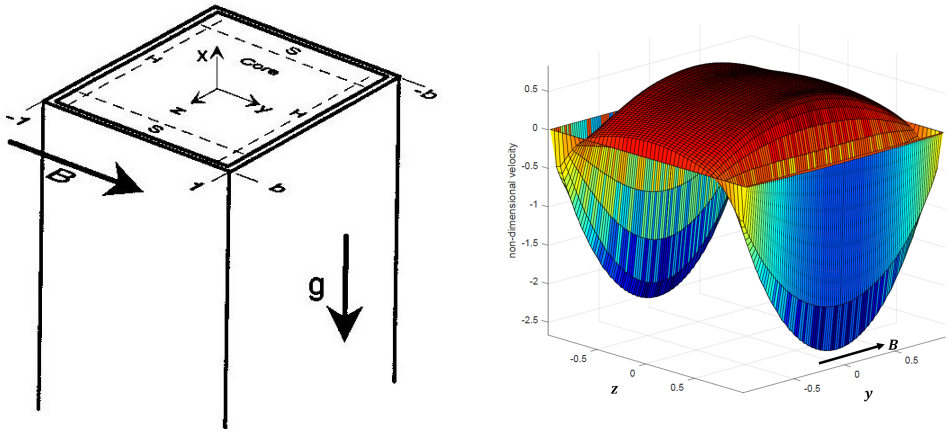

(a) Duct geometry

(b) Velocity profile for $Ha = 100$

Figure 9.15. Internally heated duct benchmark geometry [4] and velocity profile for $Ha = 100$

9.9 Magneto-convection in internally heated duct

The results presented in this Section were part of an activity described in more detail within Ref. [131]. The analytical solution developed by Bühler [4] is employed to validate the results of this benchmark. A channel with square cross-section and infinite axial length is considered. A strong uniform external magnetic field is applied and it is parallel with one pairs of duct walls. All the walls are perfectly conducting, gravitational acceleration is in the direction of the channel axis and a uniform volumetric heat generation across the duct is present. Hartmann walls are assumed adiabatic and the heat is removed only at the sidewalls, which are both kept at the same constant temperature. The heat source determines a parabolic temperature profile along z-direction. The flow is supposed laminar during the whole analysis.

The velocity, current density, pressure, volumetric heat source and electric potential are scaled with $u_0 = \nu Gr/LHa^2$, $j_0 = \sigma u_0 B$, $Lj_0 B$, $\kappa\Delta/L^2$, and $Lu_0 B$. L is the duct half-width and, in this case, the duct aspect ratio is equal to $b = 1$. The dimensionless analytical solutions for temperature, electrical potential and velocity take the form

$$T = -1/2 \cdot z + \Theta \tag{9.19}$$

Table 9.7. Grid sensitivity test matrix for the internally heated duct benchmark

Hartmann number	Side layer elements	Selected mesh number of elements
500	10, 50, 100	$6.6 \cdot 10^5$
5000	10, 50, 80, 150*	$1.5 \cdot 10^6$
10000	50, 200*	$5.1 \cdot 10^6$
15000	50, 200, 250*	$5.35 \cdot 10^6$

$$\phi = \phi_H - z/2 \cdot (y^2 - 1) \tag{9.20}$$

$$U_{core} = 1/2[1 - y^2 - (1 + C_H^{-1})z^2] + (1 + C_H^{-1})\Theta \tag{9.21}$$

$$U_{side} = \frac{\sum_{k=1}^{\infty}(-4 \cdot \alpha_k)}{\beta_k}\left[b + c_s^{-1} \cdot \left(\Theta - \frac{b^2}{2}\right)\right] \cdot Ha^{1/2} e^{-\zeta\alpha_k} \sin(\zeta\alpha_k)\cos(\beta_k y) \tag{9.22}$$

where coefficients Θ, ϕ_H, C_H, and ζ are dependent by Hartmann number and are defined in Ref. [4]. The velocity solution is obtained by the sum of core velocity (eq. (9.21)) and the side layer correction (eq. (9.22)), for which only the leading order term is considered.

In Figure 9.15b, a typical velocity profile for this kind of flow is presented. Despite all the walls being perfectly conducting, high velocity jets are found in the side layers while they are not observed in classical pressure-driven duct flow problems. In these jets, the fluid flow has opposite direction respect to the core region. For strong values of magnetic field, the asymptotic solution shows also the presence of "positive jets" in the region matching core and side layer. The results demonstrate that the internally-heated buoyant flow in the core is far from being two-dimensional in the core, even if it is fully developed.

ANSYS CFX is employed to simulate the buoyancy-driven flow for $Ha = 500$, $Ha = 5000$, $Ha = 10000$, and $Ha = 15000$. Periodic boundary conditions at the top and bottom of the duct are used to simulate an infinite long channel, and the walls are modeled with the "ground" boundary condition to simulate a perfectly conducting material. The fluid filling the duct is PbLi, which is represented by the physical properties listed in Table 4.2. No-slip condition is enforced at the walls.

The mesh grid for every simulation depends on Ha. Velocity gradients that occur in the Hartmann and side layers require a minimum number of elements for being detected properly and, since the layer thickness scales with Ha^{-1} and $Ha^{-1/2}$, the mesh must be scaled accordingly. Two node resolution in the Hartmann layer is considered for all the test cases, whereas for the side layers, where high velocity jets take place, a grid sensitivity analysis has been performed. In Table 9.7, an overview of the grid sensitivity test matrix is collected. Additional simulations with refined core mesh in the y-direction are employed for $Ha = 5000$, $Ha = 10000$, and $Ha = 15000$. The final mesh is selected when the error percentage respect to the analytical solution is below 8% for the local jet velocity and 3% for the velocity integral. In Figure 9.16, the error trend for the side jet peak velocity is presented for the sensitivity grid analysis.

In Table 9.8, the code results are evaluated according to three indexes: the error on the side jet peak velocity, core jet peak velocity and on the velocity integral.

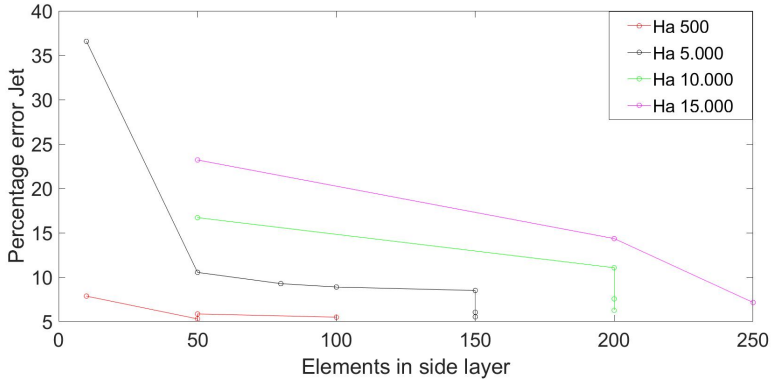

Figure 9.16. Percentage error on side wall jet plotted against number of elements in the side layer region for the internally heated benchmark. Refined core mesh results are reported as well

Table 9.8. Validation error for the internally heated duct

Hartmann number	Side jet error (%)	Core jet error (%)	Velocity integral error (%)
500	5.5	0.1	2.23
5000	5.5	9.8	2.18
10000	6.3	27.6	2.49
15000	7.2	38.4	2.8

ANSYS CFX shows an excellent agreement with the analytical solution with an error $\approx 2\%$ for the error on the velocity integral. The core jet usually features a bigger error compared with the side jet, but its overall influence on the flow is negligible since its velocity is much lower. In general, to obtain the same error a higher mesh resolution in the side layer is required for increasing Ha.

In Figure 9.17, the comparison with the analytical solution for the velocity profile across the side walls is presented, whereas in Figure 9.18 the complete velocity field in the duct is shown. The dimensionless core velocity from eq. (9.21) is not dependent on the magnetic field intensity but only on the dimensionless temperature (Θ) and the wall conductivity, therefore its contribution is equal for all the cases considered. In Figure 9.18a, it is possible to easily observe the parabolic distribution along the magnetic field lines of the core velocity. Conversely, the side layer correction described by eq. (9.22) is proportional to $Ha^{1/2}$ and this promotes the formation of stronger and thinner side jets with the increase of the magnetic field intensity, as it is possible to see in Figures 9.18b to 9.18d.

CFX predicts perfectly the non-uniform flow in the core region for all the cases considered, whereas the code struggles to properly render the steep gradients associated with the counter-flowing jets in the side layer. Acceptable performances in the representation of the jets ($\approx 20\%$ error) can be obtained even for a coarse mesh, as it is demonstrated in Figure 9.16, but perfect agreement can be achieved only for prohibitively dense mesh requirements.

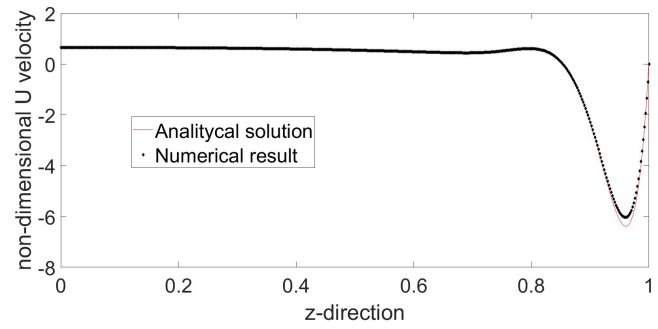

(a) $Ha = 500$

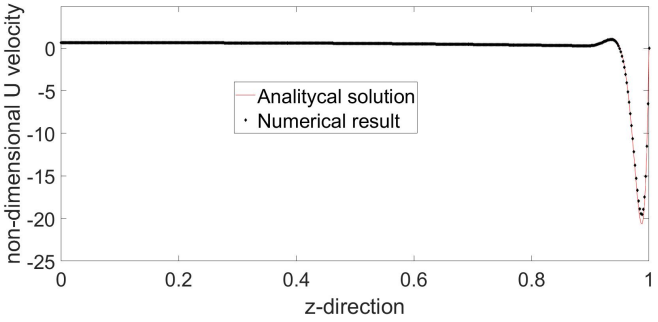

(b) $Ha = 5000$

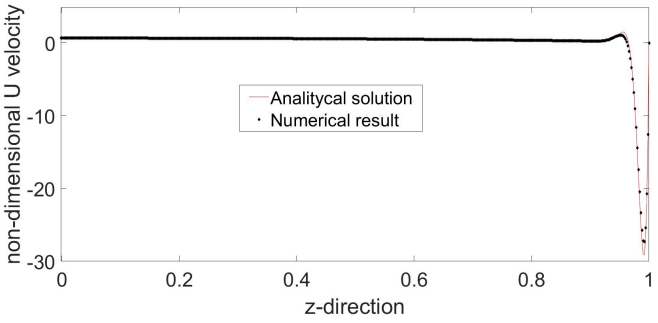

(c) $Ha = 10000$

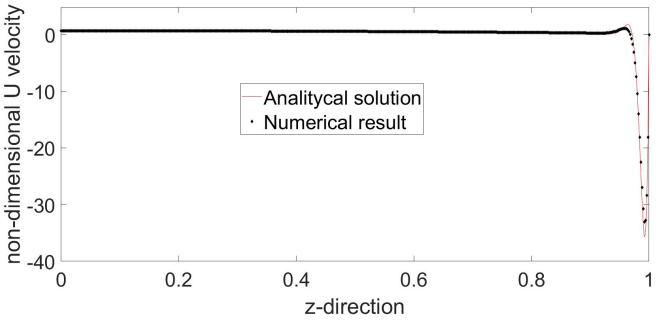

(d) $Ha = 15000$

Figure 9.17. Velocity profile validation against the analytical solution by Bühler [4]. The profile is symmetric across the $z = 0$ axis.

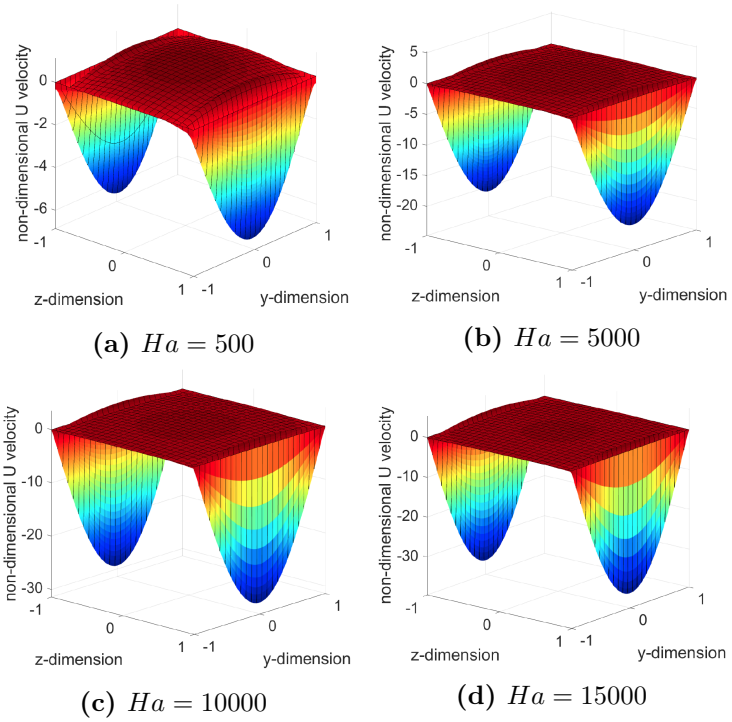

(a) $Ha = 500$ **(b)** $Ha = 5000$

(c) $Ha = 10000$ **(d)** $Ha = 15000$

Figure 9.18. Velocity field in the internally heated duct

9.9.1 Summary

In this benchmark, the magneto-convection in a internally heated duct is studied for the limiting case of perfectly conducting walls. CFX results are validated against the analytical solution proposed by Bühler [4] for magnetic field intensity up to $Ha = 15000$. An excellent agreement is found for all the cases considered, even if the side wall jet peak velocity is slightly underestimated by the code even for very refined mesh. The lack of theoretical results about finite conductivity and insulating walls has restricted the validation procedure for this case, but it would be desirable to extend the benchmark parameter range to more realistic wall conductance ratio. However, it should be noted that the results of a simplified analysis conducted for finite conductivity and insulating walls, presented by Sposito and Ciofalo in the context of mixed magneto-convection [132], have highlighted the absence of any significant flow rearrangement compared with the perfectly conducting case. A case could be made that the extension of the code validation to these conditions will not be worthy enough to justify the time and computational costs incurred.

9.10 Fully developed thin-film free surface flow

In this Section, the case of a steady fully developed thin-film flow of liquid gallium is analyzed to assess the capability of ANSYS CFX to simulate free surface flows in MHD conditions. Thin-film flows is of interest essentially for their application in Plasma-Facing Components (PFC), both divertor and first walls, where they could provide many attractive features compared with the traditionally considered

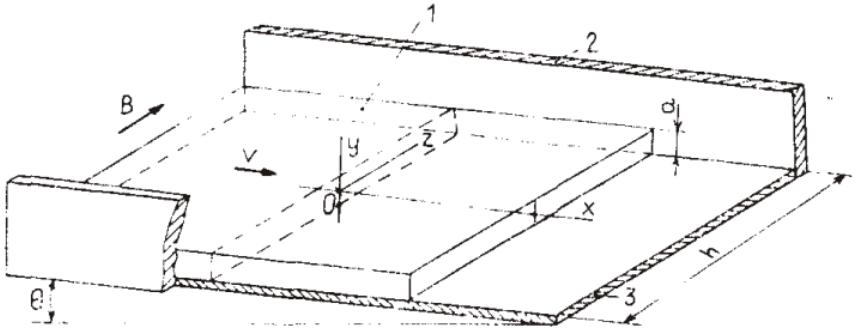

Figure 9.19. Thin-film flow case geometry. 1) Gallium, 2) lateral wall, 3) backing plate

Table 9.9. Gallium physical properties evaluated at $T = 30\ °C$ [135]

Density [kg/m^3]	ρ	6093
Kinematic viscosity [m^2/s]	ν	$3.1{\cdot}10^{-7}$
Electrical conductivity [S/m]	σ	$3.85{\cdot}10^{6}$

configurations. Among these advantages the most important are enhanced power removal capability, thanks to the liquid metal being able to fulfill the roles of both armor and coolant, and less susceptibility to permanent damage from the extreme reactor environment [133]. The results presented in this Section were part of an activity described in more detail in Ref. [134].

In Figure 9.19, the geometry of the duct hosting the liquid metal is represented. The flow is located in a rectangular channel with non-conductive walls and a steady, uniform, and perfectly coplanar magnetic field is applied. The magnetic field, gravity acceleration vector and flow direction are aligned respectively with the z, y, and x axes. The liquid gallium is assumed to be isothermal and its properties are evaluated at $T = 30\ °C$ (see Table 9.9).

This case was analytical resolved by Shishko et al. [5]. A fully developed flow is characterized by a precise correlation between the height (a) and the width (h) of the film, expressed by the parameter $a^* = a/h$, and the mean velocity u_0, through the relation

$$u_0 = \left(\frac{h}{2}\right)^2 \frac{\rho g \sin\theta}{\mu Ha} \frac{F}{t_f} \tag{9.23}$$

where F and t_f are functions depending on the geometry and boundary conditions of the case studied, and θ is the inclination of the duct holding the flow against the horizon (i.e. x-axis) [5].

9.10.1 Numerical strategy and test matrix

The mean velocity in the duct is obtained through eq. (9.23) assuming a negligible duct inclination ($\theta \to 0$) and for given values of a^* and Ha. To get a fully-developed solution, translation periodicity BCs with an imposed mass flow rate $\Gamma = ah\rho u_0$ is established between the inlet and the outlet. This interface model allows to realize with a small computational cost a channel of "infinite length" but, however, to ensure

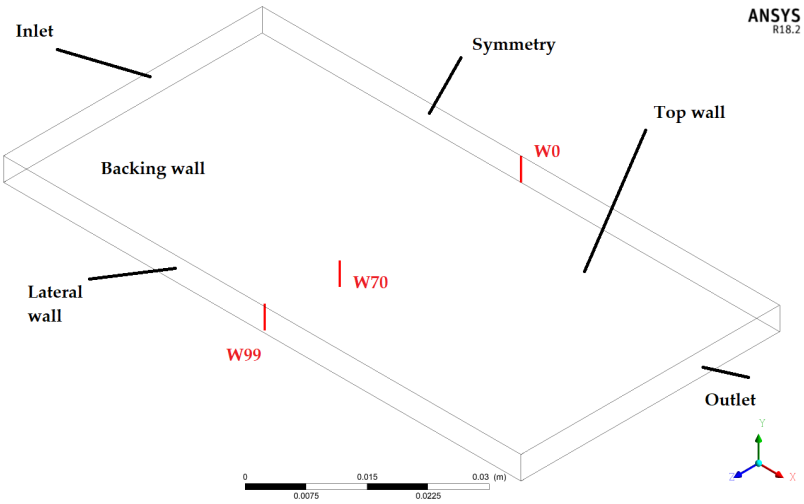

Figure 9.20. Domain, boundary conditions, and location for error evaluation. The geometry refers to Test Case A.

that no numerical instability appears in the model the stream-wise duct extension must be at least of the same order of magnitude as the channel width. Under these assumptions, the velocity in the channel is relatively small and the flow can be treated as induction-less and laminar.

An overview of the numerical model is presented in Figure 9.20. The lateral and backing wall employs the no-slip and perfectly insulated boundary conditions. The top wall is coincident with the thin-film free surface and, therefore, is modeled with the free-slip condition. A momentum source equal to $S_y = -\rho g \cos\theta \hat{y}$ is added to the fluid computational domain to allow the flow to retain the realistic pressure distribution in the film caused by gravity. This is necessary to ensure a physical velocity distribution in the film and, being the flow isothermal, is not possible to represent it through the CFX built-in buoyancy models that are only supported in the case of a model involving heat transfer[2].

The structured mesh is realized applying a manual non-uniform sizing (cell-to-cell ratio 1.1), refining the mesh at the Hartmann and side boundary layers (20 nodes each) and with a coarser resolution along the outflow direction. An example of the computational grid employed in this section is shown in Figure 9.21.

The quality of the numerical results is evaluated by comparing the integral value of the dimensionless velocity distributions through the thickness of the film at three different distance in the width direction placed at the centre of the length of the channel, as shown in Figure 9.20.

The benchmark test matrix is presented in Table 9.10. For $Ha = 500$, three a^* values are considered, which correspond to different flow features since for increasing a^* a slug-like flow develops at the center of the film. For $a^* = 0.1$, the $Ha = 1000$ case is also considered. Simulations are conducted at higher magnetic field intensity ($Ha = 2000$) for similar geometries to the one covered in Table 9.10 but failed to

[2] An analogous momentum source is formally required for the x-direction too, but $S_x = \rho g \sin\theta \hat{x} \approx 0$.

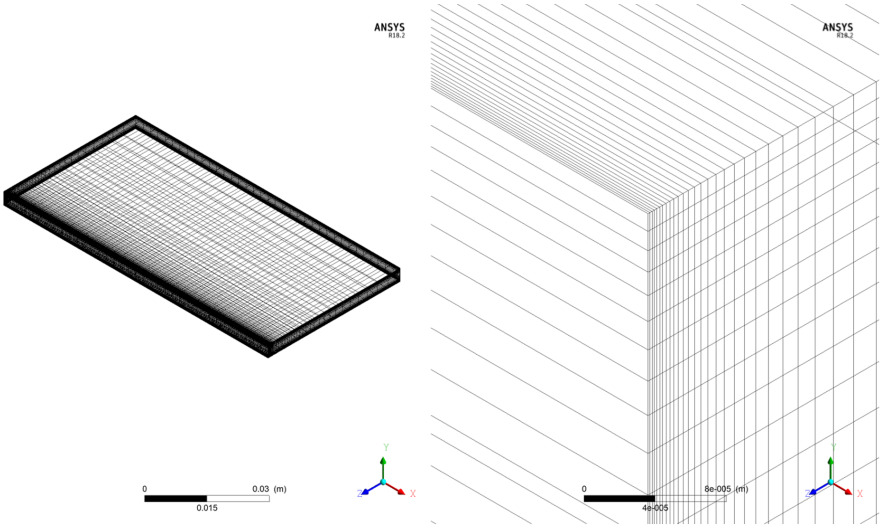

Figure 9.21. Numerical model mesh (left) and detail for the corner between the Hartmann wall and free surface (right)

Table 9.10. Matrix of simulation parameters

		Case A	Case B	Case B1	Case C
Film thickness (mm)	a	4	5		10
Relative thickness	a^*	0.044	0.1		0.2
Hartmann number	Ha	500	500	1000	500
Mean velocity (mm/s)	u_0	95.7	38.5	19.5	39.1
Interaction parameter	N	17.9	80.1	633	78.8

converge to a physical solutions.

9.10.2 Benchmark results

For constant Harmann number, an increasing a^* corresponds to an enhancement of the MHD effects through the flow, with the progressive definition of a core region, where a quasi-slug flow is observed, and two well-defined boundary layers, how reported by Shishko [5].

The velocity contours of the dimensionless velocity $u(y,z)/u_0$ are reported in Figure 9.23 for case A, B and C. It is noted that the different ratio between the thickness of the film and the width of the channel influences the velocity distribution also for the hydrodynamic flow, but it is particularly evident for the MHD results.

For $a^* = 0.044$, no core region is yet defined and, in fact, the film is so thin that it is not possible to discern a separation with the boundary layers at the backing plate and free surface. For $a^* = 0.1$, the increased relative thickness of the film causes the appearance of new flow features among which the flow suppression at the interface between the free surface and lateral walls. For $a^* = 0.2$, the two side layers at the free surface and backing plate are clearly defined, with the former one being a jet with peak velocity $u/u_0 = 1.8$. In the center of the film, a core with uniform velocity develops. This behavior can be explained because an increase in a^*

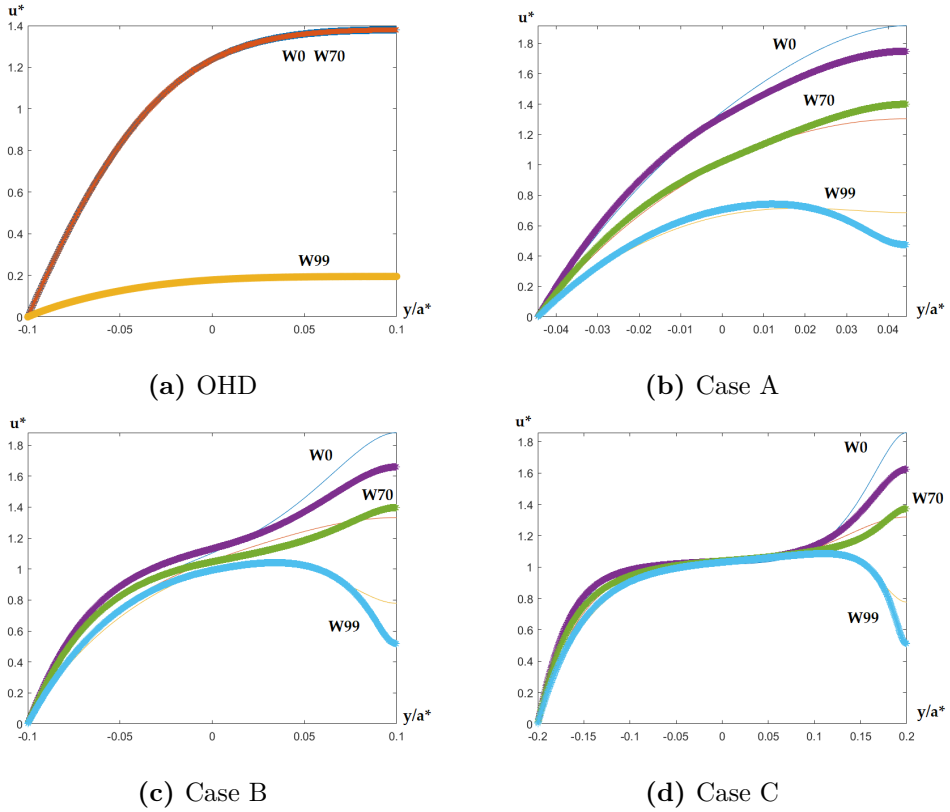

(a) OHD **(b)** Case A

(c) Case B **(d)** Case C

Figure 9.22. Velocity plots at W0, W70 and W99 and comparison with Shishko's analytical solution [5]

corresponds to an increase in the "active length" with respect to the "passive length" of the currents path through the film.

Figure 9.22 reports the velocity plotted against the scaled film thickness and compared against the velocity distribution obtained with Shishko's analytical solution. The thick lines represent the numerical results, whereas the thin lines are the theoretical benchmark. For reference, in Figure 9.22a the same comparison is made for the hydrodynamic flow in the case B geometry. The code is able to represent properly all the flow features but its performance is noticeably poorer in predicting the flow velocity at the free surface. In particular, the W0 peak velocity is under-predicted by around 15%, and an ever larger error is observed close to the wall.

The validation results are collected in Table 9.11. The integral error for the velocity profile is found to be below 4% for all the cases considered. Duct characterized by an higher relative thickness ratio a^* featured, in general, a better performance compared with thiner films. No significant error is found for the transition between the $Ha = 500$ and $Ha = 1000$ case.

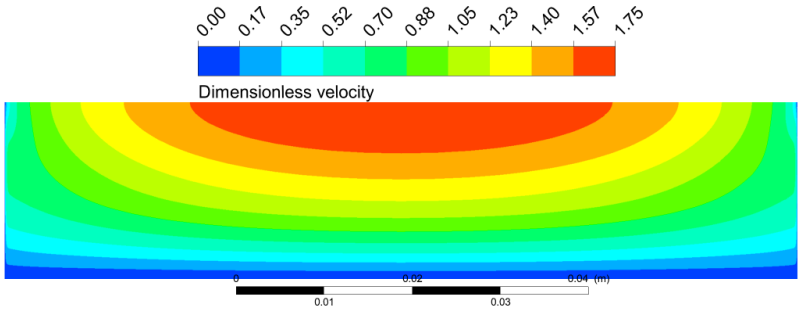

(a) $a^* = 0.044$

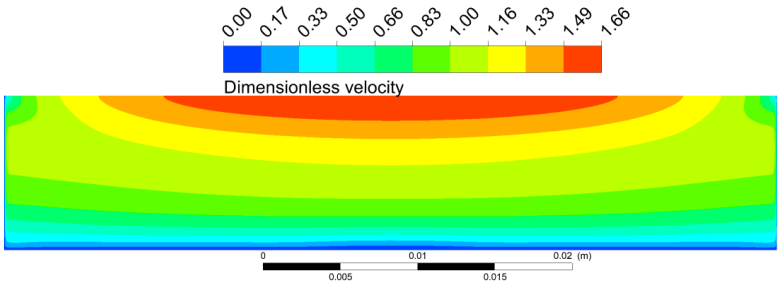

(b) $a^* = 0.1$

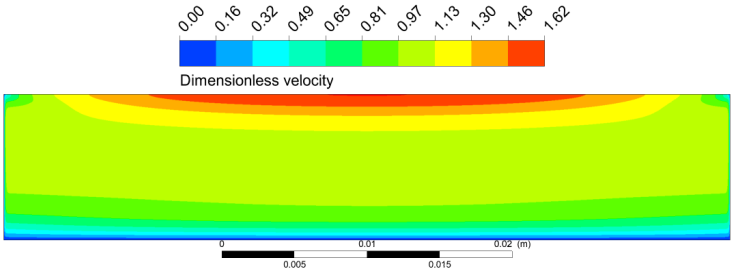

(c) $a^* = 0.2$

Figure 9.23. Velocity contour for Case A, B and C

9.10.3 Summary

The fully developed thin film flow in a rectangular channel enclosed by perfectly insulating walls is employed to validate ANSYS CFX performances for a free surface MHD flow. The simulation is performed adopting a single-phase model suitable for the treatment of fully developed, constant thickness flows. The numerical result quality are validated against the theoretical solution proposed by Shishko [5].

The code is able to accurately represent the flow features up to moderate film thickness and $Ha = 1000$. Simulations conducted with higher magnetic field intensity highlighted the impossibility to obtain a converged solution for $Ha > 1000$ even for a very simple case. Moreover, exorbitant computational time is required to reach the convergence, typically more than two weeks even for relatively low magnetic field intensity. Multi-phase models, tested in Ref. [134] alongside the single-phase model whose results are reported in this document, does not provide any significant

Table 9.11. Integral error of velocity profile compared with Shishko's analytical solution [5]

		Case A	Case B	Case B1	Case C
Center	W0	3.9%	1.6%	1.8%	0.95%
Middle	W70	3.9%	1.4%	1.4%	0.74%
Wall	W99	1.6%	0.79%	0.27%	0.15%

advantages, but conversely only further increase the computational cost.

Due to these limitations, the code will probably be of limited use in supporting the design of liquid metal PFCs in a tokamak environment. The development of custom numerical models for the investigations of free surface flows is advisable.

9.11 Conclusions

The electromagnetic model included in ANSYS CFX has been employed in this chapter to simulate a wide range of MHD phenomena expected in the blanket and other fusion reactor components: laminar 2D and 3D forced convection, magneto-convection in differentially and internally heated ducts, and free surface flows. The results have been validated with recommended analytical solutions and experimental data to assess their quality and the limitations of the code capability.

The code has shown an excellent agreement with the validation data up to $Ha = 10^4$ for simple geometries and fully developed flow condition in both forced convection and magneto-convection benchmarks. A typical 2% error is found for the non-local validation indexes, i.e. dimensionless flow rate and integral of velocity profile, and the code is able to properly represent all the expected flow features. The performances slightly degraded for the 3D forced convection benchmark where a significant error ($\approx 30\%$) on the peak transverse pressure difference is observed. Similar results obtained by dedicated MHD codes performing this benchmark have been reported in the literature, see for instance Ref. [105, 128], and they can be ascribed to the approximation of the experimental 3D magnetic field to a 1D best fit and the sensitivity of the results to the particular best-fit method adopted. Finally, the simulation of free surface flows has good agreement with analytical solutions for but, even for simple cases, it is limited in the current implementation to relatively low magnetic field intensity ($Ha = 10^3$) and, therefore, it is of questionable utility to support the design of LM PFCs.

The results collected by the validation benchmarks described in this chapter demonstrate that the capabilities of ANSYS CFX are consistent with the state-of-the-art of CMHD codes and that, therefore, it can be judged as a useful tool for performing numerical analyses to support LM blanket designs and investigate basic MHD phenomena. An example of the latter use is reported in Chapter 10 where the code is employed to perform numerical analysis of the forced convection around a refrigerated cylinder of arbitrary conductivity. Similarly, the mixed convection in the FW channel of the WCLL breeding zone is investigated in Chapter 11.

It should be noted how the results summarized in this chapter do not constitute a definitive assessment of the CFX capabilities and that, conversely, a more extensive

validation of the code including heat transfer, quasi-two-dimensional (Q2D) and 3D MHD turbulence and other relevant phenomena is strongly desirable. Proposed follow-ups of this validation procedure include the benchmarks recommended by Smolentsev et al. in Ref. [1] not considered herein, recreation of the experimental data that will be produced by the next generation of experimental MHD loops, etc.

Chapter 10

Forced convection flow around a transverse pipe

10.1 Introduction

The case of an incompressible fluid flowing around a cylinder of circular cross-section, whose axis is perpendicular to the stream-wise direction, is one of the classical and most studied problems in fluid-dynamics thanks to both its relative simplicity and importance for industrial applications. For an unbounded flow the main parameter of interest is the Reynolds number, which controls the transition between successive flow regimes. For $Re \to 0$, the observed flow is two-dimensional, steady and the velocity streamlines stick to the cylinder surface without the occurrence of any flow recirculation. This phenomenon, called *creeping flow* or *Stokes flow*, is strongly dominated by viscous forces and, thus, can exist only for low Re. Indeed, when Re increases the inertial forces cause flow separation in the cylinder wake with the formation of a recirculation region composed of two steady counter-rotating vortices, which are symmetrical across the wake centerline, and then the transition to an unsteady regime characterized by the alternated detachment of the vortices (*von Kármán vortex street*). A further increase in Re leads to the breakdown of the periodic laminar regime and the emergence of 3D features. Exhaustive reviews on the flow dynamics in the cylinder wake have been published by Zdravkovich [136,137] and Williamson [138].

The formation and evolution of vortical structures in the wake is the most important phenomenon for industrial applications since it is responsible for both beneficial and detrimental effects. In particular, the vortex shedding has a large effect on drag, heat transfer, noise and vibration problems, thus the wake control and the means to achieve it are an active topic of research. For an electro-conductive

fluid, like an electrolyte or a liquid metal, the application of a magnetic field has been proposed as a tool to control the wake structure and, starting from the '60s, many studies have been devoted to characterize this fundamental MHD problem. For a unidirectional magnetic field there are three possible orientations with regard to the flow and obstacle that can be consider: *aligned* with the stream-wise direction, perpendicular to both the flow and the obstacle (*transverse*), and oriented along the obstacle axis (*spanwise*).

Historically, the first to investigate the effect of a transverse magnetic field on the flow around an elliptic cylinder was Ludford who considered the unbounded, inviscid, case for $N \gg 1$, $Re \gg 1$ and $Re_m \ll 1$ [139]. The theoretical analysis was successively extended to a two-dimensional and three-dimensional confined flow by Hunt and Leibovich [140], and Hunt and Ludford [141], whereas, more recently, Kapila and Ludford treated the 2D case for non-inertialess conditions [142]. The configuration where the magnetic field is aligned with the stream-wise direction allows to control the wake structure without introducing significant electromagnetic drag and it is the one most considered with regard to industrial applications. Some relevant experimental studies can be found in Ref. [143–145], whereas some noteworthy papers on the subject are Ref. [146–150]. The transverse case is studied experimentally in Ref. [151, 152], and numerically in Ref. [148, 149, 153]. The spanwise case is investigated experimentally in Ref. [154–158] and numerically in Ref. [114, 159–161].

For all three orientations, the magnetic field exerts a stabilizing effect on the flow, delays the transition between flow regimes to higher Re compared with the purely hydrodynamic case and suppresses the vortical structures, whose velocity oscillations are strongly dampened. For an aligned magnetic field, the favorable orientation of the wake structure guarantees only a mild recirculation region suppression, whereas the onset of the vortex shedding is strongly impeded and the magnetic field affects the position of the separation and reattachment points. Peculiar features observed for this case are the existence of a steady 3D flow pattern, due to the magnetic field actively preventing the transverse velocity oscillations responsible for the 2D instability and instead promoting the stream-wise vortices that cause the transition to flow three-dimensionality, and the appearance of a recirculation region upstream of the cylinder (*upstream wake*). For the transverse case, the magnetic field has a more significant effect on the flow with the complete suppression of the flow recirculation being observed even for small Re. The spanwise case exhibits wake control features similar to the transverse case but the suppression effect is weaker with the critical Re for the regime transition increasing linearly with Ha.

Beside materials and processing industries, this case is relevant also for LM fusion reactor blankets due to cylinders being employed as turbulence promoters, in self-cooled and dual-cooled concepts, and breeding zone cooling elements for designs that employ the liquid metal only as tritium breeder and carrier, relying on secondary, non electro-conductive, fluids for the power extraction function. Despite this, not many studies are found in the literature covering both the wake flow-dynamics and its impact on the heat transfer. An experimental work by Kolesnikov and Andreev [162] studied conducting cylinders close to a heated wall for an aligned magnetic field and found that the vortical structures in the wake were able to provide a 5-6 times heat transfer increase compared with a channel without obstacles. A similar problem was investigated numerically by Hussam et al. [163] who considered

the case of an insulating cylinder and spanwise magnetic field for $0.1 \leq \beta \leq 0.4$, $50 \leq Re \leq 3000$ and $0 \leq Ha \leq 1200$. They found that the Nusselt number is a function of both the blockage ratio and the Hartmann number with the heat transfer rate being particularly sensitive to the former for small magnetic field intensity. However, the stronger effect on the wake structure limited the increase to twofold compared with an empty channel. Successively, Hussam et al. extended the study to a cylinder offset from the duct centerline toward the heated wall [164] and for several cross-section shapes [165].

The unbounded forced convection flow around a fixed temperature cylinder for an aligned magnetic field was studied by Yoon et al. [166] for $10^{-2} \leq N \leq 10$, $2 \cdot 10^{-2} \leq Pr \leq 7$ and $Re = 100$. They found that for increasing N the heat transfer rate initially decreases to a minimum value at N_{cr}, corresponding to the transition to the steady regime, before starting to grow and exceeding the hydrodynamic value for the liquid metal case ($Pr = 2 \cdot 10^{-2}$). Chatterjee and Chatterjee [167] considered the heat transfer from a bounded cylinder ($\beta = 0.25$) for both aligned and transverse magnetic field at low magnetic field intensity. They found a qualitative agreement with the results of Yoon et al. for the former case and observed how the transverse magnetic field is more efficient in increasing the heat transfer for $N > N_{cr}$, at least for high Prandtl number fluids. The mixed convection unbounded case for an horizontal cylinder subjected to an aligned magnetic field was considered by Udhayakumar et al. [168] for several Prandtl number fluids that found that the asymmetrical wake structure promoted by the buoyancy forces is stabilized similarly to what is observed in the forced convection case and that, for a liquid metal, the heat transfer rate converges rapidly to the forced convection behavior for an increasing N. To the best knowledge of the author, no study has been reported in the literature for a fixed temperature cylinder and a spanwise magnetic field.

10.2 Rationale and problem formulation

This study is aimed to provide useful information about the fluid-dynamics and heat transfer for the flow around the breeding zone cooling pipe of the configuration WCLL2017v01.A. Literature results for the bounded flow around a fixed temperature cylinder are scant and mostly focusing on basic configurations and low magnetic field intensity, see for instance Ref. [167], therefore, they are of limited relevance for operative blanket conditions. Hence, the analysis is focused on high magnetic field intensity and low fluid velocity, whereas neglecting any contribution from natural convection and preserving the characteristic geometrical features of the WCLL design: non-uniform thickness of the bounding walls, pipe offset from the duct centerline and high aspect ratio. Moreover, the study will characterize the influence on the flow pattern and heat transfer for two scenarios that have not found so far much attention in the literature: electro-conductive obstacles and multi-directional magnetic field.

The results presented in this chapter have been partially published in Ref. [22, 85, 169, 170].

Table 10.1. Geometry parameters and wall conductance ratio

Duct and Cylinder parameters						Wall thickness (δ_i)			$c_i \times 10^2$
L	117	mm	d	13.5	mm	Top (t)	1	mm	1.25
H	30.25	mm	d_i	8	mm	Bottom (b)	6	mm	7.5
F_u	74.25	mm	G/d	0.5		Side (s)	10	mm	10
F_d	202.5	mm	β	0.223		Obstacle (o)	2.75	mm	$0/3.73/\infty$

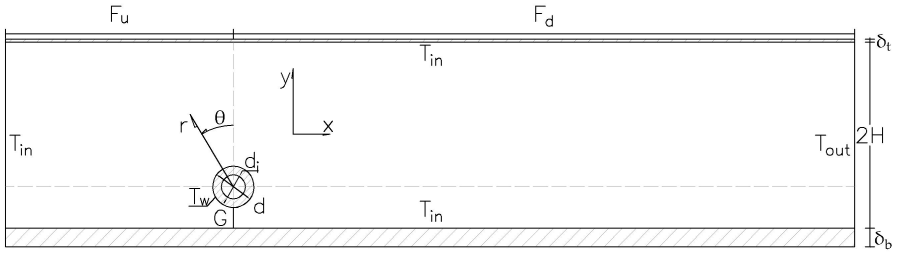

Figure 10.1. Toroidal-poloidal cross section, inlet surface at the left of the model

10.2.1 Geometry and materials

For the purpose of this study, the BZ central channel of the WCLL2017v01.A configuration is employed as a reference to derive the numerical model geometry.

A rectangular duct, defined by a toroidal (z-axis) half-length L and poloidal (y-axis) half-length H, accommodates the cylindrical obstacle. Such cylinder represents the DWT carrying the coolant in the WCLL breeding zone, therefore it is hollow and it is defined by an outer diameter d and inner diameter d_i. The obstacle axis is aligned with the toroidal direction, hence it is transverse to the radial, stream-wise, direction (x-axis). Furthermore, the cylinder geometry is defined by a blockage ratio($\beta = d/2H$) with regard to the duct poloidal extension, whereas its position is specified by the normalized offset from the duct centerline (G/d), where G is the distance between the cylinder bottom and the closest duct wall. Moreover, the upstream (F_u) and downstream (F_d) lengths identify the obstacle radial position in the duct and are, respectively, equal to $5d$ and $15d$. The duct walls that are bounding the flow can be divided into three classes (top, bottom and side walls) that are characterized by different thickness values (δ_w), but are all thin compared with the characteristic length ($\delta_w \ll L$), as well as the cylinder wall.

An overview of the model geometrical parameters is available in Table 10.1, whereas Figure 10.1 and 10.2 show the toroidal-poloidal and radial-poloidal cross section of the model.

The fluid considered in the study is the eutectic alloy PbLi that, due to the small temperature range envisioned in the model, is modeled with constant physical properties, that are evaluated at the average temperature $T_{ref} = 558\,K$ according to the correlations by Jauch et al. [61]. For the duct and pipe walls, the same approach is followed for the RAFM Eurofer steel employing the correlations presented by Mergia and Boukos [62]. For all the materials, the magnetic constant (μ_0) is employed to define the magnetic permeability. An overview of the physical properties employed in this study is presented in Table 10.2.

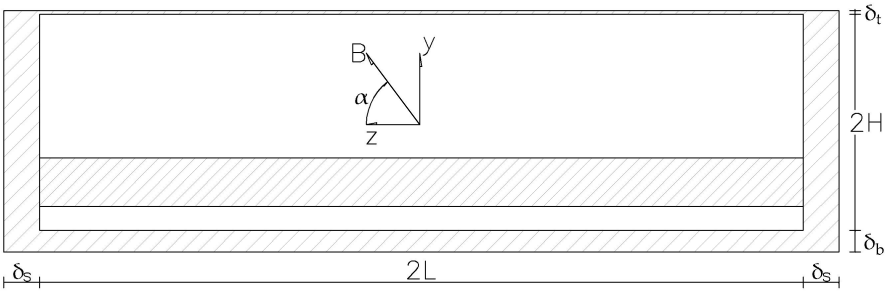

Figure 10.2. Radial-poloidal cross section, view from inlet

Table 10.2. Physical properties of Lithium-Lead (PbLi) [61] and Eurofer steel [62]

Property (unit)	Symbol	PbLi	Eurofer
Density (kg/m^3)	ρ	9856	7695
Electrical conductivity (S/m)	σ	$7.932{\cdot}10^5$	$1.259{\cdot}10^6$
Thermal conductivity (W/mK)	κ	12.831	30.060
Kinematic viscosity (m^2/s)	ν	$2.332{\cdot}10^{-7}$	n.a.
Thermal diffusivity (m^2/s)	α_t	$6.885{\cdot}10^{-7}$	$7.193{\cdot}10^{-6}$

10.2.2 Numerical model and boundary conditions

Since the duct and the pipe walls are, in general, characterized by a finite conductivity, to properly resolve the electric potential equation and then obtain the current distribution in the problem geometry, it is necessary to employ a model containing both a solid and fluid computational domain, that are coupled at the interface through appropriate boundary conditions. These are the conservation at the fluid/solid interface of the potential and current density described in Section 3.5. Conversely, the perfectly conducting and insulating obstacles do not require the modeling of the solid surface, since the electric potential distribution is fully defined by the boundary condition (see Section 3.5), and thus, for these cases, the pipe was not modeled in the solid domain. The external surfaces of the solid domain, as well as the inlet/outlet, are modeled with the hypothesis of immersion in a perfectly dielectric medium (i.e. air). For the finite conductivity case, the same boundary condition is employed for the internal pipe surface.

The magnetic field is uniform and constant with non-null components both in the poloidal and toroidal direction ($\vec{B} = (0, B_y, B_z)$). The magnetic field inclination on the toroidal axis is defined with the parameter

$$\alpha = \tan^{-1}(B_y/B_z) \tag{10.1}$$

In a fusion reactor blanket, the toroidal magnetic field is the dominant component, with the poloidal magnetic field being considerably less intense and usually ranging between 10% and 40% of the toroidal one depending on the position in the blanket. For the purpose of this study, the typical inclination on the equatorial outboard plane, $\alpha = 16°$ is considered as reference value. Moreover, during the fusion reactor

Table 10.3. Matrix of simulation parameters.The symbol c_o refers to the obstacle conductance ratio and E identifies the finite conductivity case ($c_o = 3.73 \times 10^{-2}$); for $c_o \neq 0$, $\alpha = 16°$

Ha	Re	Pe	N	$\alpha(°)$	c_o
10	20	0.68	5	0, 8, 16, 24, 32	0, E, ∞
	40	1.36	2.5	0, 8, 16, 24, 32	0, E, ∞
	60	2.04	1.67	16	0
	80	2.72	1.25	16	0
30	20	0.68	45	16	0
	40	1.36	22.5	16	0
	60	2.04	15	16	0
	80	2.72	11.25	16	0
50	20	0.68	125	16	0, E, ∞
	40	1.36	62.5	16	0, E, ∞
	60	2.04	41.67	16	0
	80	2.72	31.25	16	0
100	20	0.68	500	16	0
	40	1.36	250	16	0
	60	2.04	166	16	0
	80	2.72	125	16	0

operation, the intensity of the poloidal component can vary up to ±50% due to the necessity of achieving a better plasma stability, therefore the influence of the magnetic field inclination on heat transfer and pressure drop is investigated in the range $\alpha = [0°, 32°]$ [171]. Time concerns forced the study on magnetic field inclination to be limited to low magnetic field intensity case (see 10.3). Due to the complex magnetic field topology considered in the model, a fully 3D computational domain is required to complete the simulation. Since no currently available CMHD codes can perform such 3D simulations at the Hartmann range characteristic for an operative blanket, the magnetic field intensity is scaled down to a more accessible value. Employing the cylinder outer diameter (d) as length scale, the range considered for this study is $Ha_d = [0, 100]$[1]. In the following section, the subscript d it is dropped, and the Hartmann number is referred simply with Ha.

Concerning the momentum equation, classical no-slip boundary conditions are applied to the solid/fluid interface. At the inlet of the duct, the flow is assumed to be in fully developed conditions with an average velocity u_0. To obtain a suitable velocity profile, 2D simulations are performed on a simplified model that represents a thin duct slice ($x \ll L$) with the aid of periodic interfaces to speed up the run time [172]. The complete velocity profile sampled at the outlet of the 2D simulation is then loaded at the inlet surface of the 3D model to represent the fully developed state. Typical velocities for blanket BZ that employ a secondary, non electrically conductive, fluid as coolant range between 0.1 mm/s and 5 mm/s depending on the particular model. The coupled effect of the low velocity and the stabilizing action of the magnetic field ensures the maintenance of a steady and laminar regime [22, 27, 53, 173]. The range chosen for this study is $Re = [20, 80]$,

[1] As reference, the conversion factor to a more conventional Hartmann number based on the toroidal half-length of the model is $Ha_L = 8.67 Ha_d$

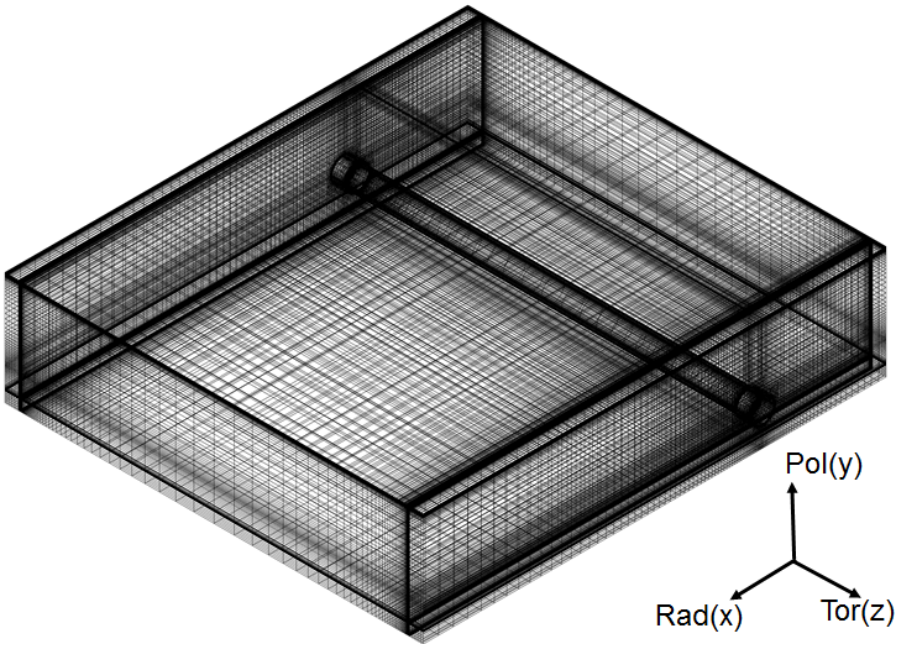

Figure 10.3. Isometric view of the model mesh

which translates to 0.345 mm/s $\leq u_0 \leq$ 1.38 mm/s.

The fluid at the inlet enters the computational domain with a fixed temperature $T_{in} = 573$ K, that is also employed as initialization value for the model, whereas the external surface of the pipe is kept at $T_w = 543$ K, therefore creating a constant temperature difference $\Delta T = 30$ K. For the finite conductivity case, where the pipe wall is actually represented in the model geometry, the internal surface of the pipe is kept at $T = T_w$ and, to obtain results better comparable with the other simulations, the Eurofer material was modified to give to the pipe a very high thermal conductivity, thus neglecting the pipe wall thermal resistance. For the same reason, an infinite thermal resistance is added to the interface between the duct walls (modeled in regular Eurofer) and the pipe. The duct external surface is assumed to be adiabatic.

10.2.3 Domain discretization, mesh sensitivity and code validation

The bounded MHD flow around a cylinder is a problem usually modeled employing the quasi-2D approximation developed by Sommeria and Moreau [174], e.g. see Ref. [163, 164, 167]. In this study, the complex magnetic field topology and non-uniform wall conductivity considered make the use of a full 3D computational domain an unavoidable necessity to properly represent the relevant physical phenomena. In Figure 10.3, it is possible to see the computational grid employed comprising separate domains to simulate the fluid and solid components of the model. A non-uniform structured mesh is employed to discretize the computational domain. An increased refinement in the area immediately surrounding the cylinder is foreseen to capture more efficiently the phenomena happening in this region and for the wall boundary layers, as it is possible to see in Figure 10.4.

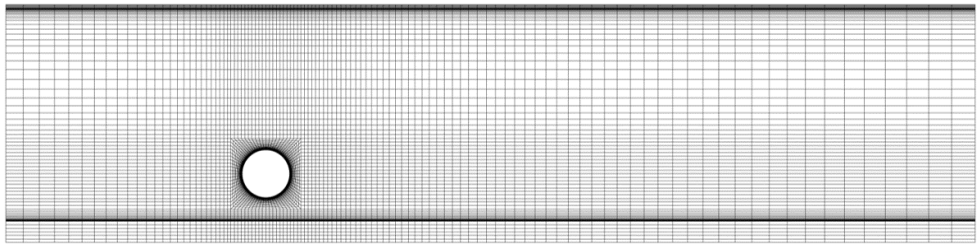

(a) Poloidal-radial view of the computational grid

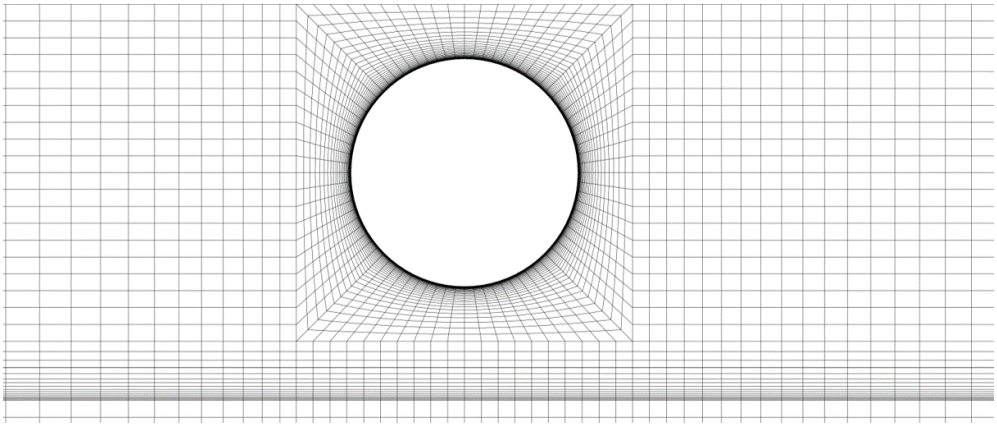

(b) Detail of the mesh around the obstacle

Figure 10.4. Model geometry

A critical aspect of MHD simulations is represented by the necessity to employ a grid that completely resolves the boundary layers encountered close to walls with a non-null normal component of the magnetic field, the Hartmann layers, since these are characterized by steep velocity gradients and carry high current densities that have a direct influence on the overall flow behavior. Insufficient mesh resolution can lead to the introduction of unacceptable numerical errors due to the underestimation of boundary layer current density and, thus, mean velocity. For this reason, common guidelines prescribe from 4 to 10 elements for the mesh in these regions.

The Hartmann layer thickness follows the scaling law $\delta_H \propto Ha^{-1}$ and, when 3D MHD simulations the parameter range close to fusion blanket conditions, the layer quickly becomes extremely thin and time expensive to resolve due to both the large computational grids required and slow convergence speeds. However, such boundary layers are characterized by high electric resistance and, when attached to a conductive wall, play a smaller role in the definition of the flow features due to the shunt of the currents to the less resistive path provided by the solid domain.

This phenomenon can be used to obtain acceptable accuracy with significantly coarsened mesh for the MHD flows in conductive ducts: Subramanian et al. demonstrated that even for a fully unresolved Hartmann layer the error on the pressure gradient calculation is around 1% for $c_w \approx 10^{-2}$ [175]. The mesh employed in this study adopts a fully resolved strategy with 10 elements for the layer attached to the perfectly insulating obstacle, whereas for the duct wall and the conductive obstacle layers the resolution is reduced to 4 elements. The difference in scale between the

Table 10.4. Mesh sensitivity study for the reference case $Ha = 10, Re = 20, c_o = 0, \alpha = 16°$. Selected mesh is underlined

Mesh parameters	G_1	G_2	$\underline{G_3}$	G_4	G_5
$\varnothing$	100	120	160	200	240
F_u	24	29	39	49	59
F_d	48	58	77	97	115
$N_{el} \times 10^5$	4.56	6.79	14.2	24.9	39.6
Control parameters					
T_{out}	0.318	0.331	0.325	0.321	0.322
Δp	76.628	76.605	76.580	76.574	76.575

two layers can be observed in Figure 10.4b, where it is evident the reduced resolution for the layer attached to the conductive wall with regard to the one found close to the perfectly insulating cylinder. The grid was scaled for each Ha considered to keep a consistent layer resolution throughout the study.

Another aspect to be considered is the numerical coupling between the solid and fluid domain to allow the proper resolution of the electric potential equation. A conformal mesh is employed in order to have a 1:1 node correspondence between the domains and avoid the introduction of any numerical errors due to the interpolation on a non-conformal interface. In Figure 10.4a, it can be seen how the interface conformity extends throughout the radial extension of the duct. Although the duct walls considered satisfy the thin-wall condition and no electric potential gradient should be present in the wall thickness, a uniform resolution of 6 elements in the solid domain is employed.

A mesh sensitivity study was carried over to ensure the independence of the results obtained from the grid resolution. Five meshes with increasing number of elements on the cylinder circumference ($\varnothing$), the upstream (F_u) and downstream (F_d) direction were considered (Table 10.4). The monitored dimensionless parameters were the average dimensionless temperature of the fluid at the outlet ($(T_{out} - T_w)/\Delta T$) and the dimensionless pressure drop in the channel ($\Delta p/\rho u_0^2$) for the reference case $Ha = 10, Re = 20, c_o = 0, \alpha = 16°$. An error range of less than 2% was found compared with the result of the most refined mesh (G_5) for all the parameters considered. Since the results obtained are independent of the mesh resolution, the mesh G_3 was chosen as the reference for the study.

Regarding code validation, ANSYS CFX is shown to have acceptable performances for the representation of MHD pressure-driven flows for both insulating (Shercliff case) and finite-conductivity (Hunt case) ducts, as detailed in Section 9.6.

10.3 Results and discussion

In this section, the results obtained are discussed focusing first on the general features of the MHD fully developed flow observed in the upstream section of the model, that is assumed also as inlet boundary condition, for the reference configuration ($\alpha = 16°$, insulating obstacle). The flow pattern around the (insulating) obstacle is then discussed and the influence of the governing parameters (Ha, N, α, c_w) is

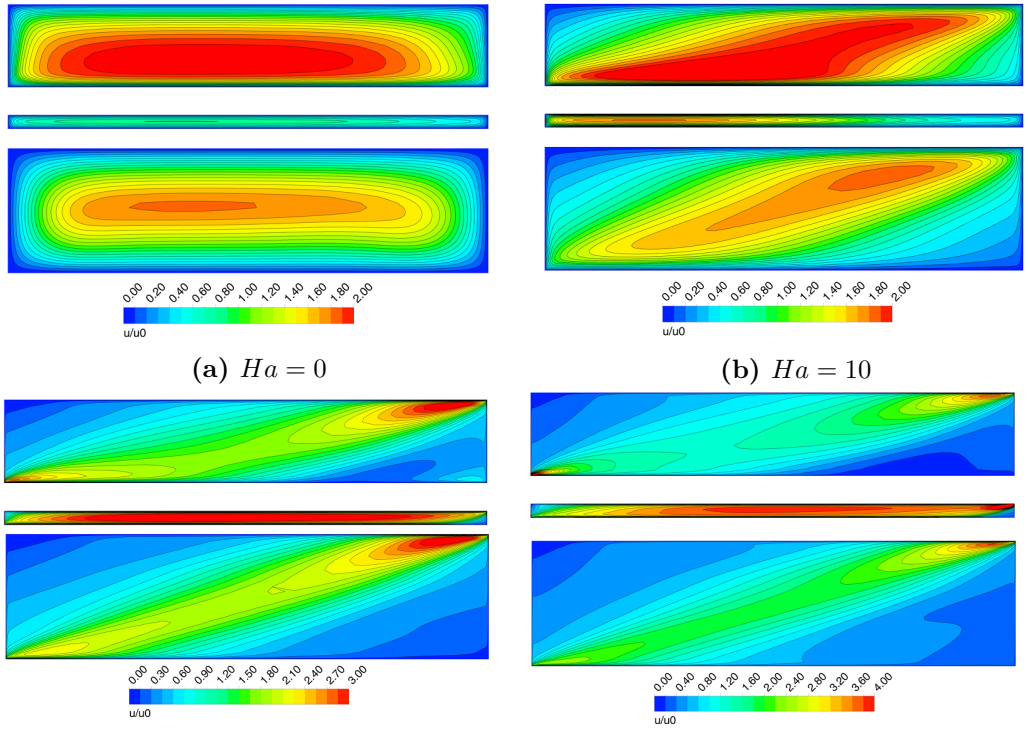

(a) $Ha = 0$ **(b)** $Ha = 10$

(c) $Ha = 50$ **(d)** $Ha = 100$

Figure 10.5. Velocity contour for the flow about the cylinder ($x/d = 0$) and downstream ($x/d = 10$). Results shown for $Re = 20$ and increasing Hartmann number. Magnetic field inclination $\alpha = 16°$. Toroidal-poloidal cross section view from outlet. Note that the velocity scale for $Ha \geq 50$ covers a higher range. The cylinder is perfectly insulating.

highlighted. The pressure drop penalty introduced by the obstacle and the effect of the transition to the MHD regime for the heat transfer are also discussed.

10.3.1 Channel MHD flow

For a pressure-driven MHD flow in a rectangular channel, the flow cross section can be separated into three zones characterized by different features: the core region in the centre of the duct (where the flow velocity can be considered uniform), the *Hartmann boundary layers* close to walls perpendicular to the magnetic field (these having thickness $\delta_h \propto Ha^{-1}$), and the *Shercliff boundary layers* close to walls parallel to the magnetic field direction (these having thickness $\delta_s \propto Ha^{-1/2}$). For a strong magnetic field ($Ha \gg 1$), these layers become increasingly thin and, thus, are characterized by steep velocity gradients. The Shercliff layers are often characterized by high velocity jets with their shape and intensity controlled by the wall conductance ratio.

In the case of skewed magnetic field with $\alpha \gg Ha^{-1/2}$, where α is measured in radians and Ha is expressed using the toroidal half-width of the channel, the Hartmann layer behavior is observed for each wall with a non-null normal component of the magnetic field [33] [176]. The Shercliff layer flow structures detach from the associated wall and are smeared out into the duct core.

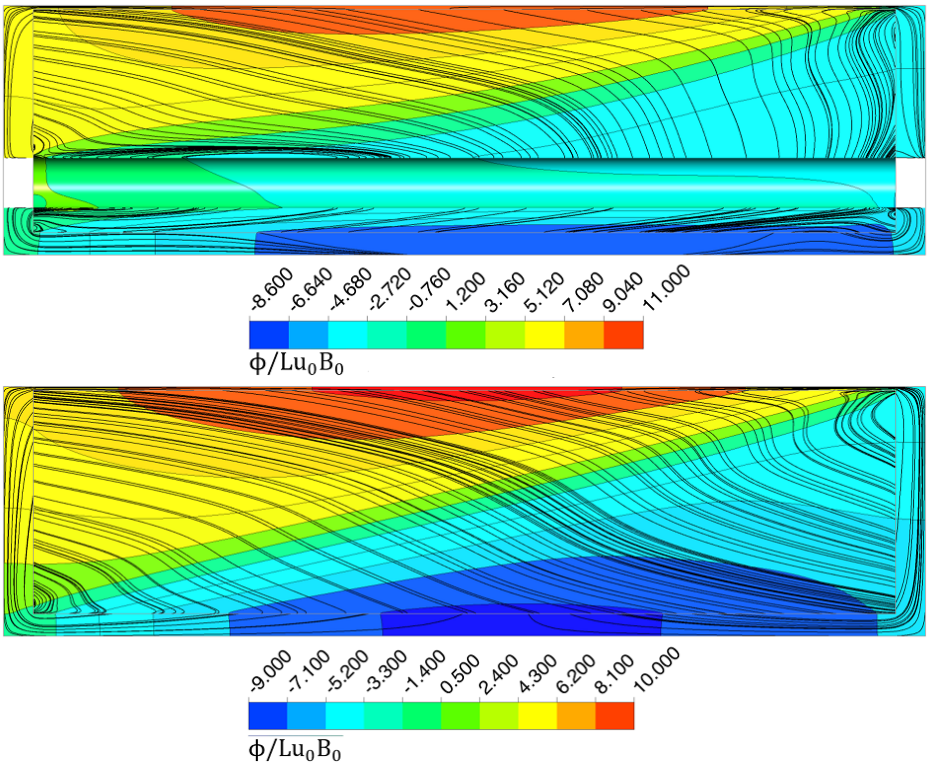

Figure 10.6. Electric potential contour and current density streamlines for (top) the flow about the cylinder ($x/d = 0$) and (bottom) downstream ($x/d = 10$). Results shown for $Re = 80$ and $Ha = 100$. Magnetic field inclination $\alpha = 16°$. Toroidal-poloidal cross section view from outlet. The cylinder is perfectly insulating.

From Figure 10.5a to 10.5d, this phenomenon can be clearly observed for the magnetic field inclination $\alpha = 16°$, where the velocity contours for the poloidal-toroidal plane passing through the cylinder centre ($x/d = 0$) and far downstream ($x/d = 10$) are presented.

For $\alpha \ll Ha^{-1/2}$, the Shercliff layer behavior is dominant close to the top and bottom wall due to the toroidal magnetic field component being dominant ($B_z \gg B_y$) and, since these walls are electro-conductive, the formation of jets in the Shercliff layers is observed. Increasing the magnetic field inclination leads to the reorganization of the flow: the jets detach from the top and bottom wall and coalesce in a single internal one that connects the duct corners parallel to the magnetic field direction and it is separated by the two opposite core regions centered around the other duct corners by free shear layers. For $Ha \to 100$, the internal jet splits into two distinct velocity peaks close to each corner with the appearance of a saddle point in the duct centre. The non-uniformity of the wall conductance ratio influences the flow features as well with the bottom wall being thicker and more conductive compared with the top one leading to a suppression of the flow in its proximity, which is highlighted by the difference in the velocity peaks between Figure 10.5b, 10.5c, and 10.5d.

The flow distribution on the duct cross-section is directly related to the electric potential one which, in turn, determines the current paths. For the fully developed

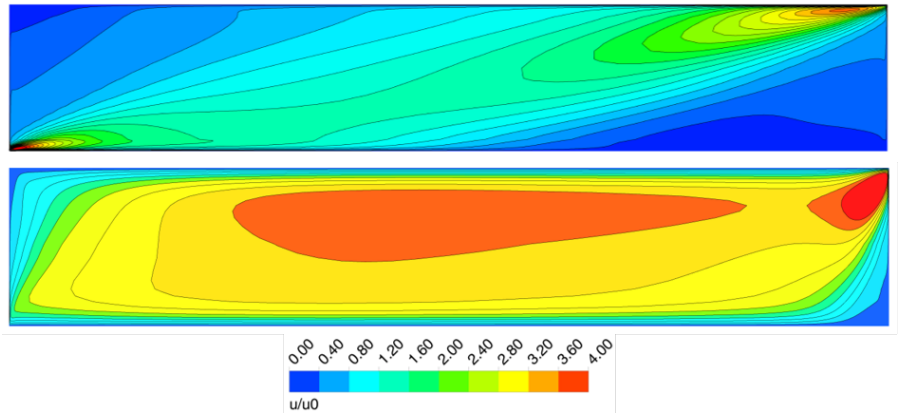

Figure 10.7. Velocity contour comparison for the flow about the cylinder ($x/d = 0$) in the upper ($y > 0$, top) and lower sub-channel ($y < 0$, bottom). Results presented for $Re = 80$ and $Ha = 100$. Magnetic field inclination $\alpha = 16°$. Toroidal-poloidal cross section view from outlet. For ease of visualization, the lower sub-channel dimension has been magnified by six times in the vertical direction.

flow, the electric potential presented in Figure 10.6 is asymmetrical due to the contribution of both the toroidal and poloidal component of the magnetic field: the former imposes the dominant top/bottom potential difference and the latter offsets the maximum and minimum away from the duct centreline and toward the duct corners. This effect results in the deformation of the current streamlines which, in turn, generate zones of differential electromagnetic drag on the cross section where the currents are not perpendicular to the magnetic field direction. For instance, current loops are observed close to the duct corners aligned in the magnetic field direction where, since the currents are mostly aligned with the magnetic field, the resistant Lorentz force, $\vec{F_L} \propto \vec{J} \times \vec{B}$, is greatly weakened and causes the formation of the jets described earlier (see Figure 10.5). A similar effect applies on the duct diagonal creating the internal jet and the accompanying free shear layers.

A comparison between the velocity contour of each sub-channel for the perfectly insulating obstacle is presented in Figure 10.7. The same general behavior observed for the fully developed flow is found for the flow in the upper sub-channel, accounting for the different aspect ratio. Conversely, just the variation in the aspect ratio is not enough to explain the drastically different flow behavior exhibited by the lower sub-channel, where the current paths are mostly parallel to the magnetic field direction, and the area is interested by higher velocities compared with the other sub-channel. Moreover, the flow features a larger core, occupying most of the sub-channel cross-section, and the reorganization of the velocity jets. In the lower sub-channel, the bottom wall is much more conductive than the top wall and, thus, the jet that we will expect to observe in the corner nearby it is instead suppressed and merges with the core. Contrariwise, the much less conductive cylinder surface promotes the jet in the corner nearby and, in addition, triggers the formation of a high-velocity structure close to its mid-point that has no corresponding one in the upper channel.

Influence of magnetic field inclination

Four different values were considered, starting from a purely toroidal magnetic field ($\alpha = 0°$) to a maximum inclination of $\alpha = 32°$, to investigate the influence of the magnetic field inclination (α) on the flow features and to compare the results with the behavior for the reference inclination ($\alpha = 16°$) [169]. This parameter mainly affects the boundary layers behavior. In Figure 10.8 and 10.9, the velocity and electric potential contour for the magnetic field inclination $\alpha = 0°, \alpha = 8°, \alpha = 24°$ and $\alpha = 32°$ are shown and can be compared with the result for the reference inclination shown in Figure 10.5b.

For $\alpha = 0°$, the magnetic field has no poloidal component, therefore the side walls exhibit Hartmann layers, whereas the other walls are characterized by the thicker Shercliff layers. Due to the low intensity of the magnetic field and negligible conductivity of the top wall, in Figure 10.8a the flow is dominated by the top jet, which occupies most of the available cross section and merges with the bottom jet that, being suppressed by its own related high-conductive wall, it is no longer discernible. In Figure 10.9a, the main potential difference is between the top and bottom walls with the current streamlines flowing in two counter-rotating loops separated by the poloidal symmetry axis of the channel and, consequently, the side walls are characterized by the same potential distribution.

Using the cylinder diameter as length scale and for $Ha = 10$, the magnetic field inclination for which the Shercliff layers are expected to detach from the walls is $\alpha_{cr} \approx 6°$, employing the relation proposed by Shercliff [176], whereas for increasing Ha this value is expected to diminish. For $\alpha \neq 0°$, the poloidal field component affects the electric potential causing the formation of a relevant potential difference among the side walls. The gradual shift of the electric potential with an increasing field inclination, that can be observed from Figure 10.9b to Figure 10.9d, warps the current paths and causes the rearrangement of the flow features, that can be observed from Figure 10.8b to Figure 10.8d, with the formation of two opposite core regions and the internal layer separating them as described for the $\alpha = 16°$ result (see Figure 10.5b). In Figure 10.8b and 10.9b, the poloidal component intensity for $\alpha = 8°$ is still insufficient to provoke the full detachment of the Shercliff layer and the linked jet is still found close to the top wall: this condition is highlighted by the thickness of the boundary layer for the bottom wall that instead for the $\alpha = 24°$ result, shown in Figure 10.8c, has already transitioned to the Hartmann layer behavior. For $\alpha > 45°$, the poloidal component becomes dominant over the toroidal one and, thus, the electric potential distribution for the top and bottom wall approach that for a Hartmann wall. The internal layer will split in two separate jets with a single core occupying the central region of the channel and, at $\alpha = 90°$, these structures will move close to the side walls where Shercliff layers will be formed.

10.3.2 Flow pattern about the insulating obstacle

For the ordinary hydrodynamic behavior, the dynamic of a laminar unbounded flow about a circular cylinder can be divided into three different regimes with the transition to each one being controlled only by the Reynolds number.

Starting from $Re = 0$, the first regime observed is a creeping flow where the

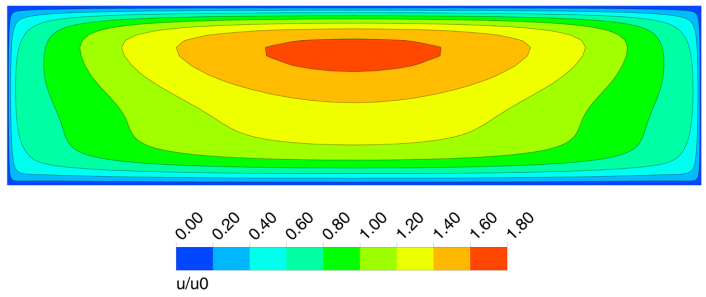

(a) $\alpha = 0°$

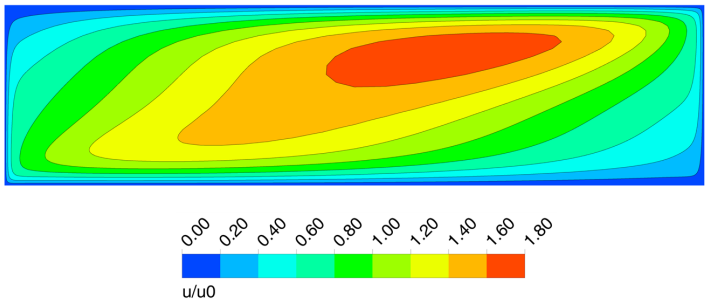

(b) $\alpha = 8°$

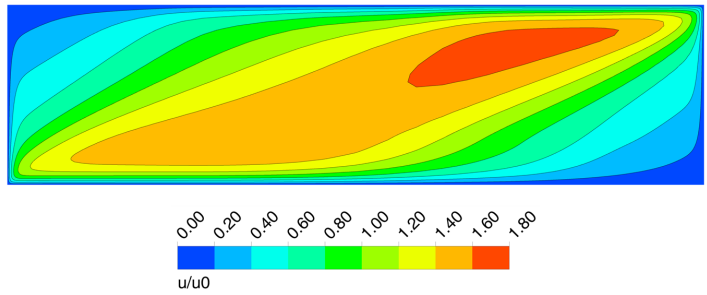

(c) $\alpha = 24°$

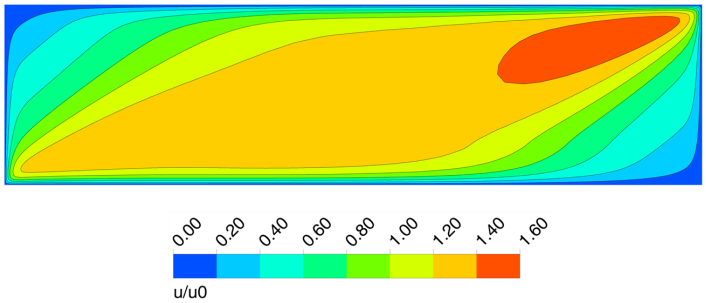

(d) $\alpha = 32°$

Figure 10.8. Fully developed velocity contour for ($Ha = 10$, $Re = 20$) versus magnetic field inclination (α). For reference, the result for the blanket operative parameter ($\alpha = 16°$) is presented in Figure 10.5b

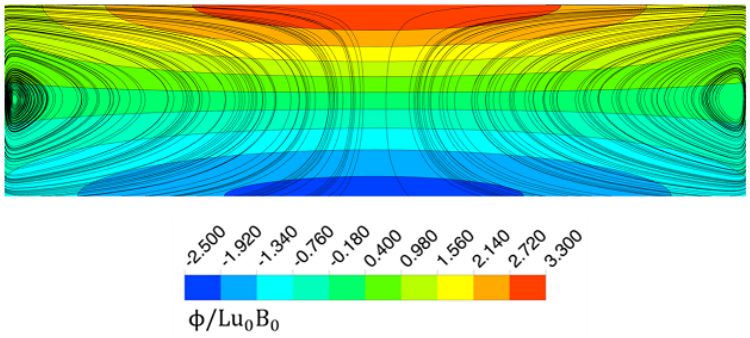

(a) $\alpha = 0°$

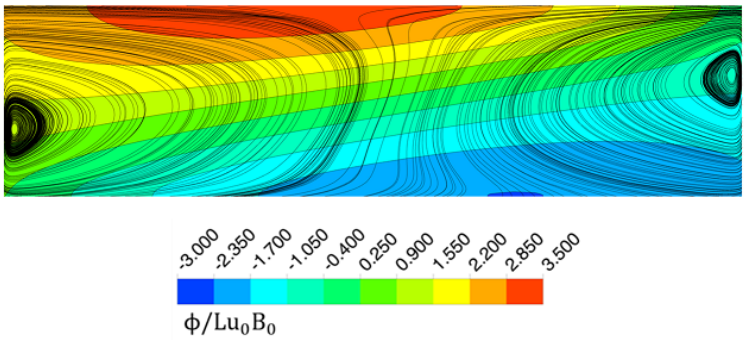

(b) $\alpha = 8°$

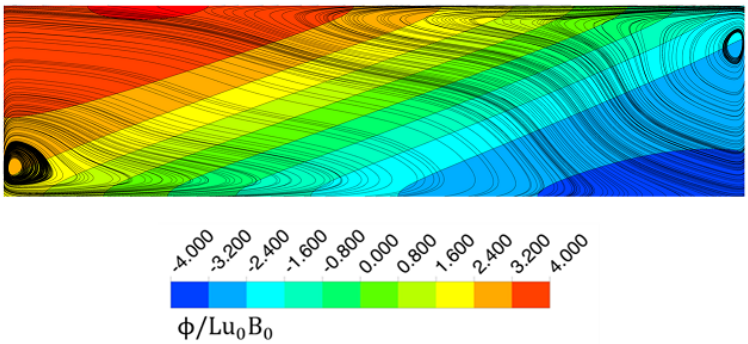

(c) $\alpha = 24°$

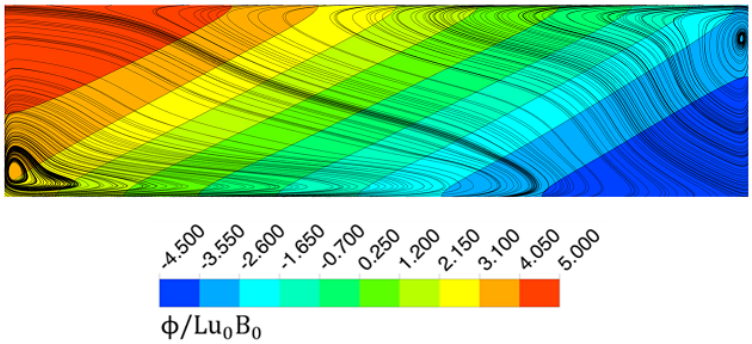

(d) $\alpha = 32°$

Figure 10.9. Electric potential contour and current streamlines for ($Ha = 10$, $Re = 20$) versus magnetic field inclination (α). For reference, the result for the blanket operative parameter ($\alpha = 16°$) is presented in Figure 10.5b

streamlines exactly follow the boundary of the obstacle without the occurrence of any noticeable flow separation. Further increasing the flow velocity leads to the formation of a recirculation zone characterized by two steady, symmetrical, vortices attached to the cylinder rear and afterward to an unsteady flow with the vortices separating alternatively from the obstacle (von Kármán vortex street) [138].

The same behavior is observed for an obstacle confined between solid walls, but two additional parameters must be introduced to completely characterize the flow: blockage ratio (β) and normalized offset from the duct centreline (G/d). The former is strongly correlated with the obstacle pressure penalty and for $\beta > 0.2$, like in the case studied in this chapter, it delays the transitions between regimes at a higher Reynold number compared with the unbounded flow. The normalized offset characterizes the wall influence on the flow and it is responsible for wake flow asymmetry and, for $G/d \to 0$, can dampen the vortex shedding, thus increasing the critical Reynold number for the regime transition [161, 177, 178].

For the geometrical parameters considered in this study ($\beta = 0.223$, $G/d = 0.5$), the flow around the obstacle is expected to exhibit a regime transition to a higher Re_c compared with the unbounded flow and a significant asymmetry in the wake. From Figure 10.10a to 10.10d, it is possible to observe how the wake behavior is influenced by an increasing Reynolds number. At $Re = 20$, the flow exhibits an incipient transition to the steady vortex regime and only a barely discernible wake is present. The proximity of the bottom wall ($G/d = 0.5$) introduces a significant asymmetry in the flow that it is clearly highlighted by the shifting of the rear stagnation point toward the top of the cylinder. Increasing the Reynold number, two steady vortices form attached to the cylinder rear; however, the perturbative effect of the nearby wall strongly suppresses the mass flow rate in the lower sub-channel and, thus, breaks the symmetry of the wake. The top vortex structure is deformed by the higher mass flow rate in the larger sub-channel and it is much better defined than the vortex formed on the bottom side, which it has a shape of a small recirculation zone that scarcely moves away from the obstacle surface. At $Re = 60$ and $Re = 80$, the lower vortex becomes larger and better defined, nevertheless the asymmetry in the wake is still noticeable. The combined effect of the wall proximity and channel blockage retards the transition to the unsteady regime, not depicted in Figure 10.10, that does not occur until $Re_c \approx 120$.

The effect of the magnetic field on the cylinder wake is described qualitatively in Figure 10.10 and 10.11. It is well known that a magnetic field transverse to the stream-wise direction introduces an additional Hartmann friction component, proportional to Ha/Re, that further delays the transition between the laminar regimes [114, 178, 179]. This phenomenon is clearly observed through Figure 10.10g, 10.10h, 10.11g, and 10.11h, where increasing Ha progressively reduces the wake length and, in the end, causes the shift of the flow from the steady vortices to the creeping regime.

The perturbation introduced by the wall presence on the wake is counteracted by the magnetic field. Already for a low intensity, i.e. $Ha = 10$, the vortex structures are evidently regularized and regain the symmetry across the cylinder mid-line, as it is clearly evident in Figure 10.10e and 10.10f. It is interesting to note that, in Figure 10.11g, the mass flow rate increase in the bottom sub-channel triggered by the magnetic field overcomes the wall effect and causes the formation of a dominant

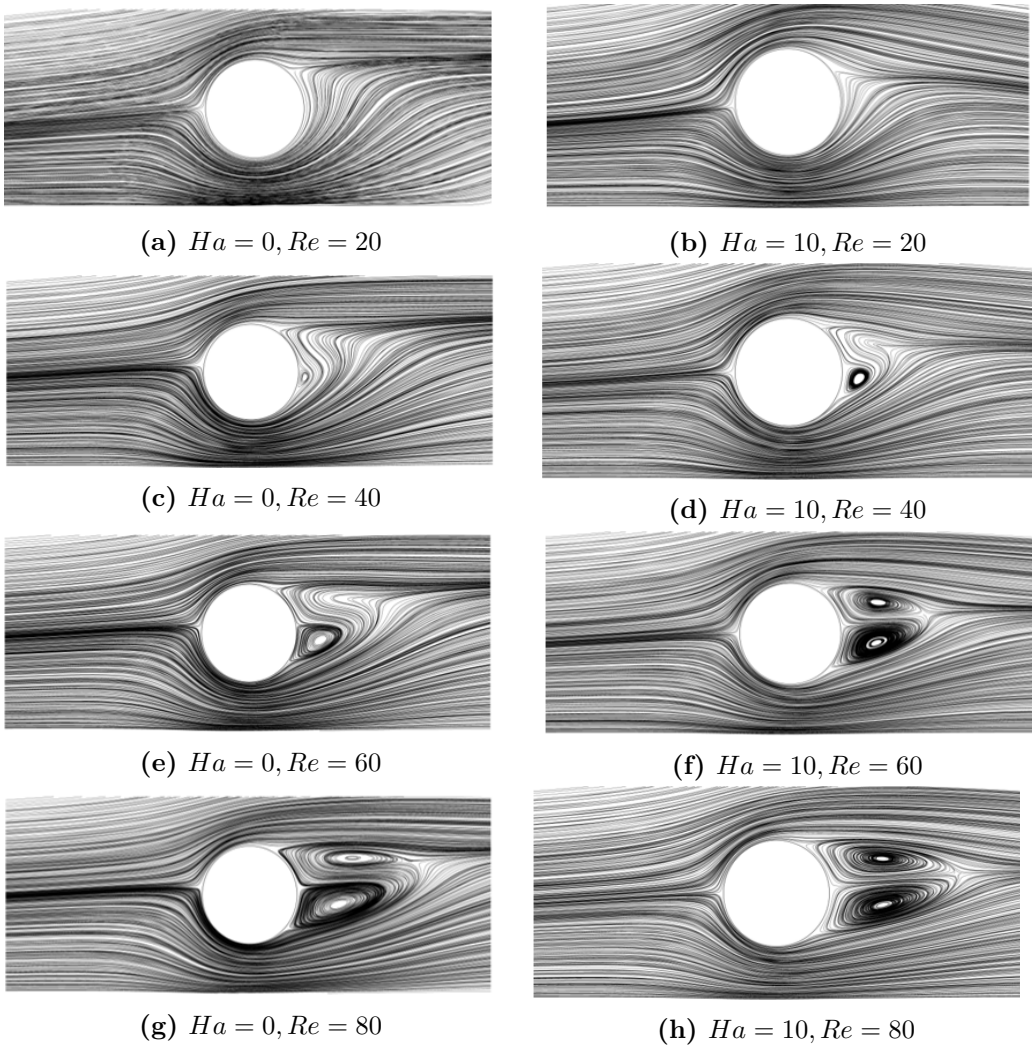

(a) $Ha = 0, Re = 20$ **(b)** $Ha = 10, Re = 20$

(c) $Ha = 0, Re = 40$ **(d)** $Ha = 10, Re = 40$

(e) $Ha = 0, Re = 60$ **(f)** $Ha = 10, Re = 60$

(g) $Ha = 0, Re = 80$ **(h)** $Ha = 10, Re = 80$

Figure 10.10. Velocity streamlines around the dielectric obstacle for the radial-poloidal plane at $z = 0$ for $Ha = [0, 10]$ and $Re = [20 - 80]$

lower vortex: the opposite phenomenon than the one observed at $Ha = 0 - 10$. For $Ha \geq 50$, the dampening effect is predominant: the vortices disappear and the wake can be considered completely suppressed.

A more quantitative description of the wake behavior is possible by defining more rigorously the wake length (L_w), which it is expressed as the distance between the cylinder rear, identified with the position ($x = d/2, y = 0, z = 0$), and the farthest point belonging to the isosurface $u_x = 0$ on the $z = 0$ poloidal-radial plane. Such a distance is then projected on the radial axis ($x-$direction) and normalized with the outer diameter (d).

A plot of the wake length as function of the Hartmann and Reynolds numbers is available in Figure 10.12. For a given magnetic field intensity, the wake length is proportional to the Reynolds number and, for $Ha = 0$, it spans the range $L_w(Ha = 0) = [0.21, 1.32]$. If the suppression condition is defined as $L_w \leq 0.05$, it is found that the wake is suppressed when $N \to 20$. The critical interaction

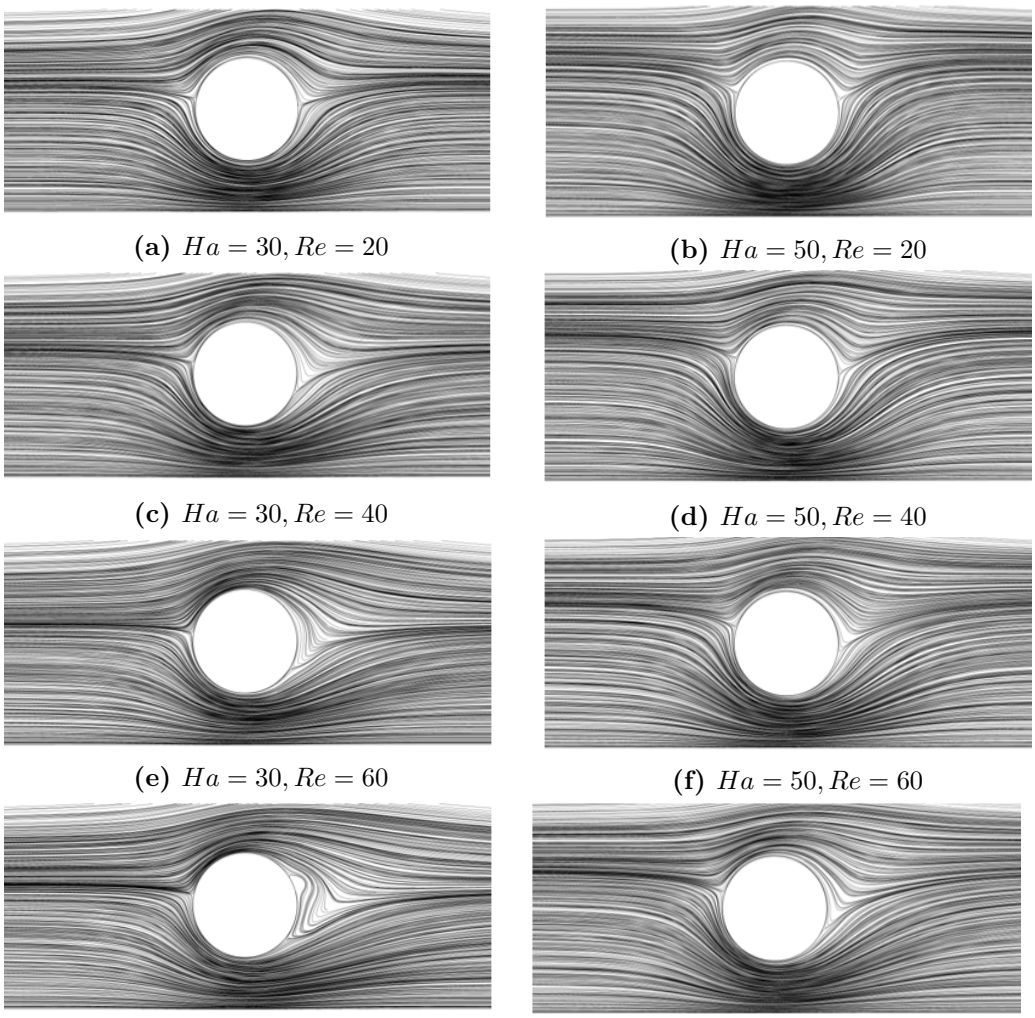

(a) $Ha = 30, Re = 20$ **(b)** $Ha = 50, Re = 20$

(c) $Ha = 30, Re = 40$ **(d)** $Ha = 50, Re = 40$

(e) $Ha = 30, Re = 60$ **(f)** $Ha = 50, Re = 60$

(g) $Ha = 30, Re = 80$ **(h)** $Ha = 50, Re = 80$

Figure 10.11. Velocity streamlines around the dielectric obstacle for the radial-poloidal plane at $z = 0$ for $Ha = [30, 50]$ and $Re = [20 - 80]$

parameter (N_c) for the wake suppression is dependent also on the magnetic field inclination, as it can be seen in Figure 10.12, where L_w is plotted as a function of α for $Ha = 10$. The maximum wake length is observed for an exclusively toroidal magnetic field ($\alpha = 0°$), the recirculation zone extension then gradually decreasing with the application of the poloidal component. For $Re = 20$, the wake is completely suppressed at $\alpha = 24°$, which according to the employed criterion will correspond to $N_c = 5$, whereas for the $Re = 40$ results the same condition is found for $\alpha = 32°$ and $N_c = 2.5$. This phenomenon can be explained with the co-planarity between the wake and the poloidal magnetic field that leads to a more efficient suppression compared with the toroidal component [167, 178].

The ordinary hydrodynamic behavior is characterized by a significant imbalance between the mass flow rate carried by the top (Γ_t) and the bottom sub-channel (Γ_b). In Figure 10.13, it is possible to observe that the latter never exceeds the 10% of the

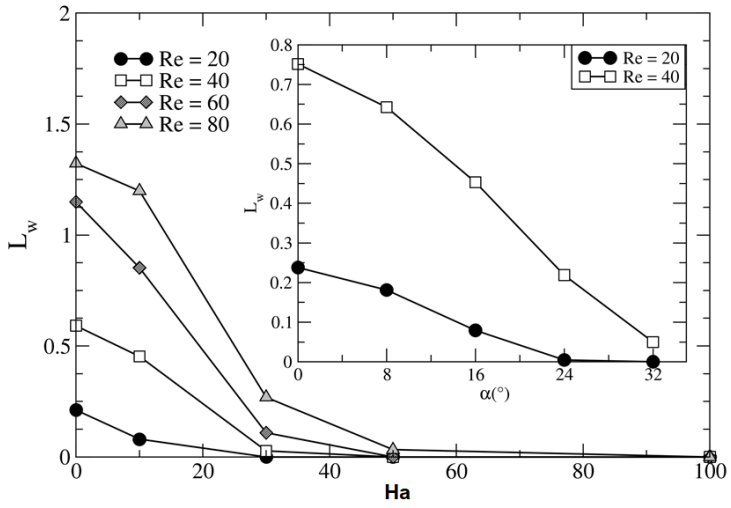

Figure 10.12. Wake length in the stream-wise direction normalized with the obstacle diameter (L_w) versus the Hartmann number (Ha). Inside: Effect of magnetic field inclination for $Ha = 10$

total mass flow rate for the Re range considered. This is an expected result, since the cross-section of the bottom sub-channel amounts to only 16% of the top one which, in turn, provides a much less resistive path for the flow. When the magnetic field is applied an additional drag component is introduced that, being independent by the cross-section and much larger than the viscous forces since $Ha \gg 1$, leads to a redistribution of the flow rate across the sub-channels that is more favorable to the bottom one. Accounting for the different wall conductance ratio exhibited by the bounding walls of the sub-channels for $Ha \to \infty$, the bottom one should carry around 25% of the total mass flow rate. However, it is observed that, already for $Ha = 100$, the bottom mass flow rate exceeds the theoretical value.

This discrepancy is explained by the electro-conductive side walls that, being shared among the sub-channels, allow the leakage of the currents generated in one to close through the other, like it can be observed in Figure 10.14. This phenomenon, called the Madarame effect, causes the coupling of the channels interested by the leakage leading to variations in the flow behavior, such as increased pressure drop and mass flow rate redistribution, that tend to increase with the intensity of the magnetic field [180]. In the case studied, the main coupling effect is the increase of the mass flow rate carried due to the inversion of the poloidal currents in the bottom channel, which generate a positive - non-resistive to the flow - Lorentz force in the axial direction.

At $Ha = 10$, the current density in the channel is low and the coupling is very weak: in both the sub-channel the poloidal current density component is positive ($J_y > 0$), the toroidal one is negative ($J_z < 0$), and, thus, the resulting Lorentz force in the stream-wise direction is resistive, since $F_{L,x} = -(J_y B_z - J_z B_y)\hat{x}$. The

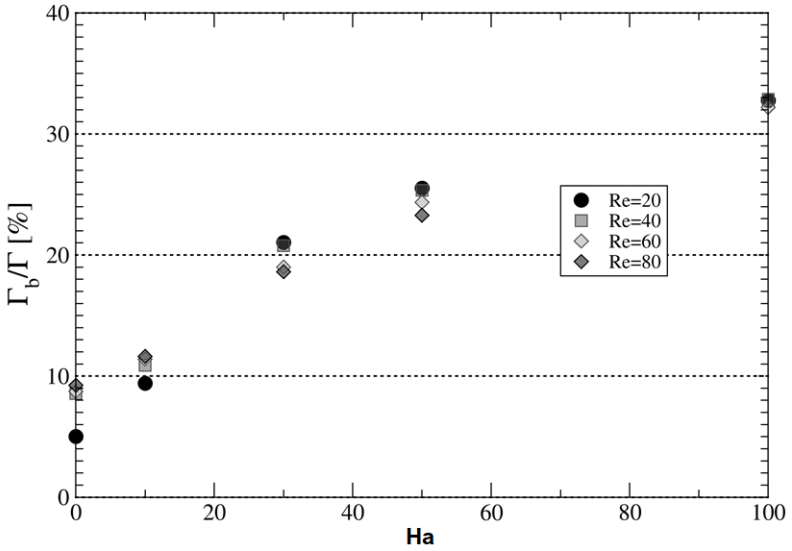

Figure 10.13. Mass flow rate increase in the bottom sub-channel with the intensity of the magnetic field, expressed with the Hartmann number (Ha)

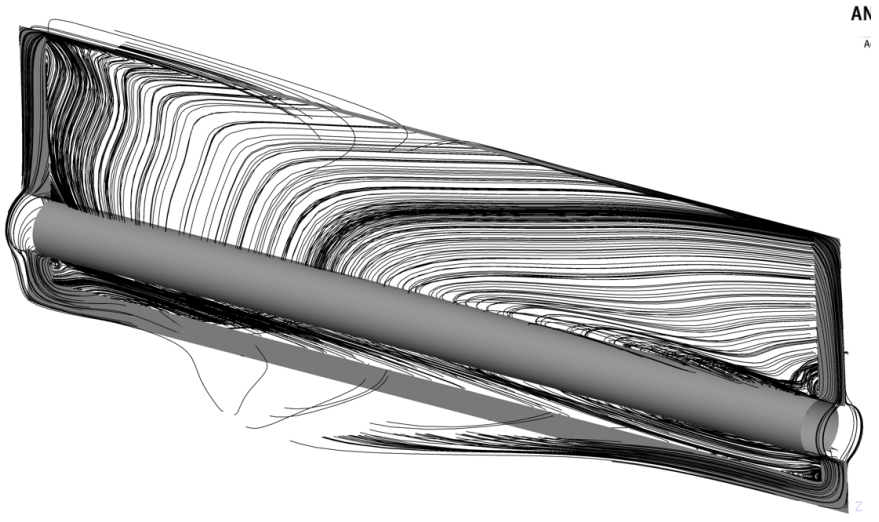

Figure 10.14. 3D current streamlines for the toroidal-poloidal plane passing through the obstacle center ($x = 0$). The grey overlay mark the solid structures (pipe and duct walls)

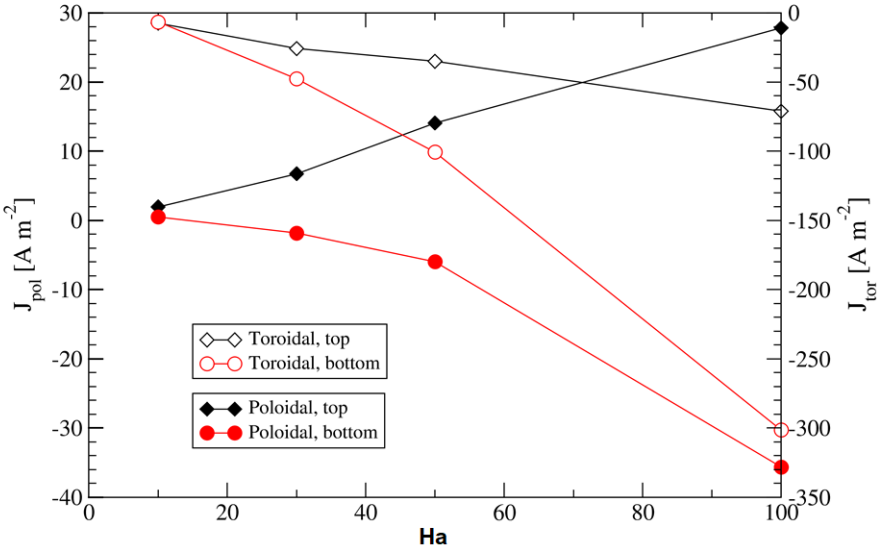

Figure 10.15. Poloidal (filled symbol) and toroidal (blank symbol) current density in the top (diamond) and bottom (circle) sub-channel plotted with the Hartmann number. Data reported for $Re = 80$. The same qualitative behavior is observed for other Re numbers.

two components agree in sign and add up to give a net resistive force. When the magnetic field increases this is no longer the case, as it can be seen in Figure 10.15, since the poloidal component in the bottom sub-channel becomes negative due to the leakage currents, whereas the toroidal component remains negative. The component of the Lorentz force due to J_y no longer agrees with the one supported by J_z, and the result is a net reduction of the electromagnetic drag experienced by the bottom sub-channel compared with the top one, which leads to a corresponding surge in the mass flow rate. However, the flow that develops in the channel will be characterized by higher velocities and, since $J_z \propto u$, it will cause the induction of more intense toroidal currents which, being responsible for the resistive component of the Lorentz force, restore the equilibrium. At $Ha = 100$, the toroidal currents in the bottom sub-channel exceed by four times the ones calculated above the obstacle. This flow pattern variation leads to a significant effect on the heat transfer that will be described in more detail in Section 10.3.4.

Influence of obstacle conductivity

The presence of an electro-conductive obstacle instead of a perfectly insulating one alters the electric potential distribution in the surrounding area and, consequently, affects the current paths and the flow pattern around the cylinder.

This phenomenon can be clearly described by studying the current streamlines around the obstacle, which are presented in Figure 10.16. For a perfectly insulating

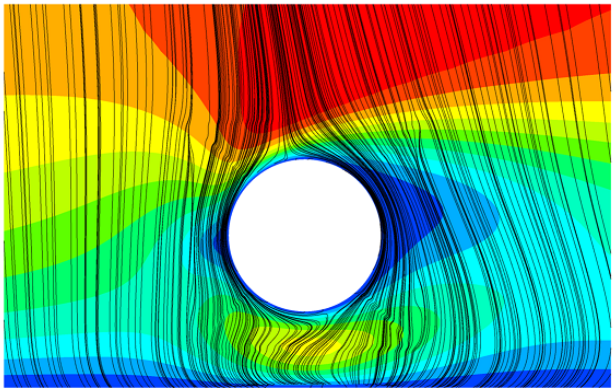

(a) $c_o = 0$

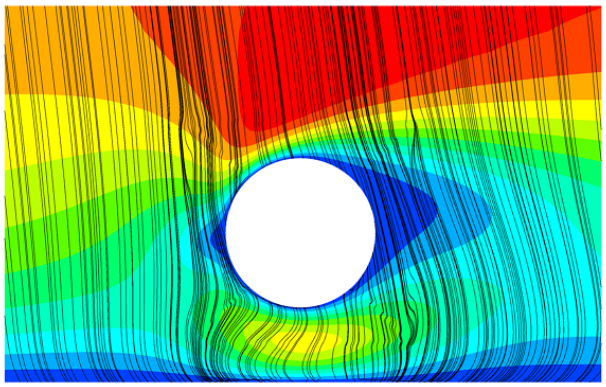

(b) $c_o = 3.73 \cdot 10^{-2}$

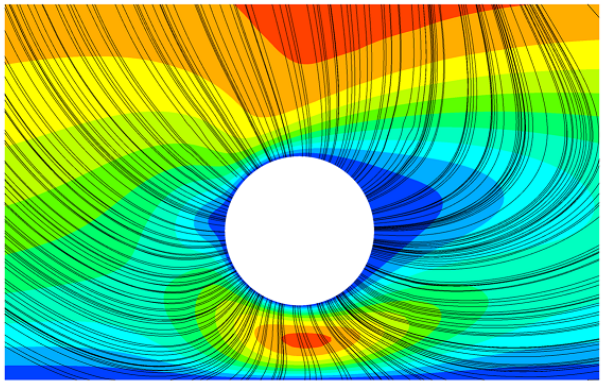

(c) $c_o = \infty$

Figure 10.16. Influence of obstacle conductivity on surrounding currents for $Ha = 10, Re = 20$ on the plane $z/L = 0$. Inlet is on the left.

pipe $c_o = 0$, the liquid metal-cylinder interface does not allow the currents to penetrate inside the obstacle, forcing them to close through the thin and highly resistive Hartmann layers. Therefore, the presence of the obstacle modifies the current streamlines, that will otherwise be perfectly vertical and aligned with the flow cross-section for a channel devoid of obstacles, causing the appearance of significant radial currents, which are responsible for the Δp_{3D} term. In Figure 10.16a, it can be seen how this phenomenon affects the current paths by comparing the vertical streamlines upstream from the cylinder with the ones close to the obstacle. In particular, the currents flowing through the boundary layer are clearly visible.

On the other hand, if the pipe has an electro-conductive wall, this offers a less resistive path to follow for the currents, that will therefore tend to close inside the pipe surface, instead of flowing in the more resistive boundary layer. In Figure 10.16b, this is shown by the currents passing through the non represented cylinder surface instead of flowing in the boundary layer as in Figure 10.16a. The pipe conductivity is relatively small, though, and the effect is mostly evident for the currents that will flow through the boundary layer otherwise, whereas currents further upstream or downstream are unaffected.

Conversely, the effect of the obstacle conductivity on the current streamlines is much more noticeable for the perfectly conducting case ($c_o = \infty$). The very low electrical resistance makes the path through the pipe surface so attractive that even current streamlines far upstream and downstream are redirected in the radial direction. In Figure 10.16c, it can be seen how the region where the currents are warped toward the obstacle is wider than the one for the finite conductivity pipe.

The reorganization of the current paths for a conductive obstacle directly impacts the flow feature and the three-dimensional pressure drop term, how it is described in Section 10.3.3. Regarding the flow pattern, the perfectly conducting obstacle is characterized by a stronger stabilization effect from the magnetic field that causes enhanced suppression of the wake structures compared with the insulating case and the formation of vortices surrounding the cylinder.

These vortices are localized close to the side walls and their appearance is dependent on the Hartmann number. In Figure 10.17, it can be seen how the high velocity jet, localized in the upper sub-channel close to the wall at $z/L = -1$, is accompanied by a clockwise rotating vortex that spans across the whole height of the lower sub-channel for $Ha = 10$. The vortex is characterized by a very weak recirculation velocity ($u/u_0 \approx -0.1$), as it can be seen in Figure 10.17a, and no corresponding structure is found close to the opposite side wall at $z/L = +1$, where a creeping regime can be observed instead (see Figure 10.17b.

Increasing the magnetic field intensity at $Ha = 50$ leads to the formation of a similar vortex also close the to right lateral wall ($z/L = 1$), which is spinning counter-clockwise and it is sustained by the jet flowing in the lower sub-channel, as it can be seen in Figure 10.17d. On the opposite wall, the vortex already present is promoted and the recirculation velocity increases to $u/u_0 \to -1$. Correspondingly to the increase in angular velocity, the clockwise vortex characteristic length shrinks.

In Figure 10.18a and 10.18c, it is shown how the onset of the clockwise vortex can be explained by the shift in the currents path caused by the conductive obstacle. The obstacle pulls the currents and, as result, the poloidal component of these increase

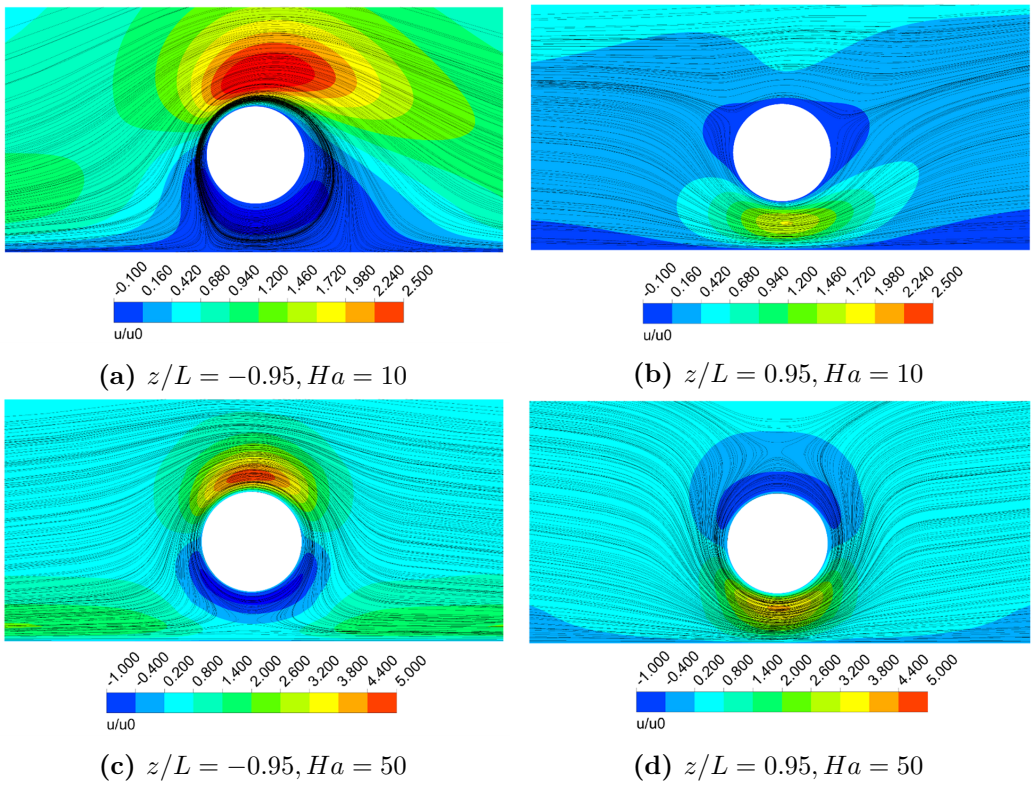

(a) $z/L = -0.95, Ha = 10$ **(b)** $z/L = 0.95, Ha = 10$

(c) $z/L = -0.95, Ha = 50$ **(d)** $z/L = 0.95, Ha = 50$

Figure 10.17. Near-wall vortex formation for perfectly conducting obstacle ($c_o = \infty$) and $Re = 20$. Left: streamline and dimensionless velocity contour at $z/L = -0.95$ and; right: at $z/L = 0.95$. Top row: results at $Ha = 10$ and; bottom row: at $Ha = 50$.

in both the lower and upper sub-channel compared with the insulating obstacle case, which is shown in Figure 10.18b and 10.18d. This leads to a stronger, resistive, Lorentz force due to enhanced poloidal component of the current that causes the flow reversal in the lower sub-channel. Conversely, the opposite phenomenon in the upper sub-channel causes the further promotion of the jet, already present in the insulating case, and its offset toward the lateral wall. The counter-clock vortex close to the other side wall is similarly formed due to the specular flow suppression and promotion in these regions of the sub-channels.

10.3.3 Pressure drop analysis

For a fully developed flow in a channel devoid of obstacles, the induced currents are confined to the plane perpendicular to the main flow direction and, therefore, are called cross section currents, with the flow being essentially 2D. This behavior is fundamentally altered when an internal obstacle is added, since it forces the flow to assume a new velocity field topology and the transition from the fully developed state observed upstream to a more complex and 3D flow. Significant velocity gradients in the radial and poloidal directions appear which, in turn, translate to electric potential differences that drive currents no longer confined to the duct cross-section. The most important potential difference is the one that arises in the radial direction, which

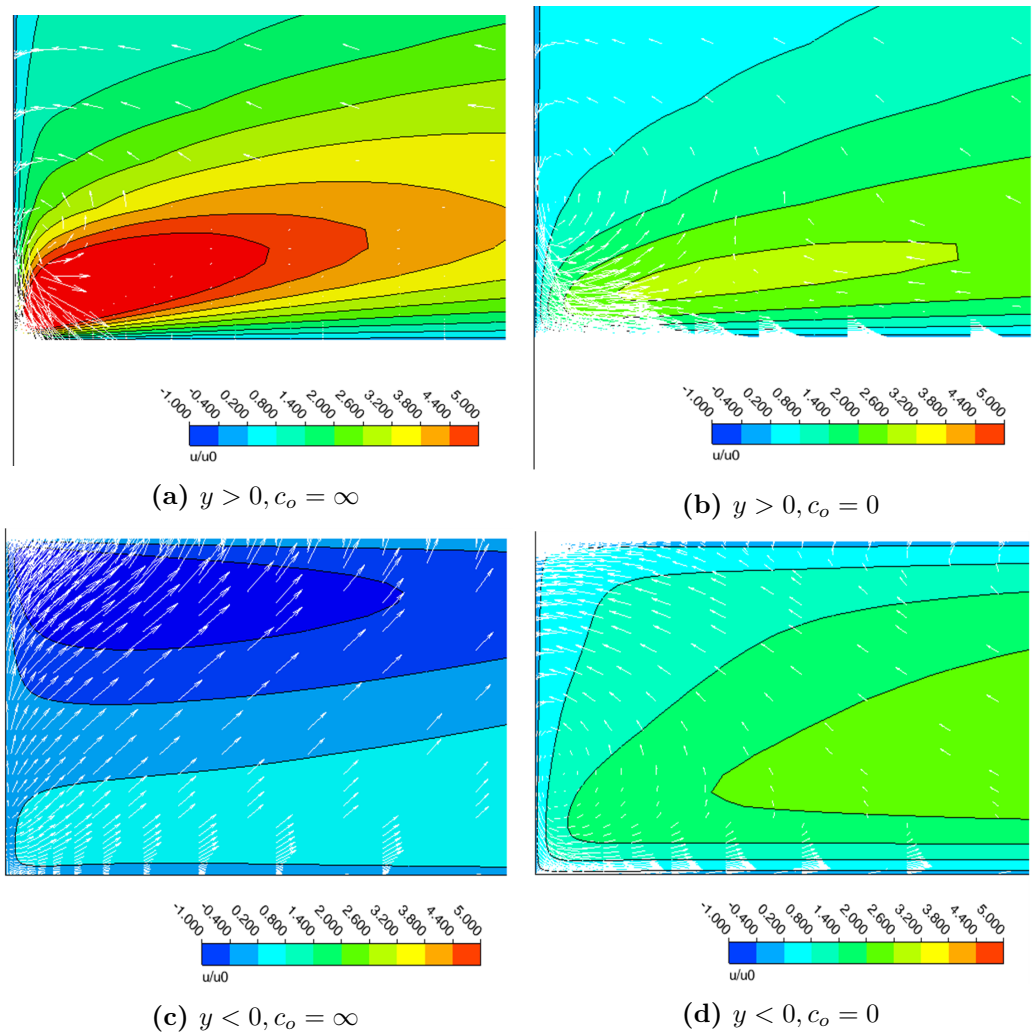

(a) $y > 0, c_o = \infty$ **(b)** $y > 0, c_o = 0$

(c) $y < 0, c_o = \infty$ **(d)** $y < 0, c_o = 0$

Figure 10.18. Detail of the velocity contour about the cylinder in the upper and lower sub-channel close to the side wall ($z/L = -0.95$). The arrows represent the current density vectors. Results presented for $Ha = 50, Re = 20$

drives currents flowing both upstream and downstream from the obstacle. These one then interact with the magnetic field and cause the increase in the electromagnetic drag experienced by the flow. For this reason, the pressure loss for a 3D MHD flow can be described as the sum of two terms: the pressure loss due to the flow three-dimensionality (Δp_{3D}) and the pressure loss due to flow in the duct devoid of obstacles (Δp_{2D}).

$$\Delta p = \Delta p_{2D} + \Delta p_{3D} \tag{10.2}$$

The two-dimensional term Δp_{2D} is dependent on the pressure gradient for the fully developed flow. For the flow in a rectangular duct, the pressure gradient value is mostly controlled by the conductance ratio of the walls bounding the flow that, for finite conductivity walls, can be expressed by the relation

$$\frac{\partial p}{\partial x} = k_p \sigma u_0 B_0^2 \tag{10.3}$$

where, in general, the pressure coefficient $k_p = f(c_w, \gamma)$, with $\gamma = a/b$ being the channel aspect ratio. Therefore, it can be said that the Δp_{2D} is proportional to both the flow mean velocity u_0 and the square of the magnetic field intensity B_0.

The three-dimensional term Δp_{3D} strongly depends on the flow geometry and features, therefore no simple relation exists to estimate its intensity [53]. However, since it is related to the radial current intensity, in general it would be dependent from the fluid velocity and magnetic field intensity. The intensity of the radial current can be expressed through Ohm's law

$$J_x = \sigma \left(-\frac{\partial \phi}{\partial x} + u_y \cdot B_z \right) \tag{10.4}$$

where the term $u_y \cdot B_z$ represents the induced electric field due to the displacement of the fluid caused by the obstacle, when no significant velocity in the toroidal direction is present ($u_z = 0$).

Electric potential and three-dimensional flow

To provide some insights about the phenomenology of the Δp_{3D} term, we analyze the electric potential distribution in the stream-wise direction. In Figure 10.19a and 10.19b, the electric potential for $Ha = 10$ and $Re = 20 \div 80$ is plotted against the dimensionless radial coordinate for five poloidal positions: lower sub-channel mid-line ($y/d = -1$), cylinder bottom ($y/d = -0.5$) and top ($y/d = 0.5$), upper sub-channel at one diameter ($y/d = 1.5$) and two diameters ($y/d = 2.5$) from the obstacle. For a duct devoid of obstacles, the fully developed state is enforced everywhere, therefore it must be that $\partial\phi/\partial x = 0$, and, since $\vec{u} = u_0, 0, 0$, it follows from Eq. (10.4) that $J_x = 0$. If now an obstacle transverse to the stream-wise direction is introduced, the fluid must flow around it and a poloidal component of the velocity appears that, interacting with the applied magnetic field, it generates an electrical potential difference in the radial direction.

It is possible to observe, both in Figure 10.19a and 10.19b, how the radial potential gradient caused by the obstacle is not confined to the cylinder immediate surroundings, but instead stretches to all the poloidal heigth of the duct and upstream and downstream in the radial direction. Above and below the cylinder, the poloidal velocity has opposite direction, i.e. respectively $u_y > 0$ and $u_y < 0$ upstream of the obstacle, and this is reflected in the electric potential, where we have $\partial\phi/\partial x < 0$ and $\partial\phi/\partial x > 0$, and, thus, we observe the current streamlines bend toward and away from the cylinder. The trend is obviously reversed downstream from the obstacle, when the flow slowly recovers the fully developed state under the stabilizing action of the magnetic field.

The potential profile is influenced by the wake structure. For $Re = 20$, the weak recirculation observed in the wake is mostly confined to the top part of the cylinder (see 10.10b) and the flow on the line $y/d = -0.5$ experiences a behavior very close to the creeping regime which, consequently, leads to the symmetric profile across $x/d = 0$ observed in Figure 10.19a. Contrariwise, the potential gradient on the $y/d = 0.5$ is carried downstream by the wake and matches the behavior of the other profiles probed in the upper sub-channel. For $Re = 80$, the wake is well developed and influences with the same intensity the flow in both sub-channels (see 10.10h):

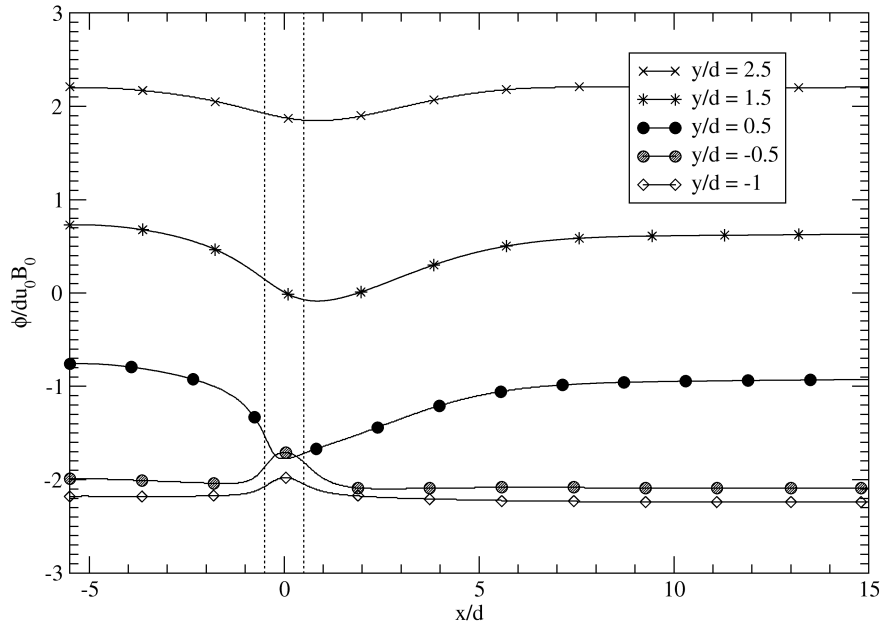

(a) $Ha = 10, Re = 20$

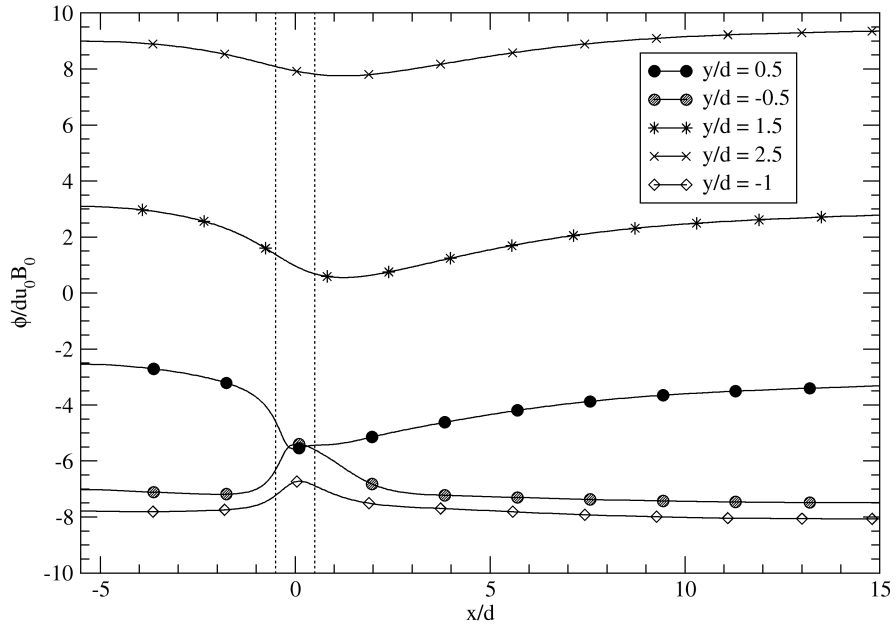

(b) $Ha = 10, Re = 80$

Figure 10.19. Electric potential profile in the radial direction for $Ha = 10$ and five poloidal positions plotted at the toroidal duct center ($z/L = 0$). Dotted lines identify the cylinder.

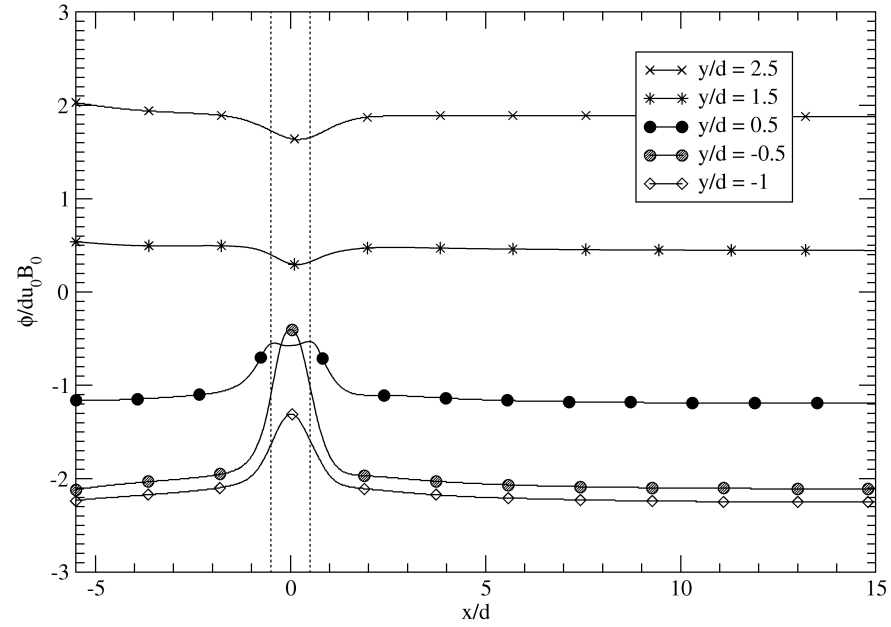

(a) $Ha = 100, Re = 20$

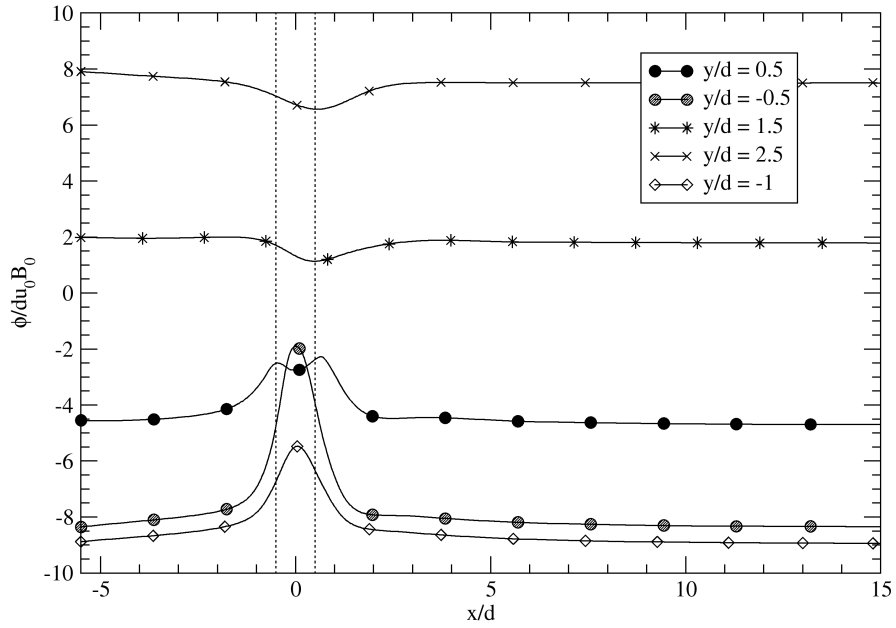

(b) $Ha = 100, Re = 80$

Figure 10.20. Electric potential profile in the radial direction for $Ha = 100$ and five poloidal positions plotted at the toroidal duct center ($z/L = 0$). Dotted lines identify the cylinder

the potential profile for $y/d = -0.5$ is no longer symmetric across the $x/d = 0$ line, but it is slanted downstream similarly to the profile sampled at $y/d = 0.5$. Interestingly, far from the obstacle the peak of the electric potential is not found on the line passing through the cylinder center ($x/d = 0$), but downstream from it at $x/d \approx 1$).

In Figure 10.20a and 10.20b, the same plot is provided for $Ha = 100$. The wake is completely suppressed and the creeping regime well established for both $Re = 20$ and $Re = 80$. Due to this transition, a more complex pattern is observed for the plot on the top of the cylinder($y/d = 0.5$) compared with Figure 10.19: the flow is at first pulled from the top to the bottom sub-channel ($u_y < 0$), to make possible the mass flow rate increase described in Section 10.3.2, and then is directed upward before reaching the obstacle ($u_y > 0$). Moreover, the high field intensity allows the flow to recover the fully developed state more quickly, thus restricting the radial extension of the region where the 3D currents can appear. This phenomenon intuitively leads to the conclusion that a higher magnetic field causes the lessening of the Δp_{3D} weight on the total pressure drop.

In Figure 10.21, the potential profile for a line tangent to the cylinder bottom is plotted for an increasing magnetic field intensity. As expected, the enhanced velocity caused by the mass flow rate redistribution in the bottom sub-channel triggers increasingly higher peaks for the electric potential. Moreover, in Figure 10.22b, it is possible to observe in more detail the effect of the wake on the potential profile, which becomes gradually symmetric across the cylinder center in parallel with the transition to the creeping regime. In Figure 10.22, the behavior for a line far from the cylinder in the upper sub-channel is presented. The peak of the electric potential gradually regresses toward the cylinder center with an increasing magnetic field and, moreover, its intensity decreases, thus reducing the radial current magnitude.

Pressure penalty

To characterize the Δp_{3D} term, the concept of obstacle pressure penalty is introduced

$$p_o = \frac{\Delta p - \Delta p_{2D}}{\Delta p_{2D}} \tag{10.5}$$

In a channel without obstacles, from Eq. (10.2) it follows that $p_o = 0$, since $\Delta p \approx \Delta p_{2D}$, and, therefore, any additional pressure drop calculated in the model are due to the 3D effects triggered by the obstacle, i.e. the "penalty" to pay pressure losses-wise compared with the empty duct. To estimate the pressure penalty with Eq. (10.5), the area-weighted average of the pressure on the inlet is taken as Δp, whereas Δp_{2D} is evaluated from area-weighted average of the the pressure gradient calculated at the outlet and multiplied for the duct total length, according to the relation

$$\Delta p_{2D} = (F_u + F_d)\frac{\partial p}{\partial x}\bigg|_{outlet} \tag{10.6}$$

In Figure 10.23, the pressure penalty (p_o) is plotted versus the magnetic field intensity. For $Ha \to 100$, the pressure penalty is found to sharply decrease from around 25% at $Ha = 10$ to the final value 6.5%. This trend can be explained with the Δp_{3D} weaker dependence on the magnetic field intensity compared with the

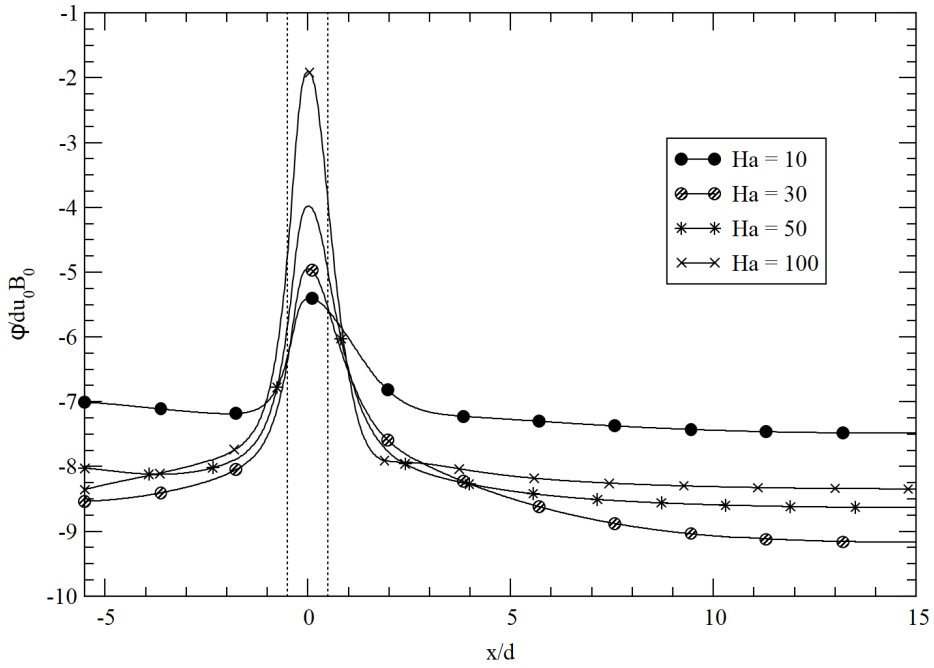

(a) $Re = 20$

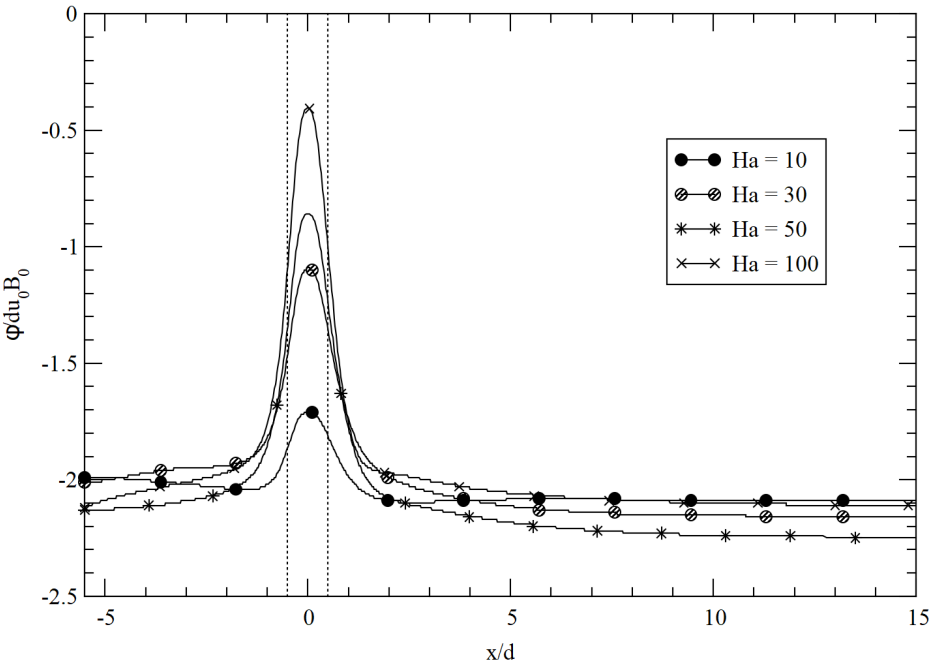

(b) $Re = 80$

Figure 10.21. Electric potential profile in the radial direction for a line tangent to the cylinder bottom ($y/d = -0.5$) with increasing magnetic field intensity. Dotted lines identify the cylinder position

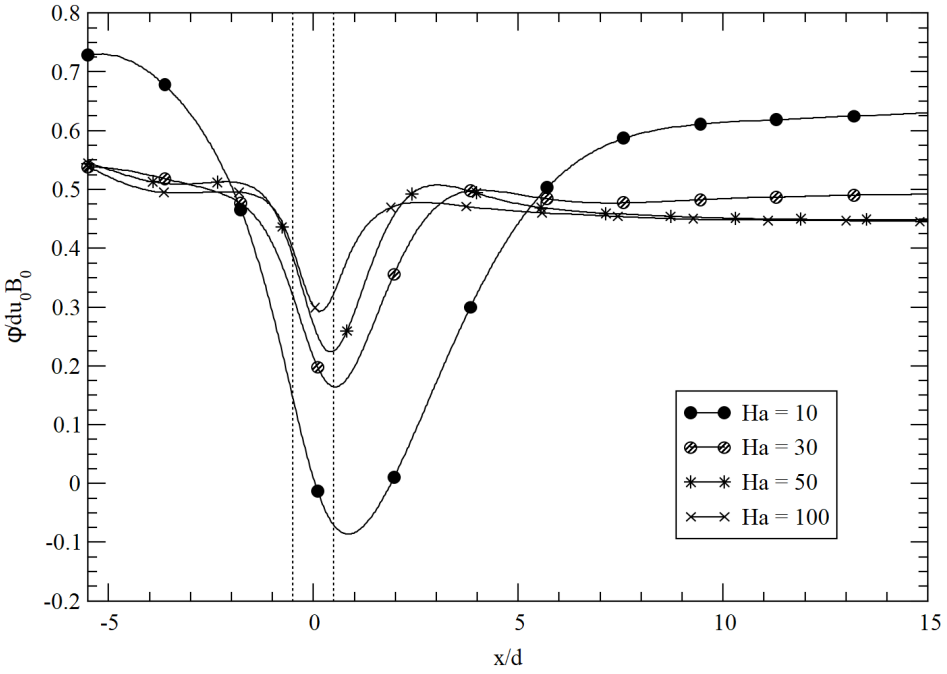

(a) $Re = 20$

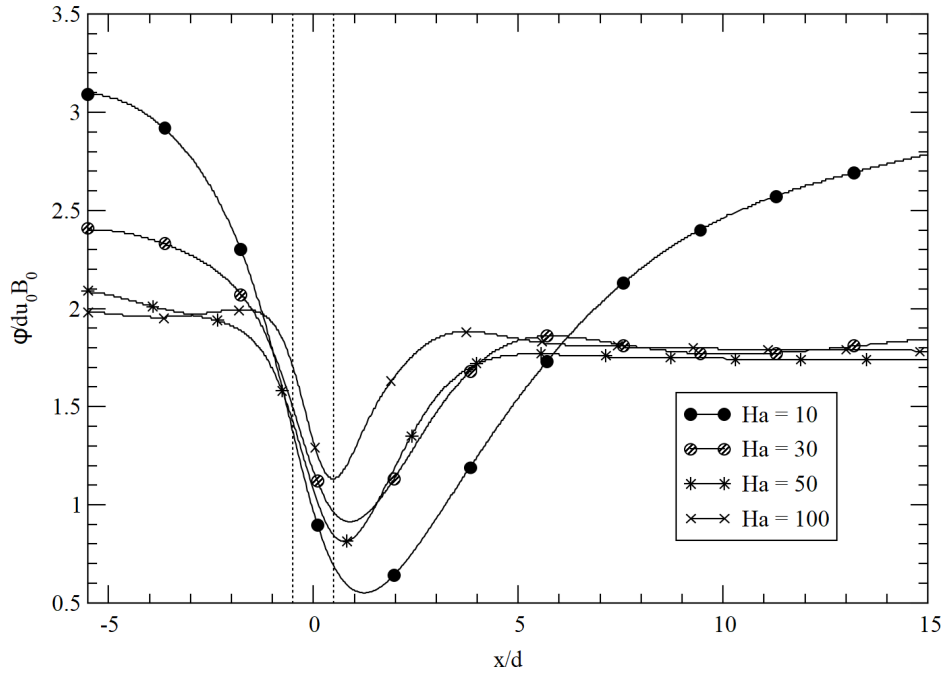

(b) $Re = 80$

Figure 10.22. Electric potential profile in the radial direction for a line in the upper sub-channel ($y/d = 1.5$) with increasing magnetic field intensity. Dotted lines identify the cylinder position

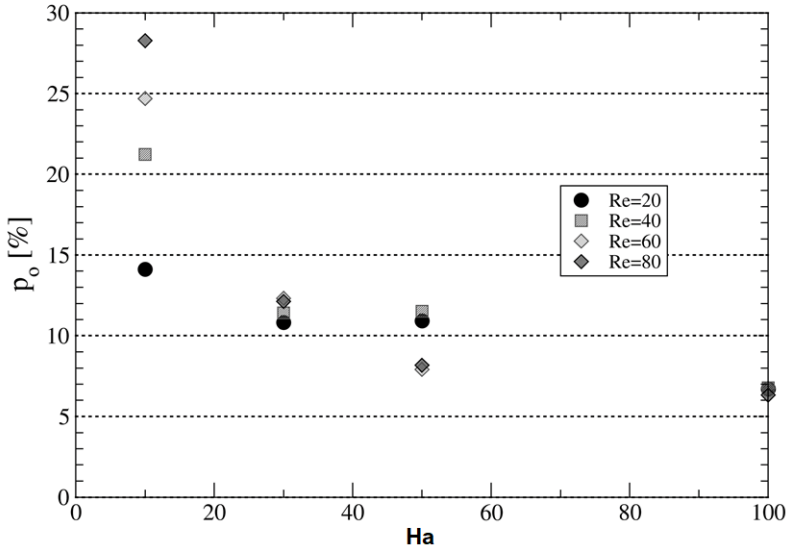

Figure 10.23. Pressure penalty as function of the magnetic field intensity for the insulating obstacle and magnetic field inclination $\alpha = 16°$

fully developed pressure gradient for electro-conductive walls. This leads to the reduction of the importance of the 3D pressure drop with the increase of the magnetic field, a result consistent with that reported by Hua for a similar configuration [181]. Moreover, this result appears to be consistent with the general electric potential behavior exhibited by the model.

However, for $Ha = 10$ the pressure penalty is found to vary considerably with the Reynolds number, whereas this effect gradually reduces with the increase of the Hartmann number and it is no longer observed for $Ha = 100$. The reason for this behavior can be found in the relative intensity of the inertial forces for the weak magnetic field case. If $N \gg 1$, the flow can be considered inertia-less, and the flow features are controlled only by two parameters, Ha and c_w. In Figure 10.24, it can be seen how, since the inertia-less condition is not met, the flow features for $Ha = 10$ are far from being invariant with Re, and the same it is obviously true for the local poloidal velocities that directly generate the radial currents responsible for the Δp_{3D} term. When the flow regime is not inertia-less, a term representing the pressure drop due to the inertial effects ($\Delta p_{inertia}$) must be added in Eq. (10.2), which is the one that causes the wide data spread at $Ha = 10$ in Figure 10.23. Conversely, the velocity contour for $Ha = 100$ are nearly identical since $N \gg 1$, and no discernible spread is found for the pressure penalty data, as shown in Figure 10.23.

Influence of magnetic field inclination

The flow feature rearrangement with the magnetic field inclination causes an analogous variation in the pressure gradient of the rectangular channel. In particular, the

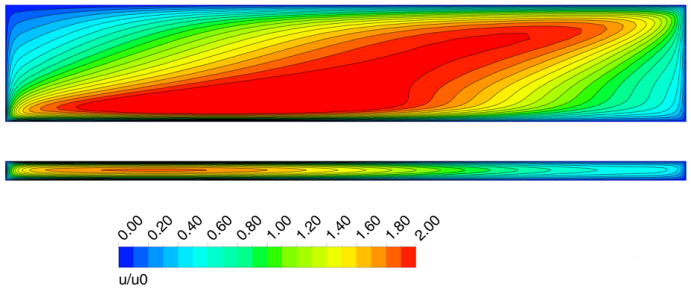

(a) $N = 5$

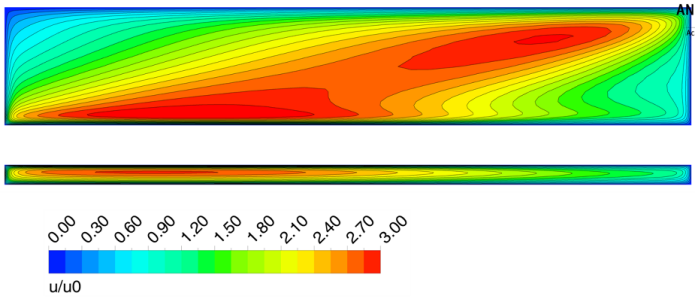

(b) $N = 1.25$

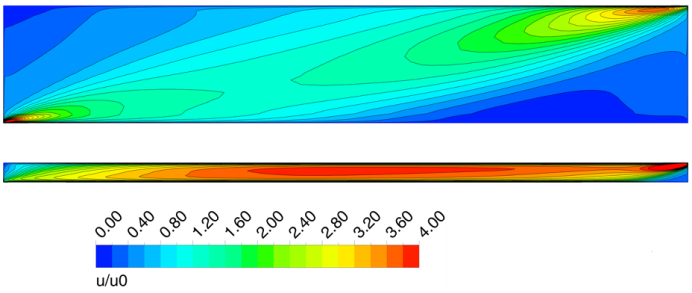

(c) $N = 500$

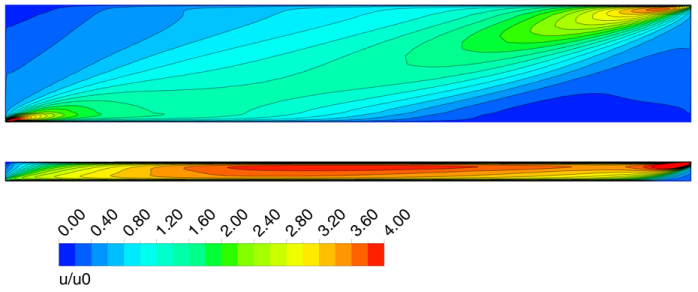

(d) $N = 125$

Figure 10.24. Inertial effects on the velocity contours for the flow about the cylinder. Top: $Ha = 10$, bottom $Ha = 100$. Left: $Re = 20$, right $Re = 80$. Magnetic field inclination $\alpha = 16°$. View from outlet

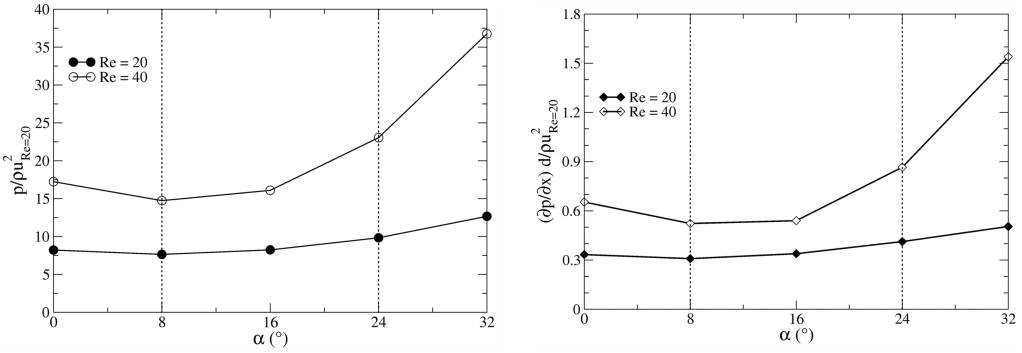

Figure 10.25. Pressure drop (left) and outlet pressure gradient (right) for a variable inclination of the magnetic field on the toroidal direction ($Ha = 10, Re = 20 - 40$). The dotted lines mark the blanket operative range from the reference inclination ($B_y \pm 50\%$)

increase of the intensity of the poloidal component is expected to provoke a rise in the two-dimensional pressure drop term due to the pressure gradient being a function of the channel aspect ratio. Employing the Hua correlation for channels with walls of non-uniform conductivity [44], the pressure coefficient k_p can be expressed as

$$k_p = \left[1 + c_H^{-1} + \gamma/6 \left(c_{S,1}^{-1} + c_{S,2}^{-1}\right)\right]^{-1} \tag{10.7}$$

where c_H is the conductivity ratio of the Hartmann walls and $c_{S,i}$ the one for the Shercliff walls. If we employ Eq. (10.7) to calculate the pressure coefficient for a purely toroidal ($\alpha = 0°$) and poloidal ($\alpha = 90°$) magnetic field[2] we obtain a characteristic ratio $k_{pol}/k_{tor} \approx 2.958$. Experimental results presented by Kirillov [44] suggest that, for a duct with a variable magnetic field inclination, the pressure coefficient variation can be approximated with a sinusoidal law ($k_p \propto sen(\alpha)$), although not without significant discrepancies with the experiment.

In Figure 10.25, the pressure gradient and total channel loss are presented against the magnetic field inclination. Qualitatively, both the plots agree with the proposed sinusoidal law and, in particular, they are very similar, thus suggesting that the dependence from the magnetic field inclination for the three-dimensional pressure drop term is not significantly different from the fully developed pressure gradient. However, the sinusoidal law cannot account for the local minimum of the pressure gradient found in Figure 10.25 at $\alpha = 8°$, since the theory predict a monotone trend even for low magnetic field inclination. The pressure gradient increases, overcoming the $\alpha = 0^{circ}$ value in the range $16° \leq \alpha \leq 24°$. This phenomenon can probably be explained with the low intensity of the magnetic field and the proximity to α_{cr}, but further study is needed to characterize it completely and investigate the role of the inertial effects.

For the inclination range foreseen in a blanket ($8° \leq \alpha 24°$), the pressure drop is fairly consistent with its limit variation in the range $0.9 \leq \Delta p(\alpha)/\Delta p(\alpha = 16°) \leq 1.25$ for the $Re = 20$ case and $0.8 \leq \Delta p(\alpha)/\Delta p(\alpha = 16°) \leq 1.32$ for the $Re = 40$.

[2] In this case, we assume for the Hartmann wall $c_H = \frac{c_t + c_b}{2}$ and, of course, for the Shercliff wall $c_{S,1} = c_{S,2} = c_s$

Table 10.5. Pressure penalty for different obstacle conductivity. The label E stands for the Eurofer obstacle ($c_o = 3.73 \cdot 10^{-2}$)

Ha		10			50		
c_o		0	E	∞	0	E	∞
p_o (%)	$Re = 20$	14.119	15.337	34.971	10.919	11.319	12.678
	$Re = 40$	21.128	22.105	40.741	13.356	10.686	14.613

Influence of obstacle conductivity

In Section 10.3.2, it has been discussed how the presence of a strongly conductive obstacle warps the current streamlines in the surrounding region and causes the formation of counter-rotating vortices close to the side walls. Similarly, this phenomenon influences the three-dimensional pressure drop term.

An overview of the pressure penalty value for the finite and infinite conductivity obstacles with regard to the insulating one is available in Table 10.5. For $Ha = 10$, the pressure penalty is found to be slightly higher for the Eurofer pipe ($c_o = 3.73 \cdot 10^{-2}$ compared with the insulating obstacle, whereas for the perfectly conducting one a more than twofold increase is observed.

This phenomenon can be explained by the redirection of the current paths already discussed in Section 10.3.2: since the finite conductivity pipe is only a slightly better path for the currents compared with the insulating one just a rather small portion of these is redirected through the obstacle surface and it does not triggers a consistent increase in the Δp_{3D}. On the other hand, the perfectly conducting obstacle is a very favorable path and triggers the appearance of much more intense radial currents, which in turn account for the pressure penalty increase. Increasing the Re causes a parallel growth in the pressure penalty due to the inertial effects, a phenomenon already discussed for Figure 10.23.

For $Ha = 50$, the pressure penalty for the finite conductivity pipe is still slightly higher than the insulating one. A variation is observed instead for the perfectly conducting case, where the pressure penalty is relatively not much different from the finite conductivity case, a striking difference with the $Ha = 10$ results.

A possible explanation for this phenomenon can be found in the electric potential distribution in the radial direction that, as discussed in Section 10.3.3, are correlated to the 3D currents. In Figure 10.26a, it is possible to observe that the electric potential gradient in the radial direction for the perfectly conducting case occupies a larger region of the duct compared with the insulating one due to the intense warping of the current paths seen in Figure 10.16. Conversely for $Ha = 50$, the plots for the two cases are nearly coincident, since the obstacle influence is restricted to a narrower region, and just a minor discrepancy for the electric potential is found in correspondence of the obstacle center (see Figure 10.26b). As a consequence, for $Ha \to \infty$, it can be seen that there is no significant effect of the obstacle conductivity on the pressure penalty.

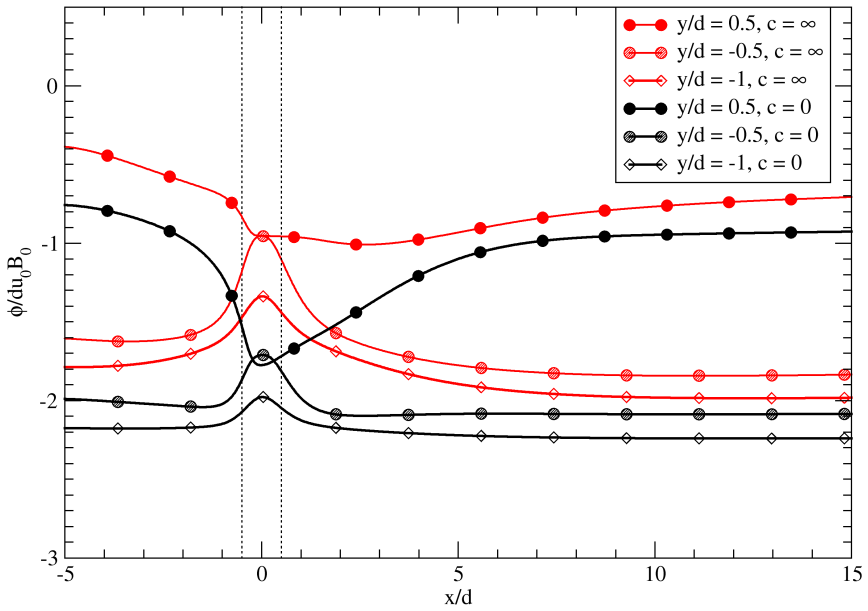

(a) $Ha = 10$

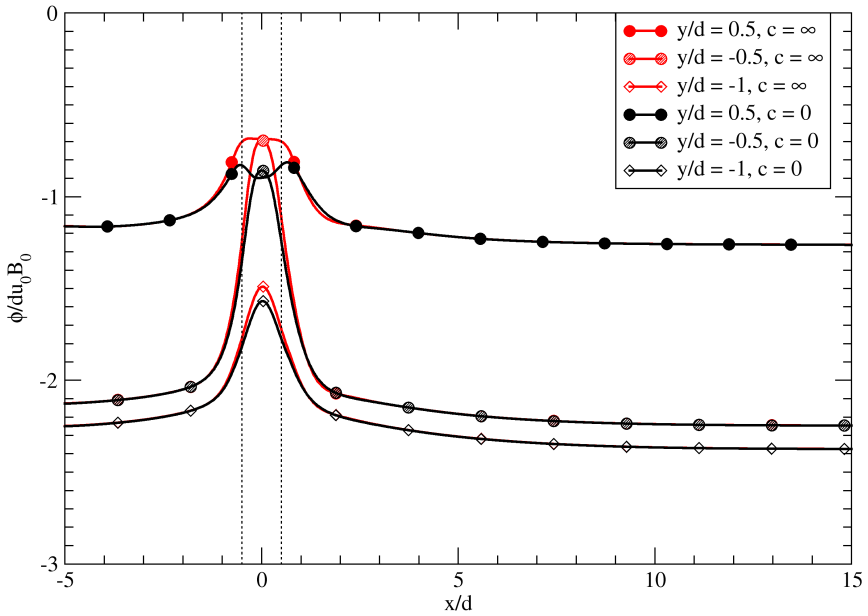

(b) $Ha = 50$

Figure 10.26. Electric potential profile in the radial direction for arbitrary conductivity obstacle. Dotted lines identify the cylinder. Results for $Re = 20$

Three-dimensional pressure drop correlation

Starting from the data collected about the pressure penalty detailed in the previous section, an engineering correlation is developed to aid the estimation of the three-dimensional pressure drop term for a similar configuration as the one studied in the present chapter.

Conventionally, the 3D pressure drop can be expressed with two different formulations. The more widespread technique relies on a local MHD resistance coefficient (ζ) that, as described in Section 4.3.2, is a function of the interaction parameter N and Hartmann number Ha, other than the problem geometry and magnetic field orientation, and, therefore, represents in an implicit way the increased electromagnetic drag due to the 3D currents [53]. An alternative methodology, originally proposed by Bühler for the 3D flow in pipes with circular cross-section [68], argues that the 3D pressure drop term can be represented as the 2D pressure loss for the fully developed flow in a channel with $c_w = 1$ and length equal to the penetration distance of the 3D currents in the liquid metal. Due to the difficulty in the estimation of the penetration length of the 3D currents, the "indirect" approach is usually favored.

If the former approach is employed, the 3D pressure drop can be expressed as

$$\Delta p_{3D} = \zeta \frac{1}{2} \rho u_0^2 \tag{10.8}$$

with the local MHD resistance coefficient

$$\zeta = kN = k \frac{\sigma B_0^2 L_{3D}}{\rho u_0} \tag{10.9}$$

where L_{3D} is the characteristic length scale for the 3D flow and the coefficient k is generally in the range $0.25 \leq k \leq 2$, according to the literature consensus [53]. However, Bühler pointed out how the upper limit is usually based on experimental results that were conducted at N and Ha far from actual blanket operative conditions and, since $\zeta = f(Ha, N)$, even larger values could be possible [68]. On the other hand, several references are reporting $k < 0.25$, especially for $N \gg 1$ and flow in bends, therefore care must be taken when determining the value of the k coefficient [44]. Substituting Eq. (4.10) into Eq. (4.9), it is possible to arrive at the expression

$$\Delta p_{3D} = \frac{1}{2} k \sigma u_0 B_0^2 L_{3D} \tag{10.10}$$

Eq. (10.10) is employed as starting point to develop a correlation for the 3D pressure drop term. The outer diameter of the pipe (d) is chosen as length scale for the 3D effect (L_{3D}). According to the pressure penalty and electric potential data collected, the weight of the 3D pressure drop on the total loss in the channel decreases gradually with an increasing magnetic field, which can be taken as indirect evidence that the 3D pressure drop term features a weaker dependence on the field intensity B_0 compared with the 2D losses that becomes dominant for $Ha \to \infty$. For this reason, the magnetic field power index k_2 for the 3D term is considered a variable parameter and it is assumed to be bounded by the 2D term power index ($k_2 < 2$). Numerical data obtained at $Ha = 10$ are not considered to develop the correlation in order to remove the inertial effects that dominate the flow around the

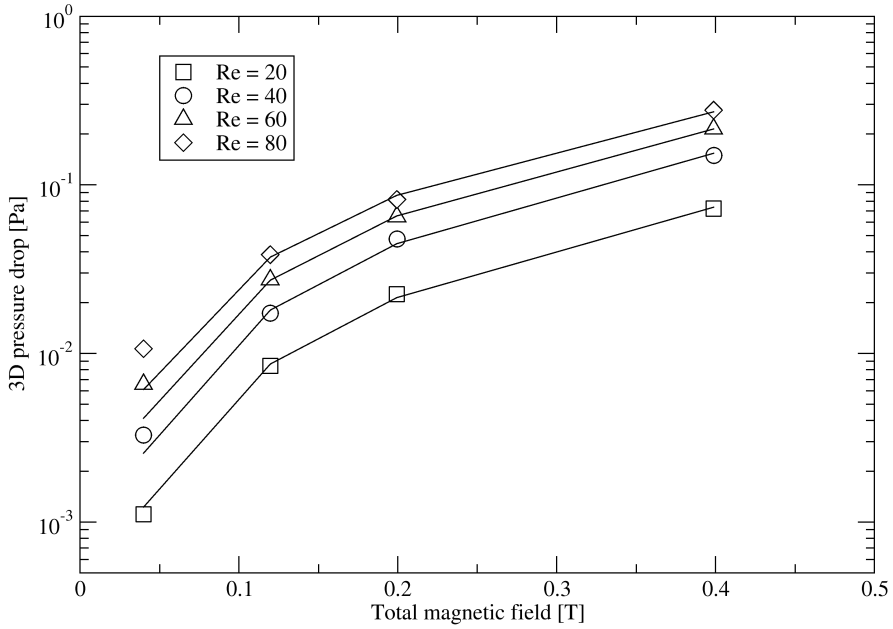

Figure 10.27. Comparison between best-fit correlations and $Re = const$ plots. Symbols indicate numerical data.

pipe for weak magnetic field intensity and derive a law for the more blanket-relevant inertia-less regime ($N \gg 1$).

The results for the three-dimensional pressure drop term with regard to the Hartmann number are employed for the best-fit of the numerical data. From Eq. (10.10), the three-dimensional pressure drop term can be described as a power law, $y = a \cdot x^b$, where the coefficient a is a non-linear term, which is function of the inlet average velocity ($a = \frac{1}{2} k \sigma u_0 L_{3D}$), and b is the magnetic field power index. To decouple the dependence from the velocity and the magnetic field intensity in the 3D pressure drop term, the numerical data are divided into four $Re = const.$ plots that are then subjected to the best-fit procedure employing a power law. In Figure 10.27, the correlations obtained are compared with the numerical data.

The coefficients of these correlations are then averaged to derive a more general law. For the magnetic field power index, the following value was found for the B_i averaging

$$\bar{B} = 1.730075 \pm 0.031897, \quad \sigma_{sd} = 0.063794 \tag{10.11}$$

where σ_{sd} is the standard deviation of the B_i sample. For the coefficient A, the parameter of interest k_i is derived from the A_i sample

$$k_i = A_i / \left(\frac{1}{2} \sigma u_{0,i} L_{3D} \right) \tag{10.12}$$

where $u_{0,i}$ is the inlet average velocity of each $Re = const$ plot. The k_i sample thus obtained is then averaged to obtain the searched constant

$$\bar{k} = 0.193047 \pm 0.010552, \quad \sigma_{sd} = 0.021104 \tag{10.13}$$

The sample sets for the coefficients a_i, b_i and k_i are reported in Table 10.6.

Table 10.6. Correlation coefficients from Figure 10.27

	$Re = 20$	$Re = 40$	$Re = 60$	$Re = 80$
a_i	0.3783	0.79139	1.0335	1.23
k_i	0.204852	0.214272	0.186549	0.166513
b_i	1.7795	1.7802	1.7142	1.6464

Finally, the proposed correlation law can be written as

$$\Delta p_{3D} = \frac{1}{2} k \sigma u_0 B_0^m d \tag{10.14}$$

where the coefficients determined from the best-fit of the considered numerical data are $k = 0.1931$ and $m = 1.73$. The range of applicability for the fundamental parameters is $N = [11.25, 500], Ha = [30, 100], Re = [20, 80], c_o = 0, \beta = 0.223, G/d = 0.5$ and $\alpha = 16°$.

To assess the quality of the proposed correlation in predicting the numerical data, it is possible to employ the coefficient of determination R^2, that is defined as

$$R^2 \equiv 1 - \frac{SS_{res}}{SS_{tot}} \tag{10.15}$$

where SS_{res} is the residual sum of squares

$$SS_{res} = \sum (y_i - f_i)^2 \tag{10.16}$$

and SS_{tot} is the total sum of squares

$$SS_{tot} = \sum (y_i - \bar{y})^2 \tag{10.17}$$

with y_i the expected (numerical) data and their average $\bar{y}$, and f_i the predicted data from the correlation [182]. In Table 10.6, the coefficients of determination for each $Re = const$ set (R_i^2) and the whole data set are reported, together with the relative error for each data point. Due to the low number of data points available for the best-fitting the R^2 is relatively high, even if Eq. (10.14) is not able to predict accurately the trend of the pressure drop term at the lower boundary of the data set ($Ha = 10$), where the inertial effects, unaccounted by the correlation, are significant. However, the error for the application range ($Ha = 30 - 100$) is relatively small and the correlation shows a good agreement with the numerical data, thus providing a reasonable approximation of the physical behavior, mainly due to the low standard deviation for the magnetic field power index. The principal source of uncertainty is represented by the coefficient k that, due to the methodology employed for its determination, is influenced by the pressure drop dependence on the velocity. To reduce the uncertainty, further numerical results are required to both enhance the number of data points available for the best-fitting and to better characterize the three-dimensional pressure drop behavior in the inertia-less regime ($Ha > 100$).

10.3.4 Heat transfer analysis

Since the Joule heating is considered negligible in the induction-less form of the MHD governing equations presented in Section 3.4, no source of power is present within

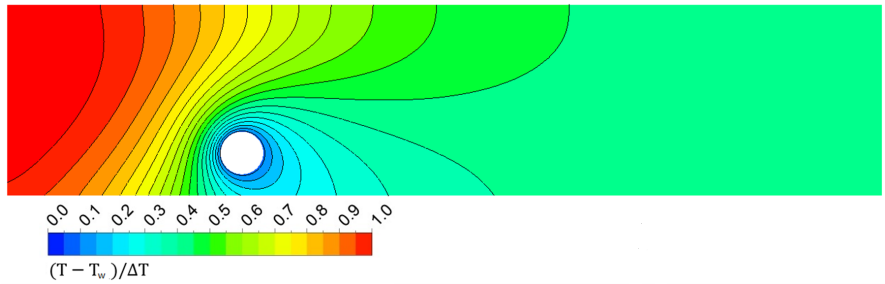

(a) $Ha = 10, Re = 20$

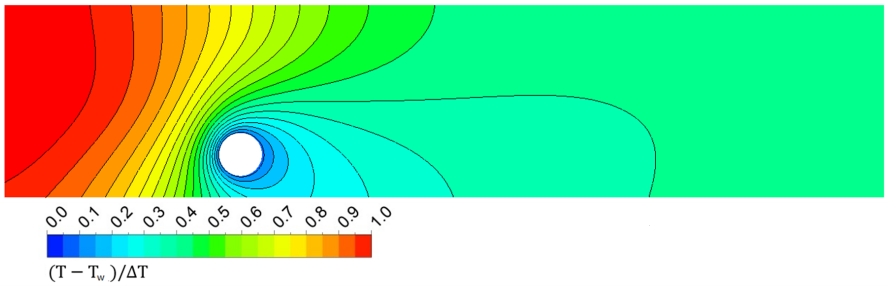

(b) $Ha = 100, Re = 20$

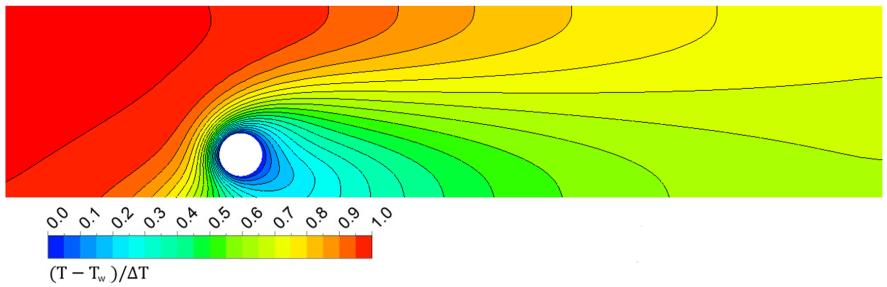

(c) $Ha = 10, Re = 80$

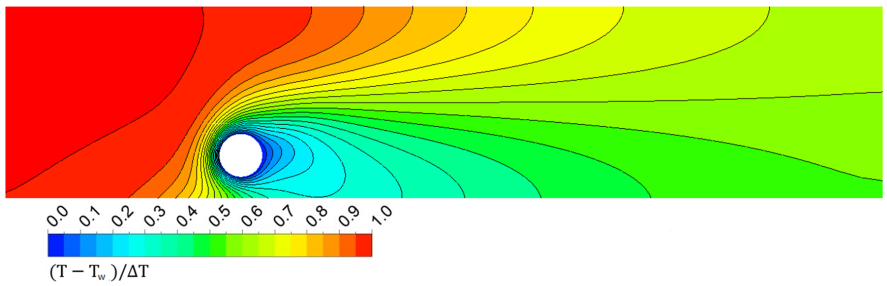

(d) $Ha = 100, Re = 80$

Figure 10.28. Dimensionless temperature contour comparison for the z/L=0 plane for some selected cases

Table 10.7. Relative error for estimated values from Eq. (10.14) and coefficient of determination R^2

Ha	$B(T)$	$Re = 20$	$Re = 40$	$Re = 60$	$Re = 80$
10	0.0399	21.537	-17.700	-38.258	-49.251
30	0.1196	7.419	4.075	-0.564	-6.015
50	0.1994	-2.461	-8.519	1.407	7.118
100	0.3988	0.526	-2.992	1.472	4.834
R_i^2		0.99990271	0.997234033	0.999369685	0.994959983
R^2			0.996947357		

the channel and the cylinder surface is the only non-adiabatic one. Consequently, the magnetic field can alter the heat transfer in the model just through the modification of the flow pattern that has been described in Section 10.3.1 and 10.3.2.

For the lowest velocity considered ($Re = 20$), the Peclet number is less than one ($Pe = 0.68$) and the heat transfer in the channel is dominated by the conduction mechanism. In Figure 10.28, it can be observed how the thermal conduction efficiently cools the fluid upstream of the obstacle, nearly reaching the inlet, where the isotherms are parallel to each other and slightly slanted in the stream-wise direction due to the higher mass flow rate in the upper channel. Downstream from the obstacle, the combined action of convection and conduction quickly normalizes the temperature reaching a constant value in the duct at around $x/d = 5$. Increasing the magnetic field intensity for this case leads to further warp the isotherms downstream and toward the duct centerline, due to the enhanced mass flow rate in the bottom sub-channel, which promotes the heat transfer in this region, but the conduction mechanism remains dominant.

If the flow velocity is increased then the Peclet number rises and becomes greater than one. The convection mechanism becomes more efficient and it can be seen how, for the $Re = 80, Pe = 2.72$ results presented in Figure 10.28c and 10.28d, no relevant cooling of the fluid upstream of the cylinder is observed anymore. The distortion of the isotherms downstream from the obstacle follows the same pattern that is observed for the low velocity case in Figure 10.28a and 10.28b but is even more significant, especially in the cylinder wake, where the flow transitions from the steady vortex to the creeping regime.

A local Nusselt number is defined to assess the heat transfer between the obstacle and surrounding fluid through the local temperature gradient normal to the cylinder surface (A)

$$Nu_w(\theta, z) = \frac{d}{T_{bulk} - T_w} \left.\frac{\partial T(\theta, z)}{\partial r}\right|_A \tag{10.18}$$

where the fluid bulk temperature T_{bulk} is computed as the average temperature on the cylindrical surface S, placed at a distance $r = d$ from the obstacle center weighted for the velocity distribution

$$T_{bulk} = \frac{\iint_S uT \, d\theta dz}{\iint_S u \, d\theta dz} \tag{10.19}$$

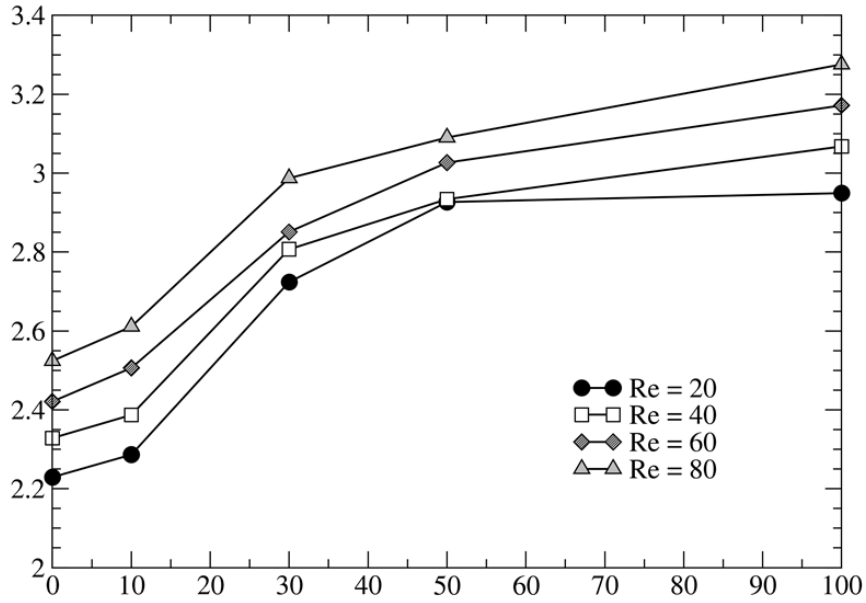

Figure 10.29. Average Nusselt number as function of the magnetic field intensity

The average Nusselt number is then obtained by the integration of (10.18)

$$Nu = \frac{1}{A} \iint_A Nu_w(\theta, z)\, d\theta dz \tag{10.20}$$

The average Nusselt number computed with Eq. (10.20) is found to increase with the intensity of the applied magnetic field throughout the Re range considered, as it can be observed in Figure 10.29, and, for constant Ha, to be also dependent on the Re. The enhancement of the heat transfer with increasing Re is not surprising due to the better efficiency of the convection mechanism with the higher flow velocity. The influence of the magnetic field is more complex to understand due to the many variations introduced in the flow pattern and the significant differences in the flow features for increasing Ha.

In Figure 10.30, the local Nusselt number plotted on the cylinder circumference on the radial-poloidal plane $z/L = 0$ shows that the maximum heat transfer is observed for the frontal part of the obstacle, whereas it steadily decreases moving toward the back due to the reduced ΔT among the fluid and the heating element. This general behavior is shared by both the OHD and MHD regime. Conversely, in the back of the cylinder (see Figure 10.31a) the magnetic field dampening effect on the cylinder wake reduces the heat transfer compared with the hydrodynamic case, whereas in other areas the heat transfer is generally increased, for instance the promoted flow in the bottom sub-channel nearly doubles the Nusselt number in that region between $Ha = 0$ and $Ha = 100$ (see 10.31d). The departure from the hydrodynamic regime is evident also at the top of the cylinder ($\theta = \frac{1}{2}\pi$) and front ($\theta = \pi$) of the obstacle (see Figure 10.31b and 10.31c). The local Nusselt number is almost constant for $Ha = 0$ over the toroidal length of the cylinder, whereas the modifications introduced in the flow pattern drastically alter this trend for $Ha > 0$.

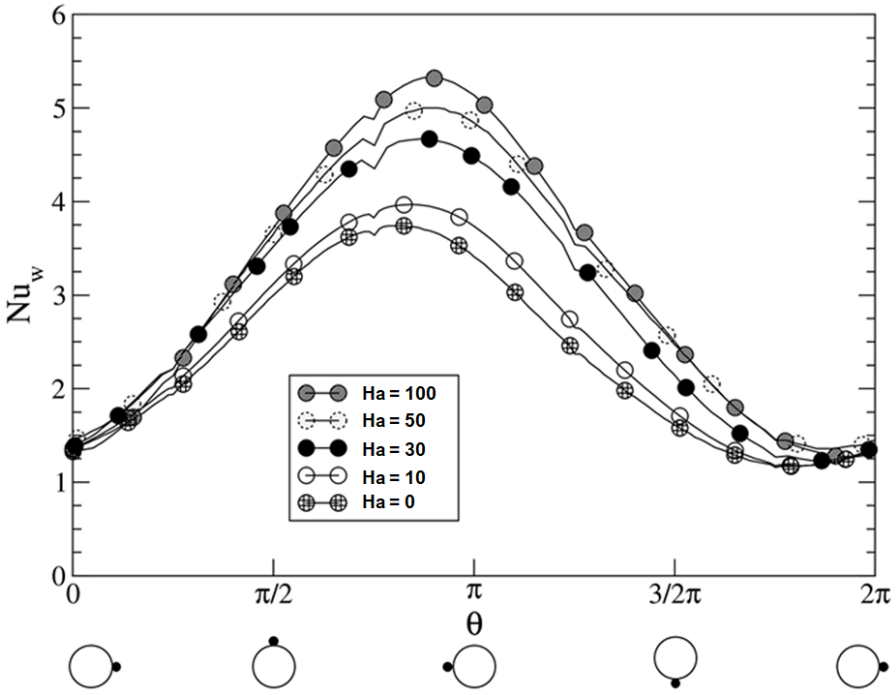

Figure 10.30. Local Nusselt number on the obstacle circumference at $z/L = 0$ for $Re = 20$ as a function of the azimuthal coordinate θ. The back of the obstacle is identified by the coordinate θ=0.

At the top, a peak is observed at the obstacle center accompanied by a reduced heat transfer close to the lateral walls. A similar trend is found at the cylinder front, where the quicker fluid in the internal layer close to the wall at $z/L = -1$ enhances the heat transfer compared with the slow flow observed in the opposite wall.

A possible explanation for the increase in the heat transfer with the magnetic field intensity is the surge in the mass flow rate carried by the bottom sub-channel, which, as it is discussed in Section 10.3.2, can be explained with the leakage currents originated in the top-channel that enter the region through the shared electro-conductive lateral walls. These currents generate a Lorentz force that it is not resistive to the flow movement but actively weakens the retarding action exerted by the cross-sectional currents generated in lower the sub-channel, which in turn leads to the development of jets with velocity much higher than the one observed in the upper sub-channel. It is difficult to foresee if this trend will be maintained for values of the Hartmann number higher than the one considered in this study, but it is safe to assume that increasing the magnetic field intensity will cause a stronger electromagnetic coupling and, therefore, an increase in the flow rate in the bottom sub-channel. However, this will reduce the mean flow velocity in the top sub-channel, leading to the gradual weakening of the leakage currents generated there and, thus, of the flow-promoting Lorentz force responsible for the surge in the mass flow rate below the cylinder. For $Ha \to \infty$, this phenomenon will probably lead to an equilibrium between the flow rate of the sub-channels and, therefore, to a Nusselt number no longer function of the magnetic field intensity.

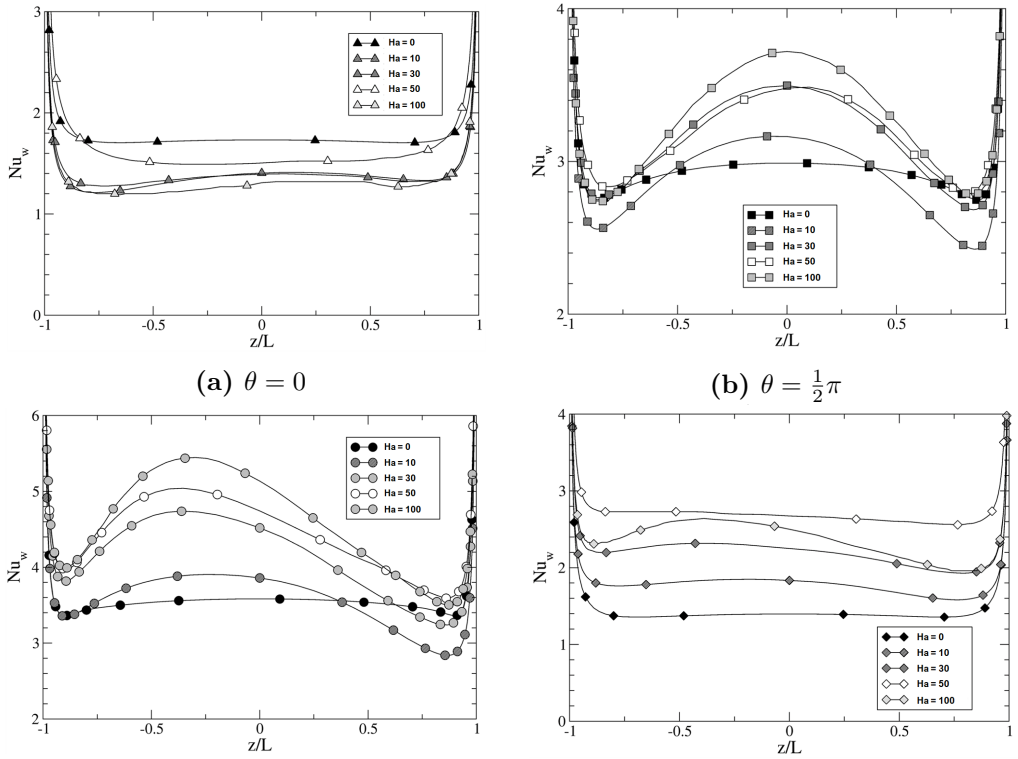

(a) $\theta = 0$ **(b)** $\theta = \frac{1}{2}\pi$

(c) $\theta = \pi$ **(d)** $\theta = \frac{3}{2}\pi$

Figure 10.31. Local Nusselt number as function of the toroidal coordinate for 4 relevant azimuthal positions: a) back, b) top, c) front, d) bottom of the cylinder. Results for $Re = 20$.

Influence of obstacle conductivity

The effect of this parameter is mostly limited to low magnetic field intensities and it is connected to the changes in the flow pattern detailed in Section 10.3.2. An overview of the results is presented in Table 10.8. No significant difference is found about the heat transfer between the insulating and Eurofer case, with the latter performing slightly worse. For $c_o = \infty$, the flow pattern modifications and a slightly higher mass flow rate in the bottom sub-channel, thanks to stronger leakage currents, causes an increase in the Nusselt number compared with the $c = 0$ case. At $Ha = 10$, an increase in the heat transfer $\Delta Nu = +4\%/+5.9\%$ is found with the latter value referring to the $Re = 20$ result. The plots of the local Nusselt number on the cylinder surface along four relevant azimuthal positions are presented in Figure 10.32.

Table 10.8. Average Nusselt number for different obstacle conductivity. The label E stands for the Eurofer obstacle ($c_o = 3.73 \cdot 10^{-2}$)

Ha		10			50		
	c_o	0	E	∞	0	E	∞
Nu	$Re = 20$	2.5549	2.5427	2.6340	3.1440	3.1325	3.1513
	$Re = 40$	2.6019	2.6046	2.6634	3.1502	3.0893	3.1219

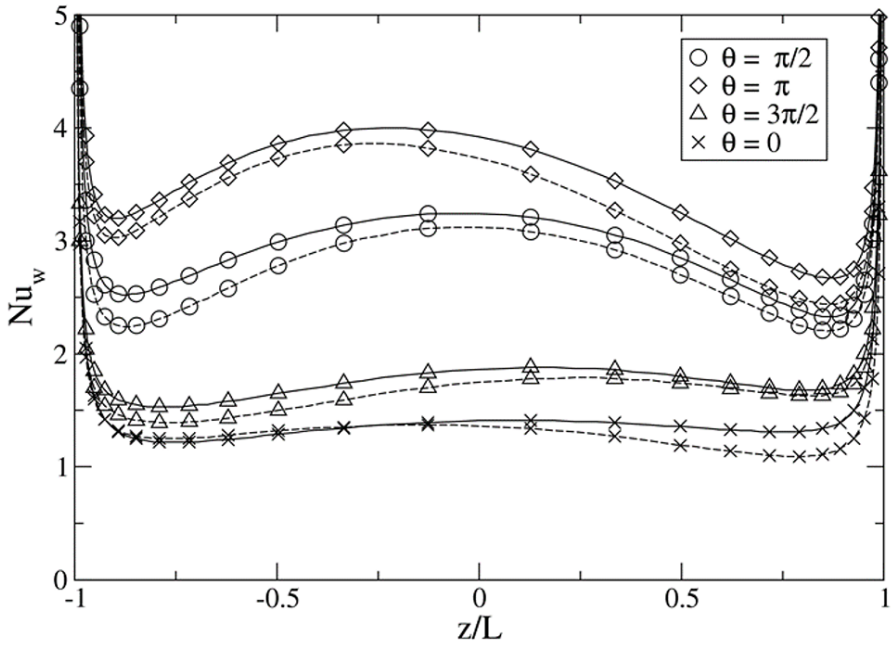

Figure 10.32. Local Nusselt number along the toroidal coordinate for 4 relevant azimuthal position for the perfectly conducting (full line) and insulating (dotted line) obstacle. Result presented for $Ha = 10$ and $Re = 20$

Increasing the magnetic field intensity causes a reduction in the performance difference between the two cases, which records a smaller increase $\Delta Nu = +1.2\%/+1.5\%$ with the latter value still referring to the $Re = 20$ case. Again, no significant difference is found between the Eurofer and insulating case at $Ha = 50$. Therefore, for design purposes a cooling pipe can be assumed to be electrically insulated without introducing any significant error for the heat transfer evaluation [85].

Influence of magnetic field inclination

For $\alpha = 0°$, the magnetic field is purely toroidal and, due to the low local conductivity, the flow is mostly centred in a jet close to the top wall. Alongside the wall, the side layer shows a velocity parabolic profile, which connects the peak with the Hartmann layers. When α increases, the side layer detaches from the wall and most of the flow is carried over by the internal layer. This condition is more favourable for the heat transfer since the average velocity of the fluid hitting on the obstacle increases. An increment of $\approx +6\%$ was found for the average Nusselt number between the purely toroidal case and $\alpha = 32°$, however, in the range considered for the tokamak operation ($8° \leq \alpha \leq 24°$), the deviation with respect to the reference inclination ($\alpha = 16°$ is found to be $\pm 2\%$ (see Figure 10.33). Therefore, the fluctuation of the poloidal component during the blanket operation can most probably be neglected without introducing any significant error for the heat transfer evaluation [169].

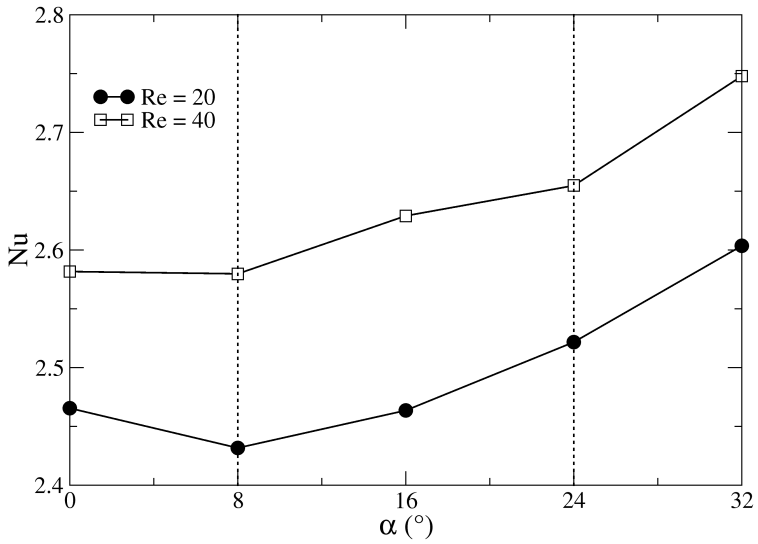

Figure 10.33. Average Nusselt number for a variable inclination of the magnetic field on the toroidal direction ($Ha = 10, Re = 20 - 40$). The dotted lines mark the blanket operative range from the reference inclination ($B_y \pm 50\%$)

10.4 Final remarks

In this chapter, the MHD flow around a breeding zone cooling pipe for one of the WCLL configurations (see Section 7.2) has been investigated in the range $20 \leq Re \leq 80$, $0 \leq Ha \leq 100$, and $1.25 \leq N \leq 500$. The simplifying assumption of a perfectly insulated pipe ($c_o = 0$) is employed to characterize the channel flow and the influence of the toroidal-poloidal magnetic field ($\alpha = 16°$) on the flow pattern, the pressure drop, and the heat transfer.

The magnetic field effect on the wake structure is discussed and found consistent with the result already published in the literature regarding the dampening of the vortical structures and the shifting to higher Re_{cr} for the transition from the creeping flow to the steady 2D recirculation regime. The heat transfer rate is found to increase with both Re and Ha, and, in particular, the latter trend has been explained with the surge in the mass flow rate in the smaller sub-channel below the cylinder compared with the ordinary hydrodynamic behavior. This phenomenon can possibly be explained with the combination of a reduced magneto-hydraulic resistance due to a higher aspect ratio and leakage currents coming from the sub-channel above the cylinder that actively promote the stream-wise velocity component. The pressure penalty due to the obstacle presence has been characterized and found to decrease with Ha, other than being independent from Re at $Ha \to \infty$. A correlation is proposed to estimate the pressure drop term related to the 3D effects introduced by the obstacle for Ha closer to operative blanket conditions.

Furthermore, the influence of two additional parameters has been investigated

for a more restricted range of cases: the magnetic field inclination (α) and the obstacle conductivity (c_o). For the former, the analysis focused on the low magnetic field intensity case ($Ha = 10$) and $0° \leq \alpha \leq 32°$. The field inclination is found to dramatically influence both the flow pattern around the obstacle and the features of the channel flow, but, for the blanket operative range ($0° \leq \alpha \leq 32°$) has a rather limited effect on both the total pressure loss and the Nusselt number. However, these results must be integrated with more extensive simulations at higher Ha. The obstacle conductivity analysis how this parameter significantly affects the flow for low magnetic field intensity, causing higher pressure penalty and Nusselt number, but becomes negligible already for moderate Ha due to the enhanced 3D effects triggered by the electro-conductive surface being confined close to the obstacle. For the perfectly conducting case ($c_o = \infty$), vortices that flow around the obstacle are observed close to the side walls.

Chapter 11

Mixed convection in rectangular channel with curved pipes

11.1 Introduction

In this chapter, a CFD analysis is carried over to characterize the MHD flow in the BZ channel of the WCLL configuration T02, the general layout of which has been described in Section 7.4. The channel is aligned with the poloidal direction and the PbLi is driven to flow upward by the imposed pressure gradient. Intense volumetric heating caused by the neutron capture reactions in the liquid metal generates large temperature gradients in the radial direction that are responsible for the appearance of significant buoyancy forces in the channel. Therefore, the flow in the channel must be treated as a mixed convection case to account for the interaction between the pressure-driven and buoyant convection.

The main objectives of this study are:

- Characterize the MHD flow for the BZ channel close to the FW, which is subjected to the highest volumetric heating [183].
- Assess the capacity of the BZ cooling system to ensure the Pb Li refrigeration
- Identify optimization strategies to improve the performances of the BZ cooling system, if necessary

To achieve these objectives, a CFD model of the FW channel has been realized in ANSYS CFX focusing the attention on the elementary region, which is defined as

the region of the channel that is refrigerated by a single cooling element. The cooling element for the FW channel is constituted by two nested U-pipes that are inserted from the back and are characterized by a medium blockage ratio ($\beta \approx 0.3$). Therefore, the flow in the FW channel can be more accurately described as a mixed convection around transverse curved pipes. Hydrodynamic and magnetohydrodynamic simulations have been performed to characterize the flow behavior and to compare the performances of the cooling system with and without an applied magnetic field.

To assess the BZ cooling system performances, a criterion is introduced to specify the maximum acceptable PbLi temperature in the most intensely heated channel, i.e. close to the FW. Even if there is no design criterion regulating the maximum PbLi temperature, it is well known that the bulk and interface maximum temperature in the blanket structural elements must be kept below $T_{Max} = 823$ K to avoid the Eurofer mechanical properties degradation [25, 184]. In this study, we assume that the maximum acceptable PbLi temperature in the FW channel should not exceed $T_{Max} = 823$ K that, by itself, is a even more stringent requirement. If the cooling system will be able to meet this condition for both purely hydrodynamic and magnetohydrodynamic flow regime, we will be able to conclude with some confidence that even the Eurofer temperature limit will be met in realistic operative conditions.

Part of the results described in this chapter are also available in Ref. [185].

11.2 Rationale and problem formulation

Configuration T02 is one of the four alternative concepts investigated as design reference for the WCLL blanket and a preliminary estimate of the pressure drop in the PbLi flow path envisioned therein was discussed in Part II. In Figure 11.1, the general layout of the configuration T02 is presented. The stiffening plates arrangement splits the space available for the breeding zone into rectangular channels, which when grouped together resemble a "geometrical matrix" with rows and columns in the radial and toroidal direction. Depending on the stiffening plate arrangement, several matrices can be envisioned: the reference disposition for the T02, optimized to minimize mechanical stresses, is composed of 8 and 4 channels in the toroidal and radial direction, for overall 32 channels in the BZ. Each one of this channel runs along the entirety of the blanket length and the PbLi within them flows exclusively in the poloidal direction. No stiffening plate is foreseen in the radial-toroidal plane, therefore the channels run uninterrupted from the blanket bottom to the top. The T02 breeding zone layout is presented in Figure 11.2.

The refrigeration is provided by double-walled tube (DWT) pipes that convey the coolant from the manifolds located in the BSS region to the BZ channels. The pipes are bended in a elongated U-shaped configuration and the BZ cooling element is composed of two nested pipes, which is inserted in the blanket from the BSS and crosses the stiffening plates separating the channels through designated openings. These perforations, that can be seen in Figure 11.2, follow the general shape of the cooling pipe assembly and are drilled as wide and narrow as possible to minimize the weakening of the pierced stiffening plate. Every radial array of BZ channels is thus served by the same cooling element, which geometry is then maintained in the poloidal direction to ensure the required refrigeration to the whole extension

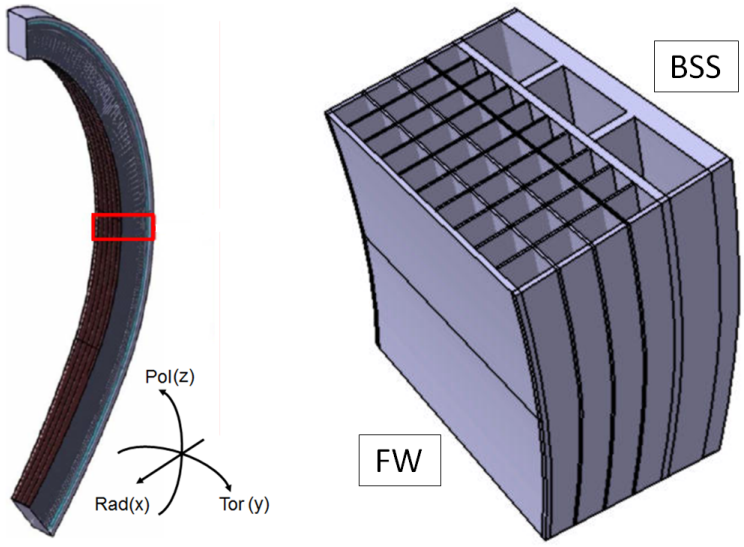

Figure 11.1. Configuration T02 general BZ layout. Left: central outboard blanket segment and coordinate axis. Right: detail of breeding zone channel arrangement [84].

of the channel. The vertical (i.e. poloidal) pitch between cooling elements (p_v) is a considered a characterizing parameter for the blanket layout, since it defines the extension of the elementary breeding blanket cell.

A sketch of the cooling element layout is presented in Figure 11.3. Only the FW channel (leftmost) features the portion of the cooling element constituted by curved pipes, whereas for the other channels the pipes are straight and occupy the region close to the radial-poloidal stiffening plates. The different obstacle layout means that, even neglecting the contribution of the buoyancy forces, not all the BZ channels can be represented with the same model. For the purpose of this study, the analysis is focused on the FW channel because of its intense volumetric heating and the complex obstacle geometry involved.

The power density deposited by the nuclear reactions responsible for the tritium breeding decreases exponentially moving away from the FW in the radial direction, therefore the channel selected is the one where it is most difficult to meet the PbLi temperature limit. The FW channel would be the one characterized by the most intense temperature gradient and, thus, where the buoyancy contribution to the PbLi motion is the most significant in the BZ. For these reasons, it is the most suitable to assess both the efficiency of the proposed cooling system layout and the buoyancy effect on the MHD flow.

The particular obstacle geometry in the FW channel offers the opportunity to study a problem similar to the one discussed in Chapter 10, yet with interesting differences introduced by the fact that the pipe, since it is bended from the radial to the toroidal direction, it is at the same time perpendicular and coaxial with the magnetic field, albeit in different sections. To the best of author's knowledge, no studies are present in the literature concerning such a configuration and, therefore, this analysis could provide some novel insights about the MHD flow about a more realistic obstacle layout.

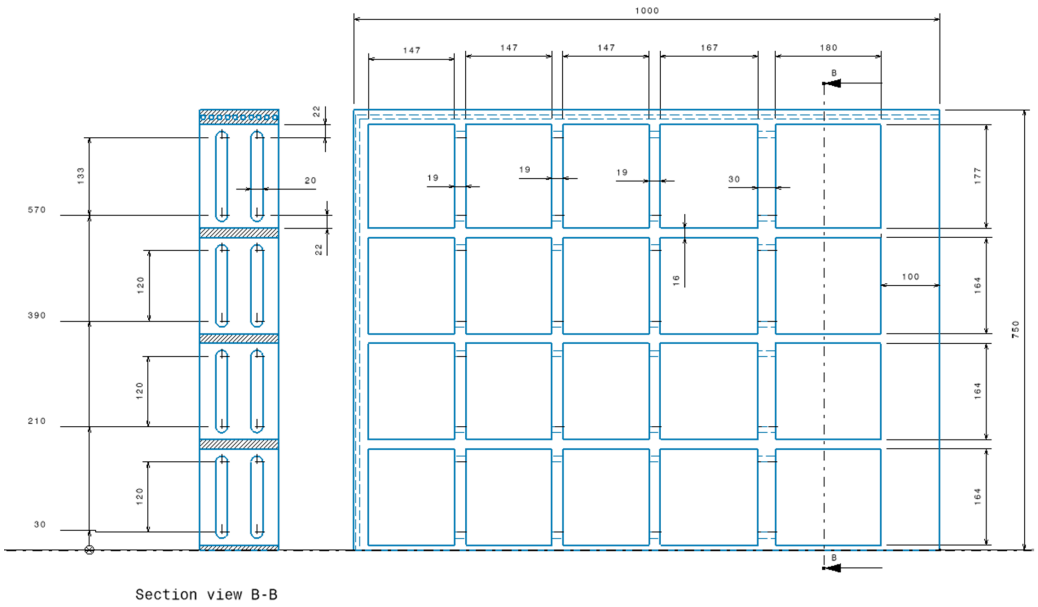

Figure 11.2. Stiffening plate arrangement for the BZ layout, radial-toroidal view. Left: Detail of SP openings for the pipe passage, toroidal-poloidal cross section along B-B. Dashed line at the bottom is a symmetry axis [84].

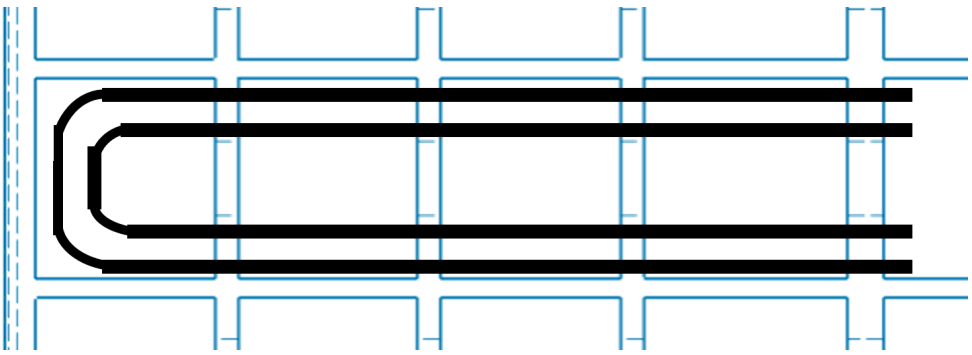

Figure 11.3. T02 BZ cooling element layout. Radial-toroidal view, first wall on the left [84].

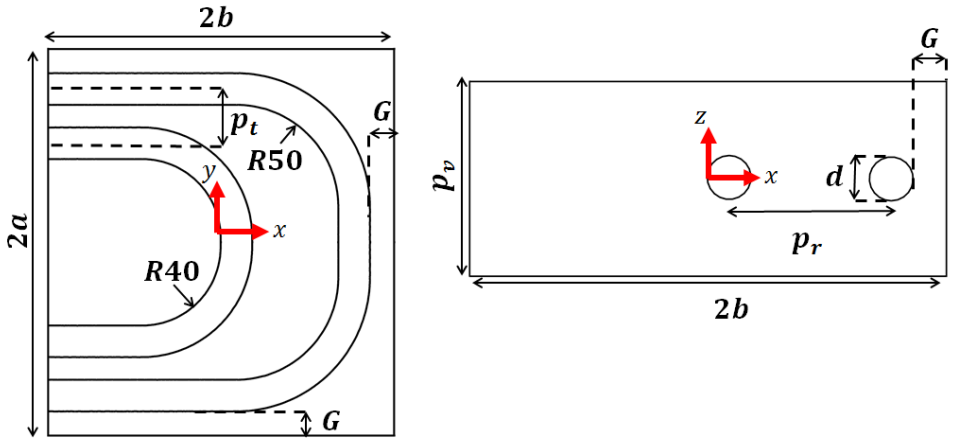

Figure 11.4. FW channel model geometry. Left: radial-toroidal view. Right: radial-poloidal view. For model dimensions, refer to Table 11.1

11.2.1 Geometry

The model for the FW channel is derived from the available data on the configuration T02. Recalling the BZ layout presented in Figure 11.2, the analysis is focused on the smallest (and most common) channel that it is identified by a toroidal dimension $2a = 164$ mm and radial width $2b = 147$ mm. Other relevant geometrical parameters are reported in Table 11.1, including the dimensionless normalized pipe-wall distance (G/d) and blockage ratio (β). The latter is defined for the curved pipes as the ratio between the area on the toroidal-radial plane occupied by the pipes and the area of the empty channel.

In Figure 11.4, the FW channel geometry is shown. The model presented and the investigation is focused on the single elementary portion of the channel corresponding to a poloidal length equal to the vertical pitch p_v, which it is cooled by a single couple of nested U-pipes. The pipes have the same outer (d_o) and inner (d_i) diameter. For the purpose of this study, the influence of the copper insert separating the two halves of DWT on the thermal and electrical conductivity of the pipe is assumed to be negligible.

Longer stretches of the poloidal channel can be represented by simply stacking copies of the elementary channel in the poloidal direction and this strategy has been adopted for the simulation of the hydrodynamic flow in Section 11.3, where vortices of characteristic length $L = p_v$ can appear between the cooling elements.

It should be noted that the geometry presented considers exclusively the volume occupied by the PbLi, whereas the solid structures are not represented. This decision is taken to simplify the model and its assumptions will be discussed in Section 11.2.2. The opening on the toroidal-poloidal SP at $x = -b$, that in the actual blanket would be necessary to allow the pipes to penetrate in the channel, is not considered and eliminated in the present model, thus neglecting any cross-flow between the channels belonging to the same radial array. The volume of the elementary cell, neglecting the space occupied by the cooling pipes is $Volume = 2a * 2b * p_v = 1.446 \cdot 10^{-3}\mathrm{m}^3$.

Table 11.1. FW channel geometry parameters, length in mm.

Parameter	Symbol	Value	Parameter	Symbol	Value
Toroidal half-length	a	82	Vertical pitch	p_v	60
Radial half-length	b	73.5	Radial pitch	p_r	50
Pipe ext. diameter	d_o	13.5	Toroidal pitch	p_t	23
Pipe wall thickness	t_w	2.75	Pipe-wall distance	G	10.25
Pipe int. diameter	d_i	8	Channel hydraulic diameter	d_H	76
Dimensionless parameters					
Parameter	Symbol	Value	Parameter	Symbol	Value
Aspect ratio	a/b	1.116	Blockage ratio	β	0.274
Norm. pipe-wall distance	G/d_o	0.76			

Table 11.2. Material physical properties, in brackets the temperature assumed for constant ones

PbLi (T_{ref}) [61]		
Density [kg/m^3]	ρ	9675.21
Expansion coefficent [K^{-1}]	β	$1.23{\cdot}10^{-4}$
Specific heat [J/kgK]	c_p	188.49
Permeability [H/m]	μ_0	$4\pi \cdot 10^{-7}$
Kinematic viscosity [m^2/s]	ν	$\frac{1.87{\cdot}10^{-4}}{\rho} e^{(1400/T)}$
Thermal conductivity [W/mK]	κ	$1.95 + 1.95 \cdot 10^{-2}\, T$
Electrical conductivity [S/m]	σ	$(1.02 \cdot 10^{-2} + 4.26 \cdot 10^{-6}\, T)^{-1}$
Eurofer (T_{ext}) [62]		
Thermal conductivity [W/mK]	κ_{EU}	29.94
Water (T_{ext}) [186]		
Density [kg/m^3]	ρ_{H2O}	701.28
Specific heat [J/kgK]	$c_{p,H2O}$	5795
Kinematic viscosity [m^2/s]	ν_{H2O}	$1.12{\cdot}10^{-7}$
Thermal conductivity [W/mK]	κ_{H2O}	0.54

11.2.2 Numerical model

Materials

Due to the intense power deposition foreseen in the WCLL blanket, the temperature range expected in the model is quite large, i.e. $T = 600 \div 825\,K$, and, therefore, the dependence upon temperature of the PbLi physical properties can not be easily neglected. In particular, for the range considered, the kinematic viscosity, thermal and electrical conductivity all show a variance $\Delta\Phi = \Phi(T_{Max}) - \Phi(T_{ref}), \Phi(T_{Min}) - \Phi(T_{ref}) > \pm 5\%$, where the assumed reference temperature is $T_{ref} = 710\,K$, and, thus, are implemented in the model as temperature-dependent according to the correlations presented by Jauch et al. [61]. This is not the case for density, expansion coefficient and specific heat, which in turn exhibit $\Delta\Phi < \pm 5\%$, and are modeled as constant at their value estimated for T_{ref}. As a result, the average Prandtl number in the model is $Pr = 0.016$. Furthermore, the PbLi is assumed to have a magnetic permeability equal to the vacuum. In Table 11.2, the complete overview of the PbLi implementation is reported.

Table 11.3. Dimensionless parameters at $T_{\mathrm{ref}} = 710$ K

Parameter	Symbol	Value
Grashof number	$\mathrm{Gr} = g\rho^2\beta b^3\Delta T/\mu^2$	$5.7 \cdot 10^{10}$
Hartmann number	$\mathrm{Ha} = Ba(\sigma/\mu)^{0.5}$	8550
Lykoudis number	$\mathrm{Ly} = \mathrm{Ha}^2/\mathrm{Gr}^{0.5}$	306
Peclet number	$\mathrm{Pe} = \mathrm{PrGr}/\mathrm{Ha}^2$	12.5
Prandtl number	$\mathrm{Pr} = c_p\mu/\kappa$	0.016
Reynolds number (u_0/u_{nc})	$\mathrm{Re} = \rho u_i d_H/\mu$	$2038/5.6 \cdot 10^5$
Richardson number	$\mathrm{Ri} = \mathrm{Gr}/\mathrm{Re}^2$	$1.37 \cdot 10^4$
Wall conductance ratio	$\mathrm{c_w} = \sigma_{\mathrm{w}}\mathrm{t_w}/\sigma\mathrm{a}$	∞

Water properties are evaluated at the average water temperature in the plant thermodynamic cycle $T_{ext} = 584.65\,K$ and for the nominal pressure $P_{H2O} = 15.5$ MPa, according to the IAPWS standard [186]. The duct and pipe walls are composed of Eurofer. The property implementation is restricted to the thermal conductivity (κ_{EU}), which it is evaluated at T_{ext}, employing the correlation reported by Mergia and Boukos, and assumed to be temperature-independent [62].

Kinematic boundary conditions

At the start of the simulation, the PbLi filling the cell is assumed to be at rest. The no-slip boundary condition (BC) $u = 0$ is enforced at the cooling pipe and duct surfaces.

Periodic BCs are used at the bottom (inlet) and top (outlet) surfaces of the model in order to simulate an infinite poloidal array of cooling elements. An absolute mass flow rate $\Gamma = 0.431$ kg/s^{-1} is imposed among the periodic surfaces to provide a momentum source representative of the primary forced convection flow, which is equivalent to a mean velocity $u_0 = 1.825$ mm/s [60].

Under these conditions, the Reynolds number at T_{ref} is $Re = 2038$ (see Table 11.3). Accounting for the additional momentum source provided by the buoyancy forces, the characteristic velocity for natural convection is estimated from Equation (3.38) as $U_\infty \approx 0.2$ m/s, which results in $Re_b = 2.23 \cdot 10^5$. The Boussinesq approximation is employed for the buoyancy model with the reference density (ρ_0) and expansion coefficient as listed in Table 11.2.

Thermal boundary conditions and volumetric power deposition

At the start of the simulation, the PbLi filling the cell is assumed to be at the uniform temperature $T_0 = 600$ K. Duct walls are modeled as adiabatic ($\frac{\partial T}{\partial n} = 0$). A source term is employed to represent the volumetric power deposition (Q) in the PbLi due to fusion neutron flux employing the data reported by Chen et al. for the outboard equatorial module of the PPCS Model A design [183]. Following the approach described by Martelli et al., these data are scaled down to account for the different neutron wall load between the PPCS study and the DEMO 2015 baseline specifications [179]. The result is the plot available in Figure 11.5. The volumetric power deposition decreases exponentially away from the FW, therefore it

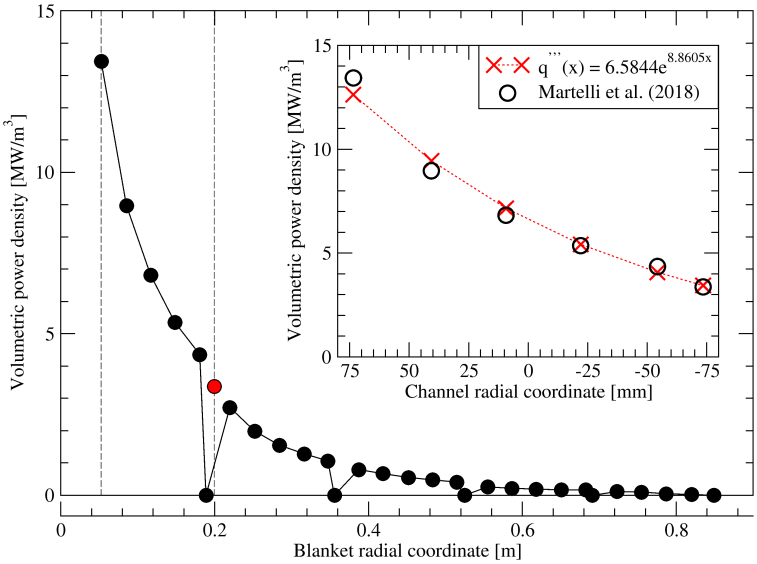

Figure 11.5. Main plot: PPCS Model A PbLi neutronic power deposition scaled down to represent the DEMO 2015 case. The dashed lines enclose the region corresponding to the WCLL2017v02 BZ first channel, where the red dot represents an interpolated data point not present in Chen et al. [183]. Internal plot: Comparison between reference data and implemented correlation (cross).

is possible to represent the $Q(x)$ distribution with a function $Q(x) = n \cdot e^{mx}$ where $n = 6.5844$ MW/m^3 and $m = 8.8605$ m^{-1}.

In Figure 11.5, the function obtained with the best fit of the volumetric power deposition in the first channel is compared with the scaled numerical data reported by Chen et al: the average error is found to be $< 5\%$ and such correlation is implemented in the numerical model. Instead, the volumetric power generation in the Eurofer and water has been neglected. Under these assumptions, the power deposited in the elementary cell is $Q = 9.684$ kW.

At T_{ref}, the average volumetric power deposition ($\bar{Q} = Q/\text{Volume} =\approx 6.7\,\text{MW/m}^3$) corresponds to a characteristic temperature difference $\Delta T = \frac{\bar{Q}b^2}{\kappa} = 2290$ K, and to a Grashof number equal to $Gr \approx 5.70 \cdot 10^{10}$ (see Table 11.3). Since $Ri = Gr/Re^2 \approx 1.37 \cdot 10^4$, it is expected that, in hydrodynamic conditions, the flow in the BZ channel will be dominated by the natural convection. Moreover, we can also conclude that the hydrodynamic flow in the channel is going to be turbulent, since the Rayleigh number for the channel $Ra = Gr \cdot Pr \approx 9 \cdot 10^8$.

The Heat Transfer Coefficient (HTC) BC is employed to model the heat transfer water-side without simulating the coolant and accounting for the pipe thermal resistance. This method allows to reduce the problem to a single computational domain containing only the PbLi by removing the necessity to simulate the thermal conduction in the pipe and an additional fluid domain for the water in the pipes, thus drastically improving the calculation speed. The HTC BC requires the specification

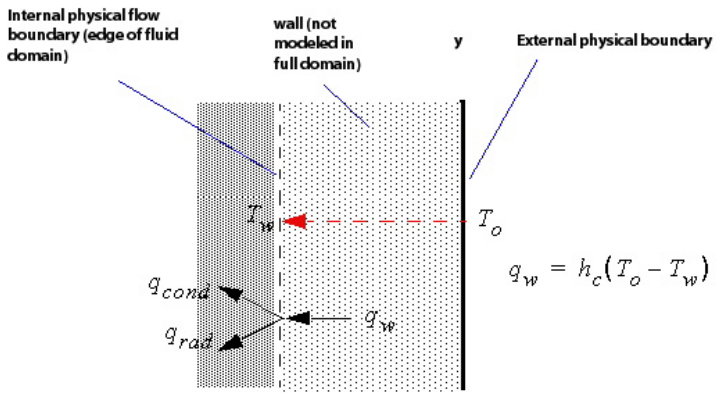

Figure 11.6. Heat Transfer Coefficient boundary condition [172]

of only two parameters: h_{ext} and T_{ext} [172]. The external HTC (h_{ext}) is calculated as

$$h_{ext} = (1/h_{pipe} + 1/h_{H2O})^{-1} = 1.05 \cdot 10^4 \text{ W/m}^2\text{K} \tag{11.1}$$

where the pipe double-wall equivalent coefficient (h_{pipe}) is estimated according to the relation for a thick-walled pipe[1]

$$h_{pipe} = 2\kappa_{EU}/(d_i ln(d_o/d_i)) = 3.91 \cdot 10^4 \text{ W/m}^2\text{K} \tag{11.2}$$

and the HTC water-side (h_{H2O}) is evaluated from the well-known Dittus-Boelter correlation for the internal turbulent flow in a smooth pipe

$$\frac{h_{H2O} d_i}{\kappa_{H2O}} = Nu = 0.023 Re^{0.8} Pr^{0.4} \tag{11.3}$$

assuming a conservative average velocity $u_{H2O} = 5$ m/s, which is lower than the maximum velocity ($u_{H2O} = 7$ m/s) allowed by the design requirements. Water properties are evaluated at the average water temperature in the plant thermodynamic cycle $T_{ext} = 584.15\,K$, thus neglecting the temperature increase in the pipe, and for the nominal pressure $P_{H2O} = 15.5$ MPa [186] [22]. Under the assumptions made, it is found that $Re_{H2O} = 3.34 \cdot 10^5$, $Pr_{H2O} = 0.902$ and $Nu_{H2O} = 579.15$. Employing these values, the code proceeds to estimate the heat flux (q_w) at the wall employing the relation

$$q_w = h_{ext}(T_{ext} - T_w) = q_{cond} + q_{rad} \tag{11.4}$$

where T_w is the (wall) surface temperature of the fluid domain edge calculated for turbulent flows from a surface energy balance and for laminar flows as the boundary temperature field. For the problem studied the radiation mechanism is neglected, thus $q_w = q_{cond}$, where q_{cond} is determined only by the LM-side heat transfer coefficient [172]. The heat flux q_w calculated through eq. (11.4) is then applied to the pipe surface via a traditional fixed heat flux boundary condition and is in general non-uniform. A diagram of the HTC boundary condition is available in Figure 11.6.

[1]The thermal resistance of the copper insert between internal and external wall of the DWT is neglected

Although a very attractive option, the HTC boundary condition introduces a relevant simplification in the model since it ignores the temperature distribution in the coolant and its effect on the local value of h_{H2O} that it is, in general, not uniform on the pipe internal surface. To evaluate the uncertainty introduced by the use of the HTC boundary condition, a comparison is made in Section 11.2.2 between the results obtained with the simplified model and the full heat transfer.

Electromagnetic boundary conditions

A uniform and constant magnetic field is applied in the toroidal (y) direction $\mathbf{B} = (0, B, 0)$ with the magnetic field intensity considered equal to $B = 4.4$ T, which corresponds to $Ha = 8.55 \cdot 10^3$ for the properties at T_{ref} (see Table 11.3) [29].

Since the hydrodynamic flow is buoyancy-dominated, we are going to employ the magneto-convection dimensionless groups to characterize the relative ratio between the electromagnetic forces and the other relevant phenomena. Using eq. (3.39), the Lykoudis number is equal to $Ly = Ha^2/Gr^{0.5} \approx 303 \gg 1$ and, therefore, we can conclude that at the assumed magnetic field intensity the flow is dominated by the electromagnetic forces and, since the interaction parameter $Ly^2 \gg 1$, the inertial effects in the momentum equation can be neglected.

Similarly, the influence of the inertial effects on the energy equation can be evaluated with the Péclet number that, recalling eq. (3.42), is equal to $Pe = GrPr/Ha^2 = 12.6$. Since the inertia-less condition for the energy equation is not met ($Pe \ll 1$), we can expect that the heat transfer in the BZ channel will be at least partially affected by a convection contribution.

The solid surfaces bounding the fluid domain are considered as perfectly conducting ($c_w = \infty$) and their electric potential is fixed to the ground value ($\phi = 0$). This assumption simplifies the model by removing the need to simulate the solid walls, it is conservative in terms of the Lorentz force experienced by the flow and allows to relax the mesh resolution requirements in the boundary layers [33] [175]. Moreover, no significant error should be introduced in the estimate of the additional obstacle pressure drop and of the heat transfer, since in Chapter 10 it was observed that for increasing Ha the influence of the obstacle conductivity on the flow becomes negligible.

Turbulence model for hydrodynamic simulation

To preliminary assess the performance of the cooling system and to provide reference for comparison with the magnetohydrodynamic results a ordinary hydrodynamic simulation is performed and its results are described in Section 11.3. From the thermal boundary conditions defined, the flow in the model is going to be dominated by the buoyancy forces ($Ri \gg 1$) and turbulent.

The turbulence model employed is the k-ω Shear Stress Transport developed by Menter [187]. This turbulence model is considered the standard approach to be followed for low Reynolds number simulations and its near-wall treatment is generally more accurate and robust compared with k-ϵ models [172]. Since we are interested in the determination of the heat transfer in the near-wall region, a mesh resolution with $y^+ \leq 1$ is required.

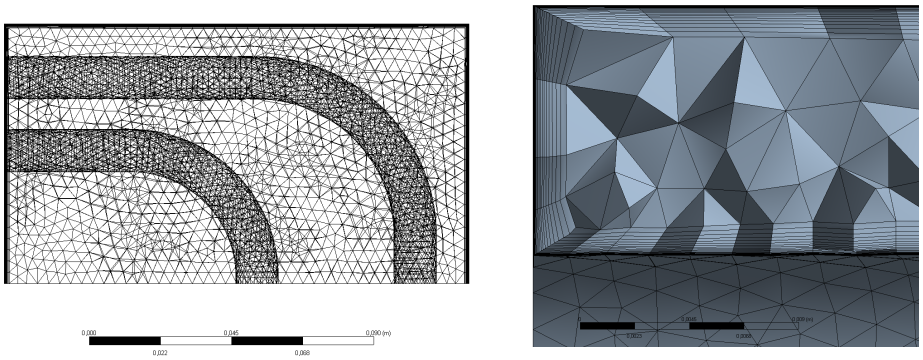

(a) Test case mesh

(b) Detail of boundary layer refinement

Figure 11.7. Test case mesh and detail of the boundary layer refinement in the gap between the lateral wall and the outer pipe

Domain and time discretization

A snapshot of the computational grid employed to discretize the fluid domain is presented in Figure 11.7a. Due to the complex pipe geometry, the mesh is unstructured everywhere in the fluid domain except for the boundary layers, which are resolved with prismatic elements adopting the inflation technique.

For a solid surface with a non-null normal component of the magnetic field the boundary layer scale follows the law defined for the Hartmann wall, such that $\delta_H = O(Ha^{-1})$, whereas if the wall is parallel to the field then $\delta_H = O(Ha^{-1/2})$. Since the boundary layers in this simulation are attached to perfectly conducting walls, they can be treated as "passive", hence they do not carry any current and their influence on the flow variables is much reduced compared with insulating walls. The mesh resolution is defined so to have at least 2 nodes in the layer thickness, enough to follow the steep velocity gradient therein, as it is possible to see in Figure 11.7b. Due to the impossibility to define separate inflation settings for contiguous walls, the same mesh resolution is employed for all the solid surfaces in the model and the layer thickness is calculated from the Hartmann wall scaling law for $Ha(T_{ref})$.

The computational grid defined for the MHD case is employed also to perform the accompanying hydrodynamic simulation required to assess the cooling system baseline performance described in Section 11.3. This can be justified by the high magnetic field intensity employed that causes the formation of very thin boundary layers which are comparable in thickness with the scale of the turbulent viscous sub-layer expected in the hydrodynamic simulation. Indeed, assuming a free-stream velocity $U_\infty = 0.2$ m/s for the hydrodynamic case, it is possible to calculate for $y^+ = 1$ a wall spacing equal to $\Delta s = 1.3 \cdot 10^{-5}$ m[2]. Similarly, following the Hartmann boundary layer scaling law, we estimate that $\delta_H = 9.6 \cdot 10^{-6}$ m, therefore the MHD computational grid is characterized by $y^+ \approx 0.17$, which it is considered suitable both for the turbulence model employed and for the calculation of the heat transfer in the near-wall region.

Since the flow is laminar and the water temperature is constant, the PbLi

[2]The dimensionless y^+ is defined following the classical formulation, see for example [41]

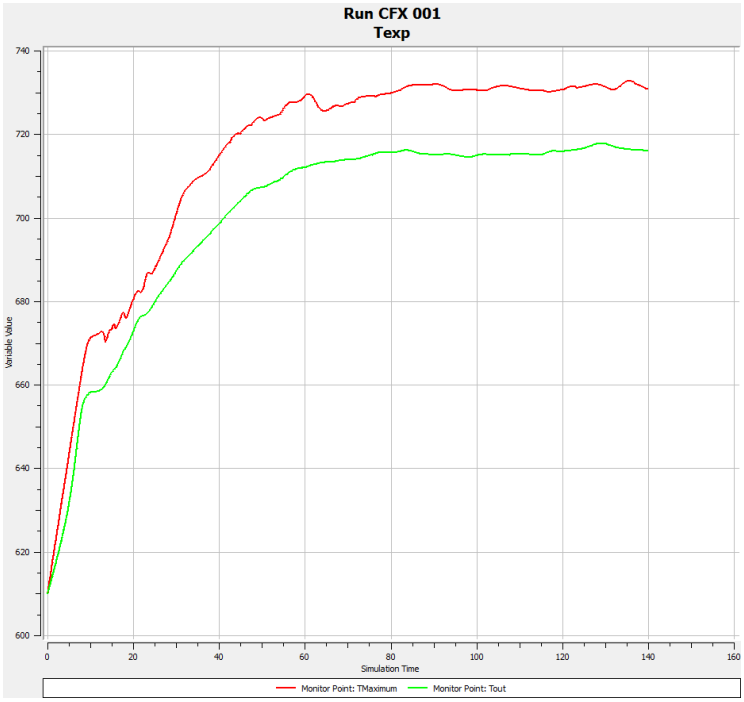

Figure 11.8. Transient OHD run monitors for maximum temperature in the model (TMaximum) and average temperature at the outlet (top surface). For this run, convergence is assumed to be achieved around $t = 120$ s.

temperature distribution is symmetrical in the MHD model with regard to the $z = 0$ plane. A symmetry boundary condition is used to reduce the grid size. The element count for the MHD model is 423'526 with maximum element size 3.5 mm, whereas for the OHD model is 2'117'630. Maximum and average skewness are reported as 0.797 and 0.187.

Two different approaches are used regarding the time discretization scheme for the hydrodynamic and MHD simulation. In the former case, the buoyancy-dominated turbulent flow regime is time-dependent, whereas for the latter the magnetic field dampens the velocity oscillations and the resulting field can be calculated with a steady-state scheme. For the MHD model, the High Resolution pseudo-transient scheme with Auto Timescale control for the virtual time step is used. An hard cap on the maximum timescale is imposed at $\Delta t = 1 \cdot 10^{-3}$ s to avoid convergence issues due to incorrect time scale estimation.

For the ordinary hydrodynamic simulation, the Second Order Backward Euler is employed for the time discretization with average time step $\Delta t = 0.015$ s. The time-step size is manually adjusted during the simulation run to keep the maximum Courant number for the developing velocity field in the simulation below five and maximize the convergence speed. The transient run total time is not decided *a priori*, rather the simulation is considered concluded when the monitor for the maximum temperature in the model and the average temperature at the outlet (top surface) have converged to a statically time-independent value. An example of the monitors behavior is presented in Figure 11.8, which refers to a test run.

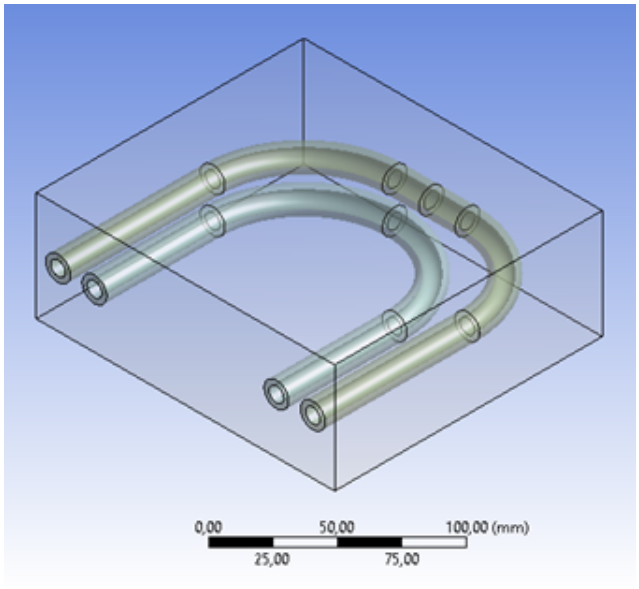

Figure 11.9. Comparative analysis model. The picture is showing the one employed for direct simulation of the cooling pipe.

Typical run times on 24-core Xeon E5-2690 (2.90 GHz) cluster are about 3 days for the OHD and 1 day for the MHD model.

Uncertainty evaluation for the HTC boundary condition

If the HTC boundary condition is employed to simulate the heat transfer between the cooling pipe and the liquid metal an error is introduced since the conduction and convection phenomena happening in the pipe thickness and coolant are modeled with a uniform heat transfer coefficient value deduced analytically. In general, it is instead locally dependent by the coolant conditions and the simplified assumption could lead to significant errors introduced in the heat flux estimated at the pipe surface.

To assess the error introduced, a comparative analysis is performed considering for the heat transfer model both the HTC boundary condition and a direct simulation of the cooling pipe. In Figure 11.9, the geometry of the elementary cell employed for the comparative analysis is shown. The numerical model is analogous to the one described so far with the exception of the periodic surfaces at the top and bottom of the cell, which are replaced with a inlet (at the bottom) characterized by $u_0 = 1.825$ mm/s and T = 600 K, and outlet (at the top) with zero relative pressure. For the direct pipe simulation, the water is assumed to enter the pipes inlet (placed on the right in Figure 11.9) at uniform velocity $u_{H2O} = 5$ m/s, $T = 576.4$ K and $p = 15.5$ MPa.

A qualitative comparison of the results obtained by the two models is presented in Figure 11.10, where the PbLi temperature field on two characteristic planes is considered. No significant discrepancy is found even if, as expected, the direct pipe simulation provides a more accurate representation of the heat transfer, which results in a slightly more efficient power removal and lower PbLi temperature close

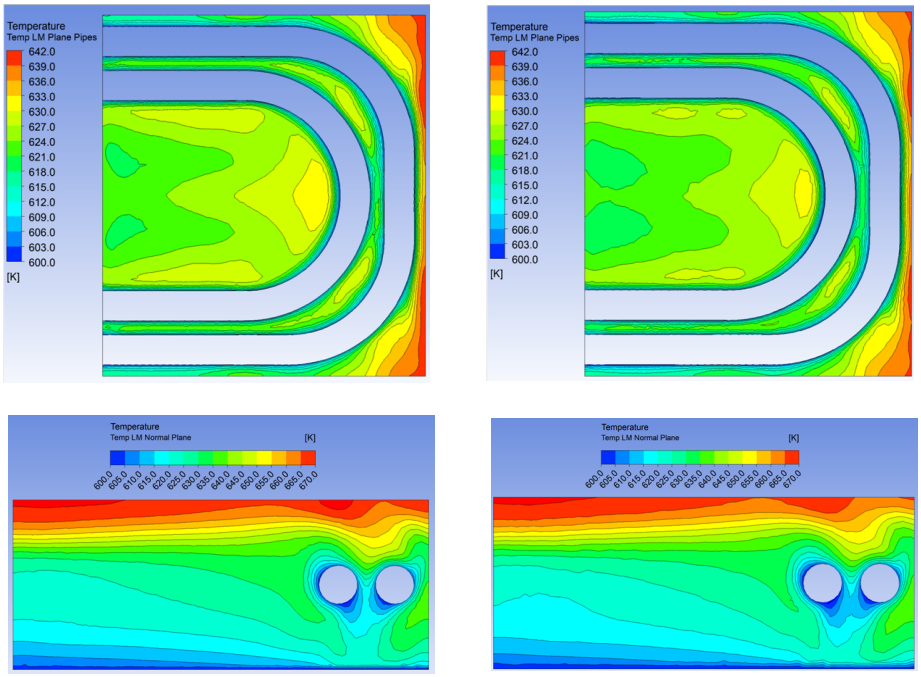

(a) HTC model **(b)** Direct pipe simulation

Figure 11.10. Comparative analysis of PbLi temperature field for HTC model and direct pipe simulation. Top: toroidal-radial plane crossing the pipes center. Bottom: radial-poloidal plane crossing the cell center.

to the pipe. A more quantitative comparison is presented in Table 11.4 for three parameters: the inner and outer pipe heat flux and the average PbLi temperature on the toroidal-radial plane crossing the pipes center. Since the discrepancy between the two cases is found to be quite small, the HTC boundary condition is preferred over the direct pipe simulation to speed up the calculation.

11.3 Ordinary hydrodynamic behavior

For the hydrodynamic analysis, the flow is expected to be dominated by buoyancy forces ($Ri \gg 1$) and to fall in the turbulent regime. Since the flow can be approx-

Table 11.4. Quantitative comparison of HTC and direct simulation model. The relative error is computed assuming the direct pipe case as the exact solution

	Symbol	HTC model	Direct Pipe	Relative Error (%)
Inner pipe average heat flux (W/m^2)	q_i	$1.574 \cdot 10^5$	$1.608 \cdot 10^5$	-2.11
Outer pipe average heat flux (W/m^2)	q_i	$1.678 \cdot 10^5$	$1.674 \cdot 10^5$	0.24
Average PbLi temperature (K)	T	623.56	622.68	0.14

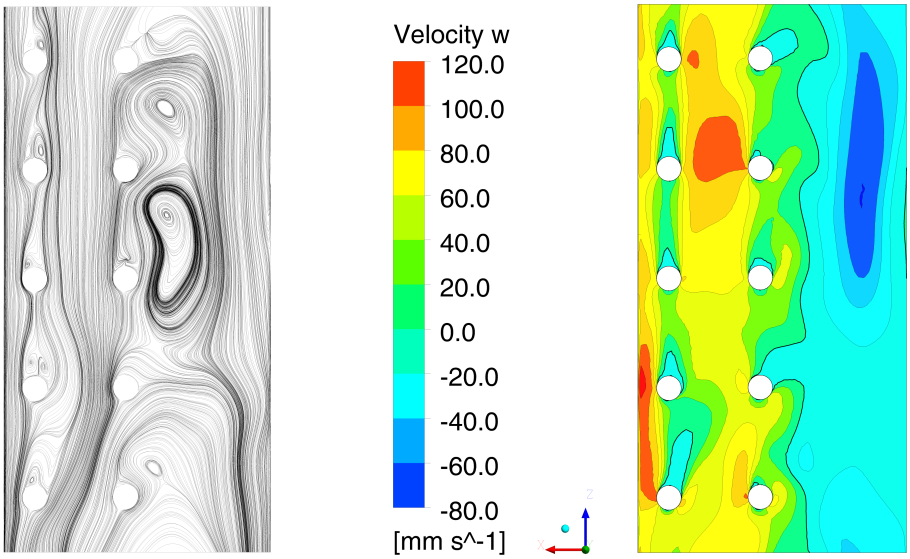

(a) Velocity streamlines **(b)** Vertical (poloidal) velocity contour

Figure 11.11. OHD velocity streamlines and contour on the radial-poloidal plane crossing the cell center. Thick dark line in Figure 11.11b identifies the $w = 0$ iso-surface.

imated to the analogous free convection case, the characteristic velocity can be estimated as $u_{ohd} = \nu Gr^{0.5}/b \approx 0.45$ m/s, which corresponds to $Re = 2.47 \cdot 10^5$. The geometry described in Section 11.2.1 is extended in the poloidal direction to represent a section of the BZ channel comprising five cooling elements. The reason for this modification is to obtain a better estimate of the heat transfer in the channel allowing the modeling of the vortical structures up to length scale $L = p_v$.

An example of the typical velocity distribution can be seen in Figure 11.11, where the velocity streamlines and contour for the vertical component at the final timestep are presented. The PbLi close to the FW is intensely heated by the volumetric power source and this phenomenon results in a strong upward flow that it is almost not affected by the cooling pipes. Conversely, the back of the channel features significantly reduced heating due to the exponentially decrease of the volumetric power source. Here, the flow exhibits large recirculation zones formed by the interaction between the rising fluid close to the FW and the descending one found at the channel back. The region around the inner pipes is dominated by large vortices that span the radial-poloidal plane of the channel and are characterized by length scale $L = p_v$. Small vortices attached to the outer pipes back are also observed. The velocity scale calculated in the model is smaller than the one predicted theoretically ($u \approx 0.185$ m/s), but it is still two orders of magnitude than the one expected for the pure forced convection.

The high average velocity of the liquid metal and the mixing operated by the vortical structures produce an efficient heat transfer in the channel that succeeds in keeping the PbLi maximum temperature at $T_{Max} = 715$ K, almost 100 K below the limit. In Figure 11.12, the temperature contours for characteristic toroidal-radial and radial-poloidal planes are presented. It can be seen how the mixing is particularly

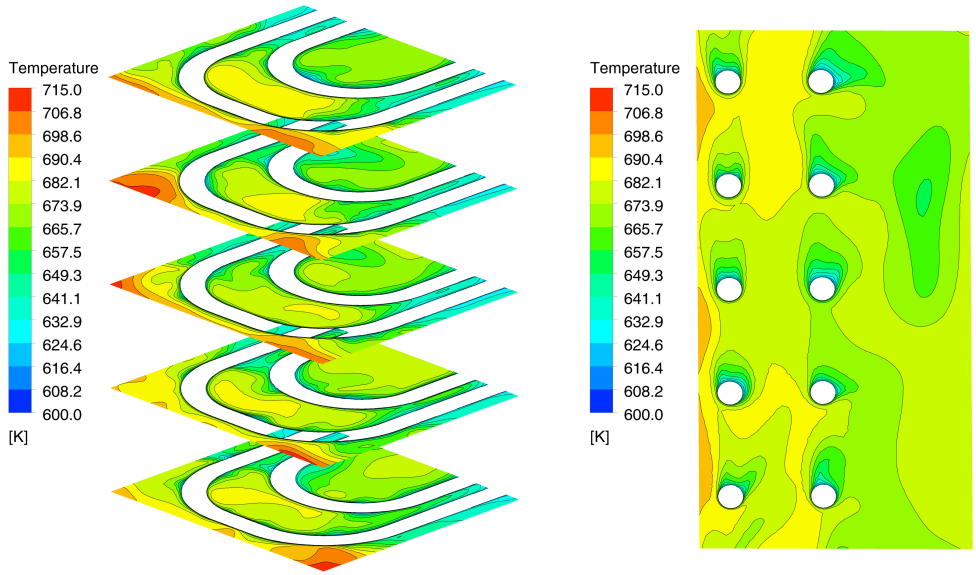

Figure 11.12. OHD 5-cell stack temperature distribution on the horizontal planes passing through the pipe center (left) and the vertical central plane (right)

effective in homogenizing the fluid temperature in the back of the channel, whereas hotspots are present in the corners with the first wall due to the marked volumetric heating and the relative distance from the cooling surface of the pipe. The middle gap between the outer and inner pipe is also a critical region since there the buoyancy forces are strong enough to prevent any significant mixing and, even if relatively distant from the FW and between the two pipes, the fluid temperature reaches up to $T = 690$ K. These regions are going to be the most affected by the heat transfer degradation caused by the magnetic field effect described in Section 11.4.

The heat flux on the cooling pipes is calculated by the code according to eq. (11.4), as it was discussed in Section 11.2.2. Such value can be used to provide an estimate of the PbLi-side heat transfer coefficient h_{LM}. If $\bar{q}$ is the area-averaged heat flux for the pipe, the thermal transmittance U can be defined as

$$U = \frac{\bar{q}}{\bar{T} - T_{ext}} = \frac{1}{\frac{1}{h_{LM}} + \frac{1}{h_{ext}}} \tag{11.5}$$

where $\bar{T}$ is the area-averaged temperature on the toroidal-radial plane crossing the pipes center. After some algebra, it is possible to rewrite eq. (11.5) to obtain an expression for the average PbLi-side heat transfer coefficient

$$h_{LM} = \left(\frac{1}{U} - \frac{1}{h_{ext}} \right)^{-1} \tag{11.6}$$

where a similar expression can be formulated for a local PbLi-side heat transfer coefficient considering the distribution of the heat flux on the pipe surface. In general, the coefficient so defined is different between the outer and inner pipe even if the considered bulk temperature ($\bar{T}$) is uniform due to the former being exposed to stronger temperature gradients compared with the latter. Moreover, the average

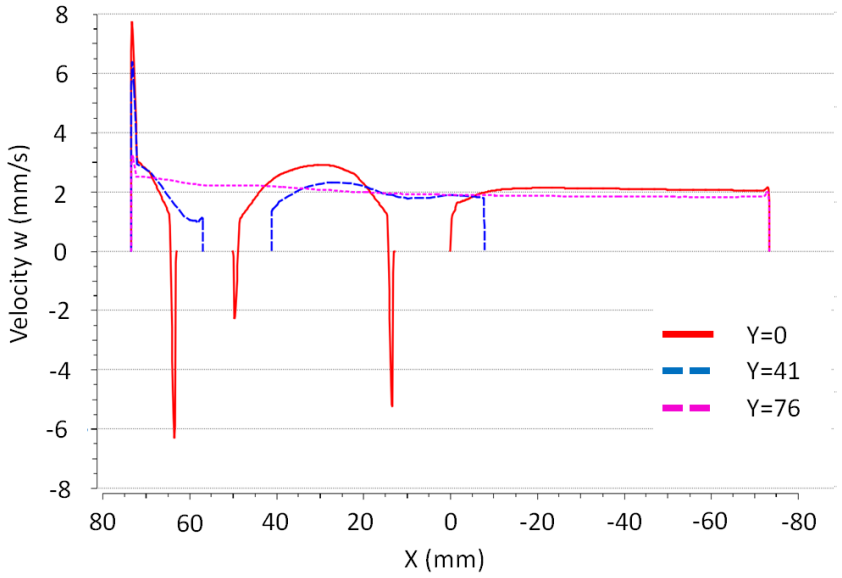

Figure 11.13. Vertical velocity profiles along the radial direction on the toroidal-radial plane passing through the pipes center ($z = 0$) for the cell center ($y = 0$), in the middle of the gap between the outer and inner pipe ($y = 41$ mm), and in the middle of the gap between the outer pipe and the lateral wall ($y = 76$ mm).

temperature on the cooling element toroidal-radial mid-plane is dependent on the channel position, albeit not strongly. Representative coefficients for, respectively, the inner pipe ($h_{LM,i}$) and the outer pipe assembly ($h_{LM,o}$) can be defined considering the average values. It follows that $h_{LM,i} = 9174$ W/m^{2}K and $h_{LM,o} = 9860$ W/m^{2}K.

11.4 Magnetohydrodynamic cell analysis

Since for the case analyzed $Ly \gg 1$, when the magnetic field is applied the velocity oscillations caused by the buoyancy forces are thoroughly dampened across the cell and the flow reverts to a behavior very similar to pure forced convection. Indeed, from **??** the magneto-convection velocity scale is estimated as

$$u_{mhd} = \frac{Gr}{Ha^2}\frac{\nu}{a} \approx 1.5 \text{ mm/s} \qquad (??)$$

which it is close to the mean velocity from the imposed mass flow rate ($u_0 = 1.825$ mm/s). Therefore, the MHD flow in the cell can be approximated as a pressure-driven case and, since $Ha \gg 1$ and $N \gg 1$, the regime is expected to be laminar and steady.

In Figure 11.13, the vertical velocity profiles plotted along the radial axis on the toroidal-radial plane passing through the pipes center are presented for several toroidal coordinates. The average vertical velocity is $w \approx 2$mm/s, which confirms the assumption that the buoyancy forces do not significantly affect the flow velocity scale. At the cell center ($y = 0$), jets are observed close to the FW and the cooling surfaces where the maximum vertical velocity is reached, whereas the velocity profile

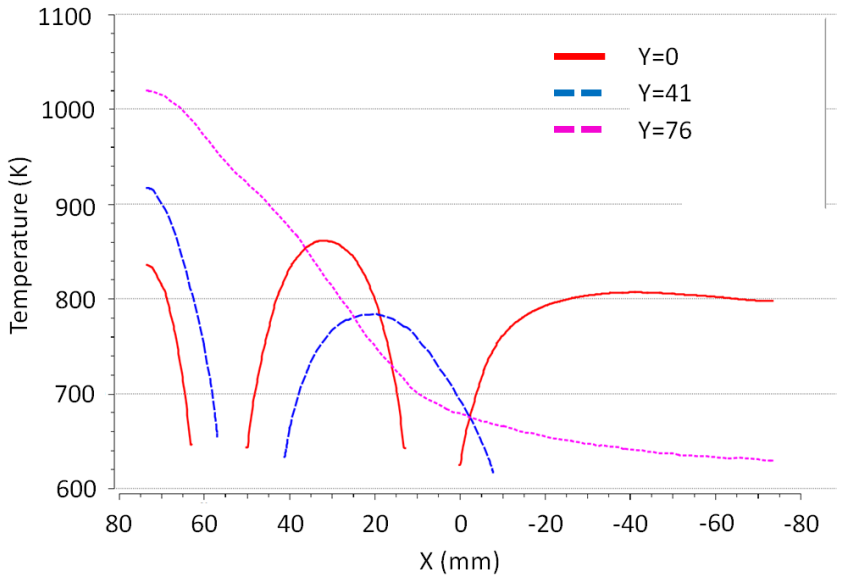

Figure 11.14. Temperature profiles along the radial direction on the toroidal-radial plane passing through the pipes center ($z = 0$) for the cell center ($y = 0$), in the middle of the gap between the outer and inner pipe ($y = 41$ mm), and in the middle of the gap between the outer pipe and the lateral wall ($y = 76$ mm).

in the back of the channel is almost flat. Interestingly enough, the flow features in the regions enclosed by the cooling pipes share some similarities with the fully developed magneto-convection cases studied in Sections 9.8 and 9.9.

The opposite jets in the space between the FW and the outer pipe are the most intense and the velocity profile in that region resembles the one for the differentially heated duct discussed in Sections 3.7 and 9.8. This is probably caused by the interaction between the steep volumetric power density gradient in the region and the close proximity with the cooling pipe that results in an almost linear temperature profile, as it can be seen in Figure 11.14.

Moving away from the FW along the radial axis, the region between the inner and outer pipe is characterized by jets close to the pipes and a core region where the velocity profile is parabolic. This behavior resembles the internally heated duct velocity profile discussed in Section 9.9 and it is indeed caused by a parabolic temperature distribution in the region, as it can be seen in Figure 11.14. However, neither the temperature or the velocity profile are symmetric across the gap mid-line with, in particular, the peak velocity shifted toward the inner pipe, which is probably responsible for the more intense jet observed therein.

Conversely, the channel region comprised between the inner pipe and the back wall features a velocity profile almost flat with a large core region. No significant jet is observed close to the pipe. The temperature profile is also mostly constant in this region. It should be noted that these peculiar flow features are limited to the immediate surroundings of the cooling element. Away from the obstacle, the jets attached to the pipe walls are suppressed and the velocity profile is smoothed in a wide core region similar to the one observed for a pressure-driven flow. However,

the effect of the buoyancy forces, albeit strongly dampened, is not suppressed in its entirety, since the velocity profile continues to be warped by the intense heating close to the FW and never quite resembles the slug flow of pure forced convection. The velocity profile in the gap between the outer pipe and the lateral wall (plot at $y = 76$ mm in Figure 11.13) is quite representative of the flow behavior away from the cooling element.

The reduced flow velocity compared with the OHD cell severely deteriorates the cooling system performance that it is no longer able to keep the PbLi temperature below the Eurofer operative threshold. The cell regions most affected are the one that already in the previous configuration were harboring hot-spots. In Figure 11.15, the temperature contours for the toroidal-radial and radial-poloidal planes are presented with the purple region representing the PbLi volume where $T > 820$ K. Even if the outer pipe is placed quite close to the FW is not enough to cool effectively the surrounding fluid, which it is above the temperature limit everywhere except for the cylinder wake. Conversely, the inner pipe is able to keep the temperature below the limit in the back part of the channel due to the less severe volumetric heating. The maximum temperature is reached in the cell corners where $T \approx 1030$ K.

Due to the larger temperature gradient in the surrounding region, the average heat flux on the outer pipe ($q_o = 4.465 \cdot 10^5$ W/m^{2}K) is slightly higher than the one for the inner pipe ($q_i = 3.519 \cdot 10^5$ W/m^{2}K) and, from eq. (11.6), $h_{LM,o} = 3550$ W/m^{2}K and $h_{LM,i} = 2608$ W/m^{2}K. Therefore, the transition from the OHD to the MHD flow regime causes a drop in the PbLi-side heat transfer coefficient equal to 64% for the outer pipe and 72% for the inner pipe. Although significantly dampened, the heat transfer in the cell can not be reduced to a purely conductive mechanism, since the convection contribution is still present and it is highlighted by the warping upward (i.e. downstream) of the isotherms in Figure 11.15. If we define the Nusselt number through the thermal transmittance U from eq. (11.5), for the outer pipe we have

$$Nu = \frac{U d_o}{\kappa} \approx 2.268 \tag{11.7}$$

where κ is the PbLi thermal conductivity at T_{ref} and d_o is the pipe external diameter. Similarly, for the inner pipe $Nu \approx 1.786$. Under the calculation methodology adopted, the PbLi-side heat transfer coefficient for pure conduction can be calculated as $h_{LM}(Nu = 1) = 1317$ W/m^{2}K. In principle, it can be said that even for a very high magnetic field intensity and perfectly conducting walls, like the one considered in this calculation, the convection contribution to the heat transfer in the BZ cell is never entirely suppressed. Therefore, the routinely made assumption of pure conduction in the PbLi for thermal-hydraulic analyses in the WCLL blanket, see for instance Ref. [86, 179] is overly conservative. However, it can still be considered a valid numerical strategy to obtain a rough but cheap assessment of the global temperature field in the BZ without recurring to more refined and computationally expensive models including the MHD phenomena.

11.5 Breeding Zone cell optimization

The transition from the OHD to MHD flow regime severely degrades the heat transfer in the BZ elementary cell and, as a result, the cooling system is no longer able

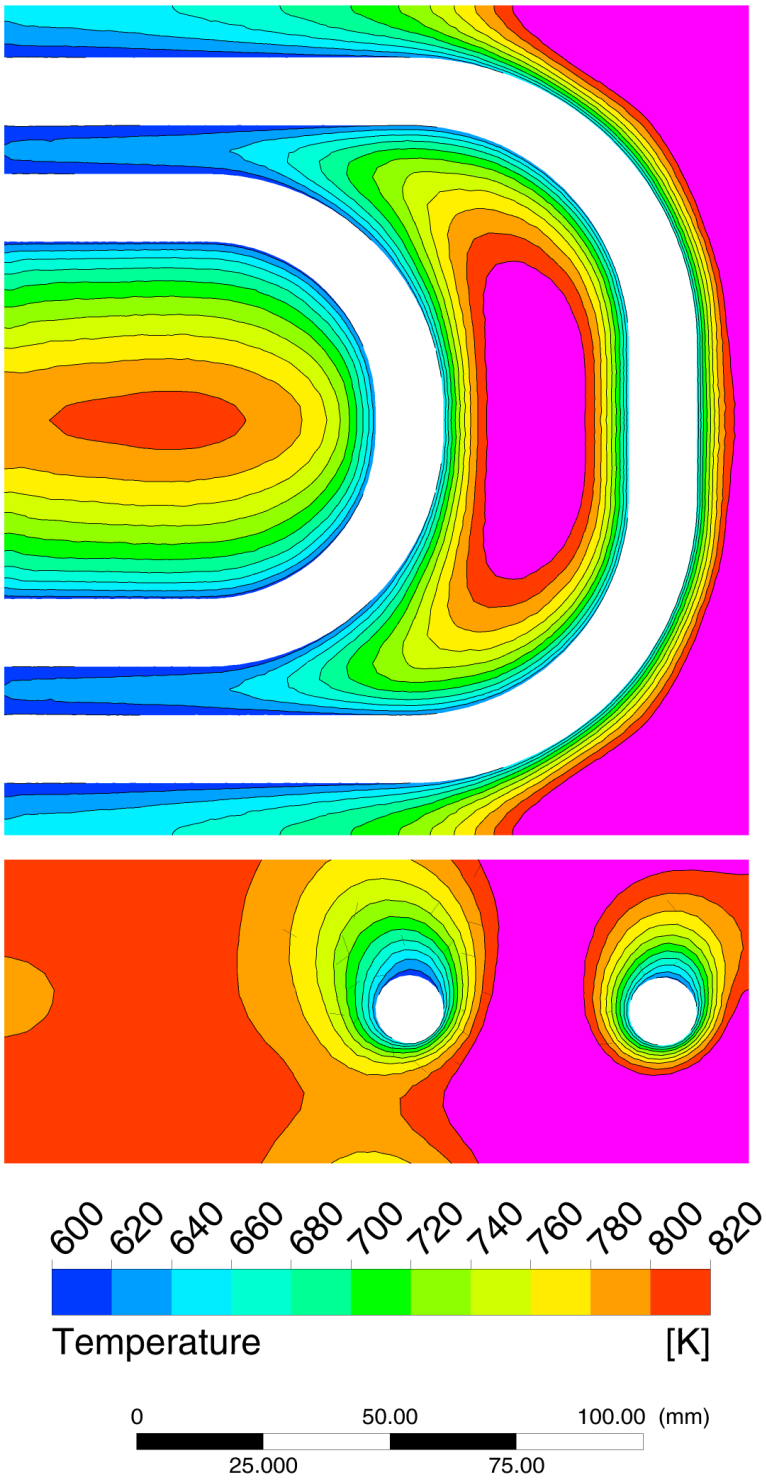

Figure 11.15. MHD cell temperature distribution on the horizontal plane passing through the pipe center (top) and the vertical central plane (bottom). Purple color identifies $T > 820$ K.

to keep the PbLi temperature under the Eurofer operative limit ($T_{Max} \leq 823$ K). In this Section, the cooling system setup is going to be tweaked to assess if it is possible to meet the design requirements also for the MHD flow. Two strategies are considered: BZ passive refrigeration from the FW cooling system and increasing the number of cooling elements in the channel.

11.5.1 Passive heat removal from First Wall cooling system

The refrigeration of the WCLL First Wall is carried out by a separate cooling system, whilst the coolant employed (water at 15.5 MPa) is shared with the BZ system. Its main task is to remove the thermal heat load deposited on the plasma-facing components, ensuring their structural integrity by keeping the Eurofer temperature below the operative limit, and to deliver it to the FW PHTS. It is composed of 7 × 7 mm square channels where the coolant is flowing alternatively in opposite directions with a maximum velocity of 7 m/s. Preliminary analyses have demonstrated that the cooling system is able to successfully refrigerate the FW for a thermal load up to 2 MW/m^2 [184, 188, 189].

Thermal-hydraulic and thermo-mechanical studies conducted to investigate the integrated (FW and BZ) cooling system performances have highlighted how the FW is passively removing power from the BZ due to the elevate temperature gradient present at the boundary between the two components. The heat flux removed from the FW cooling system was found to be mostly independent of the thermal load applied on the plasma-facing surface and to be on average equal to 130 kW/m^2 [179, 190].

The numerical model described in Section 11.2.2 is modified to account for this phenomenon and to investigate for which value of the FW heat flux (q_{fw}) the maximum PbLi temperature in the channel is kept below the Eurofer operative limit. The thermal boundary condition for the channel front surface, located at $x = b$ in Figure 11.4, is changed from adiabatic to fixed heat flux. In addition to the reference configuration, which results have been described in Section 11.4, four scenarios are considered: $q_{fw} = 50,\ 100,\ 150,$ and 200 kW/m^2. The two latter configurations are considered "optimistic", since they exceed the heat flux observed in previous studies ($q_{fw} = 130$kW/m^2).

To assess the global behavior, the maximum PbLi temperature is plotted against the FW heat flux in Figure 11.16. This strategy proves very efficient in reducing the maximum temperature in the cell since it relies on direct power removal from the most tricky region to refrigerate for the BZ cooling system. Despite this favorable feature, this strategy succeeds only for the highest heat flux considered ($q_{fw} = 200$ kW/m^2) to keep the maximum temperature in the cell under the limit.

In Figure 11.17, it is possible to observe how the increasing heat flux removed from the FW influences the temperature distribution in the cell. Even for a small heat flux, the effect on the area nearby the FW is remarkable but only for $q_{fw} \geq 150$ kW/m^2 the corner hot-spots are noticeably affected. The passive refrigeration from the FW is also not very effective in reducing the hotspot in the middle gap between the pipes, even if this one was characterized by a lower maximum temperature $T \approx 880$ K compared with the corner hot-spot $T \approx 1030$ K. At $q_{fw} = 200$ kW/m^2, the FW temperature on the cell centerline is $T \approx T_{ext}$.

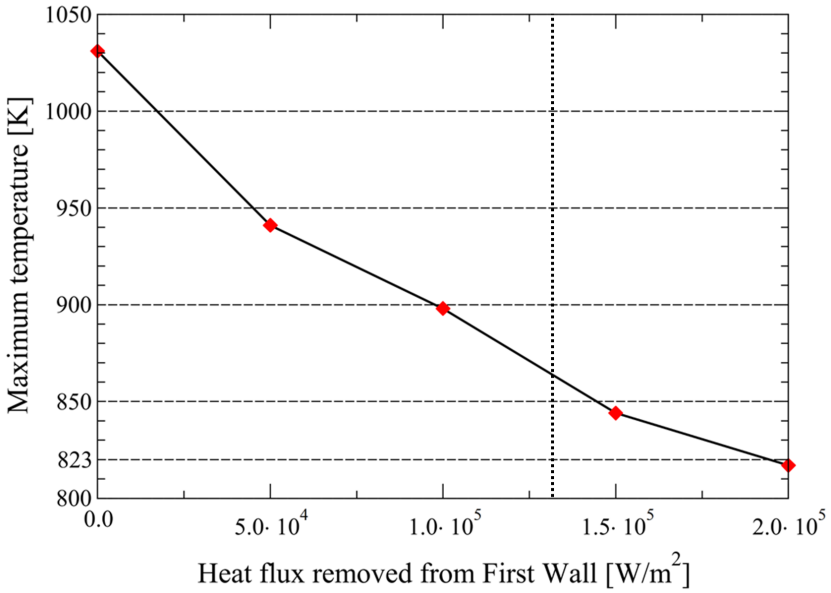

Figure 11.16. Maximum cell temperature plotted against the heat flux removed from the FW cooling system. The vertical dotted line identifies the "realistic" heat flux considered for the BZ: 130 kW/m^2

In conclusion, the contribution from the FW cooling system is very effective in curtailing the maximum temperature in the frontal part of the channel, whereas it is remarkably less efficient in reducing the hot-spot temperature between the pipes. However, the Eurofer temperature limit is met only for a very high and probably unrealistic heat flux (q_{fw} = 200 kW/m^2) and alternative optimization strategies must be proposed to do not rely too much on the FW cooling system. In the following, a moderate passive refrigeration from the FW is assumed, adopting q_{fw} = 100 kW/m^2 as a slightly conservative value with regard to the results reported in the literature [179, 190].

11.5.2 Reduction of vertical pitch

The vertical (poloidal) extension of the numerical model is equivalent to the vertical pitch separating the cooling elements along the BZ channel (p_v = 60 mm). It is possible to reduce this geometrical parameter to simulate a reduction in the pitch and an higher density of cooling elements. The reference pitch considered in Section 11.4 can be normalized with the pipe outer diameter, yielding $p_v/d_o \approx 4.4$, and we assume that the minimum feasible value is $p_v/d_o = 3 \approx 40$ mm. Further reducing the distance between the cooling elements will require extensive perforations on the toroidal-poloidal SPs to allow the pipe passage, which are considered unacceptable for the mechanical stability of the structural element.

For the purpose of this optimization study, four scenarios are considered for the vertical pitch in addition to the reference one: 55, 50, 45, and 40 mm. For these configurations, a moderate power removal from the FW is assumed (q_{fw} = 100 kW/m^2). To better characterize the thermal-hydraulic behavior of the cell,

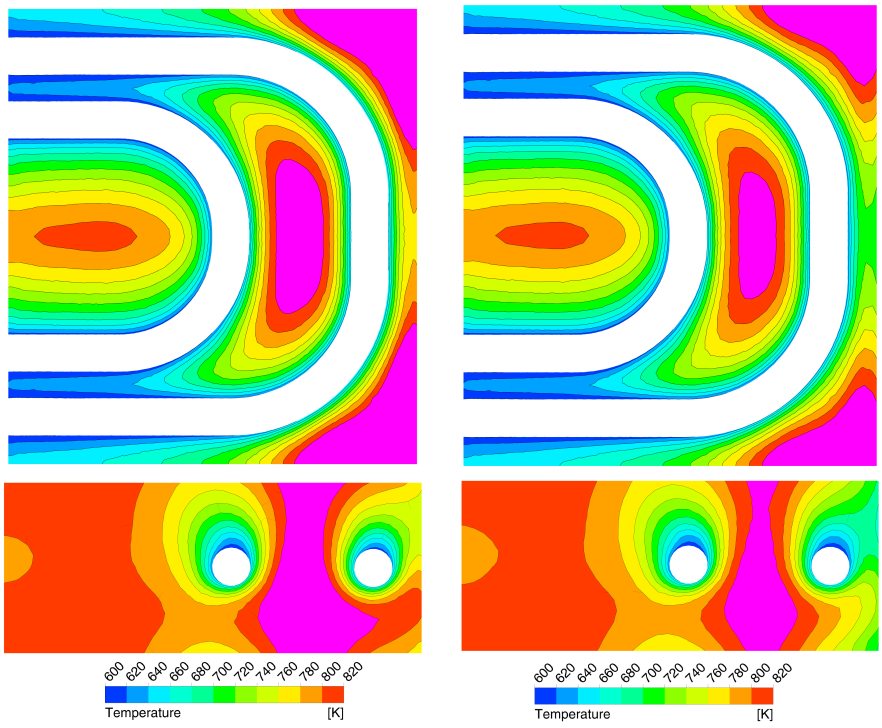

(a) $q_{fw} = 50$ kW/m^2

(b) $q_{fw} = 100$ kW/m^2

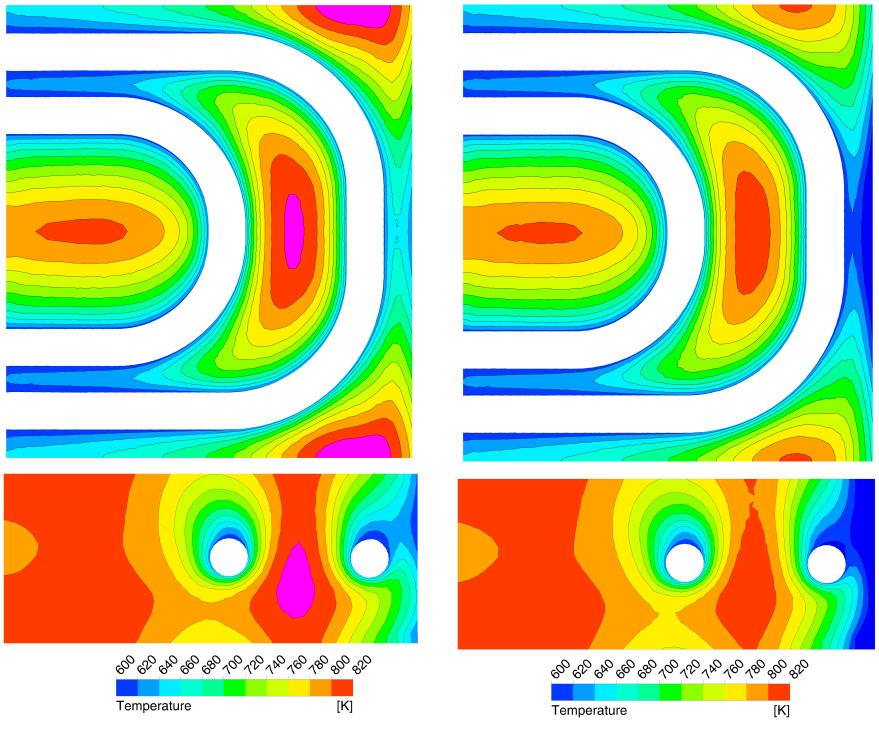

(c) $q_{fw} = 150$ kW/m^2

(d) $q_{fw} = 200$ kW/m^2

Figure 11.17. Temperature distribution on the horizontal plane passing through the pipe center (top) and the vertical central plane (bottom) for increasing heat flux removed from the FW. Purple color identifies $T > 820$ K.

two simulations for an adiabatic FW are performed adopting $p_v = 50$ mm and $p_v = 40$ mm.

Adiabatic First Wall

Reducing the vertical extension of the cell directly impacts the temperature distribution in the cell by diminishing the PbLi volume subject to neutronic heating, thus it is not surprising that even for an adiabatic FW the maximum temperature drops with a decreasing pitch. This effect is particularly significant for the hot-spot in the region between the cooling pipes, where the temperature is reduced below 800 K even for $p_v = 50$ mm, and the central portion of the FW. However, the corner hot-spots are not efficiently cooled by this strategy and for $p_v = 50$ mm the maximum temperature observed is $T_{Max} \approx 954$ K. Shortening the vertical extension of the cell pitch to 40 mm does reduce the maximum temperature in the channel by just 35 K, thus an ulterior increase in the cooling element density for $p_v/d < 3$ will probably not allow the cell to meet the Eurofer temperature limit. Tweaking the pipe layout by moving the outer pipe close to the FW could be a possible strategy to more efficiently cool the corner hot-spots without relying on the passive refrigeration from the FW. The temperature contours for the adiabatic cases are presented in Figures 11.19a and 11.19b.

Refrigerating First Wall

A moderate power removal from the BZ is assumed by the FW cooling system and it is equal to a constant heat flux $q_{fw} = 100$ kW/m^2. The maximum temperature in the cell is plotted against the vertical pitch in Figure 11.18. Comparing these results with the one obtained for the adiabatic FW, it is possible to see how the combination of the two optimization strategies is very efficient in bringing down the maximum temperature in the cell, i.e. for instance in the $p_v = 50$ mm case by ≈ 100 K. However, only for $p_v = 40$ mm the maximum temperature falls below the design requirement. The temperature contours for the refrigerated cases are presented in Figures 11.19c and 11.19d.

11.6 Summary and remarks on blanket design

In this chapter, the fluid dynamics and heat transfer for the mixed convection flow in the FW channel of the WCLL blanket (configuration T02) is analyzed for both the hydrodynamic and magnetohydrodynamic regime. The numerical model is based on the elementary cooling cell of the channel that corresponds to the area refrigerated by a single blanket cooling element that, for the FW channel, is composed by two nested DWT U-pipes inserted from the BSS. No cross-flow is allowed with the other channels in the same radial stack, which share the cooling element, by not representing the pipe opening in the channel back wall. The duct and pipe walls are assumed to be perfectly conducting and the heat transfer water-side is modeled by the Heat Transfer Coefficient boundary condition, thus allowing to represent the case with just a fluid computational domain filled with PbLi. The liquid metal is heated by a volumetric power source, which intensity decreases exponentially moving

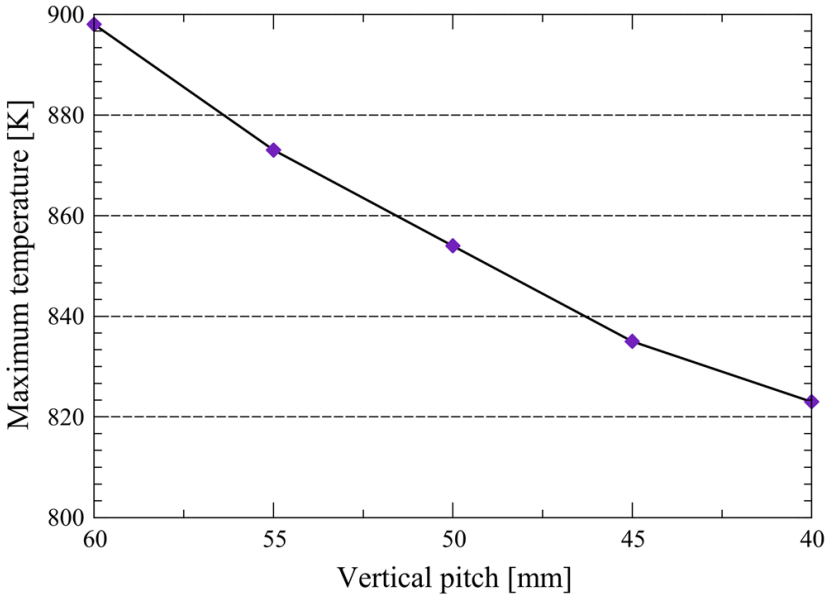

Figure 11.18. Maximum cell temperature plotted against the vertical pitch p_v between cooling elements.

away from the front wall, and it flows upward due to forced convection with a mean velocity $u = 1.825$ mm.

In hydrodynamic conditions, the flow is dominated by the buoyancy forces and the forced convection contribution can be neglected. The velocity in the cell reaches up to 185 mm/s and the ensuing turbulent regime features vortical structures spanning the cell with characteristic length of the same order of the pitch between cooling elements ($L = p_v$). The combined effect of high velocity and significant fluid mixing results in efficient heat transfer in the cell and the maximum PbLi temperature is observed to be 100 K below the Eurofer operative limit.

The transition to the MHD regime suppresses the velocity oscillations introduced by the buoyancy forces and reverts the flow to an almost pure forced convection state. This effect severely dampens the heat transfer in the cell with the PbLi-side heat transfer coefficient reduced to 33% of its hydrodynamic value. The maximum PbLi temperature rises to 1030 K and large hot-spots develop in the FW corners and in the gap between the cooling pipes. However, the heat transfer in the cell can not be described as being restricted to pure conduction, since a significant convection contribution is still present due to the non-negligible velocity of the liquid metal and the jets attached to the cooling pipe wall which are, at least partially, caused by the buoyancy forces. Therefore, the assumption of purely conductive heat transfer employed for simplified BZ thermal-hydraulic studies, for instance in Ref. [86], is valid but overly conservative.

The model is successively modified introducing BZ passive refrigeration caused by the first wall cooling system, modeled with a constant heat flux (q_{fw}), and reducing the cooling cell vertical extension, thus simulating an increased number of cooling elements. The first strategy is found to be very efficient in cooling the corners but it does not manage to similarly affect the other hot-spot and only for

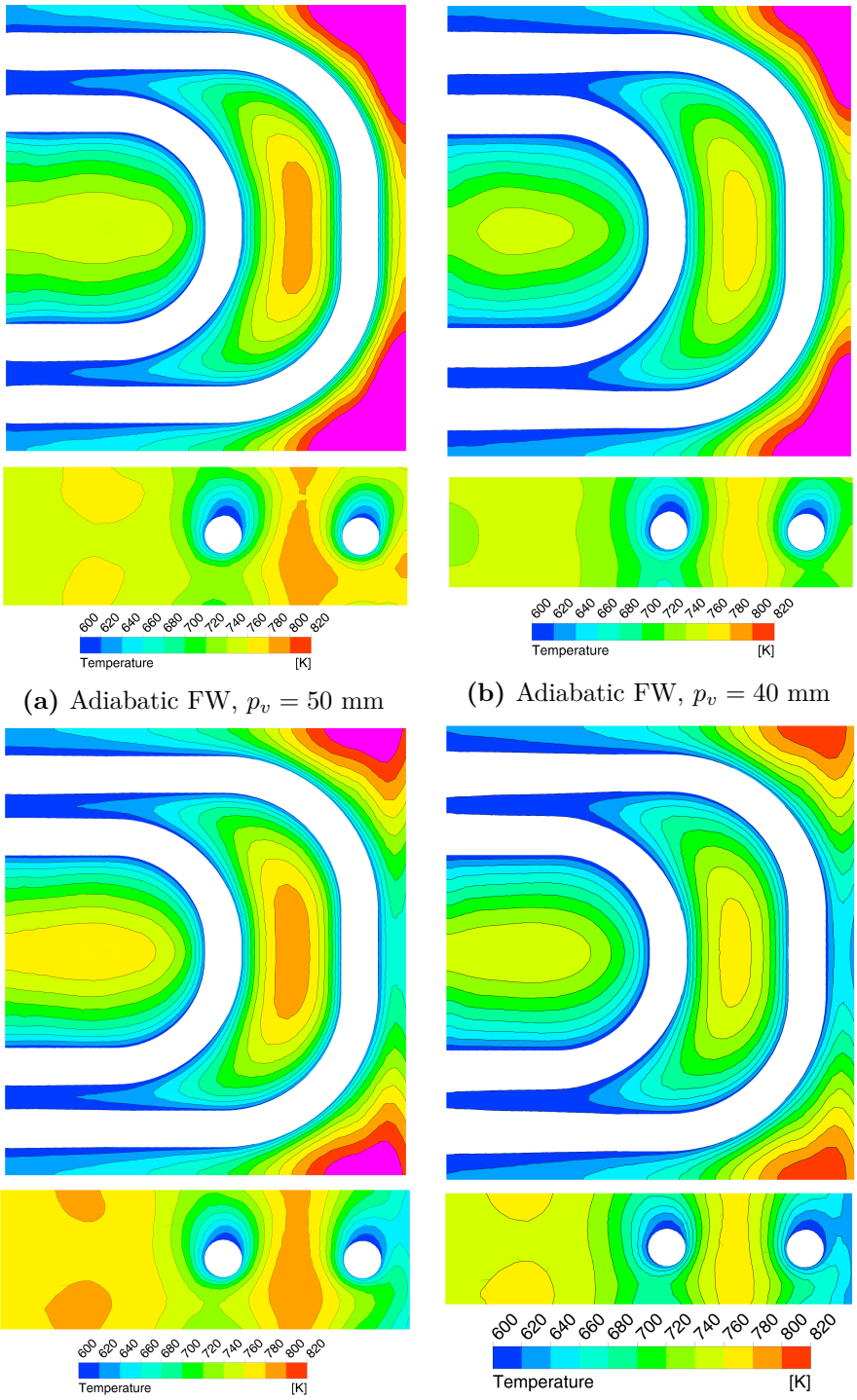

(a) Adiabatic FW, $p_v = 50$ mm

(b) Adiabatic FW, $p_v = 40$ mm

(c) Refrigerating FW, $p_v = 50$ mm

(d) Refrigerating FW, $p_v = 40$ mm

Figure 11.19. Temperature distribution on the horizontal plane passing through the pipe center and the vertical central plane for reduced vertical pitch in the case of adiabatic (top) and refrigerating FW (bottom). Purple color identifies $T > 820$ K.

$q_{fw} = 200$ kW/m^2 the maximum temperature in the cell falls below the Eurofer operative limit. Combining a moderate power removal from the FW cooling system ($q_{fw} = 100$ kW/m^2) and a reduced vertical pitch ($p_v = 40$ mm), it is possible to keep the PbLi maximum temperature below 823 K even for the MHD regime.

In principle, this result demonstrates that the BZ cooling system of configuration T02 is able to meet the design requirements for the Eurofer temperature, however, it relies on a significant albeit moderate amount of passive refrigeration from the FW cooling system and it is all but a sound design strategy: in particular, it can cause the damaging of the blanket structural materials during plasma transients when the FW heat load is not constant and uniform.

To achieve the same performances with an adiabatic FW, the reduction of the vertical pitch below 40 mm seems to be an unavoidable necessity and, moreover, it will require the modification of the outer pipe position to bring it closer to the FW and more efficiently cool the corner hot-spots. Concerns about the blanket mechanical stability are raised for $p_v/d_o < 3$, since to allow the cooling pipe to reach the FW channel it is necessary to perforate large sections of the toroidal-poloidal SPs. Moreover, manufacturing issues in the realization of the U-pipe layout pose relevant drawbacks in the feasibility of the cooling system postulated. For instance, the adoption of DWTs causes severe limitations in the bending radius achievable, which is currently limited to $r \approx 45$ mm, and in the minimum distance between two separate welds, required to anchor the cooling pipes to the BSS [191]. These constraints must be carefully assessed to assess the feasibility of this configuration.

More detailed studies considering a finite conductivity for the channel solid surfaces and simulating the actual heat transfer in the pipes could "improve" the BZ cooling system performances by removing the most conservative assumptions of this analysis. Since the BZ channels are in electrical contact with each other, the electromagnetic coupling is expected to play a crucial role in shaping the flow features and, thus, the liquid metal heat transfer coefficient, therefore a model including more than one channel is strongly suggested to assess the global thermal behavior of the cooling element and to investigate this phenomenon. In particular, the coupling of the ducts aligned in the radial direction is foreseen to suppress the flow rate in the middle channels and generate intense jets at the FW and BSS [82] that could, in principle, greatly enhance the cooling system performances in the most challenging region highlighted in this study.

Part IV

Final remarks

Chapter 12

Conclusions

12.1 Blanket comparative analysis outcome

The pressure drop due to the MHD drag has been estimated for the four alternative configurations of the PbLi in-vessel flow path (T01.A, T01.B, T02, and T03) considered for the WCLL blanket design. The analysis was focused on the central outboard segment and its maximum acceptable PbLi pressure loss was taken as $\Delta p_{\text{tot}} = 2$ MPa [53]. The estimate is carried over with the most recent boundary conditions for magnetic field and PbLi flow rate derived from the DEMO baseline data. Literature correlations for the two-dimensional and three-dimensional pressure drop term are used to estimate the head loss and, where necessary, are supported by numerical simulations conducted during this study.

The bulk of the pressure drop is observed for the connection elements with the PbLi ex-vessel loop, where the highest flow rate in the blanket is concentrated and velocity up to several cm/s is encountered. Different routing schemes from the lower and upper VV port are considered. In the DEMO baseline, the feeding pipe is assumed to pass through the former path, whereas the draining pipe is lowered from the upper port and is attached at around two-third of the blanket poloidal height (mid-point), the exception being configuration T03, for which both pipes are routed through the upper port.

A significant drawback of this configuration is caused by the tight constraints imposed by remote maintenance requirements, which are allowing a feeding pipe whose maximum nominal diameter is DN80 for routing via the VV lower port. Such a small pipe is characterized by unacceptable pressure loss ($\Delta p \approx 2.1$ MPa); indeed, the analysis demonstrated that a minimum pipe size about DN150÷200 is required to achieve reasonable head losses (≈ 0.5 MPa). On the other hand, alternative routing schemes from the upper port are more favorable for size requirements, but cause relevant issues with regard to the integration with the BZ flow path. In particular, only configuration T01.A will be reasonably amenable to them, whereas other configurations cannot be modified in a straightforward way to allow for a different feeding scheme. Moreover, a safety issue could be possibly introduced by overhauling the feeding scheme, since it will require the design of a dedicated system to unload the PbLi during unplanned plant shutdowns.

Fewer concerns are raised for the draining pipe size and position thanks to its

routing scheme being foreseen via the VV upper port, where more space is available in the current plant baseline. However, similar considerations apply and a minimum pipe size about DN150÷200 is required to do not incur in unacceptable pressure losses. Attachment to the blanket top should be preferred compared to the current design to simplify the PbLi in-vessel flow path.

Currently, the PbLi ex-vessel loop is planned to withstand $P = 4.6$ MPa and a similar design pressure is adopted to size the feeding and draining pipe ($P = 5$ MPa). The necessity to consider the over-pressurization scenario for an in-box LOCA will probably force to adopt a higher design pressure ($P = 18$ MPa) and, thus, a thicker wall than the one assumed in this study. The pressure drop estimate is very sensitive to this parameter and, even for DN200, the maximum pressure loss is exceeded in both the feeding and draining pipe. Furthermore, it should be noted that remote maintenance requirements enforce a maximum wall thickness $t_w = 15$ mm, which it is incompatible for any but the DN80 pipe.

To compensate the increased pressure losses due to this circumstance the adoption of insulating elements limited to the feeding and draining pipe must be carefully contemplated and the pipe path must be streamlined as much as possible.

Conversely to the feeding and draining pipe, the layout of manifold and breeding zone remarkably differs between the alternative WCLL configurations in terms of structural elements arrangement, flow distribution scheme, and flow path. Configurations T01.A and T01.B mostly share the same features with the former being composed of several elementary cells, each one fed by a parallel distribution scheme, whereas in the latter those are linked in a single, long, flow path that winds along the whole blanket poloidal height. The stiffening plates arrangement is altered for configurations T02 and T03 to realize a checkerboard-like geometry where the PbLi flows in long, poloidally aligned, rectangular channels. In configuration T02, the liquid metal motion is restricted to the upward direction and the cooling system layout relies on nested horizontal U-pipes, which refrigerate along their path an array of 4 ducts. Conversely, PbLi flows at first downward in the back channels and then upward close to the FW in configuration T03; vertical pipes are adopted for the refrigeration.

Manifolds are less important pressure loss-wise, but nevertheless play a fundamental role since they are responsible for flow distribution that, if unbalanced, can lead to long residence time for the LM in the blanket and large stagnation zones, both detrimental to tritium inventory management and permeation in the coolant.

The most loss-intensive manifold is found for configuration T01.A where the PbLi flows in thin and long rectangular channels along the blanket spine to reach and feed each elementary cell. A significant pressure imbalance is foreseen between the channel and lateral flow path due to the increasing blanket toroidal width. Flow characterization is badly required to validate the estimate presented in this study, accounting for the numerous obstacle crossing the reference channel and electromagnetic coupling between neighboring duct, and to investigate the actual flow distribution. Configuration T01.B manifold performances are significantly better thanks to the adoption of a simplified layout, removing the long spinal channels.

Configurations T02 and T03 share akin manifold layouts, though located in different position, that are comparatively simpler and less loss-intensive. Mechanical stability is one of the main concerns for this manifold concept, since the tank used

to minimize pressure imbalance across the BZ channels (and overall losses) also weakens the blanket bottom cap, which could conceivably fail during accidental transients. In addition, the manifold must be integrated in the BZ cooling system, since it is subjected to non-negligible volumetric heating.

Accurate numerical modeling of the manifold flow is required to characterize compact and complex geometrical elements, where the inertia-less and inviscid assumptions adopted in this study are not necessarily valid in some particular conditions, like orifices and contracting/expanding bends, and to assess the flow distribution. Particular attention should also be employed for the treatment of flow around obstacles, since multiple penetrations across the manifold are required for the breeding zone cooling system pipes. Moreover, the prediction of the electromagnetic coupling effect on flow distribution is deemed to be of the utmost necessary, especially for the complex layout foreseen for configuration T01.A.

The breeding zone is characterized by rather modest pressure losses compared with the other hydraulic regions, except for T01.B where the winding flow path and fast fluid velocity result in unsustainable pressure losses ($\Delta p \approx 2$ MPa). Flow distribution, tritium transport, and heat transfer considerations must drive the design in this region due to the limited pressure drop value.

Significant recirculation is likely to occur in the T03 back channels due to the interplay between volumetric heating, downward forced convection, and long axial length, but further study is required to characterize this flow in presence of internal vertical obstacles. Interaction between buoyancy forces and intricate flow path is also a concern for configuration T01.A, where abysmal velocities and numerous obstacles are present. Both cases will benefit from a detailed numerical study.

In conclusion, configuration T02 is found to be the blanket layout with the minimum pressure drop among the four studied, whereas configuration T01.A shows the most potential for adaptation to sub-optimal feeding schemes forced by blanket integration requirements, despite the loss-intensive manifold region. Nevertheless, all the blanket configurations examined fail to meet the maximum pressure drop criterion when extrapolated to inboard conditions. In order to develop a consistent blanket design also for the inboard, the PbLi flow path must be optimized and streamlined in order to reduce the overall pressure drop to $\Delta p_{\mathrm{tot}} = 0.5$ MPa.

12.2 ANSYS CFX validation

To support the blanket design, a numerical tool able to represent the various MHD phenomena is an essential requirement. For this purpose, the commercial CFD code ANSYS CFX is employed in this dissertation for the numerical modeling of some relevant MHD flows encountered in the WCLL blanket. A detailed and extensive validation campaign is performed to assess the code results confidence.

The code is validated against theoretical solutions for several forced and magneto-convection benchmarks and found to perform reasonably well. Part of the validation process involved free surface flows to assess the capability of the code to support the design of plasma-facing components employing liquid metal. For this last case, unfortunately, it is only possible to model low Ha flows, even if basic cases were considered. Further validation should be pursued in order to assess the code

performances for other relevant blanket phenomena like Q2D and MHD turbulence, electrically-driven flow, heat transfer, etc.

ANSYS CFX has shown performances in-line with the state-of-the-art CMHD codes available to the general public and, therefore, it can be considered as an useful tool to support a liquid metal blanket design. The main drawback of CFX is related to its nature of proprietary software: the source code is closed and it is possible to tweak the electromagnetic module only to a limited extent. This case precludes the possibility to implement more advanced numerical schemes, like the current consistent conservative interpolation method proposed by Ni et al. [38, 39], and limits the usefulness of the code, especially for the treatment of more complex problems, like the free surface flow considered in the validation process, and taking into account the likely progresses of specialized CMHD in the next years.

To circumvent these constraints, the development of MHD models based on open source CFD libraries, like OpenFOAM, could be a possible strategy. Similar numerical tools have been already developed by several research teams in the past years (see, for instance, Ref. [114–117]) and their flexibility allows to integrate advanced numerical schemes and dedicated MHD models with relative ease. Although development and maintenance of such tools is by all means time-consuming, the opportunities provided by a powerful, flexible, and easily extensible CMHD code are deemed to be invaluable for further advancing the numerical modeling of MHD flows for liquid metal blanket design.

12.3 Numerical characterization of WCLL MHD flows

The forced convection around a single transverse pipe is studied in a configuration very similar to the one encountered in T01.A breeding zone. Both skewed magnetic field and duct walls of non-uniform thickness are preserved to model realistic electric boundary conditions. The case is analyzed in the parameter range $Re = 20 \div 80$, $Ha = 0 \div 100$, $\alpha = 0 \div 32°$, and $c_o = 0 \div \infty$, where α is the magnetic field inclination on the obstacle axis and c_o is the obstacle wall conductance ratio. The pipe is assumed to be at fixed temperature such that $\Delta T = 30$ K with the inlet.

The heat transfer is found to increase with Ha due to the promotion of the flow rate in the sub-channel below the pipe. This phenomenon is caused by leakage currents coming from the upper sub-channel through the duct electro-conductive wall that couple the two sub-channels. The flow pattern around the obstacle is dampened with increasing Ha and reverts to a creeping regime for $Ha \to \infty$. Pipe wall conductivity and magnetic field inclination are found to have negligible influence on both the heat transfer and three-dimensional obstacle pressure drop term. In particular, the latter is found to be a weaker function of the magnetic field intensity compared with the two-dimensional pressure drop and its weight on the overall loss decreases with Ha. A correlation to predict the three-dimensional pressure drop term is proposed starting from the data gathered by this activity. Further studies considering mixed convection with non-uniform volumetric heating and a more complex geometry with multiple pipes are deemed necessary to completely characterize this case.

Mixed convection in the upward direction in presence of transverse curved

obstacles is investigated to gain some insights about the heat transfer for the elementary cell of configuration T02. The case is analyzed for a single cooling element of the FW channel (two nested double walled Eurofer U-pipes) in both hydrodynamic ($Ha = 0$) and MHD conditions ($Ha = 8.5 \cdot 10^3$). The non-uniform volumetric heating in the FW channel is accurately modeled, with the average volumetric power density $\bar{Q} = 6.7$ MW/m^3 corresponding to $Gr = 5.70 \cdot 10^{10}$, and the conservative boundary condition of perfectly conducting duct and pipe walls is assumed.

The breeding zone cooling system is found to perform acceptably in hydrodynamic conditions due to the flow being dominated by the buoyancy forces, which cause the onset of an intense turbulent regime. The MHD regime is accompanied by severely dampened velocity oscillations and, thus, PbLi-side heat transfer coefficient, which is reduced to nearly a third of its purely hydrodynamic value. Consequently, the maximum temperature in the cell reaches over 1000 K, which it cannot be considered acceptable due to operative temperature limit on the structural materials.

To decrease the PbLi maximum temperature in the cell, a reduction in the vertical pitch separating two successive cooling elements (i.e. increasing their density) and moderate passive refrigeration from the first wall cooling system are required. Altering the pipe layout could conceivably result in enhanced performances, but it is unlikely to be feasible due to manufacturing issues in the fabrication of the curved Eurofer pipes. Overall, the proper refrigeration of the elementary cell seems to be quite challenging even considering less conservative boundary conditions for the solid surfaces without a radical rearrangement of the breeding zone to allow for pipes meeting the manufacturing requirements and more efficient cooling of the region close to the FW.

Bibliography

[1] S. Smolentsev, S. Badia, R. Bhattacharyay, L. Bühler, L. Chen, Q. Huang, H.-G. Jin, D. Krasnov, D.-W. Lee, E. M. de les Valls, *et al.*, "An approach to verification and validation of MHD codes for fusion applications," *Fusion Engineering and Design*, vol. 100, pp. 65–72, 2015.

[2] C. Reed, B. Picologlou, T. Hua, and J. Walker, *ALEX results: A comparison of measurements from a round and a rectangular duct with 3-D code predictions*. Argonne National Lab., 1987.

[3] B. Picologlou and C. Reed, "Experimental investigation of 3-D MHD flows at high Hartmann number and interaction parameter," in *Liquid Metal Magnetohydrodynamics*, pp. 71–77, Springer, 1989.

[4] L. Bühler, "Laminar buoyant magnetohydrodynamic flow in vertical rectangular ducts," *Physics of Fluids (1994-present)*, vol. 10, no. 1, pp. 223–236, 1998.

[5] A. Y. Shishko, "A theoretical investigation of steady-state film flows in a coplanar magnetic field," *Magnetohydrodynamics*, vol. 28, no. 2, pp. 170–182, 1993.

[6] K. Miyamoto, *Plasma physics and controlled nuclear fusion*, vol. 38. Springer Science & Business Media, 2006.

[7] C. M. Braams and P. E. Stott, *Nuclear fusion: half a century of magnetic confinement fusion research*. CRC Press, 2002.

[8] EUROfusion Consortium, *European research roadmap to the realisation of fusion energy*. Euratom, 2018. Available online at: https://www.eurofusion.org/eurofusion/roadmap.

[9] C. Bachmann, T. Franke, F. Maviglia, M. Siccinio, S. Ciattaglia, C. Gliss, C. Vorpahl, T. Härtl, G. Keech, F. Cismondi, and G. Federici, *EFDA D 2KVWQZ, DEMO Plant Description Document, v1.4*. Eurofusion, 2018. Available online for EUROfusion members at https://idm.eurofusion.org/?uid=2KVWQZ.

[10] G. Federici, C. Bachmann, L. Barucca, W. Biel, L. Boccaccini, R. Brown, C. Bustreo, S. Ciattaglia, F. Cismondi, M. Coleman, *et al.*, "DEMO design activity in Europe: Progress and updates," *Fusion Engineering and Design*, 2018.

[11] F. Cismondi, L. Boccaccini, G. Aiello, J. Aubert, C. Bachmann, T. Barrett, L. Barucca, E. Bubelis, S. Ciattaglia, A. Del Nevo, *et al.*, "Progress in EU Breeding Blanket design and integration," *Fusion Engineering and Design*, vol. 136, no. Part A, pp. 782–792, 2018.

[12] R. J. Pearson, A. B. Antoniazzi, and W. J. Nuttall, "Tritium supply and use: a key issue for the development of nuclear fusion energy," *Fusion Engineering and Design*, vol. 136, no. Part B, pp. 1140–1148, 2018.

[13] M. Abdou, N. B. Morley, S. Smolentsev, A. Ying, S. Malang, A. Rowcliffe, and M. Ulrickson, "Blanket/first wall challenges and required R&D on the pathway to DEMO," *Fusion Engineering and Design*, vol. 100, pp. 2–43, 2015.

[14] R. Knitter, P. Chaudhuri, Y. Feng, T. Hoshino, and I.-K. Yu, "Recent developments of solid breeder fabrication," *Journal of Nuclear Materials*, vol. 442, no. 1-3, pp. S420–S424, 2013.

[15] F. Hernández, P. Pereslavtsev, Q. Kang, P. Norajitra, B. Kiss, G. Nádasi, and O. Bitz, "A new HCPB breeding blanket for the EU DEMO: Evolution, rationale and preliminary performances," *Fusion Engineering and Design*, vol. 124, pp. 882–886, 2017.

[16] F. Hernández and P. Pereslavtsev, "First principles review of options for tritium breeder and neutron multiplier materials for breeding blankets in fusion reactors," *Fusion Engineering and Design*, vol. 137, pp. 243–256, 2018.

[17] W. Dänner, M. Rieger, and K. Verschuur, "Progress in design and analysis of the NET water cooled liquid breeder blanket," in *Fusion technology 1986. 2 v*, 1986.

[18] G. Casini, P. Labbe, M. Rieger, L. Baraer, M. Biggio, F. Farfaletti-Casali, G. Gervaise, L. Giancarli, M. Roze, Y. Severi, *et al.*, "A water cooled, lithium lead breeding blanket for a DEMO fusion reactor," *Fusion Engineering and Design*, vol. 14, no. 3-4, pp. 353–372, 1991.

[19] L. Giancarli, G. Benamati, M. Fütterer, G. Marbach, C. Nardi, and J. Reimann, "Development of the EU water-cooled Pb-17Li blanket," *Fusion engineering and design*, vol. 39, pp. 639–644, 1998.

[20] J. Aubert, G. Aiello, N. Jonquères, A. L. Puma, A. Morin, and G. Rampal, "Development of the water cooled lithium lead blanket for DEMO," *Fusion Engineering and Design*, vol. 89, no. 7-8, pp. 1386–1391, 2014.

[21] E. Martelli, *Thermal hydraulic design of DEMO Water Cooled Lithium Lead Breeding Blanket and integration with primary system and balance of plant.* Phd thesis, Sapienza University of Rome, February 2018.

[22] A. Tassone, A. Del Nevo, P. Arena, G. Bongiovì, G. Caruso, P. A. di Maio, G. di Gironimo, M. Eboli, N. Forgione, R. Forte, *et al.*, "Recent progress in the WCLL breeding blanket design for the DEMO fusion reactor," *IEEE Transactions on Plasma Science*, vol. 46, no. 5, pp. 1446–1457, 2018.

[23] G. Bongiovì, P. Arena, P. Chiovaro, P. Di Maio, A. Del Nevo, and R. Forte, "Multi-Module vs. Single-Module concept: Comparison of thermomechanical performances for the DEMO Water-Cooled Lithium Lead breeding blanket," *Fusion Engineering and Design*, vol. 136, no. Part B, pp. 1472–1478, 2018.

[24] P. Di Maio, P. Arena, G. Bongiovì, P. Chiovaro, A. Del Nevo, R. Giammusso, and M. Richiusa, "Structural analysis of the back supporting structure of the DEMO WCLL outboard blanket," *Fusion Engineering and Design*, vol. 124, pp. 944–947, 2017.

[25] F. Tavassoli, "Eurofer steel, development to full code qualification," *Procedia Engineering*, vol. 55, pp. 300–308, 2013.

[26] AFCEN, "RCC-MRx: Design and Construction Rules for Mechanical Components in high-temperature structures, experimental reactors and fusion reactors," Standard, 2015.

[27] E. Martelli, A. Del Nevo, P. Arena, G. Bongiovì, G. Caruso, P. Di Maio, M. Eboli, G. Mariano, R. Marinari, F. Moro, *et al.*, "Advancements in DEMO WCLL breeding blanket design and integration," *International Journal of Energy Research*, vol. 42, no. 1, pp. 27–52, 2018.

[28] M. Tillack, P. Humrickhouse, S. Malang, and A. Rowcliffe, "The use of water in a fusion power core," *Fusion Engineering and Design*, vol. 91, pp. 52–59, 2015.

[29] A. Tassone, G. Caruso, A. Del Nevo, and I. Di Piazza, "CFD simulation of the magnetohydrodynamic flow inside the WCLL breeding blanket module," *Fusion Engineering and Design*, vol. 124, pp. 705–709, 2017.

[30] S. Chandrasekhar, *Hydrodynamic and hydromagnetic stability*. Courier Corporation, 2013.

[31] P. A. Davidson, *An introduction to magnetohydrodynamics*, vol. 25. Cambridge university press, 2001.

[32] R. J. Moreau, *Magnetohydrodynamics*, vol. 3. Springer Science & Business Media, 2013.

[33] U. Müller and L. Bühler, *Magnetofluiddynamics in channels and containers*. Springer Science & Business Media, 2013.

[34] G. K. Batchelor, *An introduction to fluid dynamics*. Cambridge university press, 2000.

[35] L. Bühler, "Magnetohydrodynamic flows in arbitrary geometries in strong, nonuniform magnetic fieldsâĂŤa numerical code for the design of fusion reactor blankets," *Fusion Technology*, vol. 27, no. 1, pp. 3–24, 1994.

[36] S. Molokov and L. Bühler, "Liquid metal flow in a U-bend in a strong uniform magnetic field," *Journal of Fluid Mechanics*, vol. 267, pp. 325–352, 1994.

[37] C. N. Kawczynski, *A Numerical Investigation of Moderate Magnetic Reynolds Number Fusion Liquid Metal Magnetohydrodynamic Flows*. Phd thesis, UCLA, April 2018.

[38] M.-J. Ni, R. Munipalli, N. B. Morley, P. Huang, and M. A. Abdou, "A current density conservative scheme for incompressible MHD flows at a low magnetic reynolds number. Part I: On a rectangular collocated grid system," *Journal of Computational Physics*, vol. 227, no. 1, pp. 174–204, 2007.

[39] M.-J. Ni, R. Munipalli, P. Huang, N. B. Morley, and M. A. Abdou, "A current density conservative scheme for incompressible MHD flows at a low magnetic reynolds number. Part II: On an arbitrary collocated mesh," *Journal of Computational Physics*, vol. 227, no. 1, pp. 205–228, 2007.

[40] M.-J. Ni and J.-F. Li, "A consistent and conservative scheme for incompressible MHD flows at a low magnetic reynolds number. Part III: On a staggered mesh," *Journal of Computational Physics*, vol. 231, no. 2, pp. 281–298, 2012.

[41] H. K. Versteeg and W. Malalasekera, *An introduction to computational fluid dynamics: the finite volume method*. Pearson Education, 2007.

[42] J. Shercliff, "Steady motion of conducting fluids in pipes under transverse magnetic fields," in *Mathematical Proceedings of the Cambridge Philosophical Society*, vol. 49, pp. 136–144, Cambridge University Press, 1953.

[43] R. Moreau and S. Molokov, "Julius Hartmann and his followers: a review of the properties of Hartmann layer," in *Magnetohydrodynamics: Historical evolution and trends* (S. S. Molokov, R. Moreau, and H. K. Moffatt, eds.), vol. 80, Springer Science & Business Media, 2007.

[44] I. R. Kirillov, C. B. Reed, L. Barleon, and K. Miyazaki, "Present understanding of MHD and heat transfer phenomena for liquid metal blankets," *Fusion engineering and design*, vol. 27, pp. 553–569, 1995.

[45] J. Hunt, "Magnetohydrodynamic flow in rectangular ducts," *Journal of Fluid Mechanics*, vol. 21, no. 04, pp. 577–590, 1965.

[46] Y. S. Uflyand, "Flow of conducting fluid in a rectangular channel in a transverse magnetic field," *Sov. Phys. Tech. Phys*, vol. 5, p. 1194, 1961.

[47] C. C. Chang and T. S. Lundgren, "Duct flow in magnetohydrodynamics," *Zeitschrift für angewandte Mathematik und Physik ZAMP*, vol. 12, no. 2, pp. 100–114, 1961.

[48] J. Hunt and K. Stewartson, "Magnetohydrodynamic flow in rectangular ducts. ii," *Journal of fluid mechanics*, vol. 23, no. 3, pp. 563–581, 1965.

[49] U. Burr, L. Barleon, U. Müller, and A. Tsinober, "Turbulent transport of momentum and heat in magnetohydrodynamic rectangular duct flow with strong sidewall jets," *Journal of Fluid Mechanics*, vol. 406, pp. 247–279, 2000.

[50] Z. Tao and M.-J. Ni, "Analytical solutions for MHD flow at a rectangular duct with unsymmetrical walls of arbitrary conductivity," *Science China Physics, Mechanics & Astronomy*, vol. 58, no. 2, pp. 1–18, 2015.

[51] P. M. Blosseville, S. Aleksandrova, and S. Molokov, "Buoyancy-driven MHD flow in electrically insulated rectangular ducts," *Magnetohydrodynamics*, vol. 43, no. 3, pp. 315–321, 2007.

[52] C. Mistrangelo and L. Bühler, "Numerical study of fundamental magnetoconvection phenomena in electrically conducting ducts," *IEEE Transactions on Plasma Science*, vol. 40, no. 3, pp. 584–589, 2012.

[53] S. Smolentsev, R. Moreau, L. Bühler, and C. Mistrangelo, "MHD thermofluid issues of liquid-metal blankets: phenomena and advances," *Fusion Engineering and Design*, vol. 85, no. 7, pp. 1196–1205, 2010.

[54] F. Maviglia *et al.*, *EFDA D 2NHF7E v1.0, SN-A31-k165 improvedFW correctedLowerPortFM*. Eurofusion, 2018. Available online for EUROfusion members at https://idm.euro-fusion.org/?uid=2MPG82.

[55] R. Wenninger, *EFDA D 2MG46D, DEMO1 Reference Design - 2015 April ("EU DEMO1 2015") - Initial Geometry Based on PROCESS Output - v1.0*. Eurofusion, 2018. Available online for EUROfusion members at https://idm.euro-fusion.org/?uid=2MG46D.

[56] A. Del Nevo *et al.*, *EFDA D 2N6WLQ, WCLL Design Report 2015 - v1.0*. Eurofusion, 2016. Available online for EUROfusion members at https://idm.euro-fusion.org/?uid=2N6WLQ.

[57] A. Del Nevo *et al.*, *EFDA D 2MTZP6, WCLL Design Report 2016 - v1.1*. Eurofusion, 2017. Available online for EUROfusion members at https://idm.euro-fusion.org/?uid=2MTZP6.

[58] A. Del Nevo *et al.*, *EFDA D 2MYHNE, WCLL Design Report 2017 - v1.1*. Eurofusion, 2018. Available online for EUROfusion members at https://idm.euro-fusion.org/?uid=2MYHNE.

[59] C. Bachmann and J. Anthony, *EFDA D 2M8H88, Plant Definition Document*. Eurofusion, 2018.

[60] M. Utili, A. Tincani, D. Martelli, and C. Schweier, *WPBB-DEL-BB-5.1.1-T001-D003, EFDA D 2MN9BR, Conceptual Design of WCLL/HCLL PbLi–Loops with Auxiliaries*. Eurofusion, 2017. Available online for EUROfusion members at https://idm.euro-fusion.org/?uid=2MQM7L.

[61] U. Jauch, V. Karcher, B. Schulz, and G. Haase, *Thermophysical properties in the system Li-Pb*. KIT, 1986.

[62] K. Mergia and N. Boukos, "Structural, thermal, electrical and magnetic properties of Eurofer 97 steel," *Journal of Nuclear Materials*, vol. 373, no. 1, pp. 1–8, 2008.

[63] R. Wenninger *et al.*, *EFDA D 2MUW9R, DEMO1 Reference Design - 2017 April ("EU DEMO1 2017") - SOF and EOF equilibria - v1.0.* Eurofusion, 2018. Available online for EUROfusion members at https://idm.eurofusion.org/?uid=2MUW9R.

[64] L. Bühler, *Three-dimensional liquid metal flows in strong magnetic fields.* Forschungszentrum Karlsruhe, 2008. Tech. Rep. FZKA 7412.

[65] K. Miyazaki, S. Inoue, N. Yamaoka, T. Horiba, and K. Yokomizo, "Magneto-hydro-dynamic pressure drop of lithium flow in rectangular ducts," *Fusion technology*, vol. 10, no. 3P2A, pp. 830–836, 1986.

[66] K. Miyazaki, S. Kotake, N. Yamaoka, S. Inoue, and Y. Fujii-E, "MHD pressure drop of NaK flow in stainless steel pipe," *Nuclear Technology-Fusion*, vol. 4, no. 2P2, pp. 447–452, 1983.

[67] T. Hua, J. Walker, B. Picologlou, and C. Reed, "Three-dimensional magnetohydrodynamic flows in rectangular ducts of liquid-metal-cooled blankets," *Fusion technology*, vol. 14, pp. 1389–1398, 1988.

[68] L. Bühler and P. Norajitra, *Magnetohydrodynamic flow in the dual coolant blanket*, vol. 6802. FZKA, 2003.

[69] J. Reimann, S. Molokov, I. Platnieks, and E. Platacis, "MHD-flow in multi-channel U-bends: screening experiments and theoretical analysis," in *Fusion Technology 1992*, pp. 1454–1458, Elsevier, 1993.

[70] A. G. Spagnuolo and I. A. Maione, *EFDA D 2MM7WF, BB-RM Interface Requirements - v2.0.* Eurofusion, 2019. Available online for EUROfusion members at https://idm.euro-fusion.org/?uid=2MM7WF.

[71] American Society of Mechanical Engineers, ASME B31.3a-1996, "Process Piping Specification – ASME Code for Pressure Piping," Standard, 1996.

[72] International Organization for Standardization, ISO 6708:1995, "Pipework components – Definition and selection of DN (nominal size)," Standard, 1995.

[73] International Organization for Standardization, ISO 1127:1992(E), "Stainless steel tubes – Dimensions, tolerances and conventional masses per unit length," Standard, 1992.

[74] G. Caruso *et al.*, *EFDA D 2MND5X,Interim report on accident analyses: WCLL blanket in-box LOCA - v1.2.* Eurofusion, 2018. Available online for EUROfusion members at https://idm.euro-fusion.org/?uid=2MND5X.

[75] L. Chiasso, "Magnetohydrodynamic analysis for prototypical manifolds of liquid metal fusion reactor blankets," Master's thesis, Sapienza University of Rome, October 2018.

[76] L. Bühler, H.-J. Brinkmann, and C. Koehly, "Experimental study of liquid metal magnetohydrodynamic flows near gaps between flow channel inserts," *Fusion Engineering and Design*, 2018.

[77] C. Koehly and L. Bühler, "Fabrication issues of sandwich-like flow inserts for circular pipes," *Fusion Science and Technology*, vol. 72, no. 4, pp. 660–666, 2017.

[78] F. Urgorri, S. Smolentsev, I. Fernández-Berceruelo, D. Rapisarda, I. Palermo, and A. Ibarra, "Magnetohydrodynamic and thermal analysis of PbLi flows in poloidal channels with flow channel insert for the EU-DCLL blanket," *Nuclear Fusion*, vol. 58, no. 10, p. 106001, 2018.

[79] L. Bühler and C. Mistrangelo, "Influence of non-insulated gaps between flow channel inserts in ducts of dcll blankets," in *Fusion Engineering (SOFE), 2013 IEEE 25th Symposium on*, pp. 1–6, IEEE, 2013.

[80] L. Bühler and C. Mistrangelo, "Pressure drop and velocity changes in MHD pipe flows due to a local interruption of the insulation," *Fusion Engineering and Design*, vol. 127, pp. 185–191, 2018.

[81] F. Selimefendigil and H. F. Öztop, "Influence of inclination angle of magnetic field on mixed convection of nanofluid flow over a backward facing step and entropy generation," *Advanced Powder Technology*, vol. 26, no. 6, pp. 1663–1675, 2015.

[82] M. J. Bluck and M. J. Wolfendale, "An analytical solution to electromagnetically coupled duct flow in MHD," *Journal of Fluid Mechanics*, vol. 771, pp. 595–623, 2015.

[83] C. Mistrangelo and L. Bühler, "Electric flow coupling in the HCLL blanket concept," *Fusion Engineering and Design*, vol. 83, no. 7-9, pp. 1232–1237, 2008.

[84] R. Mozzillo *et al.*, "Assessment on DEMO water cooled lithium lead alternative design configuration," *Fusion Engineering and Design*, 2018. (submitted).

[85] A. Tassone, M. Nobili, and G. Caruso, "Magnetohydrodynamic flow and heat transfer around a heated cylinder of arbitrary conductivity," in *Journal of Physics: Conference Series*, vol. 923, p. 012024, IOP Publishing, 2017.

[86] F. Edemetti, E. Martelli, A. Tassone, G. Caruso, and A. Del Nevo, "EU DEMO WCLL BB breeding zone cooling system design: analysis and discussion," *Fusion Engineering and Design*, 2018. (submitted).

[87] L. Bühler and C. Mistrangelo, "MHD flow and heat transfer in model geometries for WCLL blankets," *Fusion Engineering and Design*, vol. 124, pp. 919–923, 2017.

[88] S. Smolentsev, R. Moreau, and M. Abdou, "Characterization of key magnetohydrodynamic phenomena in PbLi flows for the US DCLL blanket," *Fusion Engineering and Design*, vol. 83, no. 5-6, pp. 771–783, 2008.

[89] ANSYS, Inc., *CFX Solver Theory Guide*. ANSYS, 2018.

[90] L. Bühler, C. Mistrangelo, J. Konys, R. Bhattacharyay, Q. Huang, D. Obukhov, S. Smolentsev, and M. Utili, "Facilities, testing program and modeling needs for studying liquid metal magnetohydrodynamic flows in fusion blankets," *Fusion Engineering and Design*, vol. 100, pp. 55–64, 2015.

[91] I. E. Butsenieks and E. V. Shcherbinin, "Hydromagnetic flow in pipes with unequal electrical conductivity of the walls in an oblique transverse magnetic field," *Magnetohydrodynamics*, vol. 7, no. 4, pp. 565–567, 1971.

[92] T. N. Aitov, A. I. Kalyutik, and A. V. Tananaev, "Numerical investigation of three-dimensional MHD flow in a curved channel of rectangular cross section," *Magnetohydrodynamics*, vol. 14, no. 4, pp. 458–462, 1978.

[93] T. N. Aitov, A. I. Kalyutik, and A. V. Tananaev, "Numerical analysis of three-dimensional MHD flow in channel with abrupt change of cross section," *Magnetohydrodynamics*, vol. 19, no. 2, pp. 223–230, 1983.

[94] J. Walker, "Laminar duct flows in strong magnetic fields," *Liquid-Metal Flows and Magnetohydrodynamics, H. Branover, PS Likoudis and M. Moon (Eds), American Institute of Aeronautics and Astronautics (new-York)*, vol. 2, pp. 3–16, 1986.

[95] K. McCarthy and M. Abdou, "Analysis of liquid metal MHD flow in multiple adjacent ducts using an iterative method to solve the core flow equations," *Fusion engineering and design*, vol. 13, no. 4, pp. 363–380, 1991.

[96] S. Cuevas, B. Picologlou, J. Walker, and G. Talmage, "Liquid-metal MHD flow in rectangular ducts with thin conducting or insulating walls: laminar and turbulent solutions," *International journal of engineering science*, vol. 35, no. 5, pp. 485–503, 1997.

[97] A. Sterl, "Numerical simulation of liquid-metal MHD flows in rectangular ducts," *Journal of Fluid Mechanics*, vol. 216, pp. 161–191, 1990.

[98] T. Kunugi, M. Tillack, and M. Abdou, "Analysis of liquid metal MHD fluid flow and heat transfer using the kat code," *Fusion Technology*, vol. 19, no. 3P2A, pp. 1000–1005, 1991.

[99] N. B. Salah, A. Soulaimani, and W. G. Habashi, "A finite element method for magnetohydrodynamics," *Computer methods in applied mechanics and engineering*, vol. 190, no. 43-44, pp. 5867–5892, 2001.

[100] S. Smolentsev, M. Abdou, C. Courtessole, G. Pulugundla, F. Li, N. Morley, R. Munipalli, P. Huang, C. Kaczynski, J. Young, *et al.*, "Review of recent MHD activities for liquid metal blankets in the US," *Magnetohydrodynamics*, vol. 53, no. 2, pp. 411–422, 2017.

[101] T. Zhou, Z. Yang, M. Ni, and H. Chen, "Code development and validation for analyzing liquid metal MHD flow in rectangular ducts," *Fusion Engineering and Design*, vol. 85, no. 10-12, pp. 1736–1741, 2010.

[102] T. Zhou, Z. Meng, H. Zhang, H. Chen, and Y. Song, "Code validation for the magnetohydrodynamic flow at high Hartmann number based on unstructured grid," *Fusion Engineering and Design*, vol. 88, no. 11, pp. 2885–2890, 2013.

[103] Z. Meng, M. Ni, J. Jiang, Z. Zhu, and T. Zhou, "Code validation for magnetohydrodynamic buoyant flow at high Hartmann number," *Journal of Fusion Energy*, vol. 35, no. 2, pp. 148–153, 2016.

[104] Z. Meng, S. Zhang, J. Jia, Z. Chen, and M. Ni, "A K-Epsilon RANS turbulence model for incompressible MHD flow at high Hartmann number in fusion liquid metal blankets," *International Journal of Energy Research*, vol. 42, no. 1, pp. 314–320, 2018.

[105] N. L. Gajbhiye, P. Throvagunta, and V. Eswaran, "Validation and verification of a robust 3-D MHD code," *Fusion Engineering and Design*, vol. 128, pp. 7–22, 2018.

[106] R. Planas, S. Badia, and R. Codina, "Approximation of the inductionless MHD problem using a stabilized finite element method," *Journal of Computational Physics*, vol. 230, no. 8, pp. 2977–2996, 2011.

[107] S. Badia, A. F. Martín, and J. Principe, "FEMPAR: An object-oriented parallel finite element framework," *Archives of Computational Methods in Engineering*, vol. 25, no. 2, pp. 195–271, 2018.

[108] P. Swain, P. Satyamurthy, R. Bhattacharyay, A. Patel, A. Shishko, E. Platacis, A. Ziks, S. Ivanov, and A. Despande, "3D MHD lead–lithium liquid metal flow analysis and experiments in a test-section of multiple rectangular bends at moderate to high Hartmann numbers," *Fusion Engineering and Design*, vol. 88, no. 11, pp. 2848–2859, 2013.

[109] C. N. Kim, "Magnetohydrodynamic flows entering the region of a flow channel insert in a duct," *Fusion Engineering and design*, vol. 89, no. 1, pp. 56–68, 2014.

[110] S. Sahu and R. Bhattacharyay, "Validation of COMSOL code for analyzing liquid metal magnetohydrodynamic flow," *Fusion Engineering and Design*, vol. 127, pp. 151–159, 2018.

[111] I. Di Piazza and L. Bühler, "A general computational approach for magnetohydrodynamic flows using the CFX code: buoyant flow through a vertical square channel," *Fusion Science and Technology*, vol. 38, no. 2, pp. 180–189, 2000.

[112] C. Mistrangelo, *Three-dimensional MHD flow in sudden expansions*. PhD thesis, FZKA, 2005.

[113] H. G. Weller, G. Tabor, H. Jasak, and C. Fureby, "A tensorial approach to computational continuum mechanics using object-oriented techniques," *Computers in physics*, vol. 12, no. 6, pp. 620–631, 1998.

[114] V. Dousset and A. Pothérat, "Numerical simulations of a cylinder wake under a strong axial magnetic field," *Physics of Fluids*, vol. 20, no. 1, p. 017104, 2008.

[115] E. M. de Les Valls *et al.*, "Modelling of integrated effect of volumetric heating and magnetic field on tritium transport in a U–bend flow as applied to HCLL blanket concept," *Fusion Engineering and Design*, vol. 86, no. 4, pp. 341–356, 2011.

[116] C. Mistrangelo and L. Bühler, "Development of a numerical tool to simulate magnetohydrodynamic interactions of liquid metals with strong applied magnetic fields," *Fusion Science and Technology*, vol. 60, no. 2, pp. 798–803, 2011.

[117] J. Feng, H. Chen, Q. He, and M. Ye, "Further validation of liquid metal MHD code for unstructured grid based on OpenFOAM," *Fusion Engineering and Design*, vol. 100, pp. 260–264, 2015.

[118] C. Kawczynski, S. Smolentsev, and M. Abdou, "Characterization of the lid-driven cavity magnetohydrodynamic flow at finite magnetic Reynolds numbers using far-field magnetic boundary conditions," *Physics of Fluids*, vol. 30, no. 6, p. 067103, 2018.

[119] R. A. Riemke, C. B. Davis, and R. R. Schultz, "RELAP5-3D code includes ATHENA features and models," in *14th International Conference on Nuclear Engineering*, pp. 209–217, American Society of Mechanical Engineers, 2006.

[120] RELAP5-3D Code Development Team, *RELAP5-3D Code Manual Volume I: Code Structure, System Models and Solution Methods.* Idaho National Laboratory, 2005. INEEL-EXT-98-00834, Rev. 4.0.

[121] S. H. Kim, M. H. Kim, D. W. Lee, and C. Choi, "Code validation and development for MHD analysis of liquid metal flow in Korean TBM," *Fusion Engineering and Design*, vol. 87, no. 7-8, pp. 951–955, 2012.

[122] M. J. Wolfendale and M. J. Bluck, "A coupled systems code-CFD MHD solver for fusion blanket design," *Fusion Engineering and Design*, vol. 98, pp. 1902–1906, 2015.

[123] M. J. Wolfendale, *A coupled systems code - CMHD solver for fusion blanket designs.* Phd thesis, Imperial College, January 2016.

[124] F. S. Hurtado, C. R. Maliska, and A. F. da Silva, "Application of flux-corrected transport to an unstructured-grid finite-volume formulation for reservoir simulation," in *Proceedings of the XXVIII Iberian Latin-American Congress on Computational Methods in Engineering CMNE/CILAMCE*, 2007.

[125] S. Aleksandrova, S. Molokov, and C. Reed, *Modeling of liquid metal duct and free-surface flows using CFX.* Argonne National Lab., 2002.

[126] L. Bühler, *Inertialess magnetohydrodynamic flows in expansions and contractions.* Forschungszentrum Karlsruhe, 2003. Tech. Rep. FZKA 6904.

[127] O. Foust, *Sodium-NaK engineering handbook*, vol. 3. Gordon & Breach Science Pub, 1972.

[128] M.-J. Ni, R. Munipalli, N. B. Morley, P. Huang, and M. A. Abdou, "Validation case results for 2D and 3D MHD simulations," *Fusion Science and Technology*, vol. 52, no. 3, pp. 587–594, 2007.

[129] X. Albets-Chico, E. Votyakov, H. Radhakrishnan, and S. Kassinos, "Effects of the consistency of the fringing magnetic field on direct numerical simulations of liquid–metal flow," *Fusion Engineering and Design*, vol. 86, no. 1, pp. 5–14, 2011.

[130] A. Tassone, F. Giannetti, and G. Caruso, "Numerical study of laminar magneto-convection in a differentially heated square duct," *Journal of Physics: Conference Series*, vol. 796, no. 1, p. 012004, 2017.

[131] L. Melchiorri, "Numerical characterization of liquid metal MHD flow in electro-conductive thick orifices with asymmetric contraction," Master's thesis, Sapienza University of Rome, January 2019.

[132] G. Sposito and M. Ciofalo, "Fully developed mixed magnetohydrodynamic convection in a vertical square duct," *Numerical Heat Transfer, Part A: Applications*, vol. 53, no. 9, pp. 907–924, 2008.

[133] R. Nygren and F. Tabarés, "Liquid surfaces for fusion plasma facing components - A critical review. Part I: Physics and PSI," *Nuclear Materials and Energy*, vol. 9, pp. 6–21, 2016.

[134] S. Siriano, "Numerical study of MHD thin-film flows for Plasma Facing Components: fundamental phenomena and code validation," Master's thesis, Sapienza University of Rome, October 2018.

[135] S. Molokov and C. Reed, *Review of free-surface MHD experiments and modeling.* Argonne National Lab., 2000.

[136] M. M. Zdravkovich, *Flow around Circular Cylinders: Volume 1: Fundamentals*, vol. 1. Oxford university press, 1997.

[137] M. M. Zdravkovich, *Flow around Circular Cylinders: Volume 2: Applications*, vol. 2. Oxford university press, 1997.

[138] C. H. Williamson, "Vortex dynamics in the cylinder wake," *Annual review of fluid mechanics*, vol. 28, no. 1, pp. 477–539, 1996.

[139] G. Ludford, "The effect of a very strong magnetic cross-field on steady motion through a slightly conducting fluid," *Journal of Fluid Mechanics*, vol. 10, no. 1, pp. 141–155, 1961.

[140] J. Hunt and S. Leibovich, "Magnetohydrodynamic flow in channels of variable cross-section with strong transverse magnetic fields," *Journal of Fluid Mechanics*, vol. 28, no. 2, pp. 241–260, 1967.

[141] J. Hunt and G. Ludford, "Three-dimensional MHD duct flows with strong transverse magnetic fields. Part 1. Obstacles in a constant area channel," *Journal of Fluid Mechanics*, vol. 33, no. 4, pp. 693–714, 1968.

[142] A. Kapila and G. Ludford, "MHD with inertia: flow over blunt obstacles in channels," *International Journal of Engineering Science*, vol. 15, no. 8, pp. 465–480, 1977.

[143] G. Branover, Y. M. Gel'fgat, S. Turuntaev, and A. Tsinober, "Effect of a transverse magnetic field on velocity perturbations behind a circular cylinder swept by an electrolyte," *Magnetohydrodynamics*, vol. 5, no. 3, pp. 41–46, 1969.

[144] J. Josserand, P. Marty, and A. Alemany, "Pressure and drag measurements on a cylinder in a liquid metal flow with an aligned magnetic field," *Fluid dynamics research*, vol. 11, no. 3, p. 107, 1993.

[145] R. Klein, A. Pothérat, and A. Alferenok, "Experiment on a confined electrically driven vortex pair," *Physical Review E*, vol. 79, no. 1, p. 016304, 2009.

[146] J. Lahjomri, P. Capéran, and A. Alemany, "The cylinder wake in a magnetic field aligned with the velocity," *Journal of Fluid Mechanics*, vol. 253, pp. 421–448, 1993.

[147] G. Mutschke, G. Gerbeth, V. Shatrov, and A. Tomboulides, "Two-and three-dimensional instabilities of the cylinder wake in an aligned magnetic field," *Physics of Fluids*, vol. 9, no. 11, pp. 3114–3116, 1997.

[148] V. Shatrov, G. Mutschke, and G. Gerbeth, "Numerical simulation of the two-dimensional flow around a circular cylinder," *Magnetohydrodynamics*, vol. 33, no. 1, pp. 2–10, 1997.

[149] G. Mutschke, G. Gerbeth, V. Shatrov, and A. Tomboulides, "The scenario of three-dimensional instabilities of the cylinder wake in an external magnetic field: A linear stability analysis," *Physics of Fluids*, vol. 13, no. 3, pp. 723–734, 2001.

[150] D. Grigoriadis, I. Sarris, and S. Kassinos, "MHD flow past a circular cylinder using the immersed boundary method," *Computers & Fluids*, vol. 39, no. 2, pp. 345–358, 2010.

[151] Z. E. Kalis, A. Tsinober, A. Shtern, and E. Shcherbinin, "Flow of conducting fluid past circular cylinder in the presence of transverse magnetic field," *Magnetohydrodynamics*, vol. 1, no. 1, pp. 18–28, 1965.

[152] A. Tsinober and P. Shtern, "Experimental investigation of the pressure distribution for constrained MHD flow past cylinders," *Magnetohydrodynamics*, vol. 9, no. 1, pp. 12–18, 1973.

[153] G. Mutschke, V. Shatrov, and G. Gerbeth, "Cylinder wake control by magnetic fields in liquid metal flows," *Experimental thermal and fluid science*, vol. 16, no. 1-2, pp. 92–99, 1998.

[154] L. Kit, Y. B. Kolesnikov, A. Tsinober, and P. Shtern, "Use of a conduction anemometer in investigating the MHD wake behind a body," *Magnetohydrodynamics*, vol. 5, no. 4, pp. 46–50, 1969.

[155] L. Kit, S. Turuntaev, and A. Tsinober, "Investigation with a conduction anemometer of the effect of a magnetic field on disturbances in the wake of a cylinder," *Magnetohydrodynamics*, vol. 6, no. 3, pp. 331–335, 1970.

[156] Y. B. Kolesnikov and A. Tsinober, "Two-dimensional turbulent flow behind a circular cylinder," *Magnetohydrodynamics*, vol. 8, no. 3, pp. 300–307, 1972.

[157] O. Andreev and Y. B. Kolesnikov, "Experimental flow around a conducting cylinder in an axial homogeneous magnetic field," *Magnetohydrodynamics*, vol. 34, no. 4, pp. 286–293, 1998.

[158] M. Frank, L. Barleon, and U. Müller, "Visual analysis of two-dimensional magnetohydrodynamics," *Physics of fluids*, vol. 13, no. 8, pp. 2287–2295, 2001.

[159] B. Mück, C. Günther, U. Müller, and L. Bühler, "Three-dimensional MHD flows in rectangular ducts with internal obstacles," *Journal of Fluid Mechanics*, vol. 418, pp. 265–295, 2000.

[160] K. Ueno, K. Saito, and S. Kamiyama, "Three-dimensional simulation of MHD flow with turbulence," *JSME International Journal Series B Fluids and Thermal Engineering*, vol. 44, no. 1, pp. 38–44, 2001.

[161] N. Kanaris, X. Albets, D. Grigoriadis, and S. Kassinos, "Three-dimensional numerical simulations of magnetohydrodynamic flow around a confined circular cylinder under low, moderate, and strong magnetic fields," *Physics of Fluids*, vol. 25, no. 7, p. 074102, 2013.

[162] Y. B. Kolesnikov and O. Andreev, "Heat transfer by cylindrical obstacles in a magnetic field," *Magnetohydrodynamics*, vol. 31, no. 4, pp. 391–396, 1995.

[163] W. K. Hussam, M. C. Thompson, and G. J. Sheard, "Dynamics and heat transfer in a quasi-two-dimensional MHD flow past a circular cylinder in a duct at high Hartmann number," *International Journal of Heat and Mass Transfer*, vol. 54, no. 5-6, pp. 1091–1100, 2011.

[164] W. K. Hussam and G. J. Sheard, "Heat transfer in a high Hartmann number MHD duct flow with a circular cylinder placed near the heated side-wall," *International Journal of Heat and Mass Transfer*, vol. 67, pp. 944–954, 2013.

[165] W. K. Hussam, A. H. Hamid, Z. Y. Ng, and G. J. Sheard, "Effect of vortex promoter shape on heat transfer in MHD duct flow with axial magnetic field," *International Journal of Thermal Sciences*, vol. 134, pp. 453–464, 2018.

[166] H. Yoon, H. Chun, M. Ha, and H. Lee, "A numerical study on the fluid flow and heat transfer around a circular cylinder in an aligned magnetic field," *International Journal of Heat and Mass Transfer*, vol. 47, no. 19-20, pp. 4075–4087, 2004.

[167] D. Chatterjee and K. Chatterjee, "Wall–bounded flow and heat transfer around a circular cylinder at low Reynolds and Hartmann numbers," *Heat Transferâ̆ĂTAsian Research*, vol. 42, no. 2, pp. 133–150, 2013.

[168] S. Udhayakumar, A. D. A. Rejeesh, T. V. S. Sekhar, and R. Sivakumar, "Numerical investigation of magnetohydrodynamic mixed convection over an isothermal circular cylinder in presence of an aligned magnetic field," *International Journal of Heat and Mass Transfer*, vol. 95, pp. 379–392, 2016.

[169] A. Tassone, M. Nobili, and G. Caruso, "Numerical study of the MHD flow around a bounded heating cylinder: Heat transfer and pressure drops," *International Communications in Heat and Mass Transfer*, vol. 91, pp. 165–175, 2018.

[170] A. Tassone, L. Gramiccia, and G. Caruso, "Three-dimensional mhd flow and heat transfer in a channel with internal obstacle," *International Journal of Heat and Technology*, vol. 36, no. 4, pp. 1367–1377, 2018.

[171] M. Tillack, A. Ying, and H. Hashizume, "The effect of magnetic field alignment on heat transfer in liquid metal blanket channels," in *Fusion Engineering, 1989. Proceedings., IEEE Thirteenth Symposium on*, pp. 376–379, IEEE, 1989.

[172] ANSYS, Inc., *CFX Solver Modeling Guide*. ANSYS, 2018.

[173] A. Del Nevo, E. Martelli, P. Agostini, P. Arena, G. Bongiovì, G. Caruso, G. Di Gironimo, P. Di Maio, M. Eboli, R. Giammusso, *et al.*, "WCLL breeding blanket design and integration for 2015: status and perspectives," *Fusion Engineering and Design*, 2017.

[174] J. Sommeria and R. Moreau, "Why, how, and when, MHD turbulence becomes two-dimensional," *Journal of Fluid Mechanics*, vol. 118, pp. 507–518, 1982.

[175] S. Subramanian, P. Swain, A. Deshpande, and P. Satyamurthy, "Effect of Hartmann layer resolution for MHD flow in a straight, conducting duct at high Hartmann numbers," *Sadhana*, vol. 40, no. 3, pp. 851–861, 2015.

[176] J. Shercliff, "The boundary layer on a wall nearly parallel to a magnetic field," *Zeitschrift für angewandte Mathematik und Physik ZAMP*, vol. 32, no. 5, pp. 546–554, 1981.

[177] M. Sahin and R. G. Owens, "A numerical investigation of wall effects up to high blockage ratios on two-dimensional flow past a confined circular cylinder," *Physics of Fluids*, vol. 16, no. 5, pp. 1305–1320, 2004.

[178] X. Wang and S. Tan, "Near–wake flow characteristics of a circular cylinder close to a wall," *Journal of Fluids and Structures*, vol. 24, no. 5, pp. 605–627, 2008.

[179] E. Martelli, G. Caruso, F. Giannetti, and A. Del Nevo, "Thermo-hydraulic analysis of EU DEMO WCLL breeding blanket," *Fusion Engineering and Design*, vol. 130, pp. 48–55, 2018.

[180] H. Madarame, K. Taghavi, and M. Tillack, "The influence of leakage currents on MHD pressure drop," *Fusion Technology*, vol. 8, no. 1P2A, pp. 264–269, 1985.

[181] T. Q. Hua and J. S. Walker, "MHD flow in rectangular ducts with inclined non-uniform transverse magnetic field," *Fusion engineering and design*, vol. 27, pp. 703–710, 1995.

[182] N. R. Draper and H. Smith, *Applied regression analysis*, vol. 326. John Wiley & Sons, 2014.

[183] Y. Chen, U. Fischer, P. Pereslavtsev, and F. Wasastjerna, *The EU Power Plant Conceptual Study: Neutronic Design Analyses for Near Term and Advanced Reactor Models*. Forschungszentrum, 2003.

[184] J. Aubert, G. Aiello, C. Bachmann, P. A. Di Maio, R. Giammusso, A. L. Puma, A. Morin, and A. Tincani, "Optimization of the first wall for the DEMO water cooled lithium lead blanket," *Fusion Engineering and Design*, vol. 98, pp. 1206–1210, 2015.

[185] A. Tassone, G. Caruso, F. Giannetti, and A. Del Nevo, "MHD mixed convection flow in the WCLL: heat transfer analysis and cooling system optimization," *Fusion Engineering and Design*, 2018. (submitted).

[186] W. Wagner, R. J. Cooper, A. Dittmann, J. Kijima, A. Kretzschmar, Hans-Joachim Kruse, R. Mareš, K. Oguchi, H. Sato, I. Stöcker, O. Šifner, Y. Takaishi, I. Tanishita, J. Trübenbach, and T. Willkommen, "IAPWS industrial formulation 1997 for the thermodynamic properties of water and steam," *IAPWS-IF97*, pp. 7–150, 2008.

[187] F. R. Menter, "Two-equation eddy-viscosity turbulence models for engineering applications," *AIAA journal*, vol. 32, no. 8, pp. 1598–1605, 1994.

[188] P. Di Maio, P. Arena, G. Bongiovì, P. Chiovaro, R. Forte, and S. Garitta, "On the optimization of the first wall of the DEMO water-cooled lithium lead outboard breeding blanket equatorial module," *Fusion Engineering and Design*, vol. 109, pp. 335–341, 2016.

[189] K. Jiang, E. Martelli, P. Agostini, S. Liu, and A. Del Nevo, "Investigation on cooling performance of WCLL BB First Wall for EU DEMO," *Fusion Engineering and Design*, 2018. (submitted).

[190] P. Di Maio, P. Arena, G. Bongiovì, P. Chiovaro, A. Del Nevo, and M. Richiusa, "On the thermo-mechanical behaviour of DEMO water-cooled lithium lead equatorial outboard blanket module," *Fusion Engineering and Design*, vol. 124, pp. 725–729, 2017.

[191] D. Sornin, A. Li Puma, and C. Schweier, *WPBB-DEL- BB-7.1.1-T003-D001, EFDA D 2NBQ6U, Assessment of Manufacturing Technologies for Blanket Development (WCLL) / 2017 status of WCLL manufacturing activities*. Eurofusion, 2018.